Design and development of magnetic resonance imaging (MRI) compatible tissue mimicking phantoms for evaluating focused ultrasound thermal protocols.

A thesis submitted to the graduate faculty in partial fulfilment of the requirements for the Degree of Doctor of Philosophy in Biomedical Engineering

Georgios Menikou

Electrical, Electronic Engineering

School of Mathematics, Computer Science and Engineering

City, University of London

June 2017

Acknowledgements

I would like to express my gratitude to my supervisors, Dr. Christakis Damianou and Dr. Panayiotis Kyriacou whose support, expertise and insight added considerably to my research goals. Also a very special thanks goes out to Christos Yiallouras and MarinosYiannakou for their scientific assistance.

I would like to thank my beloved parents Menikos and Sotiroulla for supporting me emotionally, spiritually and financially throughout my life.

Finally and most importantly, I would like to thank my wife Alexandra for her continuous support, encouragement and quiet patience that undoubtedly contributed towards the completion of this thesis.

Abstract

Animal models are often used to test the efficacy and safety of clinical applications employing focused ultrasound that range in various stages of research, development and commercialization. The animals are usually subjected to conditions that cause pain, distress and euthanasia. Access to cadaveric models is not easy and affordable for all research institutions, whereas conservation and changes of their physical properties over time can be a delimiting factor for translational research. The above set the motivation for this project, which its primary objective is to design and develop appropriate tissue mimicking phantoms using a simplistic and cost effective methodology. These phantoms are expected to contribute in reducing the need for animal testing and allow researchers to get hands experience with tools that will promote and accelerate testing in focused ultrasound thermal protocols. The main requirements for these phantoms are to be geometrically accurate, compatible with magnetic resonance imaging (MRI) and to be composed of materials that approximate the acoustic and thermal properties of the replicated tissues.

Throughout the duration of the project three ultrasonic composite phantoms (head, femur bone-muscle and breast-rib) were developed. The acoustic properties of candidate materials were assessed using pulse-echo immersion and through transmission techniques. The thermal properties were estimated by observing the rate of heat diffusion following a sonication in the soft tissue parts with MR thermometry. Acrylonitrile butadiene styrene (ABS) was used to replicate bone tissue, where its acoustic attenuation coefficient was found to be 16.01 ± 6.18 dB/cm at 1 MHz and the speed of sound at 2048 ± 79 m/s. Soft tissue parts consisted out of agar-based gels doped with varying concentrations of additives that controlled the relative contribution of acoustic absorption (evaporated milk) and scatter (silica dioxide) to total attenuation independently. Brain tissue phantom (2 % w/v agar - 1.2 % w/v SiO_2 - 25 % v/v evaporated milk) matched an attenuation coefficient of 0.59 ± 0.05 dB/cm-MHz whereas muscle and breast mimicking phantom (2 % w/v agar - 2 % w/v SiO_2 - 40 % v/v evaporated milk) were estimated of inducing an attenuation coefficient of the order of 0.99 ±0.08 dB/cm-MHz. The speed of sound for the brain and muscle/breast recipe were estimated at 1485 ± 12 m/s and 1529 ± 13 m/s respectively. The thermal conductivity of the brain phantom was estimated to be 0.52 ± 0.06 W/mº-C and 0.57 ± 0.10 W/mº-C for the muscle/breast phantom. The acoustic and thermal properties of candidate materials were within range of the replicated tissues extracted from literature, except the speed of sound in ABS compared which was lower compared to bone (~3000 m/s).

Three dimensional models of bone parts (skull, femur, rib) were reconstructed in Standard Tessellation Language (STL) format by segmenting bony tissue of interest from adult human computed tomography (CT) images. The STL bone models were 3D printed in ABS using a fused deposition modelling (FDM) machine. The final composite phantoms were fabricated by molding the agar based soft tissue phantoms inside/around the ABS bone phantoms. The functionality of all three composite phantoms was assessed with focused ultrasound sonications applied by a 1 MHz single element transducer while temperature was monitored with 1.5 Tesla MRI scanner. A spoiled gradient recalled (SPGR) pulse sequence was used to produce phase images that were analyzed using a custom coded software developed in Matlab that employed proton-resonance frequency shift (PRFS) thermometry.

Keywords: Focused ultrasound, MRI, phantoms, PRFS thermometry, skull, brain, breast, rib, bone.

Table of Contents

List of Figures

List of Tables

List of abbreviations

The following table describes the significance of various abbreviations and acronyms used throughout the thesis.

Abbreviation	*Meaning*
ABS	Acrylonitrile Butadiene Styrene
ARFI	Acoustic Radiation Force Imaging
ASPA	Animals (Scientific Procedures) Act
ASSET	Array Spatial Sensitivity Encoding Technique
ASTM	American Society of Testing and Materials
BBB	Blood Brain Barrier
BCT	Breast Conserving Therapy
BHT	Bioheat equation
BNC	Bayonet Neill–Concelman connector
BSA	Bovine Serum Albumin
BUA	Broadband Ultrasound Attenuation
CAD	Computer-Aided Design
CE	Contrast Enhancement
CEM	Cumulative Effective Minutes
CSF	Cerebrospinal Fluid
CT	Computed Tomography
DC	Direct Current
DFOV	Display Field of View
DICOM	Digital Imaging and Communications in Medicine
DOX	Doxorubicin
DQA	Daily Quality Assurance
DW	Diffusion Weighted
EBRT	External Beam Radiotherapy
ET	Essential Tremor
ETL	Echo Train Length
FA	Fibroadenomas
FDA	Food and Drugs Administration
FDM	Fused Deposition Modelling
FGRE	Fast Gradient Recalled Echo
FRFSE	Fast Recovery Fast Spin Echo
FSE	Fast Spin Echo
FSPGR	Fast Spoiled Gradient Recalled Echo
FUS	Focused Ultrasound Surgery
FWHM	Full Width at Half Maximum
GE	General Electric
GPFLEX	General Purpose Flexible
GRE-EPI	Gradient Recalled Echo-Echo Planar Imaging
GUI	Graphic User Interface
HD	High Definition
HIFU	High Intensity Focused Ultrasound
HU	Hounsfield Units
ICH	Intracerebral Hemorrhage
KZK	Khokhlov-Zabolotskaya-Kuznetsov

LAR	Least Absolute Residuals
MCA	Middle Cerebral Artery
MR	Magnetic Resonance
MRI	Magnetic Resonance Imaging
MRTI	Magnetic Resonance Temperature Imagine
NEMA	National Electrical Manufacturers Association
NEX	Number of Excitations
NIPAM	N-isopropylacrylamide
NMR	Nuclear Magnetic Resonance
NPV	Non Perfused Volume
PVA	Polyvinyl Alcohol
PRF	Proton Resonance Frequency
PRFS	Proton Resonance Frequency Shift
PUM	Piezoelectric Ultrasound Motors
PZT	Lead zirconate titanate
QM	Quantum Mechanics
rBW	Receiver Bandwidth
RF	Radio Frequency
RSD	Resultant Second Difference
rt-PA	Recombinant Tissue Plasminogen Activator
SNR	Signal-to-Noise Ratio
STL	Standard Tessellation Language
TE	Echo Time
TR	Repetition Time
TRX	Transducer
US	Ultrasound

1 Introduction

1.1 Motivation behind the project

Currently there is a large and growing number of clinical applications employing high intensity focused ultrasound (HIFU) that ranges in various stages of research, development and commercialization. Nearly in all stages of research and development, animal models are used to mimic the clinical setting of the tested applications. The animals are usually subjected to conditions that cause pain, distress or euthanasia. This ethical dilemma sets the motivation for this project, which its primary objective is to design and develop appropriate phantoms that will contribute in reducing animal testing in the area of focused ultrasound.

The preliminary results from various studies assessing the efficacy and safety of the modality clearly show that HIFU can be a disruptive technology for treating patients that would normally require an invasive approach or the use of treatments that are accompanied with high risks of toxicity. Consequently it is very important to accelerate research in the field in order to overcome the remaining obstacles that retain HIFU from becoming a standard treatment option. Therefore it is very important that the cost of fabricating these phantoms is low enough to allow researchers worldwide with limited resources to get hands on such tools.

1.2 History and Background of Ultrasound

Ultrasound technology was initially used in sonars during World War II and as a non-destructive testing tool for detecting material corrosion. It was only in the late 60's when the first commercial systems capable of producing 2D grayscale real time images of ultrasound echoes where used in diagnostic radiology. Nowadays diagnostic ultrasound imaging is an indispensable modality for any radiology department. It offers a quick and safe way of visualizing internal body structures in the search of disease or excluding pathology. The basic principle of diagnostic systems is to send ultrasound waves through the body of a patient and an image is formed by recording the intensity and travel time of echoes reflected at tissue interfaces. Ultrasound medical imaging technology has progressed significantly and modern systems can process ultrasound echoes accordingly to fuse anatomical images with quantitative maps of blood flow, tissue displacement, tissue stiffness, etc. Increased computing and processing power has also made 3D and 4D

ultrasound imaging possible. It is therefore not surprising that ultrasound imaging is the primary choice in diagnosing cardiovascular disease and obstetrics.

The use of ultrasound in medicine is not limited in diagnosis but it is also met in therapeutic applications. High Intensity Focused Ultrasound (HIFU) uses acoustic energy to non-invasively heat and destroy pathological tissues. Extracorporeal shock wave lithotripsy is an effective way of non-invasively fragmenting gallbladder or liver stones. Ultrasound is also used as a hyperthermic modality in physiotherapy sessions for accelerating bone healing and reducing inflammation caused by rheumatism, tendinitis or joint injuries.

1.3 Definition of High Intensity Focused Ultrasound (HIFU)

HIFU also referred as Focused Ultrasound Surgery (FUS), is an application that focuses a high intensity acoustic beam over a small region. Focusing leads to beam intensity amplification at a particular distance away from the HIFU transducer known as the focal length which occurs as a result of constructive interference. It is used for a number of clinical applications that are currently in different stages of research, development and commercialization [1]. For the majority of applications, HIFU can be delivered non-invasively making it a very attractive alternative to conventional therapies.

1.4 HIFU induced thermotherapy

HIFU can be justifiably categorized as a thermal treatment method. The focused ultrasonic beam raises locally the temperature of the targeted region by acoustic absorption and under certain conditions this can be sufficient enough to cause cellular necrosis, while adjacent tissue is sustained at sub lethal heat levels. It is worth mentioning that cellular death in HIFU is not only a result of thermal injury. Cellular apoptosis has been observed in in vivo experiments [2] even at sub-lethal thermal doses as a result of HIFU induced mechanical effects like cavitation, micro-streaming, and radiation force.
Open surgery, radiotherapy and chemotherapy were the gold standard until recently for treating solid tumours and metastatic disease. HIFU tries to offer a new solution to modern medicine that reduces the risk to patient's health associated with the conventional treatment modalities mentioned above [2]. HIFU is a completely non-invasive procedure, free of incisions and blood transfusions. The risk from pre and postoperative complications like infections, internal organ injury and severe haemorrhage is limited.

There is usually no need for a general anaesthesia in HIFU applications. The patient is usually fully conscious or can be lightly sedated or under light general anaesthesia and is subjected to minimum discomfort and pain. Another advantage is that there is no limit in the number of HIFU treatment sessions that a patient can receive in case of a malignant disease recurrence, unlike radiotherapy and chemotherapy. These advantages can potentially contribute overall to a reduction in recovery time and hospital stay along with an improvement in quality of life for the treated patients.

HIFU is prone to some limitations like all other treatment modalities [3]. All ultrasound specific artifacts that appear in diagnostic imaging system pose limitations to safety and efficiency in FUS systems. Targets that lie deeply in relation to bones like liver lesions are difficult to treat because of the heavy scattering and attenuation effects. Gas filled tissues like bowels and lungs reflect the beam backwards and the reflected high acoustic energy is absorbed by tissues located between the target and the transducer. Rarefaction artifacts are also known to divert the beam and deposit heat in tissue adjacent to the target. Fibrotic and fatty tissues attenuate and absorb the acoustic energy differently from soft tissue leading to unpredictable distributions of cell death. Focal sizes in HIFU are in the millimetre range and therefore treatment of large targets is time consuming. HIFU is not the only thermal treatment available. Some of the major alternative thermotherapies are listed below [4]:

Radiofrequency ablation (RFA) is the most common local thermal treatment [5], [6]. A needle like electrode is seeded inside the region of interest and an RF alternating current is passed through a closed loop circuit (RF generator- RF electrode – patient grounding pads). The current agitates ions that lie in surrounding tissue which is ablated by the induced frictional heat.

Microwave ablation is a technique where microwave antennae are positioned usually percutaneously under image guidance near the region of interest [7], [8]. Microwave radiation produced is absorbed from water content in tissue which sets the water molecules in oscillatory motion. Heat produced by frictional losses is sufficient to lead to coagulative necrosis.

Laser ablation is achieved by positioning a cannula interstitially and guide through it laser fibres. Laser radiation is emitted in tissue specific wavelengths to optimize optical absorption. The absorption of the laser energy translates to heat which conducts to the surrounding tissue [9], [10].

Cryoablation is a therapeutic modality that involves the percutaneous insertion of a needle-like applicator (cryoprobe) to the target site under imaging guidance (CT or ultrasound (US))[11], [12]. The cryoprobe is a hollow tube that allows the circulation of liquid nitrogen or argon gas cryogens. The tip of the cryoprobe creates extremely cold temperatures and destroys the surrounding tissue through multiple freeze-thaw cycles.

1.5 Physics of ultrasound.

Ultrasound belongs to the family of sound waves that corresponds to the transfer of energy via the propagation of a pressure wave in a medium. The prefix term Ultra indicates the fact that these pressure waves vibrate at frequencies higher than the audible human range (> 20 kHz). Waves produced by piston like ultrasound transducers cycle periodically in a sequence of compressions and rarefactions. The distance travelled by an ultrasound pressure wave in one cycle is known as the wavelength (λ) and it is interrelated with the velocity (v) of the wave and the frequency (f):

$$v = f \times \lambda \tag{1.1}$$

Unlike electromagnetic waves that can travel in vacuum, sound waves require an elastic medium to propagate its mechanical disturbance. Elastic mediums refer to any material that will not be permanently deform from its original structural state when disturbed and they can generally be liquids or solids. Another major difference with electromagnetic waves is that the medium's particles oscillate parallel to the direction of propagation of the wave (longitudinal wave). The source of the mechanical disturbance in the medium sets the molecules of the medium in to vibration and the pressure wave travels through. The exerted pressure creates periodic compressions and rarefactions of the medium's density which travel at the speed of the wave.

1.6 Definition of ultrasound transducers.

In general terms a transducer is any device that can convert one form of energy to another. Ultrasound transducers convert electrical energy to mechanical energy and vice versa. Ultrasound transducers are made out of piezoelectric crystals.

1.6.1 Piezoelectric effect.

Piezoelectricity refers to the property possessed by some crystalline materials. These crystals polarize and develop a potential difference across their faces when they are under a mechanical stress. The amplitude of the induced voltage is proportional to the

force/pressure exerted. The phenomenon works reversely since the application of a radiofrequency voltage across the faces of the crystal induces a periodic displacement of the faces at the same frequency. The piezoelectric effect is sustained below a temperature that is characteristic to each type of crystal and it is better known as the Curie point.

1.6.2 Piezoelectric materials used in medical ultrasound systems.

Ultrasound probes in diagnostic and therapeutic applications use solely piezoelectric materials. Usually the materials used for clinical purposes are man-made ferroelectrics like barium titanate, lead metaniobate, and lead zirconate titanate (PZT). These artificially made materials can be manufactured to be superior from naturally occurring crystals since they can possess a much higher electromechanical coupling coefficient. The electromechanical coefficient correlates to the efficiency of a crystal in converting electrical energy to mechanical and vice versa. The basic properties of selected piezoelectric crystals are showed in Table 1-1.

Table 1-1: Properties of Piezoelectric Materials used in Medical Ultrasound [13].

Materials	**Electromechanical Coupling Coefficient (K_c)**	**Curie Point (^oC)**
Quartz	0.11	550
Rochelle salt	0.78	45
Barium titanate	0.30	120
PZT-4	0.70	328
PZT-5	0.70	365

Modern ultrasound technologies employ composite piezoelectric materials that have a lower acoustic impedance from monolithic equivalents. The acoustic coupling of composite crystals with biological tissue is improved. Additionally, unwanted lateral propagation modes are suppressed by the inhomogeneous microstructure of the composite material.

1.7 Instrumentation of an ultrasound transducer.

The active element of an ultrasound transducer is made out of piezoelectric materials described in the previous section. The vibrations are induced by electrodes connected at its front and back surfaces. Maximum conversion from electrical to acoustic

energy is achieved when the active element is driven at its resonance frequency. The resonance frequency of the crystal depends on its thickness. When the thickness is equal to half wavelength (*λ/2*) of its resonance frequency, compression waves moving towards the crystal's centre are in phase with the next cycle of expansion-contraction and interfere constructively. This principle stands for thicknesses equal to odd multiples of *λ/2* but one has to consider that the extra thickness will attenuate the wave further. The back surface is covered with a backing material that is highly attenuative. By choosing a backing material with acoustic impedance closely matched to the active element's impedance, the emitted sound from the back surface is absorbed and no reflections propagate in the forward direction. A thin wear plate (matching layer) covers the front place of the crystal and its purpose is to acoustically match the active element with the medium. The selection of its thickness is crucial to bring in to phase the wave generated by the active element in the forward direction with the wave internally reflected at the faces of the matching layer. The two waves are back in phase when they exit, if the thickness of the matching layer is set to *λ/4.* A diagram of an ultrasonic transducer with its main components is shown in Figure 1.1.

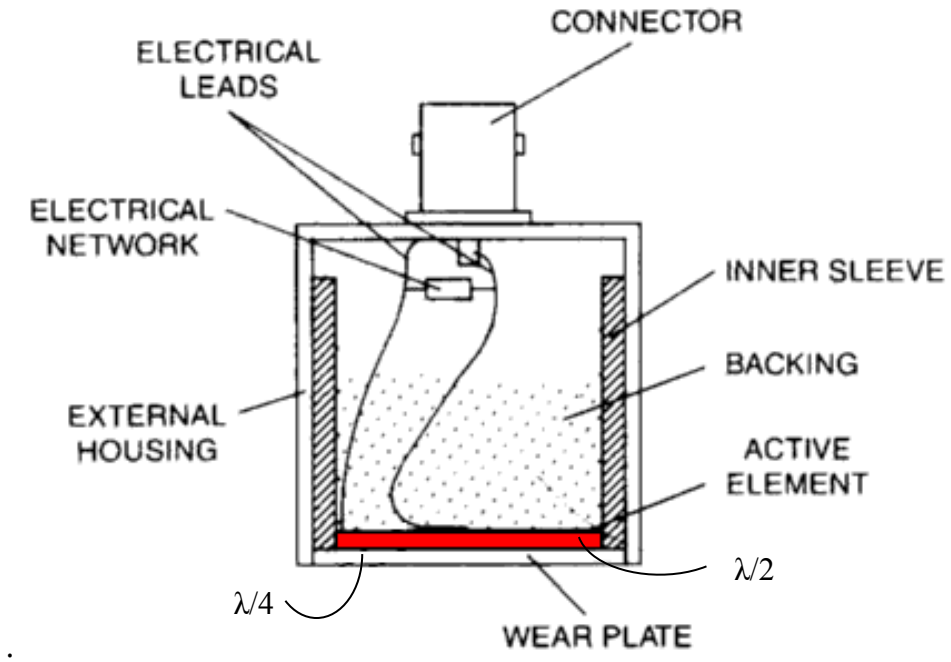

Figure 1.1: Components diagram of an ultrasonic transducer.

The active element is driven by an RF digital pulse generator. The generator allows for manual selection of frequency, waveform and voltage and can operate in continuous or pulsed wave mode. The output signal is fed to an amplifier for power amplification before reaching the active element. The amplified signal reaches the crystal through a matching

reaches the crystal through a matching circuit that matches the electrical impedance of the transducer to the amplifier. Signal conversion and transmission is optimized by observing the forward and reflected power. The output power of the transducer can be calculated by calibrating the net electric power versus acoustic power.

1.7.1 Focused Ultrasound Transducers.

Hyperthermia systems that use the thermal effects of ultrasound, employ focused transducers. Focusing the beam, amplifies the intensity at the focus compared to regions that fall outside the focal zone, making it possible to reach ablative temperatures. The effect of focusing is possible by manufacturing piezoelectric crystals with spherical geometry or through an assembly of a crystal coupled with an acoustic lens [14]. Focusing is also feasible through arrays of small transducers, which their phase and amplitude can be controlled simultaneously and independently [2]. Focusing is not the only function of phased arrays since they can steer the beam anywhere in front of the array and virtually at any depth. Phased arrays are the method of choice for the majority of clinical applications because of the obvious offered versatility along with the possibility of distortion correction of waves propagating through bone.

Each element of the phased array transducer is connected through an impedance matching circuit to a channel of the power generator/amplifier for controlling independently the phase and amplitude of the driving signal. The complexity of putting together the required hardware increases the cost and size of the phased array. In large phased array systems, the inter-element distance is a limiting factor that governs steering capabilities and the formation of grating lobes that deposit acoustic energy in unwanted directions [15].

1.8 Speed of ultrasound

The speed at which the disturbance propagates through any medium is strongly dependent on the medium's physical properties. Typical propagation speeds of ultrasound in biological tissue are shown in Table 1-2.

Table 1-2 Typical propagation speeds in biological tissue [16], [17].

Tissue	Temp (°C)	Speed of ultrasound (m/s)
Human Soft Tissues		
Brain	22 - 40	1460 - 1580

Skeletal Muscle	24 - 37, *in vivo*	1500 - 1610
Breast (pre-menopausal)	*in vivo*	1450 - 1570
Breast (post-menopausal)	*in vivo*	1430 - 1520
Liver	37, *in vivo*	1522 - 1607
Spleen	37, *in vivo*	1567
Kidney	37	1560
Human Bone Tissues		
Skull bone, whole	37	2590 - 2960
Skeletal long bones, whole	*in vivo*	3190 - 3406
Cortical bone	23	1630 - 4040
Trabecular bone	-	1688 - 2084

Gaseous media are made of molecules sparsely distributed and loosely bound that need to travel a long distance before they influence their neighbouring molecule in the direction of propagation. In reverse analogy, solids are densely populated with a constrained molecular structure that favours a very fast propagation. In biological tissues ultrasound propagates in a wide range of velocities. The two extremes consist of the lungs rich in atmospheric air where sound travels slowly and bones where propagation is relatively fast. In soft tissues, ultrasound propagates in intermediate speeds which are relatively constant. Velocity changes at tissue interfaces do not affect the frequency of the acoustic wave, but alter its wavelength according to Equation (1.1). Additionally reflection, refraction and transmission, which are all properties of ultrasound, are characteristic of the propagation's velocity.

1.9 Reflection of ultrasound at interfaces

Propagation of ultrasound involves transmitting through interfaces of different tissues. The amount of the incident acoustic energy that manages to pass the interface is highly dependent on the media properties. More specifically the matching of the acoustic impedances of the adjacent media governs the amount acoustic energy reflected.

Acoustic impedance *(Z)* refers to the intrinsic property of any material or tissue in opposing the disturbance from a longitudinal wave propagation. Typical impedance values expressed in Rayl units for different biological tissues and materials are demonstrated in Table 1-3.

Table 1-3: Acoustic impedances for different Biological Tissues [18], [19].

Biological Tissue	**Acoustic Impedance (MRayl)**
Water	1.48

Brain	1.60
Breast	1.64
Fat	1.38
Liver	1.69
Blood	1.66
Kidney	1.65
Skeletal Muscle	1.68 - 1.69
Bone	5.32

The degree of this material–specific opposition to wave propagation is proportional to the medium density (ρ) and the speed of sound (v).

$$\boldsymbol{Z = \rho \times v} \tag{1.2}$$

The fraction of reflected energy (R) at an interface between two materials with mismatched impedances is given by the following expression, where Z_1 and Z_2 refer to the impedances of each material.

$$\boldsymbol{R = \left(\frac{Z_2 - Z_1}{Z_2 + Z_1}\right)^2} \tag{1.3}$$

It is straightforward to deduce that at interfaces with great impedance mismatch like air/tissue or tissue/bone the beam will be strongly reflected and very little if at all will be transmitted. Strong reflections produced from returning echoes to the transducer will define the tissue interface clearly in a diagnostic examination but the overall effect can be deleterious for imaging tissue that resides deeper. Similarly in therapeutic applications, propagation through acoustic windows that induce strong reflections should be avoided, since no energy will be deposited at treatment site. The direction of the reflected wave is predictable if the incident wave strikes on a smooth interface (specular reflection). The reflection is unidirectional and the angle of reflection equals the angle of incidence. This is very important in diagnostic ultrasound where transducers act as receivers. A wide angle of incidence will direct the reflected echo to an equally wide angle of reflection and therefore very little energy will be detected. In the case of non-specular reflections, where the interface is uneven and/or consists of reflective structures which are smaller in size from the ultrasound's wavelength, then the reflected wave scatters randomly in many different directions.

1.10 Attenuation in biological tissues

The term attenuation refers to sum of all loss mechanisms that reduce the intensity of the acoustic beam while propagating through tissue. The total attenuation is characterized by an exponential drop of the pressure wave's amplitude with distance travelled. Attenuative mechanisms that control the degree of penetration of the beam are presented in the following sections. Attenuation coefficients for different biological tissues measured at different frequencies are shown in Table 1-4.

Table 1-4: Acoustic attenuation coefficient for different Biological Tissues [16], [17].

Tissue	Freq (MHz)	Temp (°C)	Attenuation coefficient (dB/cm)
Human Soft Tissues			
Brain	1	25	0.6
Brain	5	25	4.5
Brain (white matter)	2.2	37	1.05
Brain (grey matter)	2.2	37	0.625
Skeletal Muscle (thigh)	4.3	*in vivo*	4.71
Breast	1.7	*in vivo*	0.5 - 1.1
Breast	7	23,37	9.5 - 12.6
Liver *(rat)	100	22	130
Spleen	2, 10	37	1, 11.5
Kidney*(pig)	2, 10	37	2, 8.5
Human Bone Tissues			
Skull bone, whole	1, 3	37	22, 78
Skull bone, outer table	1	37	14.5
Skull bone, inner table	1	37	18.7
Skull bone, diploe	1, 3	37	26 - 43, 100 - 140
Skeletal long bones	1	-	12.5
Vertebra	1	-	1.5 - 38.2
Cortical bone* (cow, femur)	1	-	6.9
Cortical bone* (pig, femur)	1	32	8.4
Trabecular bone	0.5	-	1.9 - 15.7

1.10.1 Acoustic absorption in biological tissues

Absorption is recognized by studies results as the dominant process of acoustic energy loss [20]. Classical absorption phenomena are induced by the pressure wave in biological tissue. Tissues are far from ideal elastic media and due to their characteristic viscosity they oppose to any deformation causing lag between pressure and density redistribution. Viscous forces between moving particles convert part of the wave energy

to heat. Energy is also absorbed by a spectrum of relaxation mechanisms at the macromolecular scale of tissue proteins [21]. Tissue absorption coefficient (α) is dependent on frequency and tissue type. These observations are formulated in the following empirical expression, where α_0 is the absorption coefficient per MHz, f is the frequency in MHz and n is the characteristic number of tissue type.

$$\boldsymbol{\alpha = \alpha_0 \, (f^n)} \tag{1.4}$$

Studies proved little difference of the absorption coefficient amongst different mammalian species whereas the difference was significant for different tissue types of the same species. The constitution of tissues in protein content and lipids seems to increase absorption [20].

1.10.2 Acoustic scattering in biological tissues

As mentioned in Section 1.4, ultrasound waves reflect at interfaces with an acoustic impedance mismatch. Biological tissues are "doped" with inhomogeneities that have different physical properties like density and elasticity from the surrounding tissue. If the inhomogeneity's size is comparable or smaller from the wavelength of the sound wave, this leads to a generation of a secondary scattered wave in different directions. Scattering centres found in soft tissues show a small contribution to overall attenuation through scattering since their density and elasticity are close to the rest of the tissue. At low frequencies, this contribution does not exceed 10-15 % of the total attenuation [22] .

Unlike soft tissue, the effect of scattering becomes more important while propagating through the cancellous bone part of skeletal tissue. Cancellous bone consists of trabeculae which are complex structures of mineralized tissue with bone marrow with very different acoustic properties [23]. The solid matrix of the interconnected trabecular elements have a mean thickness of 50-150 μm which is much smaller than the wavelength of ultrasound in bone and generate secondary scattered waves.

1.11 Ultrasound bioeffects

The interaction of ultrasound with biological tissue can lead to a variety of effects that differ in the mechanisms involved and the conditions for initiation. These are usually separated in the following thermal and mechanical effects.

1.11.1 Thermal bioeffects

Propagation of ultrasound through tissue always results in some degree of acoustic energy absorption which leads to heat generation. Thermocoagulation can only occur if temperature is elevated for an adequate amount of time. Induced heat disrupts the weak hydrogen bonds of proteins by supplying kinetic energy to molecules that vibrate violently. The threshold of the thermal dose capable of coagulation is tissue specific. Temperature elevation in a tissue depends on the absorption, the acoustic field's intensity, conductivity and the local perfusion rate. Thermal dose is quantified in terms of thermal isoeffective dose of 43ºC exposure minutes (CEM - cumulative effective minutes) [24]. The isoeffective thermal dose in CEM's can be calculated for any temperature *T* using the following expression. The constant R is derived from *in vivo* and *in vitro* studies for a variety of mammalian tissue types using the Arrhenius relationship [7–9].

$$\boldsymbol{CEM_{43^{\circ}C,T}} = \boldsymbol{tR^{(43-T)}} \tag{1.5}$$

The above expression is valid if the average temperature *T* is constant for the duration *t* of the thermal treatment. For complex heating profiles where temperature continuously changes over time as it is the case in HIFU treatments, then the thermal dose for the entire heating is given by:

$$\boldsymbol{CEM_{43^{\circ}C,Total}} = \sum \boldsymbol{tR^{(43-T)}} \tag{1.6}$$

Arrhenius plots describe the cellular survival rate at different temperatures. Although the selection of the 43^0C reference temperature is arbitrary, it is almost equal to the "break point" temperature for human cells which is around 43.5 ºC [28] . Above the "break point" temperature, a shallower slope is observed suggesting that the thermo-tolerance of cells is decreased and the rate of cell killing doubles for every degree increase in temperature. The response to hyperthermia treatment of different cell lines of humans and rodents is shown in Figure 1.2.

The break point temperature for humans (43.5 ºC) is slightly higher than rodents (43ºC) suggesting a different thermo-tolerance between difference species. Although the break point is fairly constant for cell lines of the same species, it is obvious from the data above that there is a differentiation in survival rate of different cell lines of the same species for the same temperature.

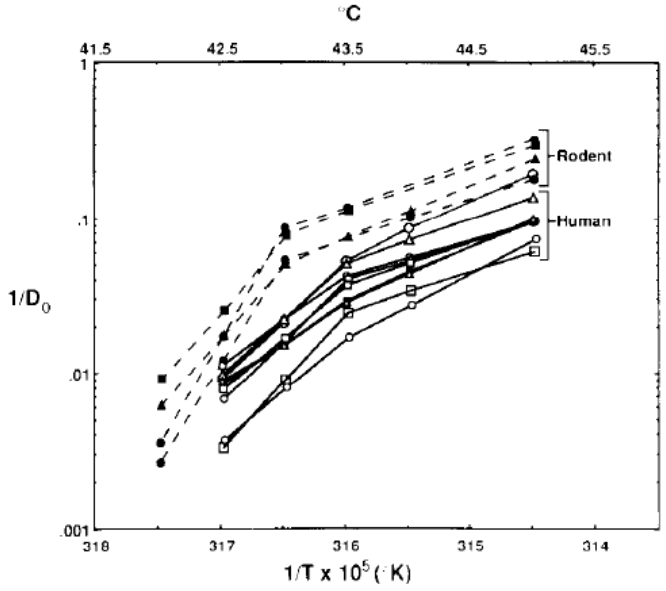

Figure 1.2: Arrhenius plots for different cell lines of humans and rodents [11].

1.11.2 Mechanical bioeffects

The effects of ultrasound interaction with biological tissue are not limited to thermal. A variety of mechanical (non-thermal) effects induced by ultrasound have been recognized by researchers and have been studied thoroughly. Some of them are exploited in some revolutionary medical applications whilst others raise patient safety risks.

Cavitation **–** The term cavitation refers to the phenomenon where the acoustic field interacts with cavities filled with gas in a medium. The prerequisite of creating such bubbles in tissue is that the tissue is a host of microscopic gaseous nuclei and the intensity of the acoustic field is large enough to diffuse dissolved gas from the tissue during every compression-rarefaction cycle. Gas bubbles can also be formed as a result of tissue boiling during HIFU treatments. Calculations from early studies have shown that microsecond pulses of ultrasound with peak intensities as low as 10–30 W/cm^2 can generate transient cavitation in water [29]. This threshold is well below typical intensities used in focused ultrasound applications.

At low acoustic field intensities, gas bubbles in tissue will oscillate with relatively small amplitude in reference with a stable radius. The expansion and contraction of the gas bubbles is out of phase with the compression-rarefaction cycle of the wave. When the pressure field is in the compression phase the bubbles contract in size and during rarefaction they expand. Through a process called rectified diffusion, bubbles can enlarge

until they reach their resonance size after a considerable number of cycles. This type of cavitation is better known as stable or non-inertial cavitation. Bubbles in stable cavitation scatter the acoustic wave in all directions (assuming that during the oscillations the bubble retains its spherical shape) and can induce an effect of fluid rapid movement known as micro streaming. If the event is near a tissue boundary, it can produce high shear forces that can disrupt cell membranes. This effect is used in HIFU applications for increasing transport of drugs or genes through impermeable cell membranes [13-14].

Inertial cavitation occurs at higher field intensities where bubbles experience a rapid growth in size after very few cycles and gain inertia. When the compression cycle arrives, the supersized bubbles cannot absorb any more energy and collapse violently. The implosion results in a shock wave of equivalent acoustic pressure of several thousands of atmospheres and high temperatures of thousands of degrees. The accompanied bioeffects of inertial cavitation include the formation of water free radicals which are chemically active and tissue integrity destruction [32]. Additionally in *in vitro* ablation studies, bubbles formed due to boiling of the tissue undergoing inertial cavitation, were found to contribute to thermal effects [33].

1.12 HIFU Safety Considerations

Patient safety during the delivery of HIFU applications depends on fine controlling of the aforementioned thermal and mechanical mechanisms.

Accidental thermal damage of critical structures (e.g. nerves) found near the focal region is a frequent safety concern that can be avoided by selecting an appropriate beam's pathway. Unwanted thermal damage from excessive heating is by all means possible even in regions far from the focus and most importantly in tissues adjacent to interfaces. Depending on the acoustic impedance mismatch (air/tissue, bone/tissue, etc.) at these interfaces, strong reflections can interfere constructively with the incident acoustic field and form a standing wave in the post focal region. Hot "spots" formed at the nodes of the standing wave are more evident in low frequency sonications used in transcranial applications that are not adequately attenuated in the intervening tissue. Additionally bones absorb acoustic energy at larger rate compared to soft tissues and their temperature can increase significantly even at mild acoustic pressures outside the focal region. The heat can conduct to adjacent soft tissues and induce secondary thermal injuries to critical structures. A typical example of the above adverse event is the transfer of heat from the conducting skull bone to brain surface or skin which can be avoided by applying external

cooling or by increasing the surface of the extracorporeal transducer. Tissue burns, pain during the procedure and visceral perforation are typical symptoms originating from thermal lesions.

Non-thermal or mechanical mechanisms related with cavitation events are always present since peak-rarefactional pressure fields used in HIFU can exceed the threshold for cavitation activation. Cavitational activity of gas bodies that pre-exist in the lung or intestines can induce local tissue injury, including cell death, rupture and hemorrhage of blood vessels. These effects are results of non-inertial cavitation where during the collapse of the vibrating gas bubbles present in tissues a shock wave is produced. The formation of a shock wave is accompanied with a local increase of temperature by several thousand kelvins and a pressure of several hundred atmospheres.

1.13 Current status of Focused Ultrasound applications.

According to the State of the Field report published in 2017 by the Focused Ultrasound Foundation [34], the current state of research and regulatory approval per application is shown in Figure 1.3. Data was collected by the Foundation from HIFU vendors and research sites worldwide demonstrates a very wide range of applications that vary from a conceptual to FDA approved stages.

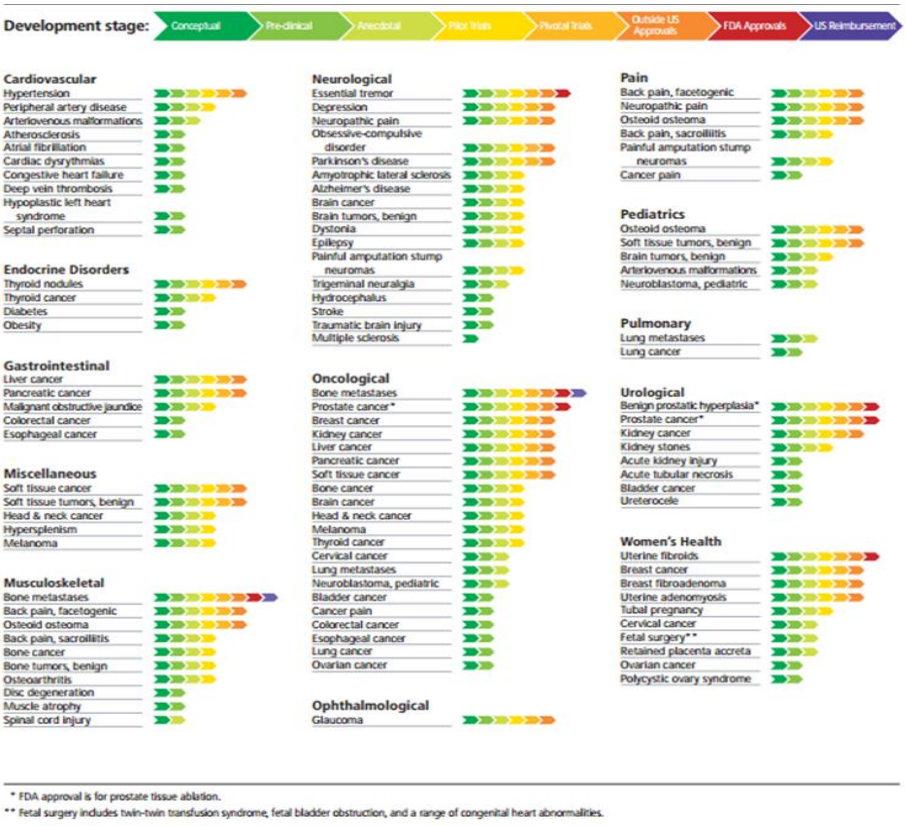

Figure 1.3: State of research and regulatory appoval categorized by indication.

The following sections run an overview of MRgFUS (Magnetic Resonance guided Focused Ultrasound Surgery) applications related to the developed composite tissue mimicking phantoms.

1.13.1 Brain MRgFUS applications.

The 'holy grail' for researchers and manufacturers in MRgFUS field is of course the application and optimization of the technology in treating brain disorders [35]. The potential of performing noninvasive transcranial surgery to treat disorders of the central nervous system has many advantages and numerous attractive applications. Noninvasive thermocoagulation of brain tumors using focused ultrasound offers an alternative option to traditional surgery, radiotherapy and chemotherapy. Early attempts involved transcranial in vivo animal studies prepared with craniotomy that tested the feasibility of detecting temperature elevations with MRI at sub ablative temperatures [36].

With the introduction of phased array systems, animal brain models in ex vivo human skulls were monitored with MR thermometry and focal lesions were correlated with histology [37]. Skull induced phase aberrations were compensated using a time reversal mirror technique, which involved field amplitude corrections calculated by using implantable hydrophones through excised human skull [15] and sheep skulls [38]. Transcranial MRgFUS through intact skulls of primates demonstrated temperature distribution in critical structures like skin, skull and brain surface while thermally ablating brain tissue [39]–[41].

Recently, in a phase I clinical trial patients with recurrent glioblastoma were treated with transcranial MRgFUS and the ultrasound focus was confirmed with MR temperature imaging [42]. Thermal coagulation of the tumor was not reached due to power limitation at the time of study, but extrapolation of the available data proved that ablation was possible with some device modifications while avoiding overheating the brain surface. Several studies have demonstrated that MRgFUS can be the future of functional neurosurgery. Essential tremor [43], [44] and Parkinson's patients [45], [46] have been treated safely and effectively with MRgFUS thalamotomy. The improvement in some of the patients was immediate and tremor symptoms were suppressed even after the first year follow up. Following the completion of a randomized, double-blind, multi-center clinical study designed for evaluating the safety and efficacy of MRgFUS thalamotomy by Elias *et al*.[47], FDA approved in 2016 the Exablate Neuro system for

the non-invasive treatment of essential tremor (ET) in patients who have not responded to medication. Patients with chronic neuropathic pain have also been treated and benefitted with considerable pain relief [48]. Cadaveric models have been used to explore the feasibility of treating trigeminal neuropathic pain along with an in vitro gel phantom encased in a human skull fitted with multiple thermocouples to examine the temperature changes in skull base while targeting the trigeminal nerve region [49].

MRgFUS has also been tested in the temporal disruption of the blood brain barrier (BBB) in animal models [50]–[52]. *In vivo* small animal and non-human primates studies showed that the disruption was possible in a range of frequencies allowing deep brain penetration and focus formation with minor adverse effects to cerebral tissue (minor extravasation) and without functional deficits [52], [53]. FUS has been applied in an attempt to treat efficiently Alzheimer's neurodegenerative disease in mouse models [54], [55] by temporarily disrupting the BBB and allowing large molecules of diagnostic and therapeutic agents to extravasate in the brain parenchyma. The introduction of ultrasound microbubbles agent during low intensity sonication proved in histological assessments to reduce the number of subjects experiencing petechiae compared to subjects treated at higher peak negative pressure fields [54]. The opening of the barrier was monitored with MRI and was confirmed in vivo with gadolinium-based, contrast enhanced MR sequences.

Sonothrombolysis is another application of therapeutic ultrasound that receives interest. *In vitro* studies of human blood clots treated with pulsed FUS in combination with a thrombolytic agent known as recombinant tissue plasminogen activator (rtPA) proved to enhance thrombolysis rate compared to rtPA treatment alone [56]. Similarly in another i*n vitro* study, enhanced lytic treatment efficacy for both tPA and liposome-loaded tPA with the parallel application of a 120 kHz unfocused ultrasound has been demonstrated [57]. The possibility of destructing transcranially an *in vitro* human clot using a hemispheric phased array FUS transducer in the absence of a thrombolytic agent, has been demonstrated [58]. In an in vivo rabbit aorta [59] and rabbit ear marginal vein [60] model studies, clots were treated with pulsed ultrasound with the synergy of rtPA whereas in other similar in vivo studies safe temperature limits and efficacy of treatment protocols was investigated [61], [62]. Currently clinical trials using sonothrombolysis are underway such as the CLOTBUST (Combined Lysis of Thrombus in Brain ischemia using transcranial Ultrasound and Systemic Recombinant Tissue-Type Plasminogen Activator rt-PA) [63], the interventional management of treating stroke patients (IMS)

[64] and the transcranial low-frequency ultrasound- mediated thrombolysis in brain ischemia (TRUMBI) [65]. The TRUMBI trial that uses non-focused, low-frequency (300 kHz) ultrasound showed an increased hemorrhage risk as compared to tPA alone. A recent simulation study [66] demonstrated that the low frequency used in this trial possibly resulted to unwanted standing waves with pressure that exceeds the threshold of inertial cavitation. This not only could possibly lead to increased hemorrhage risk, but also to elevated temperatures in the brain. Finally a randomized, placebo-controlled study with continuous transcranial 2 MHz Doppler ultrasound and perflutren-lipid microspheres was performed [67]. Table 1-5 summarizes the most important transcranial MRgFUS brain ablation studies.

Table 1-5 : Summary table of important transcranial MRgFUS brain ablation studies.

Study type	**No.**	**Purpose**	**Results and Adverse events**
Animal study (rabbit thigh and brain tissue) and soft tissue phantom with intervening ex vivo human skull [37].	4	To test a prototype MRI-compatible focused ultrasound phased array (500-elements operated at 0.7-.8 MHz) system for transcranial brain tissue ablation	Results: Sharp temperature elevations were produced. High-power sonications (600 –1080 W) produced peak temperatures up to 55°C and focal lesions were consistent with thermal tissue damage. Lesion size increased with increasing peak temperature. Adverse events: Skin burns
Animal study (rhesus monkeys) with intact skull [68].	3	To determine the amount of skull heating in an animal model with a head shape similar to that of a human.	Results: Skin and skull surface was protected by applying surface cooling. MRI thermometry was shown to be useful in detecting the tissue temperature distribution next to the bone, and it should be used to monitor the brain surface temperature. Acoustic intensity (20 s sonications) were adequate for ablating human brain provided that surface cooling is used. Adverse events: Brain surface heating
Clinical study for treating transcranially glioblastoma patients [69].	3	To assess the feasibility of transcranial magnetic resonance imaging-guided focused ultrasound surgery in glioblastoma patients.	Results: Thermal coagulation of the target was not achieved due to device power limitation. Extrapolation of the results suggested that ablation will be possible without overheating the skull. Adverse events: Sonication-related pain in one patient from heating of the dura, suggested that the targetable regions of the brain may be limited to deep, central locations in the brain.
Randomized controlled clinical trial for patients with moderate-to-severe tremor that hat had not responded to at least two trials of medical therapy [47] .	76(3:1)	MRI-guided focused ultrasound unilateral thalamotomy applied transcranially for the treatment of medication-refractory essential tremor.	Results: Hand-tremor scores improved more after focused ultrasound thalamotomy (from 18.1 points at baseline to 9.6 at 3 months) than after the sham

			procedure (from 16.0 to 15.8 points); the between-group difference in the mean change was 8.3 points (95% confidence interval [CI], 5.9 to 10.7; P<0.001). Adverse events: In the thalamotomy group reported gait disturbance in 36% of patients and paresthesias or numbness in 38%; these adverse events persisted at 12 months in 9% and 14% of patients, respectively. Intra-procedural sensations described as pain in the form of 'heat' or 'pressure' were resolved within seconds after the delivery of acoustic energy.
Uncontrolled clinical trial of patients chronic therapy-resistant neuropathic pain [48].	12	To apply the new transcranial magnetic resonance imaging-guided focused ultrasound (tcMRgFUS) technology to perform noninvasive central lateral thalamotomies (CLTs) as a treatment for chronic neuropathic pain.	Results: tcMRgFUS represents a noninvasive, precise, and radiation-free neurosurgical technique for the treatment of neuropathic pain. The procedure avoids mechanical brain tissue shift and eliminates the risk of infection. The possibility of applying sonication thermal spots free from trajectory restrictions should allow one to optimize target coverage. The real-time continuous MR imaging and MR thermometry monitoring of targeting accuracy and thermal effects are major factors in optimizing precision, safety, and efficacy in an outpatient context. Adverse events: Bleeding in the target with ischemia in the motor thalamus that occurred in one patient possibly attributed to cavitation effects or excessive heating. Study recommended maintaining sonication temperatures below 60 ºC.

1.13.2 Bone MRgFUS applications.

Bone metastases are a frequent complication observed in patients suffering from advanced stages of cancer [70], [71]. More than 60 % of advanced breast and prostate cancers, which are the most common malignancies in adults, metastasize in skeletal sites [72], [73]. Metastases in bones from other types of primary solid tumors like lung, kidneys, thyroid, bladder and melanoma also occur, but at a lower prevalence.

Pain is the most common and distressing symptom associated with bone metastases [74]. About 83 % of patients with bone metastases complain of pain at some point with wide variation in pattern and severity [75]. Therefore a lot of effort has been made in developing strategies to manage pain of patients with bone metastases and improve life quality.

For cases where there is a multifocal spread of the disease in the skeleton, pain palliation is controlled, but not limited to, by systemic therapies like hemi body irradiation

[76], [77], administration of bone-seeking radiopharmaceuticals [78]–[80], analgesic drugs and bisphosphonates [81], [82]. The gold standard though for controlling localized metastatic bone pain is external beam radiotherapy (EBRT). The mechanism underlying the analgesic effect of radiation in bone pain is not completely understood, but recent animal studies suggested that palliation is a result of reduced cancer burden and reduced osteolysis [83]. The increasing number of patients with painful bone metastases that are insufficiently palliated by radiation therapy alone, indicate the need for additional palliative localized treatments to maintain quality of life for the patients [84], [85].

Thermal ablation techniques have been extensively used as alternatives to radiotherapy for the curative and palliative treatment of primary or secondary bone tumors. The most commonly used techniques are radiofrequency ablation [86], microwave ablation [87] and laser ablation [88]. These techniques induce thermal coagulation necrosis by delivering high temperatures above 50 ºC to the target. A hypothermia technique known as cryoablation is also used by inducing cryogenic temperatures to the targeted tissue lower than -40 ºC [89]. A common characteristic of these techniques is that all require an invasive approach for implanting their delivery probes near the targeted tissue. The emerging application of FUS for the treatment and palliation of bone tumors, recently receives a lot of research interest [90]. Combined with MRI, FUS offers a completely non-invasive, and safe treatment option with excellent monitoring of the procedure. The low thermal conductivity in the periosteum and bone cortex confines the thermal damage in proximity to the treated site protecting the surrounding tissue. Additionally, the high ultrasonic absorption in bones reduces the energy levels required to induce the same thermal effect compared to soft tissues.

The major therapeutic goal of FUS applications in palliating pain from bone metastases is the denervation of the periosteum which contains pain-reporting nerve fibers through thermal coagulation necrosis [90]. The study by Catane *et al*. [91], was the first attempt to assess the safety and initial efficacy of MRI guided FUS (MRgFUS) for the palliation of pain caused by bone metastases. The treated targets involved lesions in the humerus, iliac bone, femur bone, ischium bone, sacrum and sacro-iliac joints. Pain relief was noted in the majority of patients from first assessment and prolonged improvement in pain score and reduction of analgesics dosage was reported throughout the follow up period. No severe adverse events were reported with exemption a slight increase of pain for few patients in the immediate post-procedural period that disappeared before first follow up. More clinical work in the same area were reported by Gianfelice

et al. [92], Napoli *et al*. [93], Liberman *et al*. [94], Hurwitz *et al*. [95] and Huisman *et al*. [96]. In a recent report by Joo *et al*. [97], the safety and effectiveness of the ExAblate Conformal Bone system for treating painful bone metastases was tested. Compared to the original MRgFUS systems where the transducer is fixed in the MR table, this new design has its transducer strapped on the patient with external connections. The obvious advantage of such configuration is that it enables easy and comfortable access to multiple anatomical locations. The patient position is more comfortable because lying on a painful body site is avoided, thereby decreasing discomfort experienced during treatment. Table 1-6 summarizes the most important MRgFUS bone ablation studies.

Table 1-6: Summary table of important MRgFUS bone ablation studies.

Study type	No.	Purpose	Results and Adverse events
MR-guided focused ultrasound surgery for the palliation of pain in patients with bone metastases--preliminary clinical experience [91].	13	To evaluate the safety and initial efficacy of MRgFUS for the palliation of pain caused by bone metastases, in patients for whom other treatments are either not effective or not feasible.	Results: Patients reported prolonged improvement in pain score and/or reduced analgesic dosage. Adverse events: No device-related severe adverse events were recorded. One patient was unable to tolerate the sonication-related pain and the treatment was stopped.
A multicenter study using MRgFUS for palliation of bone metastases pain [94].	31	To evaluate the safety and efficacy of MRgFUS palliative treatment of bone metastases was conducted in patients suffering from painful metastatic bone lesions for which other treatments were either ineffective or not feasible.	Results: The results suggest that MRgFUS has the ability to provide an accurate, effective, and safe noninvasive palliative treatment for patients with bone metastases. Adverse events: None
Multicenter phase III controlled clinical trial of treating patients with painful bone metastases with MRgFUS [98].	147(3:1)	This study assessed the safety and efficacy of magnetic resonance-guided focused ultrasound surgery (MRgFUS), a noninvasive method of thermal tissue ablation for palliation of pain due to bone metastases.	Results: MRgFUS is a safe and effective, noninvasive treatment for alleviating pain resulting from bone metastases in patients that have failed standard treatments. Adverse events: The most common treatment-related adverse event (AE) was sonication pain, which occurred in 32.1% of MRgFUS patients. Two patients had pathological fractures, one patient had third-degree skin burn, and one patient suffered from neuropathy.
Observational cohort study for feasibility of volumetric MRI-guided high intensity focused ultrasound (MR-HIFU) for painful bone metastases [96].	11	The first experience with volumetric MR-HIFU for palliative treatment of painful bone metastases and evaluate the technique on three levels: technical feasibility, safety, and initial effectiveness.	Results: At 3 days after volumetric MR-HIFU ablation, pain scores decreased significantly and response was observed in a 6/11 (55%) patients. At 1-month follow-up, which was available for nine patients, pain scores decreased significantly compared to baseline and 6/9 patients obtained pain response (overall response rate 67%). Adverse events: No treatment-related major adverse events were observed

1.13.3 Breast MRgFUS applications

In 2012 about 1.7 million new cases of breast-cancer were diagnosed worldwide according to the World Cancer Research Fund international [99]. Breast cancer is the most common malignant disease in women [100]. Radical mastectomy is considered the gold standard therapy [101], [102]. Another key option for breast cancer management is the breast conserving therapy (BCT) which is a less invasive therapy that potentially improves cosmesis [103]. The option of BCT is offered in combination with adjuvant treatment modalities such as radiotherapy, chemotherapy, and hormonal therapy [103]. BCT although invasive can be applied in patients with concomitant diseases, or elderly patients who are excluded from traditional surgery.

By contrast, focused ultrasound surgery (FUS) has the potential to precisely deliver coagulation to a specific location in soft tissue with an accuracy of 1 mm through the intact skin [104]. FUS can produce temperature elevations of 50 °C to 80 °C at the focus with a 10 s sonication. The delivery of this heating instantaneously induces cellular death in normal and tumor tissue [105]. Contrast enhanced MRI is usually the method of choice in breast cancer screening since it can reveal lesions that are undetected by conventional mammograms and sonograms [106], [107]. Moreover, MRI can noninvasively measure the ultrasound-induced temperature [108], [109]. In recent years, the technical feasibility of conducting FUS therapy guided by MRI has been demonstrated and improved in terms of accurate and fast temperature control in *ex vivo* tissue and animal studies *in vivo* [108]. This first experience of MRgFUS for human treatment of benign breast tumors was reported by Hynynen *et al*. in 2001 [110]. In this study it was reported that breast fibroadenomas in nine patients were treated with FUS. Eight out of the 11 lesions treated with FUS demonstrated complete or partial ablation. In 2001 Huber *et al.* [111] treated a 56-year-old patient with breast cancer using FUS. Post procedural pathologic examination indicated that FUS induced lethal and sub lethal tumor ablation without damage to the surrounding healthy tissue. In a randomized clinical trial by Wu *et al* [112], 48 women with biopsy confirmed breast cancer were randomly separated to two groups. The first control group (*n=25*) received modified radical mastectomy whilst the second group (*n=23*) was first treated with extracorporeal ultrasound guided HIFU ablation followed by modified radical mastectomy. The study concluded for the first time that US-guided HIFU is an effective, safe, and feasible treatment modality for localised

breast cancer with well-demarcated margins. The authors recognised that supplementary investigation is needed before considering extracorporeal FUS as a standard treatment option for breast cancer.

After these initial studies, Gianfelice *et al*. reported the treatment of 12 patients with invasive breast cancer using MRgFUS prior to surgery [113]. Histopathology of resected tumor in 9 patients showed that a mean of 88 % cancer tissue was necrosed. Residual tumor was observed in all cases at the periphery of the tumor mass, indicating the need for safety margins greater than 5 mm. In agreement with these findings, Zippel *et al*. [114] conducted the first phase of a human trial using MRgFUS ablation for breast cancer, using the Insightec's ExAblate 2000 system. Ten patients were treated one week prior to lumpectomy. They reported complete necrosis in only two patients (20%), and concluded that there were still several issues that needed to be resolved before MRgFUS can become a gold standard treatment for breast cancer. Furusawa *et al*. [115] conducted human trials with MRgFUS in 30 patients with breast cancer. All patients followed radical mastectomy after FUS treatment. On pathologic examination the mean percentage of tumor necrosis was 97 % of tumor volume. In another study Kovatcheva *et al.* [116] conducted clinical trials on 42 women with 51 fibroadenomas using ultrasound-guided unilateral or bilateral FUS. Ultrasound-guided FUS was well tolerated by the patients and the preliminary results showed that it could be an effective noninvasive alternative to surgery for breast fibroadenomas. Table 1-7 summarizes the most important MRgFUS breast ablation studies.

Table 1-7: Summary table of important MRgFUS breast ablation studies.

Study type	**No.**	**Purpose**	**Results and Adverse events**
Clinical feasibility study treating patients of pathological breast tissue with MRgFUS [110].	9	To test the feasibility of noninvasive magnetic resonance (MR) imaging-guided focused ultrasound surgery (FUS) of benign fibroadenomas in the breast	Results: Temperature elevations ranging between 12.8 ºC - 49.9 degrees ºC from the planned sonications were measured with MR thermometry. 8 of the 11 lesions treated demonstrated complete or partial lack of contrast material uptake on post therapy T1-weighted images. Three lesions showed no marked decrease of contrast material uptake. This lack of effective treatment was most likely due to a lower acoustic power and/or patient movement that caused misregistration. Averse events: No adverse effects were detected, except for one case of transient edema in the pectoralis muscle 2 days after therapy.
A randomized controlled clinical trial of US guided high-intensity focused ultrasound	48 (1:1)	To explore the possibility of using HIFU for the treatment of patients with	Results: Pathologic findings revealed that HIFU-treated tumor cells underwent complete

ablation for the treatment of patients with localized breast cancer [112].		localized breast cancer in a controlled clinical trial.	coagulative necrosis, and tumor vascular vessels were severely damaged. Immunohistochemical indicated that the treated tumor cells lost the abilities of proliferation, invasion, and metastasis. Adverse events: No adverse events were detected, except for one case of transient edema in the pectoralis muscle 2 days after therapy.
A preliminary phase I study for the use of MR guided focused ultrasound in breast cancer patients [114].	10	To examine the possibility of ablating breast carcinoma using MRIgFUS in place of lumpectomy.	Results: Two patients had a complete pathological response. The remaining 8 patients had varying amounts of residual tumor; 2 had microscopic foci of residual carcinoma, 3 had 10% residual tumor, and 3 had 10-30% of residual tumor. Adverse events: Procedure related pain required additional analgesia and sedation. One patient suffered from a second degree skin burn over the treated area. This adverse even suggested a better cooling is required whilst the procedure should be limited to peripheral lesions of at least 1 cm from skin and yet not in proximity to chest wall.
A multicenter ultrasound-guided high-intensity focused ultrasound treatment of breast fibroadenomas [116].	42	To assess the clinical outcome and safety of ultrasound (US)-guided high-intensity focused ultrasound (HIFU) in patients with breast fibroadenomas (FA).	Results: The FA mean baseline volume was 3.89 ml (0.34–19.66 ml). At 2-month follow-up, the mean volume reduction was 33.2% ± 19.1% and achieved significance at 6-month (59.2% ± 18.2%) and 12-month (72.5% ± 16.7%) follow-up. Adverse events: Related side effects as superficial skin burn with blister-like aspect in three patients and hyperpigmentation over the treated area in one patient were transient and resolved spontaneously. In one patient, asymptomatic subcutaneous induration persisted at the end of the study.

1.14 Potential usefulness of the designed phantoms.

The usefulness of developing application specific mimicking phantoms in a quest of researching and overcoming patient safety or procedure efficacy limitations recognized from the results of a literature overview in the previous section are presented below.

The head mimicking phantom can be used to investigate the efficacy of different HIFU devices. Literature review indicated that due to power limitations, ablative temperatures in deep seated tumours cannot be reached. Precise targeting in transcranial applications depends on the algorithm used to correct phase aberrations induced by the

human skull. The designed mimicking head phantom can be used to assess the effect of targeting accuracy, focal temperature and spatial distribution and using the aforementioned as quality criteria to optimize the algorithms. The effectiveness of cooling systems in decreasing brain surface temperature and the induced hot spots resulting from the development of standing waves near skull base can also be a matter of investigation using the head phantom.

Although palliative HIFU treatments for painful bone metastases is already an FDA approved procedure there is still room for improvement. Due to the great variety of bone shapes and accesses to targets, a customizable bone mimicking phantom will be valuable for assessing a priori the efficacy and safety of the treatment. The safety and efficacy of thermal protocols that employ novel approaches like volumetric sonications for increased treatment envelope can also be tested. A suitable bone phantom can be used to assess the functionality of newly developed HIFU transducers that provide flexibility in the delivery of the treatment to patients that cannot tolerate particular positioning.

A breast rib phantom can be used to test improved cooling systems in a search of reducing skin burns as observed in clinical studies. These studies were limited to targeted breast tissue which was far enough from tissue/air or tissue/chest wall interfaces. This was done to avoid excessive heating from intense ultrasound reflections and high acoustic absorption of ribs indicating the need to improve the technology to include patients with lesions that don't qualify for these criteria. The designed phantom can be used to test the safety and efficacy of new HIFU treatment devices that overcome the aforementioned limitations.

1.15 Aim and Objectives

The safety and efficacy of various applications that use HIFU as a thermal ablation treatment modality, have been extensively assessed through numerous animal studies. The results of these studies identified important safety and efficacy related issues and suggested that some applications are not ready for treating humans in their current status. The need for testing new or improved hardware and software HIFU related features, raises the question whether this can be done by using solely phantoms instead of animals. The use of suitable phantoms is expected to: a) reduce the number of animal studies, b) conduct experiments under controlled conditions and c) reduce the cost, implications and complexity associated with animal studies. Overall the use of suitable phantoms for testing HIFU thermal protocols will accelerate the development of several HIFU

applications and provide clinicians with a new treatment alternative that demonstrates important advantages over conventional (open surgery, chemotherapy, radiotherapy, other thermally ablative techniques, etc.).

The aim described above is expected to be accomplished by fulfilling the following research objectives:

- A literature review will be held to identify procedure related obstacles that halt some HIFU applications from becoming a standard treatment option. This information will be taken into consideration during phantom designing. The phantoms should allow researchers to exploit these defects for different treatment protocols.
- A second literature review will attempt to summarize the current state-of-the-art in HIFU phantoms. The knowledge gained from this review will be used as the base of designing improved or novel phantoms.
- Important tissue intrinsic acoustic and thermal properties that govern its interaction with ultrasound will be identified. Following a literature review the range of values of these tissue specific properties will be extracted.
- The corresponding properties of candidate phantom materials for replicating soft and bone tissue will be assessed through appropriate techniques. This will be done in order to check their matching with the values extracted from literature for human tissues. Adequate matching is vital for reproducing realistically the interaction of ultrasound in phantom materials and translating the results for human subjects.
- A set of three composite phantoms will be fabricated, each representing a different anatomy that consists of soft and bone tissue. Each composite phantom will correspond to a different application of HIFU ablation.
- The functionality of the fabricated phantoms for assessing safety and treatment efficacy issues will be demonstrated. This will involve exposing each phantom to a focused ultrasound field while monitoring the spatial distribution of thermal energy in quasi real time. This will be achieved by acquiring appropriate MRI images that encode temperature increment to signal phase change using the proton resonance frequency shift technique.

1.16 Thesis structure

This section presents a brief outline of the introductory Chapter 1 and the remaining Chapters that follow.

Chapter 1 introduces the reader to the main physical concepts of ultrasound that includes a short description of its wave-like characteristics. A description of ultrasound production process by transducers that exploit the piezoelectric effect, the different types of transducers available and the main features of the instrumentation involved is presented. The following sections cover the use of high intensity ultrasound in medicine, the interaction types of ultrasound with biological tissue and the induced thermal and mechanical bioeffects. The chapter closes with an overview of HIFU applications (brain, bone and breast) related to developed phantoms.

In Chapter 2 the current state-of-the-art of HIFU phantoms found from literature is reported. The phantoms are subcategorized in groups depending on the gelling agents used to replicate soft tissue. Details of the additives used to control the properties of the gels is given. Bone phantoms and composite phantoms that combine biological tissue with artificial materials to replicate soft and bone tissue are also presented.

Candidate materials for replicating soft and bone tissue are presented in Chapter 3. Moreover agar gels doped with silica dioxide/evaporated milk and ABS polymer were tested as mimicking materials of soft and bone tissue respectively. The method for characterizing their acoustic properties (attenuation coefficient and speed of sound) using pulse immersion techniques is described. A method for deducing the thermal conductivity and diffusivity coefficients of the soft tissue mimicking agar gels using numerical modelling of MR thermometry data is also presented.

In Chapter 4 the composite phantoms fabrication process is described. Geometrically accurate replicas of the bone parts are printed in ABS using fusion deposition modelling (FDM) technology. The digital 3D bone models were reconstructed by segmenting bone tissue from adult human CT images. The formation of three composite phantoms is demonstrated (skull-brain, bone-muscle, rib-breast) by molding agar gels either inside or around the bone ABS replicas.

Chapter 5 introduces the reader to MR thermometry, which is the most popular method for monitoring quantitative temperature elevations induced by HIFU sonications under MRI guidance. The theory of Proton Resonance Frequency Shift (PRFS), which is the primary choice of MR Thermometry techniques due to its wide temperature range linearity and independence from tissue type, is explained thoroughly. The next section

presents the development and workflow of a custom coded graphic user interface in MATLAB that takes MRI images as inputs and produces temperature maps using the PRFS technique. Finally the results of relaxometry conducted to characterize the T_1 and T_2 relaxation times of the developed soft tissue mimicking agar gel phantoms are reported.

Chapter 6 describes a series of functionality tests for each of the developed composite phantoms. Each phantom was sonicated with a 1 MHz single element spherically focused HIFU transducer with appropriate experimental setups under MRI guidance. By observing the temporal evolution and spatial distribution of temperature using the aforementioned GUI, the usefulness of the phantoms for testing these thermal protocols was proven. More specifically it was possible to observe the heating profile for different exposure parameters, the development of "unwanted" hot spots especially at tissue/bone interfaces, the effect of beam "starvation" and defocusing from intervening bone in transmit-through applications, etc.

Chapter 7 describes the work done to assess the compatibility of an MR-compatible robotic system used to drive the HIFU transducer during the aforementioned functionality tests inside the bore of the MRI scanner. The system's compatibility was assessed on the basis of signal to noise ratio drop and visual observation for induced image artifacts.

The final Chapter 8 summarizes the key findings of the thesis and emphasizes the contribution of the work done to current knowledge in the field. The limitations of the developed tissue mimicking composite phantoms are commented. Suggestions for overcoming these limitations or improving these phantoms are made in the form of future work proposals.

2 State-of-the art of FUS phantoms

2.1 Phantom models in Biomedical Research

A phantom usually refers to any artificially made object used for testing. In biomedical research, phantoms can be manufactured to replicate realistically the subjects or conditions of different applications, they can accommodate different tools suitable for parametric measurements or can be used in absolute and reference dosimetry studies. The development of such phantoms reduces the necessity of using animal models.

The use of animals in research has always been the subject of debate between the scientific community and animal welfare organizations. The ethical dilemma that much of the discussion revolves around is whether the benefits for human kind from research counterbalance the exploitation of animal rights. Animal use for research in developed countries is controlled by national committees that use targeted regulations to assess submitted research proposals. The proposals are usually reviewed based on the value and the originality of the potential outcomes and seek for justification of the inability to use alternatives. The principles of testing alternatives better known as the Three R's (3Rs), first described by Russell and Burch in 1959 [117], are included in national legislation worldwide that govern the use of animals in science. According to the National Centre for the Replacement, Refinement and Reduction of Animals in Research UK, these principles are defined as [118] :

"Replacement: Methods that avoid or replace the use of animals defined as 'protected' under the Animals (Scientific Procedures) Act 1986, amended 2012 (ASPA) in an experiment where they would have otherwise been used. Protected animals are all living vertebrates (except humans), including some immature forms, and cephalopods (e.g. octopus, squid, cuttlefish). Replacement includes the use of:

1) Human volunteers, tissues and cells.

2) Mathematical and computer models.

3) Established animal cell lines, or cells and tissues taken from animals killed solely for this purpose (i.e. not having been subject to a regulated procedure)

4) Immature forms of vertebrates, or invertebrates, such as Drosophila and nematode worms.

Protected forms are embryonic and fetal forms of mammals, birds and reptiles during the last third of their gestation or incubation period, fish and amphibians once they can feed independently, and cephalopods at the point they hatch. Embryonic and fetal forms are protected from an earlier stage of development if they are going to live beyond the stage described above and the procedure is likely to cause them pain, suffering, distress or lasting harm after they have developed to that stage.

Reduction: Methods that minimize the number of animals used per experiment or study, either by enabling researchers to obtain comparable levels of information from fewer animals, or to obtain more information from the same number of animals, thereby avoiding further animal use. Examples include improved experimental design and statistical analysis, sharing data and resources (e.g. animals and equipment) between research groups and organizations, and the use of technologies, such as imaging, to enable longitudinal studies in the same animals.

Refinement: Methods that minimize the pain, suffering, distress or lasting harm that may be experienced by the animals. Refinement applies to all aspects of animal use, from the housing and husbandry used to the scientific procedures performed on them. Examples of refinement include, using appropriate anaesthetics and analgesics, avoiding stress by training animals to cooperate with procedures such as blood sampling, and providing animals with appropriate housing that allows the expression of species-specific behaviors, such as nesting opportunities for mice."

2.2 Transcranial FUS phantom models

The potential of treating brain disorders including the revolutionary application of blood brain barrier (BBB) disruption using a noninvasive technology like FUS, promises to revolutionize current treatment approaches. The access of FUS in deep seeded brain targets without harming healthy tissue is intriguing for many research groups around the globe. The variety of models expands from purely cadaveric models, *ex vivo* skulls with tissue mimicking phantom gels and tissue mimicking phantom skulls with *ex vivo* tissue. Purely cadaveric models

Strong aberrations both in phase and in amplitude were corrected by energy adapting focusing on a clinical brain FUS system composed of 512 ultrasonic elements in a cadaver head model [119]. Adaptive focusing was optimized using acoustic radiation force imaging (ARFI) which encoded tissue displacement. Tissue displacement at focus

is considered of being linearly dependent to acoustic intensity at focus. This displacement power linearity assumption was confirmed in the same study in an *in vitro* lamb brain model. Displacement measurements were directly inverted to correct for the skull induced aberrations. The results showed that acoustic intensity at focus was 2.2 times higher than the uncorrected beam and 1.5 higher from the beam treated with adaptive focusing corrections produced by simulated time-reversed computed tomography data of the skull.

The accuracy of FUS targeting the trigeminal nerve in four unpreserved cadaver heads under MRI guidance was presented by Monteith *et al*. [49]. This was a feasibility study for testing MR guided FUS as a possible therapeutic method of treating neuropathic pain of trigeminal neuralgia. Significant focal heating in the absence of unwanted skull base and surrounding structures heating was made possible by the inclusion of no-pass regions through the petrous bone. The work of Chauvet *et al.* [120] tested the accuracy of MR guided FUS in a cadaver head in targeting part of the thalamic nucleus ventralis intermedius, which is a brain structure related with essential tremor. Using a 1 MHz FUS phased array a millimetric targeting accuracy was possible and temperature elevation at the target was detected using the proton resonance frequency shift thermometry. The authors commented the limitation of the model due to its lack of vascularization that controls thermoregulation.

2.2.1 *Ex vivo* skull with tissue mimicking phantom models

Eames *et al.* [121] suggested a model consisting of an ex vivo human skull combined with a tissue mimicking hydrogel to replicate brain tissue. The gel was melted in a microwave and oven and was molded inside the skull. This model was used to investigate the effect of scalp hair in the focal temperature elevation during transcranial treatments. The head phantom was covered with human hair wig. Sonications at 220 kHz showed no measurable change in focal temperature elevation whereas for a higher frequency sonication at 710 kHz a 17 % drop was observed. In a recent publication by Eames *et al.* [122], it was reported that their previous head model was upgraded by adding a layer of skin mimicking material. The skin layer was made from the same tissue mimicking hydrogel that the brain was created from. The authors made comparative studies between the latest model, the head model in the absence of the skin layer and a cadaver. The cadaveric phantom model, gel-filled skull model, and full head phantom model had heating efficiencies of 5.3, 4.0, and 3.9 °C/(kW/s), respectively, compared to a sample clinical heating efficiency of 2.6 °C/(kW/s).

2.2.2 Skull mimicking phantom with ex vivo tissue

Damianou *et al* [123] designed in a computer aided design (CAD) software a skull phantom made out of Acrylonitrile Butadiene Styrene (ABS) thermoplastic polymer which was printed in a rapid prototyping machine. The ABS material's attenuation coefficient was measured using the transmission-reception method and was found close to human skull. The thickness of the phantom was chosen appropriately so as to achieve the same attenuation effect as in the case of a human skull. The feasibility of focusing ultrasound through skull was tested under MRI guidance in a gel phantom and an *ex vivo* freshly excised tissue using a single element transducer operating at 0.5 MHz or 1 MHz. Temperature elevation detected with a fast spoiled gradient recalled (FSPGR) pulse sequence was confirmed with the 0.5 MHz beam.

2.3 Bone mimicking phantoms

Clarke *et al* [124] used liquid epoxy resin in conjunction with a hardener to simulate cortical bone. The measured acoustic properties of the developed material were 3.7 dB/cm at 1 MHz for the attenuation coefficient and 3168 m/s velocity. Ultrasound velocity in the bone mimicking material was within range but the attenuation coefficient was significantly lower from published value of 8.36 dB/cm at 1 MHz by Tavakoli *et al*[125].In the same study of Clarke *et al* an attempt to simulate trabecular bone was made by mixing in the liquid epoxy resin gelatine cubic granules (1 mm each side) before pouring in to moulds and left to harden. The mixture's acoustic properties were tested for different degrees of porosity by varying the concentration of gelatines granules to the total volume. The trabecular phantom material demonstrated ultrasonic characteristics similar to those of trabecular bone with high dependence in the degree of porosity. The authors reported acoustic speeds in the range of 1844 m/s to 3118 m/s and attenuation between 7 to 17 dB/cm at 0.5 MHz. In a similar study by Tatarinov *et al* [126] trabecular bone was mimicked by mixing 1 mm^3 soft rubber granules in an epoxy resin matrix to control porosity. The authors also added particles of natural bone which was first burned and grinded to control the mineral content of the phantom. In a more recent study of Tatarinov *et al* [127] cortical bone was modelled using tubular specimens of different polymers and polymer composites like ebonite, acrylic plastic, fiberglass and carbon fiber plastic. The polymers increased in stiffness with measured longitudinal velocity ranging from 2200 m/s in ebonite to 4400 m/s in carbon fiber plastic that covered that velocity range of poorly mineralize to hypermineralized compact bone. A multi-layered model of

compact bone was also presented to simulate increasing porosity between endosteum and periosteum. Pores in the layers were manufactured by randomly mixing rubber particles of bulk velocity equal to 1500 m/s in a homogeneous solid epoxy matrix with bulk velocity of about 2700 m/s. Hodgskinson *et al* [128] reported the use of Perspex plates as a cortical bone mimicking material with reported speed of sound of 2657 m/s, attenuation coefficient of 5.3 dB/cm-MHz and density of 1180 kg/m^3..

2.4 Soft tissue mimicking gel phantoms for ultrasound applications

Though there is a broad range of tissue mimicking phantoms available for ultrasound imaging, there are few material substitutes made specific for FUS, particularly which possess tissue-like properties. Although FUS corresponds to ultrasound propagation through a medium, appropriate phantoms should be appropriate for withstanding high temperature and pressure regimes involved in FUS. The following sections review the main tissue mimicking US gels.

2.4.1 Gelatin gels

Several low cost gelatin gel based recipes have been introduced for mimicking accurately soft tissue for imaging purposes. These recipes mainly differ between them in the selection of the additive materials used for controlling acoustic scattering and speed. The Madsen group [129] used gelatin gel with graphite powder and alcohol to control the attenuation coefficient and speed of sound respectively. Their measurements reported an easily controllable attenuation coefficient range of 0.12 to 1.5 dB/cm-MHz and speeds between 1520 and 1650 m/s at room temperature. Cook *et al*. [130] demonstrated a gelatin based gel for photo acoustic imaging doped with silica particles, dye and Intralipid® solution additives that controlled the acoustic speed and attenuation and the optical absorption and scattering. Measurements correlated the concentration of these additives to aforementioned properties. In another study psyllium fibers were introduced as a scattering material in a gelatin based gel that resembled the echogenicity of thyroid and testicular texture [131]. No information of the acoustic properties of this gel recipe was provided. Amongst the reported disadvantages of gelatin gels, the one that makes them unsuitable for using in FUS applications is their low melting point (35 ºC). Additionally unless treated with preservatives they are susceptible to microbial and bacterial invasion and difficult to achieve a uniform distribution of the chosen scattering material.

2.4.2 *Agar gels*

Agar based gels are the most popular soft tissue substitutes found in literature. They are cheap and easy to produce, durable in high temperatures, nontoxic and disposable. However they lack long term stability and repeatability of acoustic properties measurement over time. Under ideal storage conditions, agar gels can remain stable up to two and a half years [132]. Burlew *et al*. [133] suggested agar gels as a replacement for gelatin gels which suffered for temperature dependent structural instability. The developed recipe resulted in a speed of sound that ranged between 1498 and 1600 m/s, density between 1016 and 1100 kg/m^3 and an attenuation coefficient between 0.04 and 1.40 dB/cm-MHz. A modified agar based tissue mimicking phantom gel available in liquid or solid form was presented by Madsen *et al*. [132]. The authors used a low scattering material like evaporated milk to control the attenuation coefficient though pure absorption. The produced phantoms were capable of exhibiting attenuation coefficient slopes spanning the range 0.1-0.7 dB/cm-MHz. The advantage of this phantom is that the absence of scatterers allows the backscatter coefficient to be varied over a considerable range. Zell *et al*. [134] presented measurements of the acoustic properties and density for a 2 % weight to volume agar gel. For a 5 MHz frequency acoustic wave, it was found that the speed of sound was 1500 m/s, the acoustic impedance was 1.57 MRayl and the acoustic attenuation 0.4 dB/cm. Its mass density was found as expected very near to water's at 1040 kg/m^3. Tissue-mimicking agar gels were also employed in a study for mapping inertial cavitation activity in a HIFU sonication [135]. A study by Partanen *et al.* [136] investigated the feasibility of using an agar-silica phantom for quality assurance purposes of MR guided FUS. Silica particles served as scatterers and their concentration controlled the overall attenuation coefficient of the final product. The study concluded that an agar-silica gel with mass concentrations 2 % and 3 % respectively, mimicked a soft tissue with an attenuation coefficient 0.58±0.06 dB/cm-MHz, ultrasound speed 1490±10 m/s, mass density 1.03±0.01 g/cm^3 and acoustic impedance 1.54±0.01 MRayl.

2.4.3 *Polyurethane gels*

Kondo *et al.* [137] reported the fabrication of polyurethanes as an alternative to tissue substitutes. The molecular design of these gels is rather complex and very difficult to standardize. The authors produced a phantom with acoustic properties with an attenuation coefficient in the lower range (0.13 dB/cm-MHz), speed of sound of 1468 m/s and a mass density of 1130 kg/m^3.

2.4.4 *Polyacrylamide gels*

The use of polyacrylamide hydrogels has been a popular choice amongst researchers in HIFU. The gel itself is optically transparent and its acoustic properties can be matched closely to soft tissue, making it suitable for monitoring the therapeutic effects of HIFU in simulation studies. Different studies have used slightly different recipes for creating these gels. Lafon and colleagues [138] were the first to develop such a phantom by crosslinking copolymerization of acrylamide and N,N′-methylene bisacrylamide (bis) in an aqueous solution. Gel samples embedded with different concentrations of bovine serum albumin (BSA) were made. BSA is a concentrated protein serum derived from cows. The purpose of adding BSA was to increase the acoustic absorption of the gel, as a result of the energy loss during protein denaturation. The authors examined the acoustic and optical properties of the phantom, which were characterized as a function of BSA concentration and temperature. The measured attenuation coefficient was found to vary linearly over the 1 to 5 MHz frequency range, with the coefficients of 0.009, 0.013, 0.017 and 0.021 Np/cm-MHz measured for BSA concentrations of 3, 5, 7 and 9 %, respectively. The attenuation increased linearly with the increase in the BSA concentration. The attenuation coefficient of the phantom was approximately 8 times lower (for 9 % BSA concentration) than that for the soft tissues. The difference in attenuation coefficient was observed as a reduction in lesion volume compared in lesions created for the same HIFU dose in a sample of turkey breast. The speed of sound was found to be dependent on temperature, reaching a maximum at 1590 m/s near 60 °C. The phantom was destined to be used for HIFU therapies under ultrasound guidance. The authors reported that the optically opaque lesion created in the gel, coincided with the hyperechoic region observed in B-mode ultrasound imaging. The hyperechoic region is recognized as a result of scattering induced by bubble formation at the focus [139].

A cheaper version of Lafon's recipe was reported in another study [140]. In this study the BSA was replaced with egg white which is also known of being a rich source of protein. The variation of the acoustic properties of the gel were tested for different egg white concentrations (0-40 %). It was found that the mass density of the gel remained the same for the whole range (1.0 g/cm^3) near to water. The sound speed of the gel varied from 1537 to 1544 m/s. High speeds were correlated with large egg concentrations. More importantly, it was found that there was strong linear correlation of attenuation coefficient with egg white concentrations. Even for the highest concentration tested (40 %), the gel possessed a lower attenuation coefficient than soft tissue (0.28 dB/cm-MHz). The use of

the egg white embedded polyacrylamide gel was demonstrated in an *in vivo* animal model where the fabricated gel was implanted inside a rabbit's stomach to simulate a gastric submucosal tumor. The model was exposed to a 2.2 MHz HIFU beam with electric power of 100 W for 10 s. The authors demonstrated formation of a lesion in the gel, whilst the gastric mucosa surrounding the gel stayed unaffected. Another study used a polyacrylamide gel with egg white to test the effect of embedding nylon fibers to the phantom in order to increase heat deposition under HIFU [141].

In another study a modified recipe of the standard polyacrylamide gel with embedded BSA was proposed [142]. In order to improve the matching of the attenuation coefficient of the gel with that of soft tissue, glass beads with diameters of 40-80 μm were added. The glass beads served two purposes. They increased the attenuation coefficient of the gel by adding scattering effects, which were missing in previous recipes. The final product was an optically transparent gel with an acoustic impedance of 1.67 MRayl, a speed of sound of 1576 m/s, an attenuation coefficient of 0.52 dB/cm-MHz. The acoustic and thermal properties of the gel were very close to liver tissue. The formed lesion volume was larger using the new recipe compared to the standard polyacrylamide-BSA gel. This was attributed to the increased attenuation coefficient from the glass beads that enhanced heat deposition in the gel.

Commercially available polyacrylamide gel phantoms manufactured by Onda Corp (Sunnyvale, California, USA) are widely used for characterizing transducer geometry, frequency and power profiles. The synthetic gel is transparent and when its temperature exceeds 70 ºC, white three dimensional lesions are formed, making it easy to assess lesion growth, position and shape over time. They are suitable tools for performing quality control tests on HIFU equipment and treatment protocol testing. The manufacturer states that these gels have similar acoustic and thermal properties to soft tissue. The products have a density of 1060 kg/m^3, phase velocity of 1600 m/s, an attenuation coefficient of 0.6 dB/cm-MHz, specific heat of 3850 J/kg-K and thermal conductivity coefficient of 0.55 W/m-K [143]. Their properties are close to soft tissue and therefore they can be considered as a tissue mimicking material.

2.4.5 *N-isopropylacrylamide (NIPAM) gels*

NIPAM gels have been designed to become opaque above a threshold temperature which can be controlled by altering the concentration of acrylic acid (AAc) [144]. By testing different concentrations of AAc, NIPAM based gels were fabricated and matched

the acoustic and thermal properties of different swine tissues. NIPAM gels are superior to polyacrylamide BSA or egg white based phantoms since they are reusable. Unlike these phantoms where thermal protein denaturation induces irreversibly opaque lesions, in NIPAM gels these lesions gradually disappear and the phantom gel can be reused.

2.4.6 *Polyvinyl Alcohol (PVA) gels*

A polyvinyl alcohol cryogel (PVA) tissue mimicking phantom gel was presented by Surry *et al.* [145] suitable for MR and US imaging. The gel was solidified through a freeze-thaw cycle process and was characterized for the speed of sound which was found in the range of 1520 to 1540 m/s. The gel's attenuation coefficients were in the range of 0.075-0.28 dB/cm-MHz. T_1 and T_2 relaxation values were estimated between 718-1034 ms and 108-175 ms respectively. The authors used this gel to develop a brain and breast phantom that were used in synergy with ultrasound or MR for segmentation and biopsy. Reinertsen *et al*. [146] designed a multi-layer phantom made out of PVA gel to characterize and correct for brain shift during image guided surgery. Each gel was treated with different number of freeze-thaw cycles to control its mechanical and imaging characteristics. Brain vessels were simulated using plastic tubes filled with water and doped with glass micro-bubbles in order to enhance signal in Doppler ultrasound imaging.

2.5 Summary

The following Table 2-1 summarizes the existing phantoms extracted from literature presented in previous sections and denotes their advantages and disadvantages.

Table 2-1: Pros and Cons of existing phantoms extracted from a literature review.

Phantom type	Replicated tissue	Pros	Cons
Liquid epoxy resin treated with hardener	Bone	- Matched tissue ultrasound velocity	- Low attenuation coefficient compared to bone. - Lack of trabecular bone layer. - Requires molding.
Liquid epoxy resin doped with gelatin cubic granules (1mm) and particles of natural bone.	Trabecular bone	- Matched tissue ultrasound velocity and attenuation coefficient.	- Requires molding. - Simulated trabeculae are too large (1 mm^3). - Biological tissue.
Tubular polymer composites like ebonite, acrylic plastic, fiberglass and carbon fiber plastic.	Cortical bone	- Multi-layered model simulating increasing porosity. - Polymers covered a velocity range of poorly mineralize to hypermineralized compact bone.	- Expensive to produce. - Complicated manufacturing procedure. - No attenuation coefficient data. - Requires molding.

Perspex plates	Cortical bone	- Matched tissue ultrasound velocity and attenuation coefficient.	- Expensive to produce. - Complicated manufacturing procedure. - Produced in plates therefore no realistic anatomical geometry. - Fragile.
Gelatin gels doped with graphite and alcohol.	Soft tissues	- Cheap to produce. - Easy to produce. - Easily controllable acoustic properties.	- Low melting point. - Attenuation induced primarily with scatter agent.
Gelatin gels doped with silica particles and Intralipid solution.	Soft tissues.	- Easy to produce. - Easily controllable acoustic properties.	- Low melting point. - Expensive Intralipid solution.
Gelatin gels doped with psyllium fibers.	Soft tissues.	- Cheap to produce. - Easy to produce. - Resembled the echogenicity of thyroid and testicular texture under US imaging.	- Low melting point. - Attenuation induced primarily with scatter agent. - No information of the acoustic properties of this gel recipe was provided.
Agar gels doped with graphite.	Soft tissues	- Cheap to produce. - Easy to produce. - Matched tissue ultrasound velocity and attenuation coefficient. - High melting point.	- Attenuation induced primarily with scatter agent. - Fragile. - Visually opaque.
Agar gels doped with evaporated milk.	Soft tissues	- Cheap to produce. - Easy to produce. - Matched tissue ultrasound velocity and attenuation coefficient. - High melting point.	- Attenuation induced primarily with absorption agent. - Fragile. - Visually opaque.
Agar gels doped with silica.	Soft tissues.	- Cheap to produce. - Easy to produce. - Matched tissue ultrasound velocity and attenuation coefficient. - High melting point.	- Attenuation induced primarily with scatter agent. - Fragile. - Visually opaque.
Polyurethane gels	Soft tissues	- Acceptable ultrasound velocity.	- Complex molecular design and difficult to standardize. - Low attenuation coefficient.
Polyacrylamide gels doped with BSA.	Soft tissues.	- Visually transparent matrix with visible heated lesions. - Linear dependence of attenuation coefficient with BSA concentration. -	- Low attenuation coefficient. - Expensive to produce. - Complex to produce. - Possible toxicity during preparation. - Attenuation induced primarily with absorption agent.
Polyacrylamide gels doped with egg white.	Soft tissues.	- Visually transparent matrix with visible heated lesions. - Linear dependence of attenuation coefficient with egg white concentration.	- Low attenuation coefficient. - Possible toxicity during preparation. - Complex to produce. - Attenuation induced primarily with absorption agent.

Polyacrylamide gels doped with egg white, nylon, stainless steel and copper fibers.	Soft tissues.	- Visually transparent matrix with visible heated lesions. - Volumes of lesions formed in phantoms similar to control lesions. - Attenuation induced from both scatter and absorption agents.	- Absence of acoustic properties quantitative data. - Complex to produce. - Possible toxicity during preparation. - Use of metallic materials can induce image artifacts in MRI.
Polyacrylamide gels doped with BSA white and glass beads.	Soft tissues.	- Visually transparent matrix with visible heated lesions. - Attenuation induced from both scatter and absorption agents. - Matched tissue acoustic properties.	- Expensive to produce. - Complex to produce. - Possible toxicity during preparation.
Polyacrylamide gel phantoms by Onda Corp	Soft tissues	- Matched tissue acoustic and thermal properties.	- Expensive to purchase. - Sold in rectangular containers. - No information for additives.
N-isopropylacrylamide (NIPAM) gels	Soft tissues	- Matched tissue acoustic properties. - Reusable.	- Complex to produce. - Possible toxicity during preparation.
Polyvinyl Alcohol (PVA) cryogel	Soft tissues	- Matched tissue ultrasound velocity. - Possibility of treated with different number of freeze-thaw cycles to control its mechanical and imaging characteristics.	- Low attenuation coefficient. - Long and complex preparation through multiple freeze-thaw cycles.

Following literature review, it was concluded that soft tissue phantoms are predominantly mimicked by a variety of different gels. The gels differ between them in the gelling agent used and the preparation method. Gelatin and agar are natural products extracted for animal collagen and seaweed polysaccharides respectively, they are not toxic and their preparation does not require either special skills or equipment. Polyurethane, polyacrylamide and polyvinyl based gels are synthetic polymers that present various degrees of toxicity and the preparation can be complex varying from freeze-thaw cycles to crosslinking of multiple polymers. In order to match the attenuation characteristics of the replicated tissue, gels were doped with different types of scatterers in the form of nylon fibers, glass beads, silica particles etc. Other phantom makers chose to control the attenuation characteristics their gels with additives high in protein content like BSA, evaporated milk, egg white, etc., which induce primarily acoustic absorption. No evidence in literature was found for a soft tissue mimicking gel that combined both scatter and absorption additives except in the report of Choi *et al* [142], where glass beads

were combined with BSA in a polyacrylamide gel in order to increase the rather low attenuation coefficient and induce scattering effects.

There were very few examples of bone replicating phantoms with their majority being hardened liquid epoxy resin or different polymers and polymer composites like ebonite, acrylic plastic, fiberglass and carbon fiber plastic. Attempts of simulating trabecular bone structure were made by doping epoxy resins with rubber granules. The majority of these phantoms were manufactured in plate samples and no standardized methodology of fabricating bone structures with realistic geometry was presented.

This review revealed the need of developing composite tissue mimicking phantoms with realistic geometry and independently controlled attenuation characteristics. There was complete absence of composite phantoms made out of non-biological material. Composite phantoms of replicating both soft and bone tissue are necessary to assess the possible interactions of ultrasound with tissue residing inside and outside the acoustic field. Unwanted thermal spots rising from increased absorption and reflection at interfaces, field intensity amplification from standing waves and the absorption of scattered waves using the proposed phantoms can be examined thoroughly. The phantoms preparation method should be easy without any expertise needed. The cost of the materials used should be affordable and any technology used for their fabrication should be widely available. The remaining of the thesis will present a methodology of developing phantoms for three major focused ultrasound applications that will allow researchers to explore the extent of thermal effects.

3 Selection and testing of phantom materials

3.1 Introduction

The following chapters describe the fabrication and characterization of three phantoms suitable for testing thermal exposures using HIFU guided by MRI. All phantoms were composed by two homogenous materials, one for replicating soft tissue and the second one for bone tissue. The selection process of the candidate materials used was considered prior to fabrication. The requirements tested for assessing the materials suitability are presented in the following sections.

3.2 Agar gels for mimicking soft tissue phantoms

Agar is a gelling agent extracted from red algae which consists of a complex mixture of polysaccharides. Gels can be formed by dissolving agar in boiling water that set once cooled down. During the jellification process, agar demonstrates a hysteresis phenomenon where the melting temperature (>85 ºC) is considerably higher from the temperature range that solidification takes place (32-45 ^{0}C). The final product is a homogeneous opaque gel that can be easily molded to form well-shaped volumes with clear margins.

Agar based gels are a frequent selection for constructing soft tissue mimicking gel phantoms in ultrasound applications since they are non-toxic, low cost, easy to make and do not require special equipment to be prepared [134], [147], [148]. The high melting temperature of agar gels makes them ideal for testing HIFU applications since they can maintain their structural integrity for a considerably wide range of ablative temperatures ($60\ ^{0}C < \theta < 85\ ^{0}C$). The concentration of agar in water expressed in weight (grams of agar) per volume of water percentage (w/v %) affects the gel's stiffness and consequently controls its elasticity. By varying the concentration of agar, the stiffness of the gel can be modified to match the replicated tissue's bulk mechanical characteristics.

3.3 Silica dioxide (SiO_2) for controlling acoustic scattering in an agar matrix

The process of scattering is a significant energy loss mechanism produced in the vicinity of biological tissue inhomogeneities. Although scattering does not contribute directly to the conversion of acoustic energy to heat, it increases the overall attenuation and thus needs to be considered when designing a realistic tissue mimicking phantom.

Silica dioxide or silica is commonly added in tissue mimicking phantom gels to enhance attenuation through acoustic scattering [130], [136].

Silica is a crystalline compound found abundant in sand. It is insoluble in water with a high mass density (~ 2.6 g/cm^3) while its melting temperature exceeds 1600 ^{0}C. Due to the large acoustic impedance mismatching at interfaces of dense silica particles embedded in a tissue mimicking gel, ultrasound is reflected. Since silica dioxide crystals in powdered form are usually amorphous and with dimensions comparable or smaller to the acoustic wave's wavelength, the wave is reflected in all directions through the process of Rayleigh scattering. The degree of scattering is correlated with the population of scatterers per unit volume and their size. Scatterers can enhance secondary absorption by increasing the effective path length of the wave but for simplicity it will be assumed that attenuation in gels doped with silica is purely a result of scattering.

3.4 Evaporated milk for controlling acoustic absorption in an agar matrix

The effectiveness of HIFU induced hyperthermia and ablation applications depend on the thermal dose deposited at the targeted tissue throughout the treatment period. This loss mechanism is characterized by the associated tissue's absorption coefficient. Evaporated milk induces low scattering and has been used in various studies as an additive in gel phantoms to primarily control attenuation independently from scattering [132], [149], [150]. Acoustic energy is converted to heat via viscous frictions inside the phantom. When the temperature is raised above a threshold, heat energy is sufficient to disrupt irreversibly hydrogen bonds that retain milk proteins in a folded state. This irreversible effect is known as thermal protein denaturation and it is the primary mechanism of biological tissue necrosis under HIFU ablation. The addition of evaporated milk was tested on the hypothesis that acoustic absorption and thus attenuation is correlated to the concentration of milk in the final gel, expressed in a volume to volume percentage (v/v %).

3.5 Acrylonitrile Butadiene Styrene (ABS) for replicating bone tissue

Attenuation and loss of the acoustic wave's phase coherence distort the quality of the focusing pattern in transcranial applications. Researchers have developed various adaptive focusing techniques to overcome these skull induced amplitude and phase aberrations. These techniques involve solving back projected acoustic linear wave equations and calculating the required amplitude and time shifts for every element of the

array that converges the beam at focus. In order to solve these differential equations, the skull thickness, density and the speed of sound in the skull for each acoustic pathway needs to be calculated. Unintended heating from bone/tissue interfaces in the near or far field pose major safety and treatment efficacy problems in some HIFU applications that need to be addressed in phantom studies.

For bone modelling it was decided to test ABS as a possible candidate material. ABS is a thermoplastic polymer commonly used as a raw material in Fused Deposition Modelling (FDM). FDM is just one of the many available techniques for prototyping 3D models. During printing operation, raw ABS is heated by a filament to reach melting temperature and then it is forced through a fine nozzle to build 3D models. While fusing layer upon layer, the final product is built to a geometrically accurate representation of the model, which is important for inducing analogous acoustic field distortions to human bones.

ABS products are durable, heat resistant and chemically inert under normal conditions and therefore reusable. This is also another advantage since ABS will be used as a bone phantom for a range of different conditions without having to worry for changes to its physical properties. Being a plastic is also not expected to produce any severe artifacts while monitoring focused ultrasound exposures with MRI.

3.6 Estimation of materials acoustic properties using immersion techniques

In order to assess the suitability of the materials used to construct the phantoms, a methodology for assessing their acoustic properties is needed. The most relevant acoustic properties for phantoms designed for HIFU is the attenuation coefficient and the propagation speed. The first property controls the degree of acoustic energy to heat conversion and therefore a close matching with the attenuation coefficient of the replicated tissue is desirable. Acoustic speed and mass density set the reflection coefficient at interfaces and consequently the actual fraction of incident acoustic energy propagating through the phantom depends on it. Pulse-echo and transmission methods are broadly used for characterizing the attenuation coefficient and acoustic speed of ultrasound. They involve submerging the specimen under examination in a tank filled with degassed water. All measurements are performed with immersion unfocused ultrasonic transducers. These methods differ in experimental configuration, the assumptions taken, the type of signals measured and their advantages.

3.6.1 Methods for estimating acoustic attenuation coefficient

Transmission through method for measuring acoustic attenuation coefficient

This technique compares the transmitted signals through material specimens of different thicknesses [151]. It uses two immersion planar transducers, one for transmitting and one for receiving the signal (Figure 3.1).

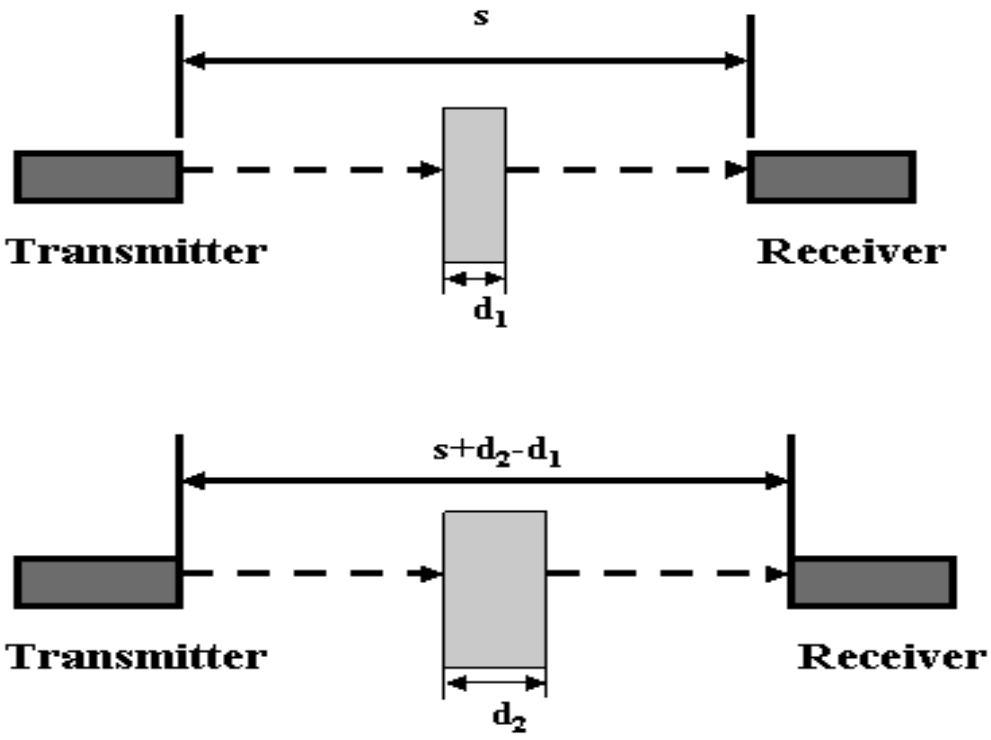

Figure 3.1: Variable thickness technique for measuring attenuation coefficient of the tested material [9].

The two transducers operate at the same central frequency and gain to ensure an identical response. The specimen is positioned between the two transducers and preferably beyond the far field of the transmitting transducer, where constructive interference of waves produced at the face of the transducer create a uniform front that decays smoothly with distance.

The advantage of the variable thickness method is that there is no need to calculate the reflection or transmission coefficients of the material. First a thinner specimen with thickness d_1 is positioned between the two transducers. The peak-to-peak voltage at the receiver side is measured (V_{d1}) on an oscilloscope. The thicker specimen with thickness d_2 is positioned at exactly the same distance from the transmitter. For strictly correct measurements the receiver in the second measurement must be moved by a d_2-d_1 distance

in order to keep the length of the immersion liquid constant between the two measurements. If water is used as the immersion liquid and the thickness difference between the two specimens is small, we can neglect this correction since water does not attenuate the beam significantly. The peak-to-peak voltage of the thicker specimen is also measured (V_{d2}). The voltage measured at the receiver is directly proportional to the pressure exerted by the acoustic wave. It is then safe to deduce that the square of the voltage measured is proportional to the sound wave's intensity. If we follow some mathematical analysis to calculate the sound intensity at the receiver's end for both thicknesses we end up with Equation (3.1) for calculating the characteristic attenuation coefficient ***(α)*** of the material in units of dB/cm.

$$\alpha = \frac{20}{d_2 - d_1}\left(log_{10}\frac{V_{d_2}}{V_{d_1}}\right) \tag{3.1}$$

The expression above contains no reflection or transmission coefficient. The coefficients cancel each other out when we calculate the ratio of intensities as a function of the measured voltages for the two different thicknesses.

Pulse echo method for measuring acoustic attenuation coefficient

The method introduced by Youssef and Gobran [152], follows a different approach from the variable thickness technique. The main difference is that measurements are performed using reflected echoes at a single transducer (*T*) working in transmit and receive mode (Figure 3.2).

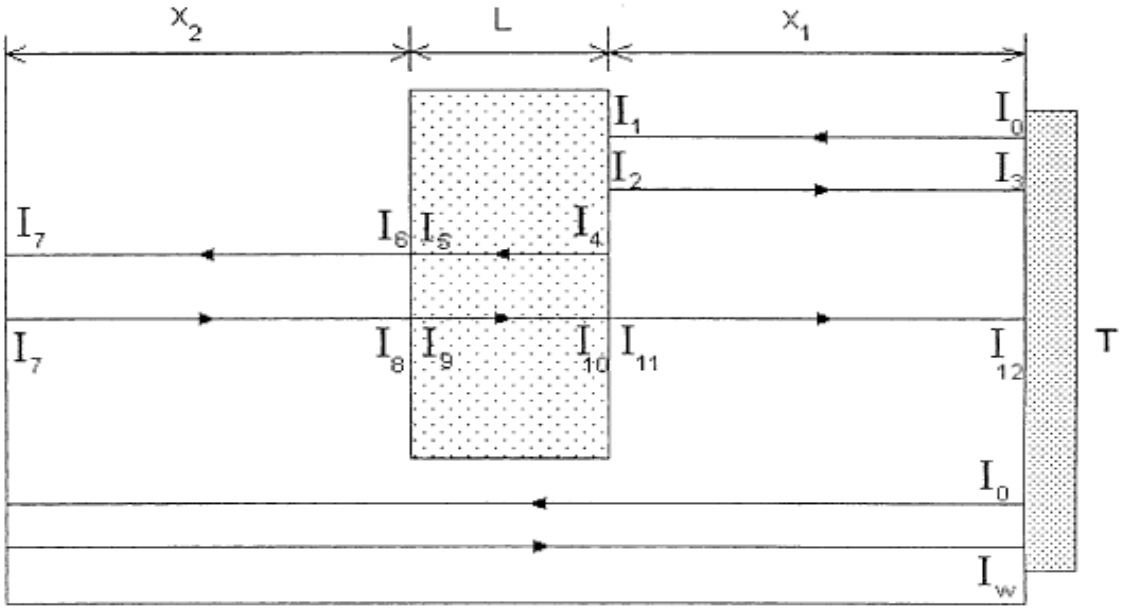

Figure 3.2: Single transducer pulse echo method [10].

The authors described equations of the acoustic intensity arriving at the transducer face for two different scenarios. First the transducer (*T*) is immersed in a tank of fixed dimensions and on the opposite side of the tank a perfect reflector is placed. The reflector can be any flat and smooth material with a high acoustic impedance like aluminum or plastic. The transducer measures the signal intensity (I_w) arriving in the absence of a specimen in the path of the beam. The intensity of the signal depends only on the attenuation coefficient of the immersion liquid and the distance travelled.

In the second scenario, a specimen of thickness *L* is positioned in the pathway of the beam. The transducer records echoes rising from reflections produced by every interface met along the wave's pathway. The echo returning from the front face of the specimen and travelling a distance $2x_1$ is denoted as intensity I_3 , while the signal with intensity I_{12} travels the full pathway of distance $2(x_1+L+x_2)$. A system of equations describing the reflected echoes intensities at every interface $(I_1 \text{ to } I_{12})$ is solved and by using multiple substitutions we end up in a simple system of two equations containing two unknown variables.

I_w and I_3 are directly measured from the transducer whereas the term r^2 is equal to the reflection coefficient of the liquid/specimen interface. The term α_1 stands for the attenuation coefficient of the immersion liquid. If degassed water is used as the immersion liquid it can be safely assumed that the attenuation of ultrasound is negligible and therefore the exponent approximates unity, which leads to a very simple expression described by:

$$\frac{I_w}{I_3} = \left(\frac{1}{r^2}\right) e^{[-4a_1(x_2+L)]} = \left(\frac{1}{r^2}\right), for\ a_1 \approx 0 \qquad (3.2)$$

The second equation of the system after all substitutions is given by Equation 3.3, where $\boldsymbol{\alpha_2}$ refers to the attenuation coefficient of the specimen.

$$\frac{I_{12}}{I_w} = (1-r^2)^4\, e^{[-4(a_2-a_1)L]} = (1-r^2)^4\, e^{(-4a_2L)}, for\ a_1 \approx 0 \qquad (3.3)$$

Once again I_{12} and I_w are deduced from the transducer's voltage signals whereas r^2 is calculated from Equation (3.2). The attenuation coefficient $\boldsymbol{\alpha_2}$ is calculated using Equation (3.3). The single transducer method is valid if the reflection and transmission

coefficients at both faces of the specimen are equal. For a homogeneous material at constant temperature, this seems to be a logical assumption.

3.6.2 Estimation of attenuation coefficient variation for agar gels doped with different concentrations of SiO_2 using transmission through technique.

Materials and Methods

Agar gels (granulated form, microbiology grade-Merck Millipore, Darmstadt, Germany) of a 2 % w/v of water concentration were used in order to produce gels of intermediate stiffness and flexible enough to withstand manual handling and high intensity ultrasound compressional forces without cracking. This selection is within the range of concentrations (2 %-2.7 %) of agar based HIFU soft tissue mimicking phantoms found in bibliography [153]–[155]. Agar gel specimens were doped with silica dioxide powder of different concentrations (0 %, 1 %, 2 %, 3 % w/v). The silica particles size ranged between 0.5-10 μm (Silica Dioxide, Sigma-Aldrich, St. Louis, Missouri , United States).

The first step in preparing the gels was to calculate and weigh the quantities needed for each of the tested four recipes. The volume of each batch was 100 ml and therefore the weights were extracted based on the concentrations previously described. Agar and silica powders were weighed using a 0.1 g precision electronic scale. To minimize attenuation from gas bubbles trapped inside the gels, 150 ml of distilled and degassed water was used. Distilled water is free from impurities that can affect the attenuation measurements. The water volume was degassed inside a vacuum chamber. Degassing time lasted for as long as we could see bubbles emerging on the surface (approximately 20-25 minutes).

Agar and silica powders were poured inside a glass beaker containing 100 ml of degassed water. The mixture was first stirred using a magnetic stirrer to ensure adequate mixing and dissolving of powder granules before boiling. Excessive boiling leads to evaporation and desired concentrations can be altered. Following 20 minutes of stirring on high revolutions the mixture was then boiled to exceed 85 ^{0}C, which is the melting temperature of agar. The amount of water evaporated during boiling was replenished to reach the initial 100 ml volume and maintain the initial agar and silica concentrations. The heater was turned off and the mixture was left to cool down to room temperature. Stirring was kept at all times during cooling period, but at lower revolutions, up until the mixture started jellifying (35-40 °C) and becoming viscous. This was vital to ensure that silica particles distributed evenly within the gel's matrix.

The variable thickness technique was followed because it does not require determination of the reflection coefficient. For each silica dioxide concentration two different thicknesses were prepared (16 mm and 26 mm). The samples were poured in plastic 3D printed plastic containers and were left to solidify overnight (Figure 3.3A – Figure 3.3B). Custom made plastic holders were designed and manufactured to accommodate the specimen containers of different thicknesses (16 and 26 mm) in between the immersion transmitter and receiver (Figure 3.3C).

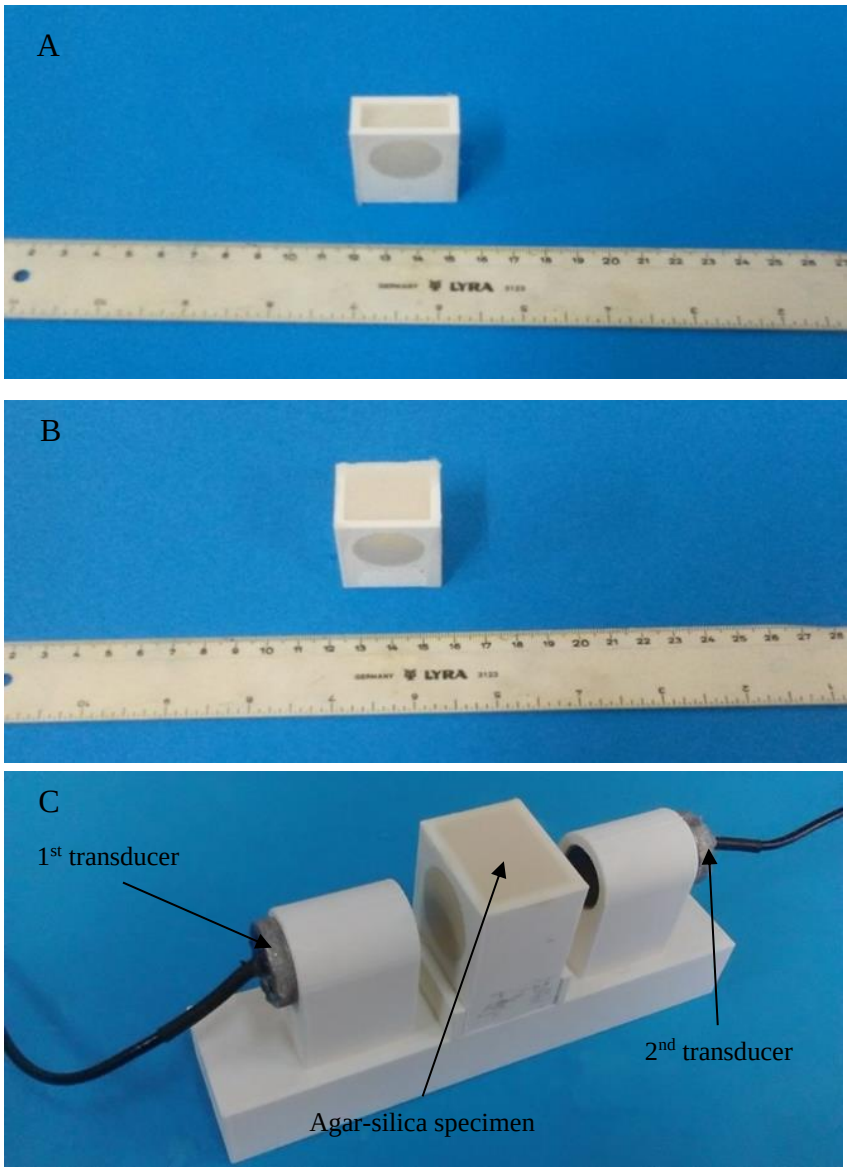

Figure 3.3: A) Agar-silica gel sample moulded inside the 16 mm sample container, B) Agar-silica gel sample moulded inside the 26 mm sample container, C) Custom made holder for agar gel transmission through measurements.

The holder had two cylindrical cavities that could fit tightly the two 10 mm circular 3.5 MHz transducers (Etalon, ESN-410-SCBI) facing each other while the specimen was positioned in between and with side openings perpendicular to the acoustic beam's

pathway emitted by the transmitting transducer. The transmitter (T/R) and receiver (R) were connected via coaxial cables to a Panametrics pulser/receiver (Panametrics 500PR, Olympus Corp, Tokyo, Japan).

A high pass filter selectable via a rear panel switch was used to change excitation pulse recovery time and reject low frequency noise. The pulser/receiver was set to operate in transmission through mode. The signal of the receiving transducer was fed to a 20 MHz oscilloscope (Hameg HM203-7, HAMEG Instruments GmbH, Mainhausen, Germany) to observe voltage over time. The transmitter and receiver gain were kept constant whilst the pulse repetition frequency was adjusted (5 kHz) to keep a single cycle of the periodic signal for the set time per division (20 μs). The attenuation coefficient in dB/cm was calculated using Equation 3.1 for every set of gels. The coefficient for different silica concentrations was normalized to more useful units of dB/cm-MHz by dividing with the transducer's frequency (3.5 MHz). This approach assumed a linear dependence of attenuation of with frequency of the prescribed heterogeneous phantom. A similar approach was used in a study by Nam *et al.* [156], where attenuation data induced by glass bead scatterers of similar size (10-100 μm) in tissue mimicking phantoms fitted almost linearly in the frequency range between 2.5-10 MHz. Figure 3.4 demonstrates the experimental setup used for the transmission through attenuation measurements.

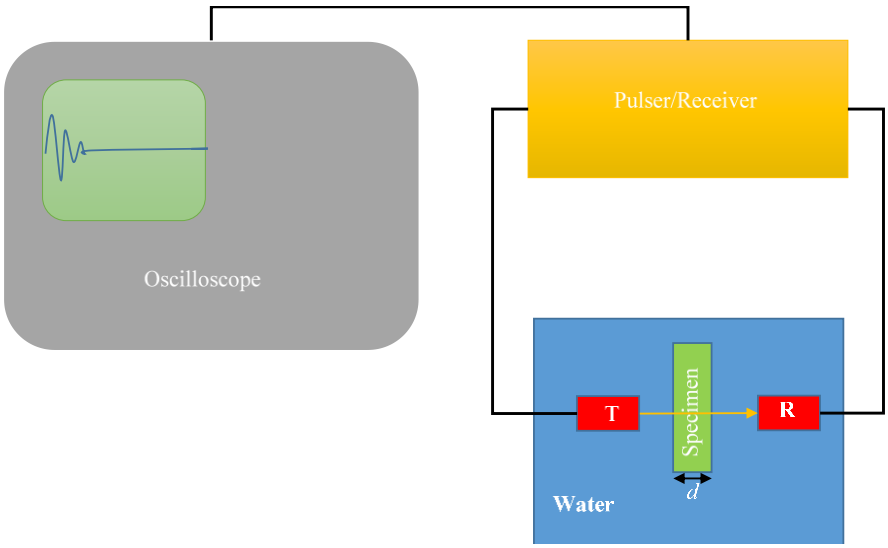

Figure 3.4: Experimental setup for the transmission through measurements of a specimen of thickness (d) in between the transmitter (T) and receiver (R) all immersed in a tank filled with degassed water.

Results

Voltages induced by acoustic waves transmitting through the specimens and reaching the receiver were monitored for each sample's thickness (16 mm and 26 mm). The measurements were repeated for each silica concentration (0 %, 1 %, 2 % and 3 %).The results are summarized in Figure 3.5 as a plot of attenuation coefficient in units of dB/cm-MHz as a function of silica concentration demonstrating a linear dependence.

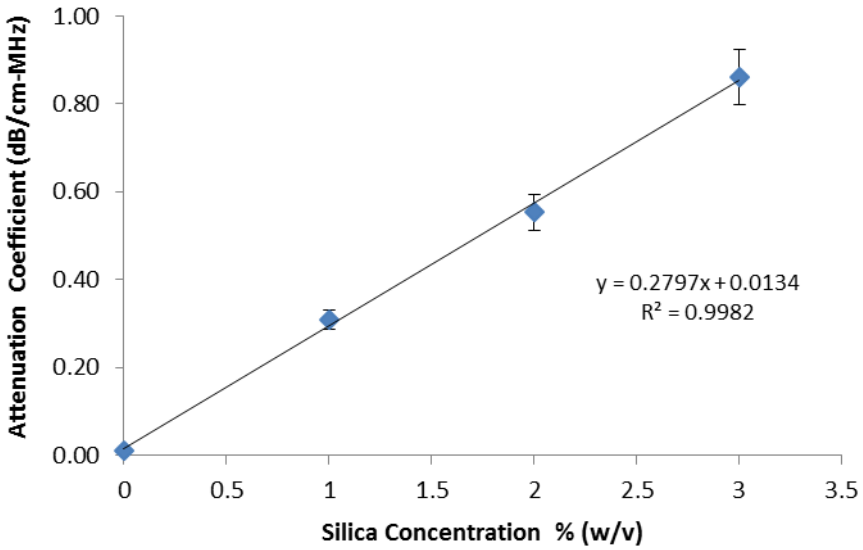

Figure 3.5: Agar-silica gel attenuation coefficient variation for different concentrations of silica dioxide.

3.6.3 Estimation of attenuation coefficient variation for agar gels doped with different concentrations of evaporated milk using transmission through technique.

Materials and Methods

A recipe described by Madsen et al. was used [132], where evaporated milk was added to agar gels to produce a solid gel of very low scatter tissue mimicking material. Evaporated milk is a dehydrated version of fresh milk, where approximately 50 % of water is removed. In the absence of silica dioxide from the gel any drop in the intensity of the acoustic field could be attributed primarily to acoustic absorption by the evaporated milk. Four sets of agar-milk gel samples of different milk concentrations (10%, 20 %, 40 % and 50 % v/v) in a 2 % w/v agar based gel were prepared. The evaporated milk used was a product by Friesland Campina, Marousi, Greece (NOUNOU condensed milk). According to the manufacturer's nutritional datasheet, 100 ml of milk included 4.2 g of fats and 3.5 g of proteins.

For each sample, agar powder was mixed with the appropriate volume of distilled and degassed water. Similarly like in silica experiments, agar–water mixture was boiled with a heater until agar melted. For each concentration sample, the correct volume of evaporated milk was boiled up to 55 °C in a separate container. Temperature was monitored in both containers using an electronic thermometer (Electrotherm Model TH-99A, Cooper Instrument Corp., Middlefield, Connecticut, USA). When the temperature of the agar-water mixture reached 55 °C, the warm evaporated milk was added and was well mixed using a magnetic stir bar. We avoided to add milk while the agar-water mixture was hot since proteins denature irreversibly above 55 °C. The agar-milk gel was poured and left to solidify overnight in the custom made plastic sample containers (16 mm and 26 mm). The sample containers were used to determine the attenuation coefficient from each agar-milk concentration sample. Once again we used the varying thickness technique and monitored the voltage drop in the signal of a 3.5 MHz ultrasound transducer- receiver while using the transmission through method.

Results

The results for each agar-evaporated milk sample concentration are summarized in Figure 3.6. A linear correlation of milk concentration to attenuation coefficient was observed, which was evident of acoustic absorption mechanism enhancement. The attenuation induced by acoustic absorption of different concentrations of evaporated milk embedded in a 2 % w/v agar gel was assessed. Attenuation increased linearly with the concentration of milk in the gel primarily due to absorption mechanism.

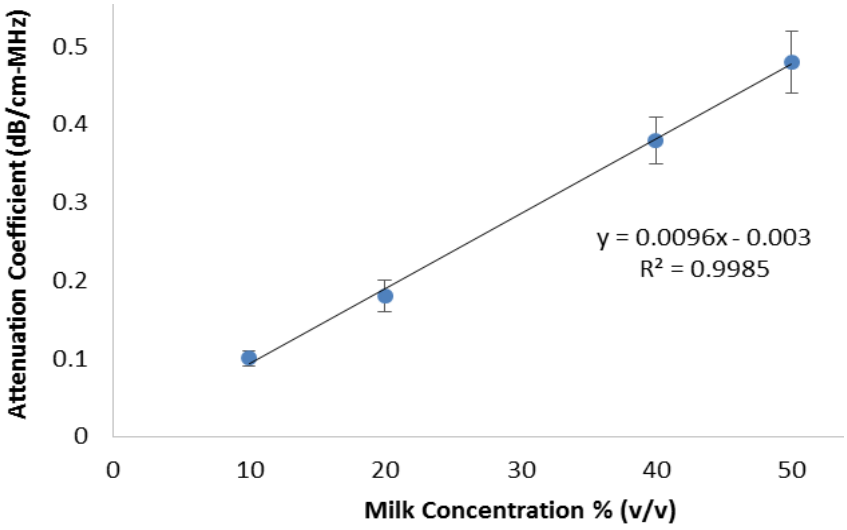

Figure 3.6: Agar-evaporated milk gel attenuation coefficient variation for different concentrations of evaporated milk.

The results are in agreement with the results presented by Madsen et al. [132], which demonstrated a broadband attenuation coefficient of 0.5 dB/cm-MHz for agar gels doped with a 50 % v/v concentration of evaporated milk for frequencies up to 8 MHz.

3.6.4 Estimation of attenuation coefficient of ABS samples using transmission through technique.

Materials and Methods

ABS was tested as the candidate material for replicating bone tissue. Two square plates of ABS specimens of different thicknesses, 2.5 mm and 5 mm respectively, were produced (4×4 cm) using a rapid prototyping machine (Stratasys, Fortus FDM 400mc, Eden Prairie, Minnesota, USA). The produced specimens are shown in Figure 3.7. A solid interior printing style was used to fill up the model completely with raw material without any air gaps. Details of the printing process will be described in the following chapters.

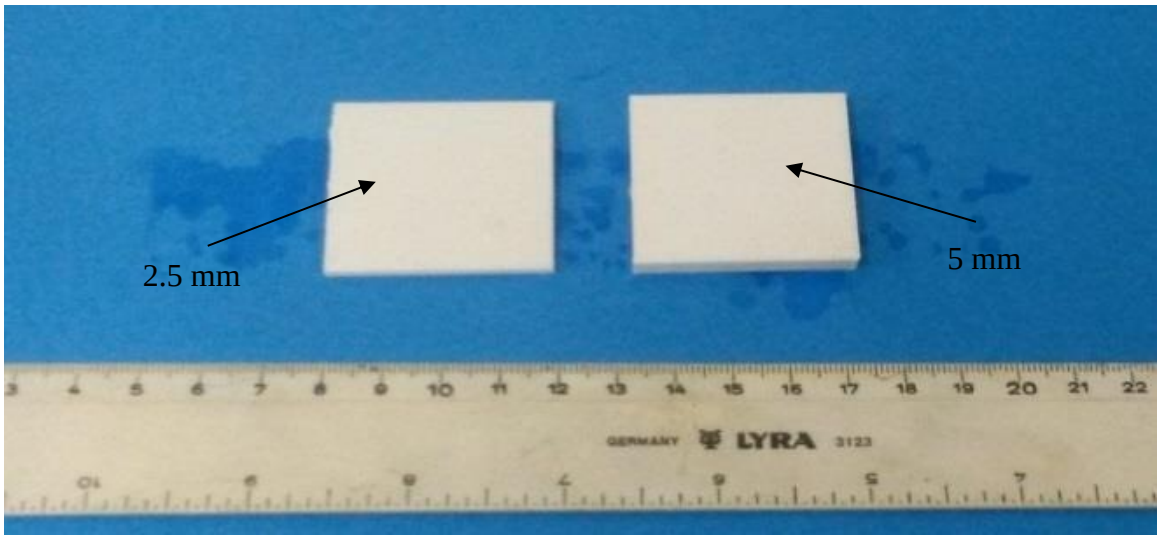

Figure 3.7: ABS specimens of 2.5 and 5 mm thickness.

The printed ABS specimens were significantly thinner compared to the agar gel samples tested. Attenuation from the plastic was expected to be large and therefore in order to measure adequately a signal, specimens' thicknesses were kept small. The ABS plates were secured tightly in the rails of a custom made holder approximately midway between the transmitter and receiver (Figure 3.8). The rails hold the ABS plates in an upright position for intersecting the field's propagation direction at right angles. The setup used was identical to the one used while testing the attenuation of agar gels doped with various additives. The emitted amplitude and the receiver's gain were set to maximum to amplify the very small acoustic signal transmitted through the plastic samples.

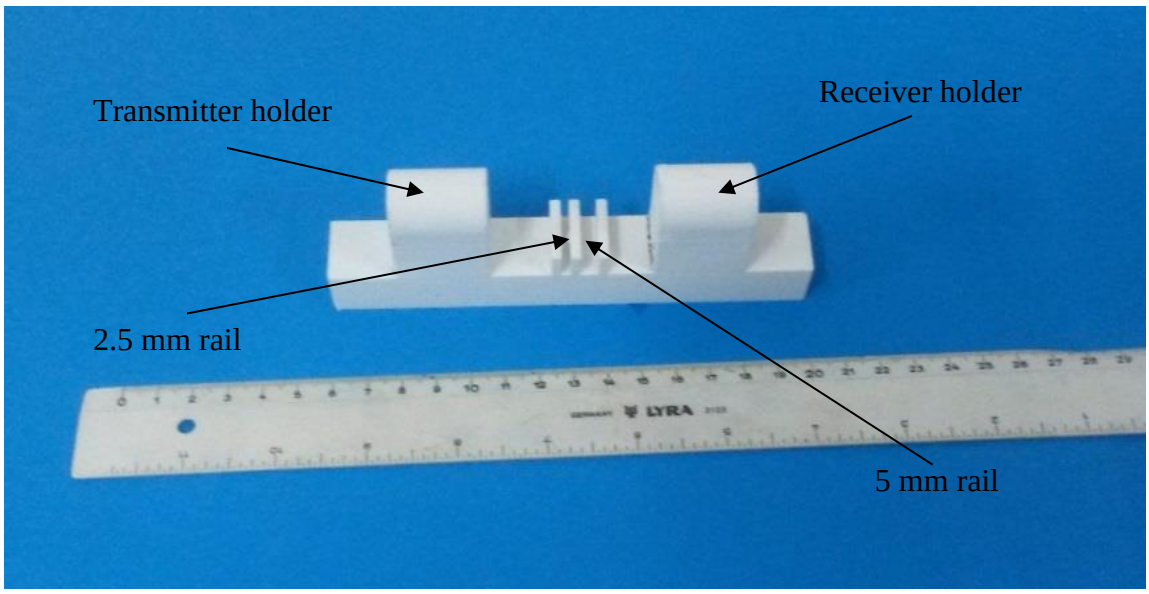

Figure 3.8: Custom made holder for ABS attenuation measurements.

Results

The ABS attenuation coefficient was calculated using the expression described by Equation 2. A linear dependence of attenuation with frequency was assumed. The attenuation coefficient was estimated to be equal to 16.01 ± 6.18 dB/cm-MHz.

3.6.5 Estimation of acoustic speed using pulse echo technique.

The pulse-echo immersion technique was used for estimating the acoustic speed in the candidate materials. The method involved one transducer (Etalon, ESN-410-SCBI). The transducer was operating at a central frequency of 3.5 MHz. Specimens of each recipe with a 2.6 cm thickness were prepared and molded in custom made containers as shown in Figure 3.3B. A pulser/receiver (Panametrics 500PR, Olympus Corp., Tokyo, Japan) supplied the electrical pulses to the transducer while set to the T/R (transmit/receive) mode. The specimen was positioned in the far field of the transducer and echo reflections from each interface were observed on an oscilloscope (Hameg HM203-7, HAMEG Instruments GmbH, Mainhausen, Germany). The transducer-specimen setup was immersed in a tank filled with degassed water as shown in Figure 3.9.

Acoustic speed in the specimen was estimated by determining the time difference Δt between the echoes returning from the interfaces of the specimen. An echo E_1 which corresponded to the reflection from the first interface (water/specimen) and an echo E_2 from the second specimen/water interface were observed (Figure 3.9).

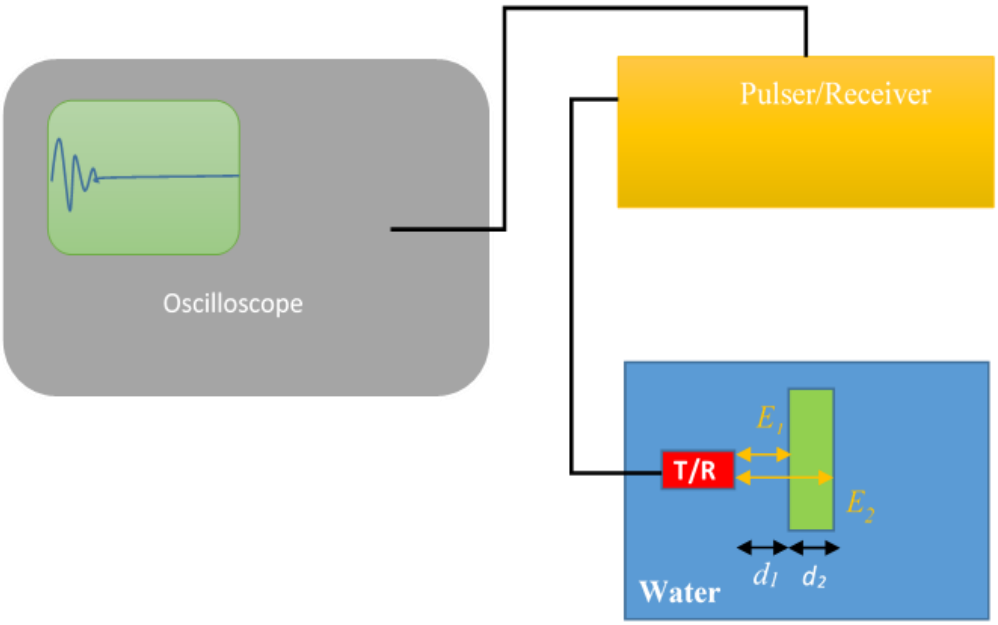

Figure 3.9: Experimental setup of pulse echo immersion technique for measuring the acoustic speed in the tested specimens.

A typical signal with the characteristic echo peaks was displayed on the oscilloscope as shown in Figure 3.10, where the 2nd and 3rd peak correspond to E_1 and E_2 respectively. The time required (t_1) for E_1 to bounce on the first interface while travelling for a distance equal to $2d_1$ in water is given by Equation 5, where v_{water} represents the propagation speed of sound in water.

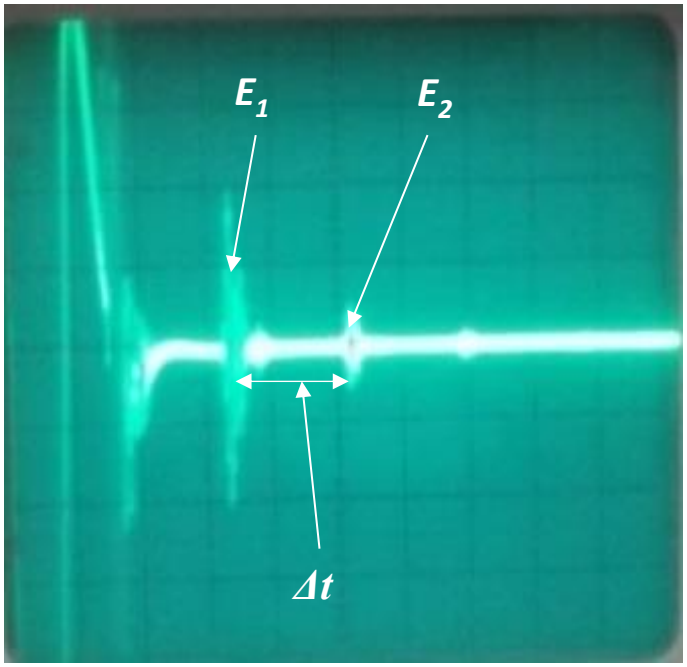

Figure 3.10: Typical signal produced by reflections at specimen's interfaces during pulse echo immersion technique for estimating acoustic speed.

$$t_1 = \frac{2d_1}{v_{water}} \tag{3.4}$$

Following the path of E_2 an expression that describes the time t_2 required for the echo to propagate through a distance of $2d_1$ in water and $2d_2$ in the specimen and return back to the transducer (Equation 3.5). The expression takes in to consideration that v_{water} and $v_{specimen}$ are different.

$$t_2 = \frac{2d_1}{v_{water}} + \frac{2d_2}{v_{specimen}} \tag{3.5}$$

The time difference Δt between the two echoes can be found by deducting t_1 from t_2 and end up with an expression which depends only on d_2 and $v_{specimen}$ (Equation 3.6).

$$\Delta t = t_2 - t_1 = \frac{2d_2}{v_{specimen}} \tag{3.6}$$

Solving for $v_{specimen}$ we end up with an expression that only Δt *needs* to be measured (d_2 is assumed to be known).

$$v_{specimen} = \frac{2d_2}{\Delta t} \tag{3.7}$$

Acoustic speed was calculated using the aforementioned pulse echo method for two agar gel recipes that combined both silica dioxide and evaporated milk. The two recipes included different concentration of additives and they were selected based on the attenuation characteristics of the soft tissues replicated. The brain phantom recipe was made out of 2 % w/w agar, 1.2 % w/w SiO_2, 25 % v/v evaporated milk whereas the second recipe mimicking muscle tissue consisted out of 2 % w/w agar, 2 % w/w SiO_2, 40 % v/v evaporated milk. Details about the selection of the exact concentrations will be given in the following chapters where fabrication of phantoms will be fully described. Specimens of both gel recipes were prepared and molded inside the 2.6 cm containers used for the attenuation measurements. A thicker sample was selected to increase the time difference between E_1 and E_2 to improve the accuracy in the acoustic speed's estimation.

Initially an attempt to estimate the acoustic speed in ABS specimens was made using the pulse echo technique but soon realized that it was not possible. The main problem with ABS was that only echoes from the front wall of the specimen were detected (E_1) by the transceiver and none from the back wall (E_2). The main reason for not

detecting the reflection echo was due to disturbance of the propagating wave from the inner layers of the specimen. During fused deposition modelling, ABS is deposited in a raster pattern and consecutive raster layers are oriented at 45º to each other to minimize void space. Transmission through method was used to determine ABS acoustic velocity by observing the change in the time of flight of the transmission signal (*S*) detected by the receiver (Figure 3.11).

In the absence of a specimen the time required (t_1) for the sound wave (*S*) travelling from the transmitter (*T*) to the receiver (*R*) positioned at distance (d_1) is given by equation 3.8, where v_{water} corresponds to ultrasound speed in water.

$$t_1 = \frac{d_1}{v_{water}} \tag{3.8}$$

If a specimen of ABS of thickness d_2 is immersed in between the two transducers, the time of flight of the transmission signal (t_2) is described by equation 3.9, where $v_{specimen}$ corresponds to ultrasound speed in the specimen.

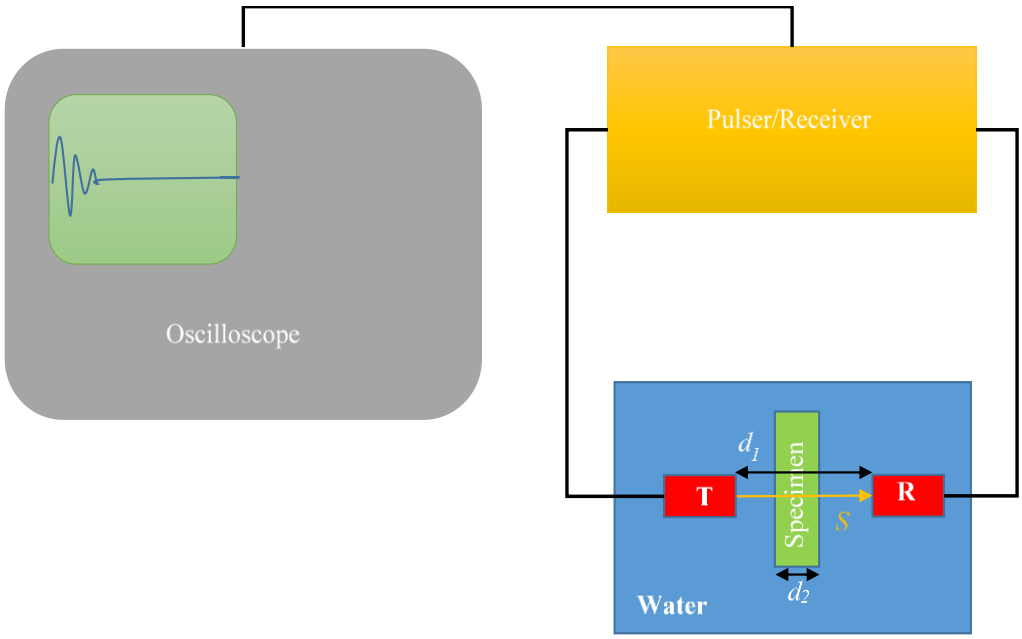

Figure 3.11: Experimental setup of transmission through immersion technique for measuring the acoustic speed in ABS specimens.

$$t_2 = \frac{d_1 - d_2}{v_{water}} + \frac{d_2}{v_{specimen}} = \frac{d_1}{v_{water}} - \frac{d_2}{v_{water}} + \frac{d_2}{v_{specimen}} \quad (3.9)$$

By substituting equation 3.8 to equation 3.9 a simple expression for calculating $v_{specimen}$, is derived.

$$v_{specimen} = \frac{d_2}{(t_2 - t_1) + \frac{d_2}{v_{water}}} = \frac{d_2}{\Delta t + \frac{d_2}{v_{water}}} \quad (3.10)$$

A specimen of intermediate thickness (d_2 = *1 cm)* was used to balance between heavy attenuation of the transmitted signal by ABS (~ -56dB at 3.5 MHz) and adequate change in the time of flight. The acoustic speed in water was taken as 1480 m/s, whereas Δt was found by measuring the relative change in the time of flight of transmission signal with (t_2) and without the specimen in place (t_1).

Results

For the brain mimicking gel recipe (2 % w/w agar, 1.2 % w/w SiO_2, 25 % v/v evaporated milk), acoustic speed was estimated at 1485 ± 12 m/s. For the muscle mimicking gel (2 % w/w agar, 2 % w/w SiO_2, 4 0% v/v evaporated milk) acoustic speed increased to 1529 ± 13 m/s. Acoustic speed in an ABS sample was calculated at 2048 ± 79 m/s.

3.7 Mass density measurements using the water volume displacement method.

The aforementioned soft tissue phantom recipes were tested to quantify their mass density. Samples of 100 ml volume for each gel recipe were prepared. The gels were sliced in approximately equal volumes, with dimensions small enough to fit inside a volumetric tube. Each piece was first weighed with a high precision (±0.01 g) electronic scale (Tanita 1479V digital mini scale, Preston, Washington, USA) and then its volume was deduced by measuring water displacement in a volumetric tube (±1 ml). The greatest source of error in these measurements was the precision of the volumetric tube, therefore the specimens used were as large as possible to minimize the fractional error in volume measurements. Six specimens were taken from the same batch and the average mass density in g/cm^3 was calculated.

The density of the brain mimicking phantom recipe (2 % w/w agar, 1.2 % w/w SiO_2, 25 % v/v evaporated milk) was found to be 1.05±0.01 g/cm^3 and similarly for the muscle recipe (2 % w/w agar, 2 % w/w SiO_2, 40 % v/v evaporated milk), mass density was estimated to be 1.07±0.01 g/cm^3. ABS density was taken from the manufacturer's datasheet [157] which was reported at 1.04 g/cm^3.

3.8 Estimation of soft tissue phantoms thermal properties

The goal of this study was to develop tissue mimicking phantoms destined for testing thermal protocols under HIFU. Therefore in order to make comparisons and extract conclusions that are either directly or indirectly transferrable to *in vitro, in vivo* or numerical simulation studies, the thermal properties of the candidate materials must be characterized.

3.8.1 Estimation of soft tissue phantoms thermal properties using a noninvasive MR thermometry technique.

Materials and Methods

Thermal conductivity is an intrinsic thermal property of materials that describes the ability of the material to conduct heat away from hotter to colder areas until thermal equilibrium is established. Numerically it is expressed as the rate of transferred heat between two conducting surfaces of the material per unit surface area (W/m^2) divided by their temperature gradient (K/m^1 or ºC/m). The units of thermal conductivity are W/m-K or W/m-ºC.

The traditional methods for measuring thermal conductivity of a material can be categorized in steady state and transient methods. In steady state methods measurements are performed while the temperature of the material under examination does not change over time, whereas in transient techniques measurements are done while heating the material. Both methods require specialized equipment like heat sources and sensors of various geometries. The aforementioned methods are partially invasive since they require embedding temperature sensors inside the material under examination, thus affecting its structural integrity. Instead a completely noninvasive approach first presented by Cheng *et al*. [158] was used, where thermal conductivity estimation is possible by combining magnetic resonance temperature imaging (MRTI) and HIFU.

The method uses HIFU to induce moderate heating to tissue whilst monitoring temperature with MRTI. Following the end of sonication, thermal clearance can be

characterized by a 2D space and time analysis of the Bioheat Equation (BHT) described by Pennes *et al*. [159]:

$$\rho_t c_t \frac{\partial T}{\partial t} = k_t \nabla^2 T - w_b c_b (T - T_a) + Q \tag{3.11}$$

, where T is the tissue's temperature, k_t is the thermal conductivity of tissue, t is time, ρ_t corresponds to tissue density, c_t and c_b are the specific heats of tissue and blood (water equivalent), w_b is the blood perfusion rate, T_a is the arterial blood temperature and Q is the total power deposition. The BHT equation assumes that thermal clearance in tissues is governed by two mechanisms: conduction and perfusion. The non-directional term of perfusion represents the cumulative effect of a dense capillary network which in the absence of a large vessel acts as spatially uniform heat sink.

Cline *et al*. [160] showed that the focusing patterns from a spherically focused transducer can be approximated with elliptical Gaussian functions with radial (r_o) and axial (z_o) radii and provide an exact analytic solution of the BHT equation. For a time impulse source of heat provided by focused ultrasound, the exact solution of BHT at focus ($z=0$) and in a plane perpendicular to sound propagation simplifies to the following 2D Gaussian function for $T(r,t)$ along the focal plane:

$$T(r,t) = A(t)\, e^{\left(-\frac{r^2}{4D(t+\tau_R)}\right)} = A(t)\, e^{\left(-\frac{r^2}{R^2(t)}\right)} \tag{3.12}$$

, where D corresponds to the diffusivity and τ_R to the heat diffusion time constant along the radial direction. In heat transfer analysis the diffusivity coefficient (D) is the ratio of thermal conductivity (k_t) divided by the tissue's density (ρ_t) multiplied by its specific heat capacity ($\boldsymbol{c_t}$) at constant pressure (equation 3.13).

$$D = \frac{k_t}{\rho_t c_t} \tag{3.13}$$

The final form of Equation 12 represents a Gaussian shaped temperature profile with a time dependent radius $\boldsymbol{R(t)}$ which expands with time. The expansion rate of $\boldsymbol{R^2(t)}$ can calculated by differentiation in Equation 3.14.

$$\frac{\partial R^2(t)}{\partial t} = \frac{\partial}{\partial t}(4D(t+\tau_R)) = 4D = \frac{4k_t}{\rho_t c_t} \tag{3.14}$$

Using the final form of equation 3.14 the unknown tissue conductivity coefficient k_t can be derived by monitoring the expansion of squared radius $R^2(t)$ of the Gaussian temperature profiles over time during cooling period as demonstrated in Figure 3.12A.

As expected from equation 3.14 a plot of $R^2(t)$ against time (t) would yield a straight line with a gradient proportional to the conductivity coefficient k_t as showed in Figure 3.12B.

The method described above was used to quantify the thermal properties of the two soft tissue phantom recipes (brain and muscle). A spherically focused ultrasound transducer (Sonic Concepts, Inc., Bothell, Washington, USA) driven by a 750 W amplifier (JJ&A Instruments, Duvall, WA, USA) was used to sonicate the gel phantoms and raise the temperature at the focus. The transducer consisted of a single element piezoelectric crystal of 4 cm diameter and with a focal length of 95 mm.

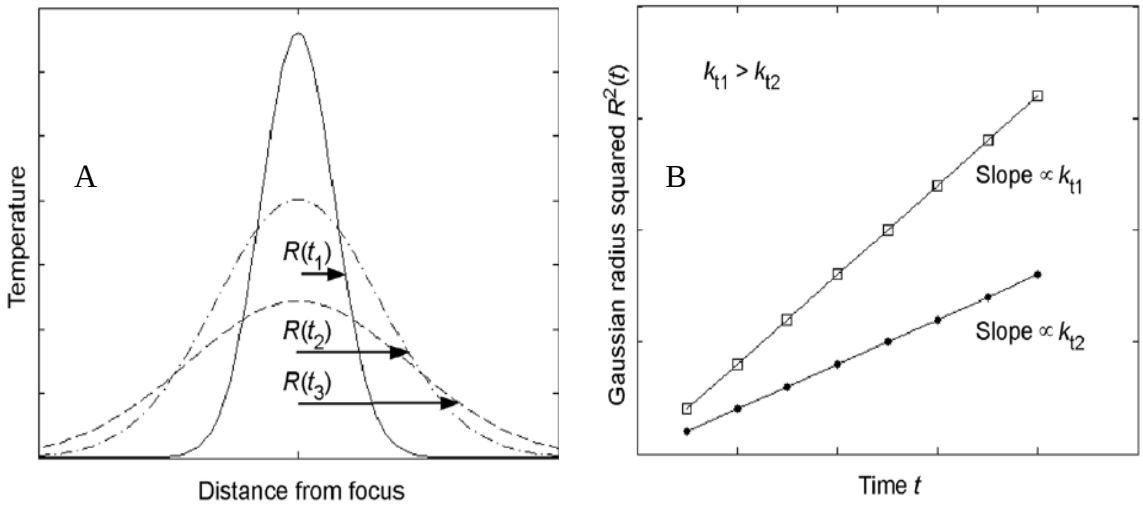

Figure 3.12: A) Temperature measured at a focal plane for different times (t) post sonication across the focus. The distribution of temperature across the focus was fitted to a Gaussian profile centred at maximum temperature for each point in time. R(t) represents the Gaussian radius which is equal to half width at half maximum of the Gaussian profile. B) Linear dependence of squared Gaussian radius $R^2(t)$ at different post sonication times (t). The gradient of the linear fit is proportional to the tissue specific thermal conductivity (k_t) [158].

Each of the phantom gels was molded inside a rectangular container with an open top to allow propagation of ultrasound. The transducer and gels were positioned inside a plastic tank filled with degassed water. The transducer was fixed using a holder on top of the gel phantom. The distance between the transducer and the gel's top surface was shorter than the focal length (< 95 mm) so that the focus is created in the center of the phantom. The experimental setup prior to moving inside the MRI bore's isocentre is demonstrated in Figure 3.13. MR temperature imaging was used to monitor temperature elevation and drop during the exposure. A flexible surface imaging coil (GPFLEX coil by General Electric, Milwaukee, USA) was positioned under the water tank. Since the surface coil had a limited sensitivity range (approximately 20 cm) by using this configuration the region of interest inside the gel phantom was brought as close as possible.

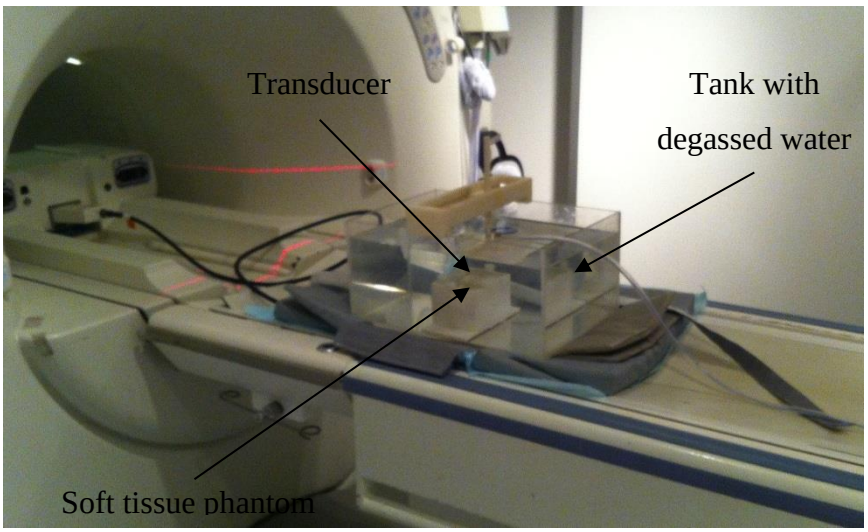

Figure 3.13: Setup for conducting measurements of soft tissue mimicking phantoms thermal properties using MR thermometry techniques.

The setup was positioned at the isocentre of a 1.5 Tesla MRI scanner (General Electric Signa Excite, Milwaukee, USA). Temperature changes were calculated using the proton resonance frequency shift method. The acquisition protocol used for thermometry is presented in 2D SPGR sequence (repetition time (TR): 38.5ms, echo time (TE): 20 ms, receiver bandwidth (rBW): 15 kHz, matrix: 128 x 128 pixels, slice thickness: 5 mm, number of excitations (NEX): 1, displayed field of view (DFOV): 25 x 25 cm^2). The thermometry slice was prescribed in a plane perpendicular to sound propagation and at the level of the focus. Following analysis a single thermal map was produced every 12 s. Details about magnetic resonance thermometry will be given in later chapters. Typical thermal maps in 2D and 3D are demonstrated in Figure 3.14.

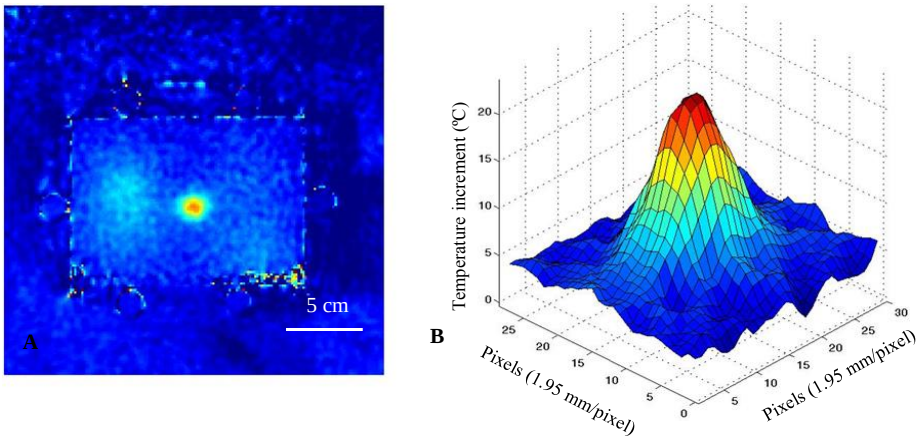

Figure 3.14: A) Representation of thermal map of the soft tissue mimicking gel in 2D, B) The thermal map is illustrated in 3D with temperature being the third dimension.

The two phantoms were heated using the same sonication protocol (Acoustic Power: 25 W, 60 s of sonication duration). Acoustic power conversion efficiency was calculated using previously acquired radiation force calibration data for this particular transducer. The efficiency was calculated approximately at 50 % conversion of electric to acoustic power. The phantoms were targeted in their center in order to maintain uniform temperature gradients in all directions. The targeted depth was not exactly the same but this was not important since according to Cheng *et al*. [158], conductivity only affected the rate of the radial expansion and not the amplitude of the Gaussian profile. Five temperature profiles post sonication (12, 24, 36, 48 and 60 s) were collected since late Gaussian peaks were masked by noise. For each profile the coefficients of the best fitted Gaussian function were found by using the least squares regression criterion between raw and modelled data. The standard deviation or sigma ($\boldsymbol{\sigma}$) of each fitted Gaussian was used to calculate the full width at half maximum (FWHM) of the Gaussian temperature profile. The FWHM of a Gaussian function and the associated Gaussian radius *R* can be calculated by:

$$\boldsymbol{FWHM \approx 2.3548\,\sigma \approx 2R} \qquad (3.15)$$

The mean Gaussian radius for each point in time was calculated by averaging the radii of two orthogonal temperature profiles which were 15 pixels long (approximately 15 mm) and centered over the maximum temperature pixel as shown in (Figure 3.15).

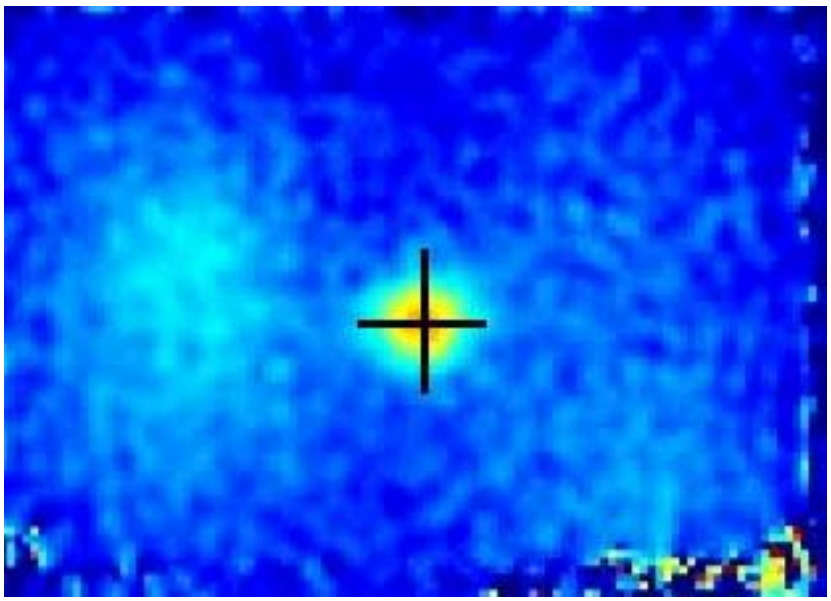

Figure 3.15: The two orthogonal 15 pixel long profiles (black lines) centred over the maximum temperature pixel used to calculate the average Gaussian radius.

Results

The average squared Gaussian radius of the temperature profile for the brain and muscle tissue mimicking phantom recipes versus the time post sonication are illustrated in Figure 3.16. The linear dependence for both sets of data between $R^2(t)$ and time demonstrated that the radial expansion of the temperature profile "decelerates" with time. The two tested recipes resulted in slightly different slopes as a result of their difference in thermal conductivity. Thermal conductivity was estimated by equating the slopes of the fitted data with the right hand side of equation 3.14. Mass density (ρ_t) for each recipe was calculated in section 3.7 using the water displacement technique. The heat capacity of each phantom was estimated by using a weighted sum of the heat capacity of the two main ingredients, which were water and evaporated milk. This was a reasonable assumption since both together consisted for more than 95 % of the gel's mass.

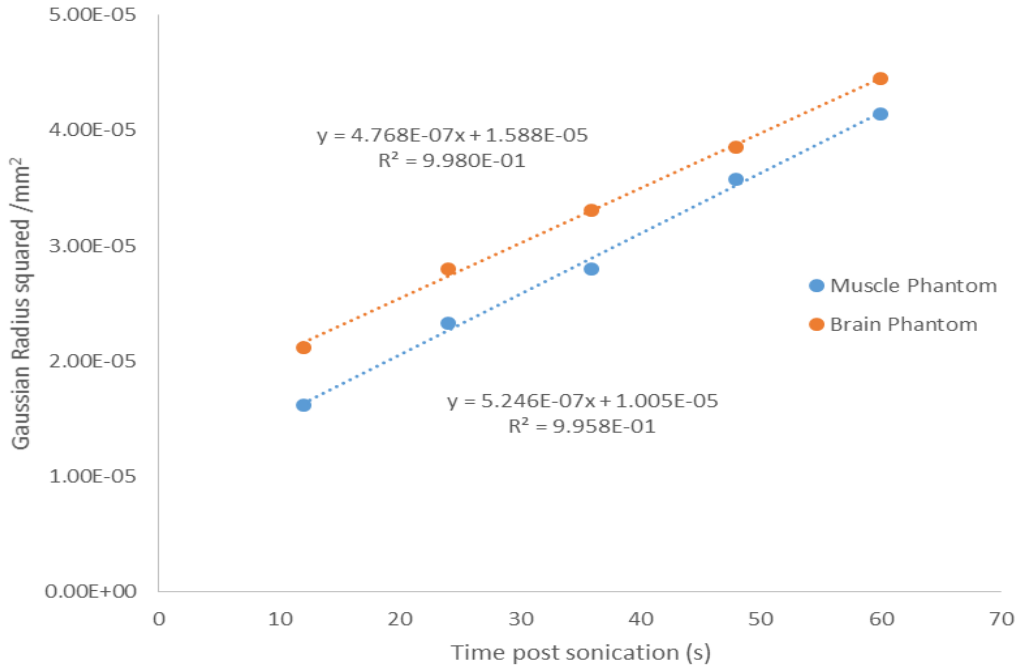

Figure 3.16: Plot of the temperature profile's squared Gaussian radius $R^2(t)$ versus post sonication time (t) for the brain and muscle agar gel phantom.

From literature it was found that the nominal heat capacities for water is 4.19 J/g-ºC and for evaporated milk 3.94 J/g-ºC [161]. The weighted heat capacity for the brain phantom (75 % v/v water, 25 % v/v evaporated milk) was calculated at 4.13 J/g-ºC and for the muscle phantom (60% v/v water, 40% v/v evaporated milk) 4.09 J/g-ºC.

By substituting the above in equation 3.13, the thermal conductivities of the brain and muscle phantom were estimated at 0.52±0.06 W/m-ºC and 0.57±0.10 W/m-ºC respectively. Thermal diffusivity (*D*) which is a thermal property derived by dividing

conductivity with density and specific heat capacity, describes how quickly a material reacts to a change in temperature. The calculated diffusivity (*D)* for the brain phantom was 0.0012±0.0001 cm^2/s and for the muscle phantom 0.0013±0.0001 cm^2/s. Errors in conductivity and diffusivity coefficients were estimated by considering the error in slope of the fitted data.

3.9 Conclusions

Two calibration curves were calculated by fitting a linear model that characterized attenuation variation with the concentration of either silica dioxide or evaporated milk embedded in agar gels of 2 % weight to volume concentration. It was assumed that silica dioxide primarily induced only Rayleigh scattering due to the small size of particles compared to ultrasound's wavelength. Evaporated milk which was introduced as a very low scattering material, was the primary source of acoustic absorption. For the range of the concentrations tested, the agar-silica dioxide gels demonstrated a linear scattering induced attenuation coefficients of up to 0.85 dB/cm-MHz. Compared with the study of Partanen et al. [4], silica produced a higher degree of attenuation for the same concentration. Similarly agar-evaporated milk gels transmission through assessment resulted in absorption induced attenuation coefficients of up to 0.38 dB/cm-MHz. The slopes of the two calibration curves were used to interpolate and calculate the required concentration for each of the two additive materials to deliver a prescribed total attenuation coefficient while independently controlling the contributions of scattering and absorption (Table 3-1).

Table 3-1: Attenuation coefficient variation with concentration of scattering and absorption enhancing additives to agar gels.

	Agar 2 % (w/v) + Silica Dioxide 0 % - 3 % (w/v)	**Agar 2 % (w/v) + Evaporated Milk 10 %-40 % (v/v)**
Attenuation Coefficient Primary Scattering **(dB/cm-MHz)**	$(0.28\pm 0.03) \times \%\ M_{\text{Silica Dioxide}}$	-
Attenuation Coefficient Primary Absorption **(dB/cm-MHz)**	-	$(0.01\pm0.00) \times \%\ V_{\text{Evaporated Milk}}$

Based on these calibration curves two soft tissue recipes were prepared. The brain recipe (2 % w/w agar, 1.2 % w/w SiO_2, 25 % v/v evaporated milk) combined the two

additives previously tested to produce a final product with a total attenuation coefficient (0.59 dB/cm-MHz) within the range of bibliographic data [17], [20], [162]. The relative contributions of scattering and absorption of 0.34 dB/cm-MHz and 0.25 dB/cm-MHz respectively were achieved according to attenuation and absorption measurements in mammalian tissues presented by Goss *et al*. [20] and Sehgal *et al*. [163]. The muscle phantom recipe (2 % w/w agar, 2 % w/w SiO_2, 40 % v/v evaporated milk) was designed with an attenuation coefficient equal to 0.99 dB/cm-MHz which agreed with values (0.5–4.1 dB/cm-MHz) found from bibliography [164], [165]. The relatively wide range of attenuation coefficients is due to the fact that muscles are highly anisotropic tissues since they have a strong directional distribution of fibers. Experiments exploring the anisotropy in acoustic speed, attenuation and backscattering in rodents skeletal muscles with fibers orientated at 90º and 45º relative to the incident beam were conclusive [166]. It was suggested that the mechanisms which are responsible for anisotropy in these parameters were related to orientation of the elastic tissue structure and to muscle fibers acting as scatterers. It was assumed that there was no directional dependence of attenuation in the muscle phantom recipe since silica particles were orientated randomly inside the gel without any directional prevalence.

ABS was tested as a bone mimicking candidate material and its attenuation coefficient was assessed using the transmission through technique. It was found that ABS was very efficient in attenuating acoustic waves (16 dB/cm-MHz). The measured attenuation coefficient was within the range of values found in literature. Human bone attenuation data reported in bibliography are very broad as a result of the wide range of porosity, mineralization, bone architecture, choice of anatomical structure and the experimental method followed. The broadband ultrasound attenuation (BUA) coefficient of cortical bone, which forms the compact outer shell surrounding cancellous bone, was measured at different frequencies and ranged between 3.5-8.5 dB/cm-MHz [167]–[172]. In a comprehensive report by Duck *et al*. [17] skull bone attenuation (all layers) was measured at 22 dB/cm at 1 MHz. Aubry *et al*. [173] presented a numerical model that correlated skull diploe layer porosity with absorption coefficient which ranged from 2-80 dB/cm at 1.5 MHz for the same skull sample.

Measurements of the longitudinal acoustic speed of the two soft tissue recipes were also within the range of biological soft tissues (1478 m/s - 1595 m/s) [162]. The speed inside the muscle phantom (1529±13 m/s) was significantly higher from the brain's (1485±12 m/s) because of its higher evaporated milk content. These observations agreed with a recent study by Farrer et *al.* [149] where acoustic speed in gelatin gels increased

with the concentration of evaporated milk concentration. Acoustic speed inside ABS (2048±79 m/s) was in the lower end of a typical range of values found in literature. Culjat *et al.* [162] reported a speed of 1886 m/s in trabecular bone and of 3476 m/s in cortical bone.

The measured mass density of the muscle phantom (1.07±0.01 g/cm3) was found higher from brain (1.05±0.01 g/cm3). The densities of both soft tissue recipes were in good agreement of the values reported individually for brain (1.04 g/cm3) and muscle (1.09 g/cm3) tissue [162]. Density of ABS (1.04 g/cm3) was obtained by the manufacturer's datasheet and was considerably lower from typical cortical bone density (1.97 g/cm3). Acoustic impedance was calculated by multiplying mass density with acoustic speed for each soft tissue recipe and the ABS bone replica. The acoustic impedance of ABS (2.13± 0.08 MRayl) was significantly lower from typical cortical bone (7.38 MRayl) [162]. This difference should be taken in to account when using the proposed phantoms for validating numerical models since the degree of reflected energy at the interface will be significantly lower compared to bone. The assessment results for the candidate materials acoustic properties are summarized in Table 3-2 and Table 3-3.

The thermal properties of the brain and muscle recipes were assessed by correlating the change of the temperature profile's Gaussian radius over time at a plane perpendicular to the thermal focus formed by a HIFU impulse sonication. The method was described in a publication by Cheng et al. [158]. Thermal conductivity (0.52±0.06 W/m-ºC for brain and 0.57±0.10 W/m-ºC for muscle) and diffusivity (0.0012±0.0001 cm^2/s for brain and 0.0013±0.0001 cm^2/s for muscle) for both phantom recipes were found to mimic published values for non-perfused soft tissues. Creeze *et al*. [174] reported a thermal conductivity range of 0.5-0.6 W/m-ºC for non-perfused muscle while in another study by Diederich *et al*.[175], a range of 0.3-0.7 W/m-ºC for unspecified tissue samples was given. Thermal of properties of ABS, which was tested as a bone candidate material, were not assessed since in the majority of focused ultrasound applications energy is delivered to soft tissue. For bone applications apparent temperature is monitored in nearby adjacent soft tissue since bone possesses a very short T_2 relaxation time and consequently the MR signal produced is short lived. The specific heat of each recipe was calculated using a weighted linear combination of the water and milk specific heat. The estimated thermal properties for the two recipes from mimicking brain and muscle tissue are summarized in Table 3-4.

Table 3-2: Acoustic properties of soft tissue mimicking materials.

	Brain phantom	**Brain tissue [17], [20], [162], [163]**	**Muscle phantom**	**Muscle tissue [164], [165]**
Attenuation Coefficient Primary Scattering (**dB/cm-MHz**)	0.34 ± 0.04	0.34	0.59 ±0.07	-
Attenuation Coefficient Primary Absorption (**dB/cm-MHz**)	0.25 ± 0.03	0.26	0.40 ±0.04	-
Attenuation Coefficient Total (**dB/cm-MHz**)	0.59 ± 0.05	0.6	0.99 ±0.08	0.5 - 4.1
Acoustic speed (**m/s**)	1485 ± 12	1460 - 1580	1529 ± 13	1550 - 1630
Mass Density (**g/cm^3**)	1.05 ± 0.01	1.03 - 1.04	1.07 ± 0.01	1.04 - 1.06
Acoustic Impedance (**MRayl**)	1.56 ± 0.02	1.50 - 1.64	1.64 ± 0.02	1.65 - 1.74

Table 3-3: Acoustic properties of bone tissue mimicking material.

	Bone phantom ABS-M30 (Stratasys Ltd)	Bone tissues of interest [162]
Attenuation Coefficient Total (**dB/cm-MHz**)	16.01 ± 6.18	22 (skull) 12.5 (long bones)
Acoustic speed (**m/s**)	2048 ± 79	2590 - 2960 (skull) 3190 – 3406 (long bones)
Mass Density (**g/cm^3**)	1.04 [157]	1.61 (skull) 1.42 (femur bone) 1.41 – 1.52 (rib)
Acoustic Impedance (**MRayl**)	2.13 ± 0.08	4.17 (skull) 4.53 – 4.84 (femur bone)

Table 3-4: Thermal properties of soft tissue mimicking gel recipes.

	Brain phantom	**Brain tissue [17]**	**Muscle Phantom**	**Muscle tissue [17]**
Thermal Conductivity (W/mº-C)	0.52±0.06	0.50 - 0.57 (* *in vitro*)	0.57±0.10	0.5 - 0.6 [174] (* *in vitro*)
Thermal Diffusivity (cm^2/s)	0.0012±0.0001	0.0014 ± 0.0001 (* *in vitro*)	0.0013±0.0001	0.0015 ± 0.0001 (* *in vitro*)
Specific Heat (J/g-ºC)	4.13	3.6 (* *in vitro*)	4.09	3.43 (* *in vitro*)

3.10 Summary

This chapter described the work done for characterizing important acoustic and thermal properties of materials destined to be used for constructing tissue mimicking phantoms, suitable for testing focused ultrasound thermal protocols. The acoustic attenuation coefficient and speed of sound of candidate materials for replicating bone (ABS) and soft tissue (agar-based gels) were investigated using pulse immersion techniques. The agar-based gels were doped with additives to control independently from each other, the two main acoustic energy loss mechanisms (scattering and absorption) of sound energy propagating through biological tissue. Agar gels were convenient to work with since they possess a high melting temperature, non-toxic, easy to prepare and can be produced with relatively low cost. ABS is a thermoplastic material used in fused deposition modelling for creating geometrically accurate models. Additionally the thermal conductivity of the finalized agar-based gel recipes was estimated since it governs the rate of heat transfer from the thermal focus to the surroundings.

The results of this study demonstrated that the selected materials can be used to approximate relevant physical properties of the replicated tissues that control the interaction of focused ultrasound. Composite phantoms that include both bony and soft tissue mimicking parts of the replicated anatomy are important for testing whether the therapeutic goal of a focused ultrasound thermal protocol has be reached, to observe the temperature spatial distribution and to investigate safety issues raised by the interaction of ultrasound with obstructions like bone. Innovations or improvements in current hardware and software need to be tested prior to clinical use and therefore a tissue

mimicking phantom is a very convenient tool for doing so. Close matching between relevant acoustic and thermal properties of the phantoms with the equivalent ones of the replicated biological tissue govern the validity of results produced by phantom studies.

4 Design and preparation of composite phantoms

This chapter describes the design and preparation of composite phantoms made out of suitable materials tested in a previous chapter. The phantoms are composed of soft and bone tissue mimicking materials. Three phantoms were developed and they were chosen to cover a wide range of HIFU hyperthermia and ablation applications guided by MRI that are currently approved as either a treatment option or are still under preclinical investigation. All three phantoms had customized attenuation properties according to the mimicked soft tissue. The bone components of each phantom affected the incident beam in a different way depending on the application. Skull bone in transcranial applications acts as an obstructing transmission medium in the near field whereas in bone applications focus is targeted on the bone directly to use constructively its high absorption coefficient and elevate the temperature locally to the diseased bone tissue. In rib-breast applications safety issues are raised from increased acoustic absorption and reflection from bone surface when it is situated in the far field.

4.1 Design and fabrication of a composite head phantom for testing transcranial MRgFUS thermal protocols

4.1.1 Human skull anatomy

The human skull consists of 28 bones that can be categorized in to two groups, the cranial and the facial bones. The cranial bones serve to protect and support the brain and the related neurovascular structures whilst facial bones hold the oral and nasal cavities, the sinuses and orbits. The largest cranial bones that surround the brain consist of the frontal bone, the left and right parietal bone, the occipital bone and the left and right temporal bones. In transcranial HIFU applications, the acoustic beam is transmitted through the cranial bones because they usually lack any obstructing bone-air cavities and coupling is easier due to the smooth geometry.

A typical cross section of a dry frontal cranial bone is shown in Figure 4.1. Inner and outer tables of cortical bone enclose a layer of trabecular bone also known as diploë. Cortical bone is dense and tough and serves to support whole body structure and protect trabecular bone. Trabecular bone which has a very porous structure, is made out by a complex network of trabeculae. Trabeculae are thin rod and plate like shaped network of bone tissue. Empty space between trabeculae is filled with red bone marrow which is responsible for producing blood cell constituents (red and white blood cells, platelets).

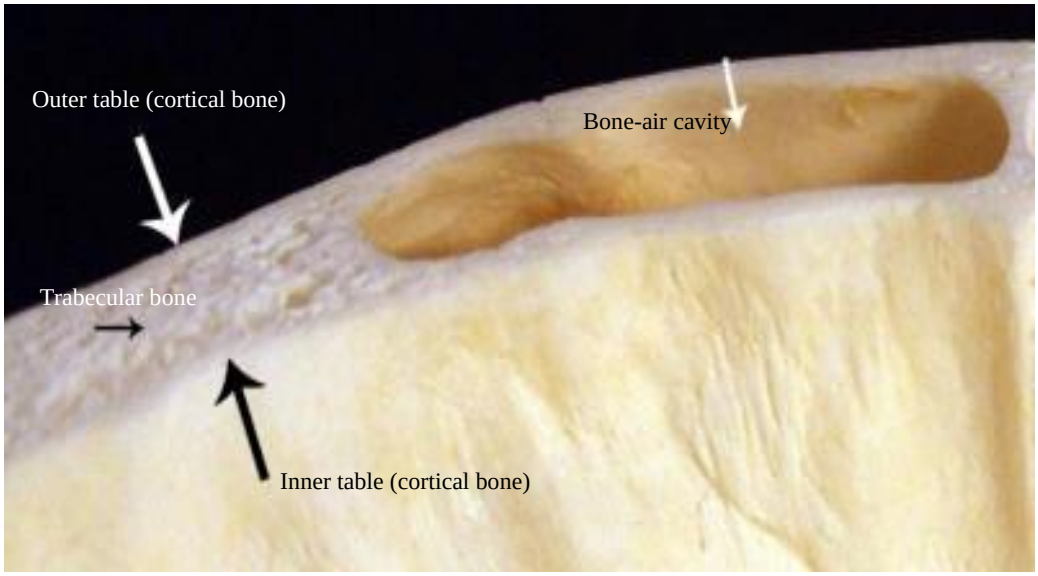

Figure 4.1: Dried human skull bone cross section [176]. *Typical adult human skull thickness varies approximately between 5-10 mm depending on age, gender, race and anatomical location.*

Some sections of red bone marrow are vascularized to supply bone with nutrients, transport blood stem cells and remove mature blood cells away from the bone and into circulation. Air cavities better known as sinuses are voids found in the forehead and in face. Nasal sinuses are known to secrete mucus that moisten air flow whilst others in the absence of bone decrease the overall weight of the skull. Frequently at the dome of a human skull the two cortical tables can fuse together in the absence of a trabecular bone layer.

4.1.2 Computed tomography (CT) of a human skull

High resolution CT head scan images of an anonymized adult male patient were randomly chosen from a public hospital's database (Limassol General Hospital, Cyprus). The selected set consisted of 219 slices acquired with a CT scanner (Toshiba Aquilion 16, Toshiba Europe GmbH) in helical mode with the following scanning parameters: 120 kV, 322 mAs, 24 cm FOV, 16 × 0.5 mm collimation, 0.73 mm effective slice thickness and a 512 × 512 matrix. Using slice thinner than 1 mm was essential in order to minimize helical artefacts on the final 3D model of the segmented skull bone. The images produced by the CT scanner were DICOM (Digital Imaging and Communications in Medicine) formatted. DICOM images do not contain only voxel data information, but come with an embedded header that contains tags with information related to the patient, the examination and study identifiers. CT images represent a map of volume elements

(voxels), where each voxel is assigned a value based on the Hounsfield scale. Hounsfield units (HU) of each voxel are obtained from a linear transformation of the measured linear attenuation coefficients. The linear attenuation coefficient describes the rate of energy loss by a photon beam per centimetre within a medium and depends on the medium's density and of course the beam's energy. This transformation is based on arbitrary definitions of the radiodensity of distilled water and air at standard temperature and pressure to 0 HU and -1000 HU respectively.

4.1.3 Skull bone segmentation

The produced CT head scan images were imported in DICOM format into an interactive segmentation software (Materialise Mimics 10.0, Leuven, Belgium). This software can be used for segmenting images produced by 3D medical modalities like CT or MRI. Segmentation refers to a process that divides an image or a set of images into regions of similar gray level (radiodensity), color, texture, brightness, and contrast [177]. Following the import of CT images, the software displayed the raw axial images and the associated multiplanar reconstructions in the coronal and sagittal planes.

Skull bone is made out of layers of cortical and cancellous bone which are dense tissues and therefore appear on CT images as pixels with high HU (Cortical bone > 1200 HU, Cancellous bone 300-1200 HU) [178]. A mask was created manually by setting the minimum and maximum threshold of radiodensities in HU to be included. Automatic selection was also available based on predefined HU ranges for specific anatomies. For this individual patient, the selected range was approximately from 360-1800 HU and included both cortical and cancellous bone of the skull. The selected mask displayed in green color is shown in Figure 4.2.

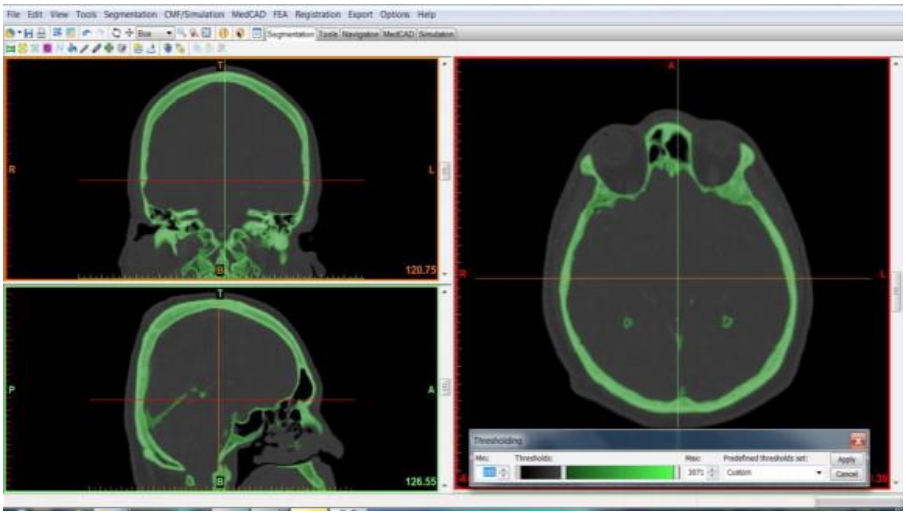

Figure 4.2: Interactive segmentation of skull while discarding surrounding soft tissue.

Once the mask was selected, a cropping tool was used to decrease the anatomical coverage in the head-feet direction. The mask was reduced to the supraorbital region since this was the region free of air cavities that can severely obstruct the acoustic beam. It was decided to create a craniotomy section on the right side of the skull's model in order to provide an easy way of performing in the future sonications with and without intervening plastic skull. The craniotomy section was created by editing the mask in 3D mode and applying a circular separation filter with a diameter of 60 mm. This diameter was made sufficiently larger from all of the transducers to ensure that the focused field propagated through the craniotomy section without any interruption. The craniotomy section was saved as a separate mask. The next step was to calculate 3D geometries through surface rendering of both masks, using optimal reconstruction settings. These 3D models were finalized by exporting them in STL format. The acronym STL stands for Standard Tessellation Language format which is a file type widely used by rapid prototyping machines. This file type approximates geometries of closed surfaces and solid entities through a triangular facet-based representation. Each facet is characterized by the x, y and z coordinates for each of its vertices and a unit normal that defines the facet's pointing out direction. A magnified wireframe view of the skull's STL is demonstrated in Figure 4.3, whereas solid views of both 3D reconstructed geometries (skull and craniotomy section) are displayed in Figure 4.4A and Figure 4.4B respectively.

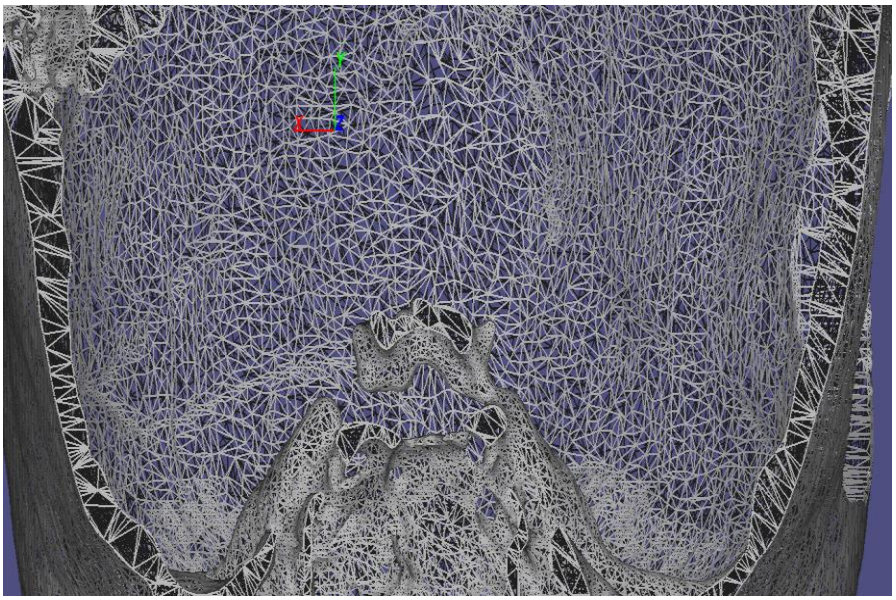

Figure 4.3: Magnified wireframe view of the skull's STL.

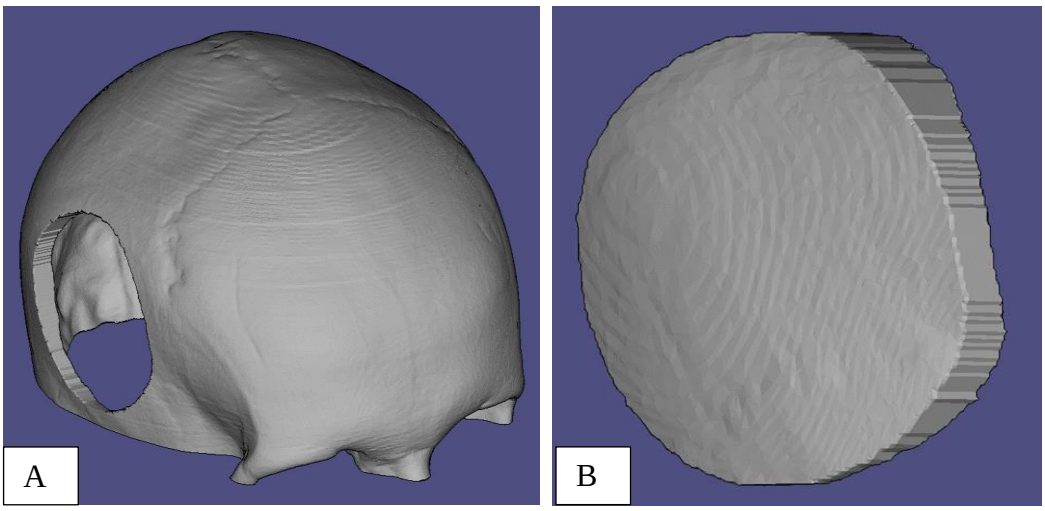

Figure 4.4: A) Solid view of the skull's STL with craniotomy, B) Magnified solid view of the skull's craniotomy section.

The STL files were fine corrected using a diameter filter of the open source MeshLab software (Istituto di Scienza e Tecnologie dell'Informazione, Consiglio Nazionale delle Ricerche (CNR), Italy). This was necessary to remove fragments of calcified vessels that were included in the radiodensity threshold range during segmentation. MeshLab's automatic filters for closing open holes in the surface were also employed in order to produce a watertight model. The dimensions of the final skull model were 142 × 187 × 105 mm.

4.1.4 Plastic skull prototyping

A rapid prototyping machine (Stratasys, Fortus FDM 400mc) that employs additive manufacturing technology was used to build a plastic replica of the segmented 3D skull model. The building envelope of this 3D printer was 355 × 254 × 254 mm and it can be upgraded to 406 × 355 × 406 mm. New layers in the bottom to top direction were added by moving the platform in the downward direction. The printer builds the parts layer by layer from the bottom up direction by moving the platform in the downward direction. The platform's displacement defines the layer thickness and consequently the replication's though plane resolution. All models of this study were printed using the minimum allowable layer thickness for optimum results which was 254 μm. During production solid thermoplastic filament was fed from a canister at the base of the printer to the extrusion head. The extrusion head which hanged from the top of the printer's oven was driven by computer controlled motors set to follow precisely the extrusion pathway in every layer. The thermoplastic material was heated until liquefied and extruded through the tip of a nozzle in ultra-fine beads along the extrusion path. The tip type used was

recommended by Stratasys as the optimal size for compromising between building time and through plane resolution for the particular part's size. The 3D printer's main parts are shown in Figure 4.5A-C.

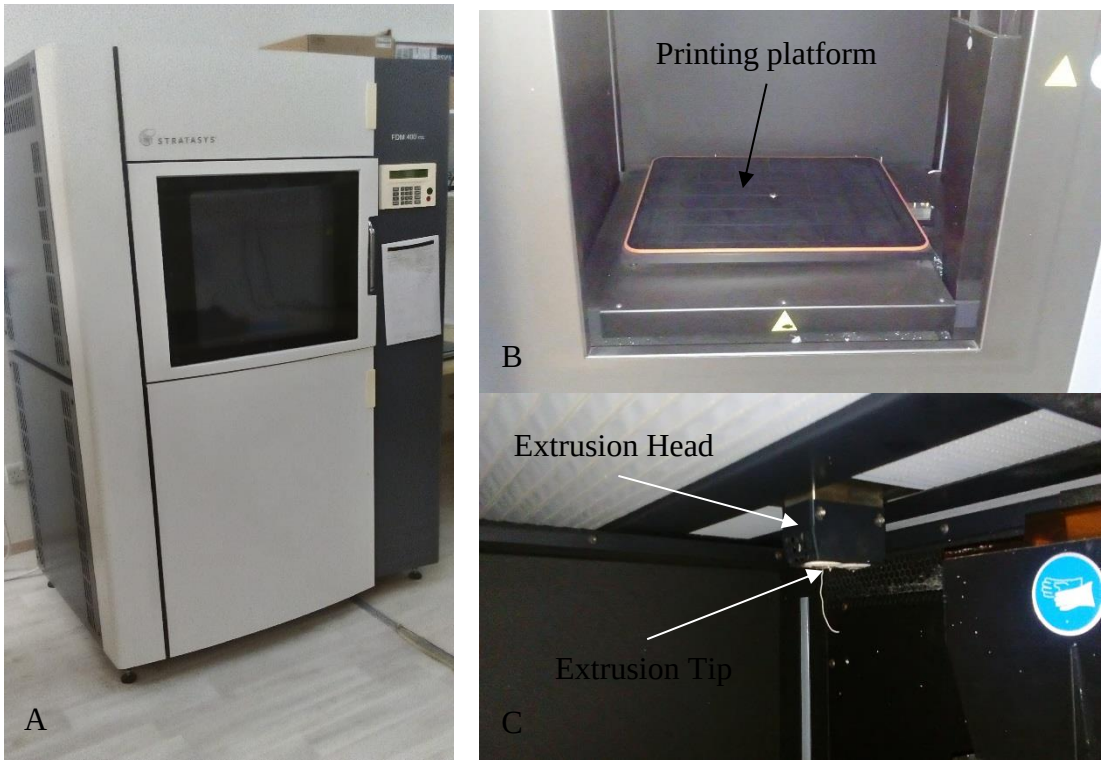

Figure 4.5: A) Stratasys Fortus FDM 400mc, B) 3D Printer's oven with platform, C) Extrusion head.

For the fabrication of the skull phantom, ivory thermoplastic ABS-M30 was selected as the building material since its acoustic properties have been characterized in a previous chapter. ABS-M30 is up to 25-70 % stronger than standard ABS and is an ideal material for conceptual modelling, functional prototyping, manufacturing tools and end-use-parts. According to the manufacturer's datasheet, ABS-M30 has greater tensile, impact and flexural strength than standard ABS. Layer bonding is significantly stronger than that of standard ABS, for more durable parts. The finalized STL files were loaded in the Insight Stratasys software (Stratasys, Version 6.4.1, Version 3927), which was used to process STL models into CMB (printer's native format) files. The CMB extension files are the files types used by the Stratasys printers that include all the necessary information to build the 3D object. During this procedure the following parameters were set by the user:

1) Modeler configuration - The type of 3D printer, the type of model and support materials, the size of the model and support extrusion tips and finally the desired layer

thickness were selected. The support material was a secondary material used in additive manufacturing technology and its purpose was to support the overhanging area of the object from base to top. The support style was set to sparse to save material by leaving air gaps.

2) STL model orientation - The STL model can be orientated manually in any possible direction. Instead an automatically optimized orientation was chosen that satisfied the least amount of support material criterion.

3) STL model slicing - The software calculated the slices of the orientated STL model in the horizontal plane based on the layer thickness set by the user in the modeler's configuration section.

4) Creating toolpath fill for model and support curves - The software calculated the pathway of the extrusion tip for each of the model and support material. This operation created the toolpaths for each layer by dividing it into regions. Each region was filled with toolpaths from the perimeter inwards. The first toolpath traced the perimeter of the region. Subsequent toolpaths followed the contour of the perimeter, until the distance from the perimeter was greater than or equal to the contour depth. The rest of the region was filled with rasters. Raster lines were 90º off between successive layers (-45º to +45º) in order to reduce gaps and produce a solid object. The whole processing ran automatically and it was completed approximately within 4 minutes on a computer equipped with an Intel Core i7 processor and 4 GB DDR3 RAM. Following the processing, the building job was manually reviewed for every slice. The processed job displayed the contour of the building material, the toolpath rasters and the support material. A snapshot of the finalized processed job is shown in Figure 4.6.

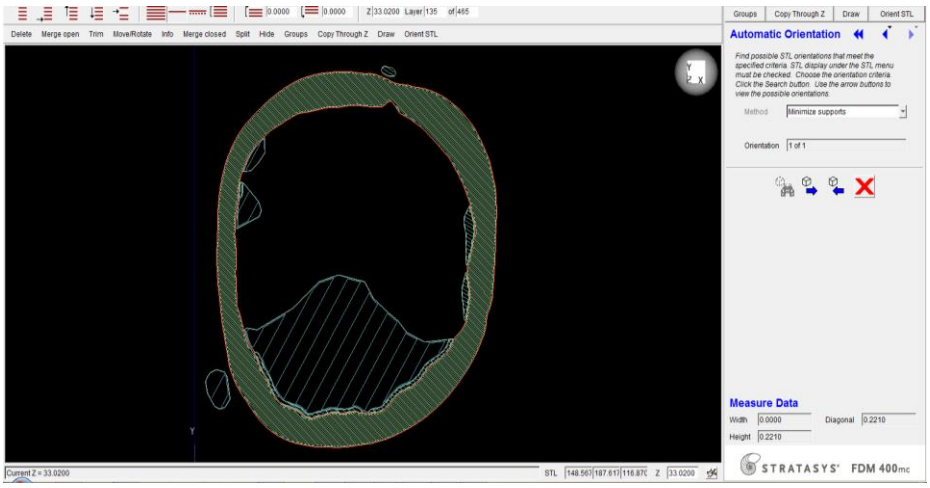

Figure 4.6: Processed and ready for prototyping skull STL file.

5) Creating a toolpath file (CMB) - The calculated toolpaths and settings for each material (model and support) were written in machine specific language files.

6) Downloading toolpath files to modeler for part building - The CMB job file was finally loaded in the FDM 400mc control center to set the position of the designed object over the available building envelope area as shown in Figure 4.7.

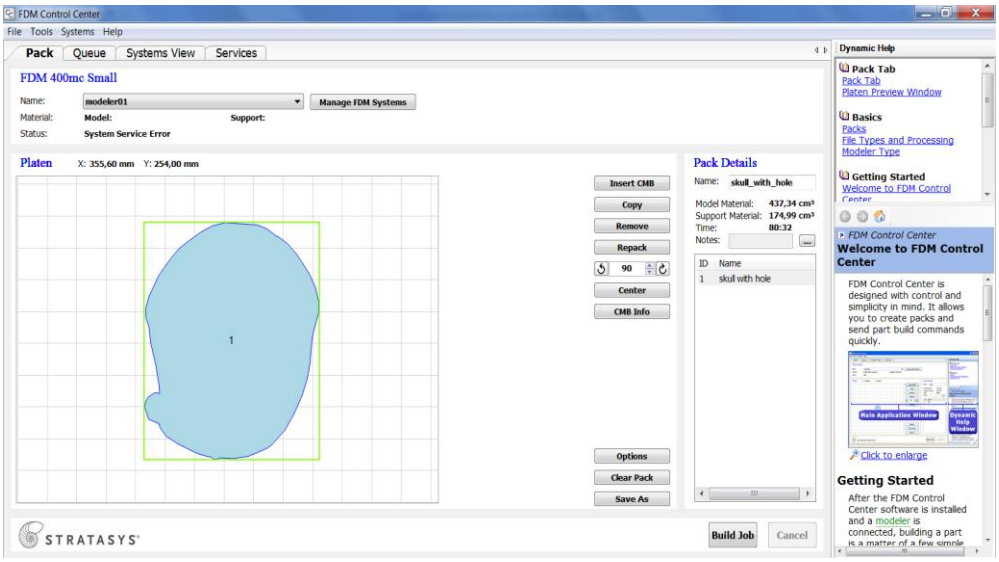

Figure 4.7: FDM 400mc control centre after loading the model's CMB file.

A thin plastic film was placed on the printer's platform that prevented the hot materials from sticking on it and secured the oven's door. The printing was initialized after the printer ran calibrations for the tips positioning system. The building time lasted about 24 hours. Once the printing job was finished, the larger parts of support material were removed manually from the printed plastic skull. The remaining parts were removed by immersing the model in a bath of warm water (70 ºC) that contained an acidic powder supplied by Stratasys (Waterworks). The ratio of water needed was 42 L of water per one bottle (950 g) of the soluble concentrate. The models were left to soak in the water bath for about 8 hours after which were removed and rinsed with clean tap water.

The craniotomy section was retrofitted with bronze pins to allow easy attachment to the plastic skull model. The pins were not expected to introduce severe MR artifacts while scanning the skull model, since bronze was not a ferromagnetic material. Stepping artifacts produced by helical CT scanning were observed on the plastic model. The artifacts were smoothed out by gently rubbing the plastic model with a cloth soaked with liquid acetone which temporarily softened ABS. A hole was drilled on the skull's top to screw the skull against a platform to prevent it from moving around during experiments.

The final ABS skull model with the associated craniotomy section are shown in Figure 4.8.

Figure 4.8: Finalised plastic skull model produced with FDM technology.

4.1.5 Composite Head Phantom

A composite head phantom was fabricated by molding agar gel inside the 3D printed plastic skull. The acoustic and thermal properties of the brain mimicking agar-based gel recipe (2 % w/w agar, 1.2 % w/w SiO_2, 25 % v/v evaporated milk) have been characterized in previous chapters. The desired total gel volume was estimated at 800 ml. The gel was prepared by dissolving 16 g of granulated agar in 660 ml of degassed and distilled water and was boiled to above 85 ºC. Throughout the whole process the mixture was continuously stirred using a magnetic Teflon stirrer. Extra 10% of water volume (60 ml) was added to mixture to compensate for evaporation during boiling. Once agar was dissolved 9.6 g of silica dioxide was added to enhance attenuation through scattering. The mixture was left to cool down to approximately 55 ºC before adding 200 ml of degassed evaporated milk mildly warmed to the same temperature. Evaporated milk is a low scatter material that enhanced attenuation through acoustic absorption. Stirring was kept for 1-2 min after adding milk up until the mixture homogenized. The inner surface of the plastic skull was covered with a Mylar film before pouring the liquid agar-silica-evaporated milk mixture. This was done to prevent the gel for sticking to the walls of the plastic skull and trapping air. The gel was poured to fill the skull phantom and was stored overnight in a refrigerator to solidify. The final composite head phantom is shown in Figure 4.9

Figure 4.9: Finalised composite head phantom.

4.2 Design and fabrication of a composite femur bone - muscle phantom for testing MRgFUS thermal protocols.

4.2.1 Femur Bone anatomy

The femur is the longest and strongest bone of the human skeleton and it is located in the thigh. The femur extends from a spherical process known as the head of femur in the proximal epiphysis and extends to the knee joint with the tibia of the lower leg in the distal epiphysis. The femur is considered as a weight bearing bone since its main function is to support the body's whole weight during everyday activities. The epiphysis of femur bone is made out of cortical and trabecular bone. The trabecular bone in the epiphysis is filled with red bone marrow which is responsible of producing blood components though a process known as hematopoiesis. At the diaphysis level cortical bone surrounds the medullar cavity where yellow marrow (fat) is stored. The bone at its proximal and distal edges is covered with articular cartilage which is a connective tissue that provides a smooth, lubricated surface for articulation and to facilitate the transmission of loads with a low frictional coefficient. Periosteum and endosteum are membranes of connective tissue that exist in the exterior and interior surface of the bone. Their main function is to accommodate the bone stem cells, the ones that are going to further develop into osteoblasts and osteoclasts, which play a very important role during regeneration or resorption of bone tissue. The main anatomical features of a human femur bone are demonstrated in Figure 4.10.

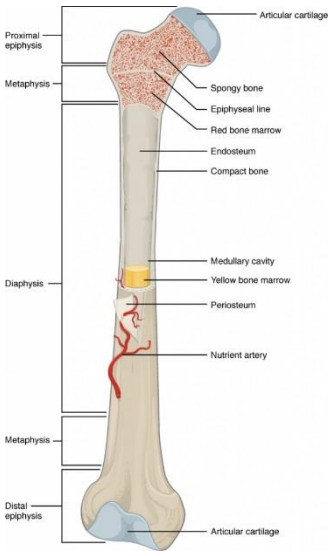

Figure 4.10: Anatomical features of a human femur bone [179].

4.2.2 CT of a human femur bone

High resolution images from a CT lower limbs scan of an anonymized adult patient were randomly chosen from a hospital's database. The selected set consisted of 1120 slices was acquired with a CT scanner (Toshiba Aquilion 16, Toshiba Europe GmbH) in helical mode with the following scanning parameters: 120 kV, automatic mA modulation (minimum 100 mA- maximum 450 mA) for a 12.50 standard deviation image quality setting, 0.5 seconds of rotation time, 38 cm of DFOV and 16×1 mm collimation. The reconstructed slice thickness was 1 mm with a 0.8 mm of inter-slice spacing. Back projected CT data were mapped in a 512 × 512 pixel matrix and with a bone reconstruction kernel for improved visualization.

4.2.3 Femur bone segmentation

The methodology and tools used for segmenting the femur bone were exactly the same as the one used for the skull bone. A mask of bone tissue was interactively created by manually selecting an appropriate density range (370-3070 Hounsfield units). The mask was cropped to include only the femur bone. Using a dynamic growth region segmentation tool, a second mask encapsulating the red bone marrow was first created and then subtracted from the initial femur bone mask. The reason of doing so was to create a void to be filled with Tissue Mimicking Material (TMM) in order to observe any temperature elevations in the medullary cavity under MR thermometry. The resulting model consisted of a hollow bone that included only the surrounding compact bone. The head and base of the femur bone were also cropped electronically to allow pouring the

tissue mimicking gel inside the bone model. Views of the original STL femur bone model and of the finalized cropped masks are shown in Figure 4.11.

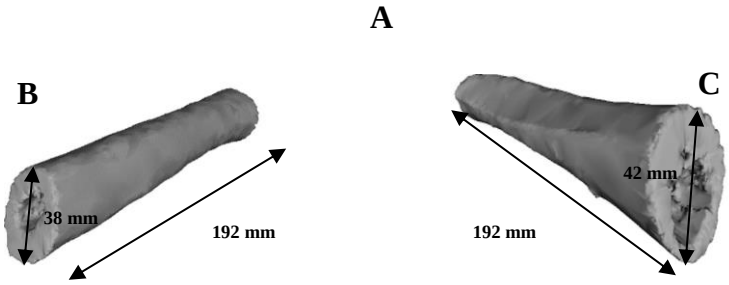

Figure 4.11: A) View of the original femur bone STL model, B) Superior to inferior view of the finalised cropped femur bone STL model, and C) Inferior to superior view of the finalised cropped femur bone STL model.

4.2.4 Plastic femur bone prototyping

The finalised STL model was printed using the Stratasys Fortus FDM 400mc. ABS-M30 was used as the build material. The prototyping settings were identical to the ones used for the plastic skull production. The maximum dimensions of the produced plastic bone model were 42 × 38 × 192 mm.

4.2.5 Composite Femur-Muscle Phantom

The printed ABS femur bone model was embedded in an agar based gel used to mimic the attenuation of the surrounding skeletal muscles and provide an adequate acoustic window from the focused ultrasound transducer to the model of bone/muscle tissue interface. The fabricated muscle mimicking agar gel (2 % w/v agar, 2 % w/v silica dioxide, 40 % v/v evaporated milk) approximately matched an attenuation coefficient of 1 dB/cm-MHz, which was typical for propagation normal to skeletal muscle fibers [164]. The muscle replica was of cylindrical shape with 15 cm diameter. The medullar cavity of the bone phantom was also filled with gel of the same recipe. Although bone marrow has a high concentration of fats and different acoustic properties from muscle tissue this was not taken into account since the main purpose was to observe qualitatively heat diffusion in the region. Figure 4.12 shows the final form of the composite femur-muscle phantom.

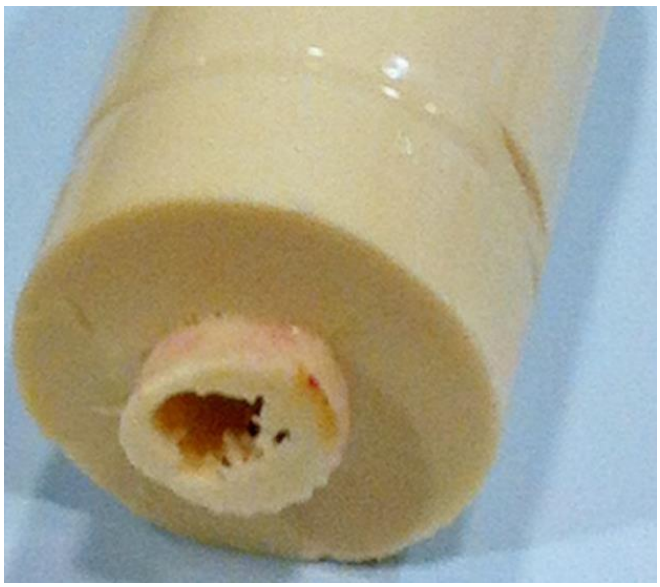

Figure 4.12: ABS femur bone embedded inside a cylindrical skeletal muscle mimicking agar gel.

4.3 Design and fabrication of a composite rib - breast phantom for testing MRgFUS thermal protocols.

4.3.1 Breast anatomy

Breast is considered as an organ of the female reproductive system since it includes a milk producing gland. The gland is made out of 15-20 lobes which are comparted between them by adipose tissue (fat). Each lobe is divided in smaller compartments known as lobules each consisting of grape like alveoli which are responsible for secreting milk. Lobules are interconnected by tiny ducts which progressively increase in size to larger ducts to propel milk to the nipple. The gland is surrounded in its majority by adipose tissue which is usually the governing tissue that controls the breast's size. Connective tissue and ligaments also exist around the mammary gland and their function is to support the breast and maintain its shape.

The breast sits over the pectoral muscles which are found posteriorly to the breast tissue. The main function of the pectoralis group of muscles is to control the movement of the arm and additionally by contracting to create void space for the ribcage to expand during deep inhalation. The ribcage is adjacent posteriorly to the pectoralis muscles and serves as a protective cage of internal thoracic organs. It consists of two bilateral sets of twelve bones (ribs) which articulate from the vertebral column and terminate anteriorly as cartilage. The cartilage endings known as costal cartilage of the first seven connect with the sternum directly, the next three with the lower border of the seventh rib costal cartilage and the remaining two are floating. The cross section of human rib is similar to

the femur bone with concentric layers of red bone marrow, trabecular and cortical bone. Typical coronal and lateral cross sections of the breast-ribcage anatomical features are shown in Figure 4.13.

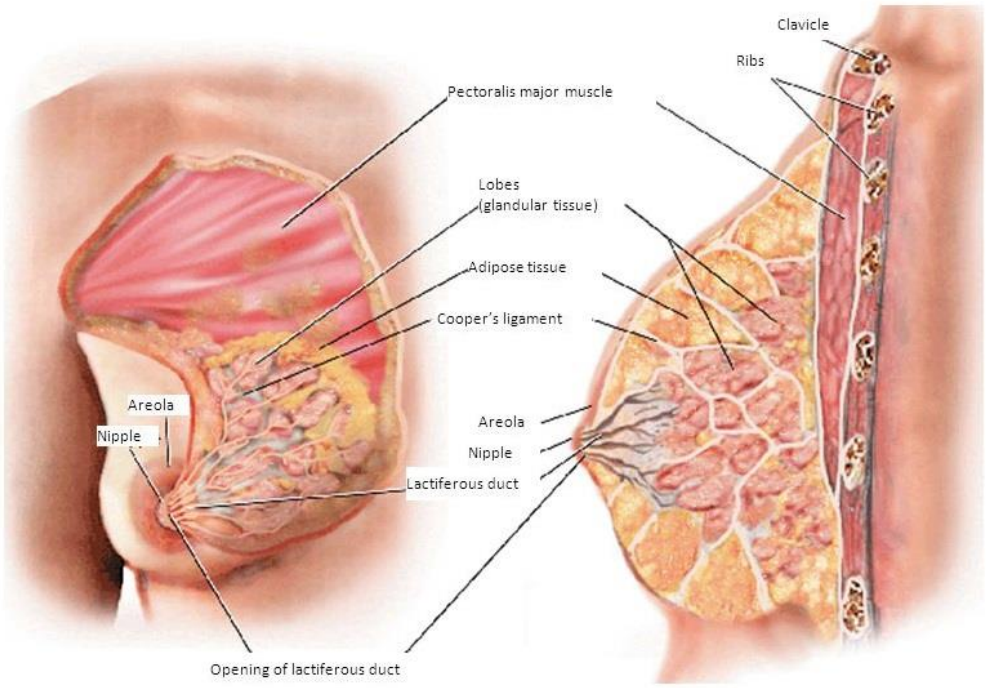

Figure 4.13: Anatomical features of breast tissue.

4.3.2 CT of a human rib cage

The rib cage model was reconstructed using a set of high resolution CT chest images of an anonymized female patient of medium frame size. The images set was acquired with a Toshiba 16-slice CT scanner (Toshiba Aquilion 16, Toshiba Europe GmbH) in helical mode with the following scanning parameters: 120 kV anode voltage, 300 mA tube current, 0.9375 pitch, 0.5 s of rotation time, 15 mm table feed per rotation, 400 mm of DFOV, 16×1 mm collimation with 1mm/1mm reconstructed slice thickness and inter-slice interval. Filtered backprojected CT data were mapped in a 512 × 512 pixel matrix and a reconstruction kernel for optimum bone visualization was used.

4.3.3 Rib cage segmentation

Rib cage segmentation was completed by repeating the procedure followed for the skull and femur bone phantom. The mask was cropped to include the right anterior first rib down to the sixth. These were the ribs found behind the breast and the pectoralis muscle of the observed patient. The model was edited in an open source 3D mesh processing software (MeshLab, ISTI - CNR research center, University of Pisa , 2005). Using MeshLab all unnecessary fragments were removed using a minimum diameter

filter. Craters and spikes were also removed using a smoothing filter. The maximum dimensions of the segmented rib cage model were 145×117×199 mm. The cropped final STL rib cage model is showed in Figure 4.14.

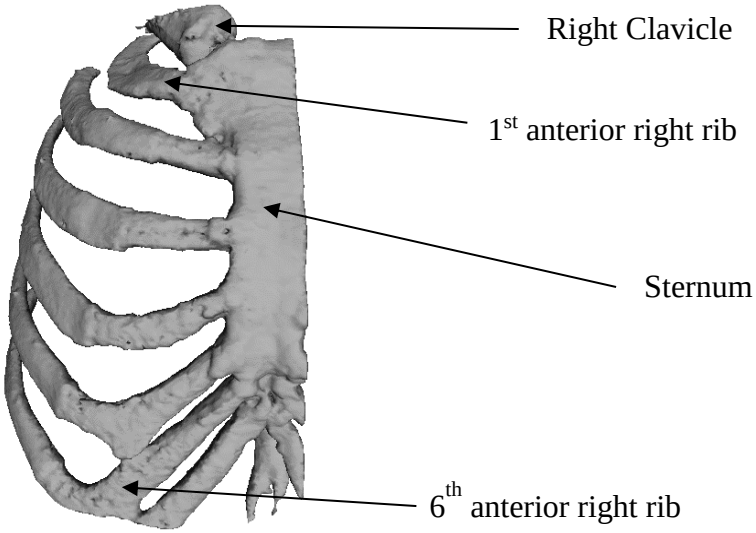

Figure 4.14: STL partial model of the right anterior rib cage produced by segmentation of patient's CT images.

4.3.4 Plastic rib cage prototyping

The STL model was 3D printed in grey ABS-M30 using the FDM-400mc (Stratasys) prototyping machine. Grey ABS-M30 had identical acoustic and thermal properties with ivory ABS-M30 used previously.

4.3.5 Composite breast-rib phantom

Breast consists mainly of adipose, glandular (lobules), connective and muscle tissue. The majority of breast cancer tumors are carcinomas, a type of cancer that starts in the cells (epithelial cells) that line organs and tissues like the breast. In fact, breast cancer is often a type of carcinoma called adenocarcinoma, which is carcinoma that starts in glandular tissue. Other types of cancers can occur in the breast, too, such as sarcomas, which start in the cells of muscle, fat, or connective tissue. Studies suggest that the mean ultrasonic speed of sound and attenuation coefficient in breasts are age related [180]. This fact is attributed to anatomic and physiologic changes associated with reproductivity and menopause. Katz-Hanani *et al*. [180] reported that the mean speed of sound decreases from 1504 ± 35 m/s at <30 y to 1452 ± 9 m/s at >60 y ($p < 0.01$), and the attenuation

coefficient decreases from 1.27 ± 0.32 to 0.96 ± 0.13 dB/cm-MHz ($p < 0.03$), respectively.

Breast tissue was mimicked with a simplistic approach. A homogeneous breast phantom was designed with an attenuation coefficient close to 1 dB/cm-MHz. The final gel product consisted of 2 % w/v agar, 2 % w/v silica dioxide and 40 % v/v evaporated milk. Evaporated milk contained about 7.5 % milk fat therefore the overall fat content to the whole volume of the breast mimicking phantom was about 3 %. This fat content was relatively low compared to a typical breast with a 50 % adipose (fat) tissue. A low fat concentration was preferred in MR thermometry studies since fat is not sensitive to proton resonance frequency (PRF) changes during heating. The gel was prepared and was left to settle inside a breast-like mold. The rib cage was sank inside the gel during molding to establish an acoustic window that will allow us to test the effect of bone's interaction with ultrasound during exposures. The finalized composite rib-breast phantom is shown in Figure 4.15.

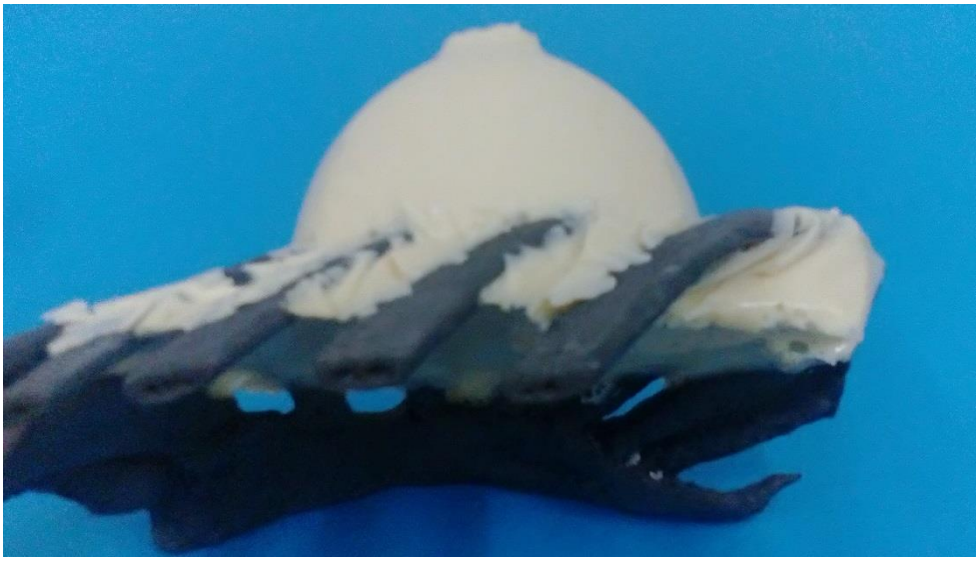

Figure 4.15: Composite breast-rib phantom.

4.4 Summary

This chapter described the design and fabrication of three composite phantoms (head, femur/muscle and rib/breast), each composed of a bone and a soft tissue bone part. The particular phantoms represented anatomies, where the application of focused ultrasound thermal therapy gathers great research interest. Bone replicas for each phantom (skull, femur and rib) were produced by 3D printing in thermoplastic ABS models of the segmented bony tissue from patients CT images. Soft tissue parts (brain, muscle and breast) were made out of agar-based gels doped with attenuation enhancing

agents. The gels were molded either inside or around the bone parts depending on the represented anatomy, to establish adequate acoustic coupling before testing their functionality with focused ultrasound under MRI guidance.

5 MR Thermometry for monitoring FUS applications

5.1 Introduction

Thermal therapy options that can be used for the treatment of malignant and benign focal diseases are gaining popularity amongst the medical community. The therapeutic goal in malignant and benign tumour ablative thermal therapies is to deliver an adequate amount of heat to induce cellular necrosis in the delineated target which usually includes a margin of 0.5-1 cm of the surrounding healthy tissue. In order to establish efficacy of the treatment and safety for the patient throughout the whole procedure, these thermal therapies are guided by imaging modalities. US and MRI are the main modalities employed to guide HIFU nowadays. MRI guided HIFU is preferred in the USA and Europe for guiding prostate and uterine fibroid procedures whereas in China ultrasound guided systems are used for treating liver carcinomas and other solid tumours [181]. None of them is perfect by itself and both demonstrate advantages and disadvantages.

5.2 MR vs US guided FUS

The success of procedural guidance during HIFU treatments depends on the ability of the imaging system in accurately targeting and positioning the focus and correlating tissue damage threshold with a measurable physical quantity or direct observation (e.g. temperature, bubble activity, tissue changes in their stiffness and attenuation). Another important aspect of an optimized HIFU guiding modality is the ability to simultaneously monitor the targeted volume with its boundaries and critical structures that sit in either pre-focal or post-focal regions in order to avoid any treatment related adverse events.

In order to fulfil the prerequisites described above, a HIFU guiding system must be capable of producing images of adequate spatial and temporal resolution. Spatial resolution controls targeting accuracy and the sensitivity of monitoring in tissue changes throughout the treatment, whereas temporal resolution controls how frequently tissue damage is assessed. Additionally in HIFU applications where the targeted or intervening tissue moves, guiding systems of high temporal resolution are needed to provide feedback to the treatment system which can use the incoming information to apply real time corrections.

Current state-of-the art US and MRI systems have comparable spatial and temporal resolution capabilities. Spatial resolution in US systems depends on the transducer's operating frequency (Axial: 0.5-3 mm, Lateral: 1-3 mm) while its temporal resolution is correlated with the frame rate (25 ms -100 ms). In MRI the size of acquisition matrix and therefore the degree of spatial resolution depends on acquisition time with the in plane resolution typically ranging from 0.5 to 4 mm. Images of high spatial resolution come at cost of decreased temporal resolution ranging between 30-120 ms. A finer matrix requires a larger number of phase encoding steps which increases acquisition time. Accelerated MR techniques that use gradient echo planar imaging (GRE-EPI) or segmented-EPI sequences can produce temperature maps fast enough to control treatment outcome by filling the whole or part of k-space in one TR duration [182], [183]. Partially parallel imaging techniques have been successfully used in phantom studies to improve the temporal resolution required for temperature imaging in HIFU without compromising spatial resolution, slice coverage or phase sensitivity [184].

Amongst the disadvantages of ultrasound guidance is its inability to penetrate bone and gas that raises important safety issues when critical tissue structures under monitoring reside in an acoustic shadow area. On the other hand in US guided systems the diagnostic ultrasound transducer is usually positioned concentrically relatively to the spherical transducer and produces a beam's eye view. This enables the user to recognise acoustic shadowing along the pathway of the therapeutic beam which could potentially induce unwanted hot spots during HIFU sonication unless corrected. MRI is immune to bone and gas and can provide high quality images in adjacent areas. The FOV used in MRI are large which is desirable while monitoring pre-focal and post focal areas whereas in ultrasound the FOV is limited by operating frequency, penetration, power and transducer geometry. Ultrasound guided systems are compact, affordable and they do not raise image quality and safety concerns in the vicinity of metallic implants or objects compared to MR guided systems. Conventional scanning used in MRI for pre procedural treatment planning can be time consuming while relatively ultrasound imaging is fast.

The biggest difference between these two types of guidance systems that makes MR guided systems the primary choice when budgeting is not an issue, is its ability to monitor quantitatively the degree of tissue damage. MR thermometry techniques correlates pixel values of image produced by special sequences in quasi-real time with local temperature with adequate accuracy and sensitivity. By observing the produced thermal maps, the operator monitors the distribution of thermal dose delivered [185]. The threshold of cellular necrosis is tissue specific and by estimating the thermal dose

delivered, the efficacy of the treatment at the targeted volume can be assessed. Additionally temperature raise in critical structures is also continuously monitored and irreversible adverse effects from exceeding the threshold of thermal dose can be avoided. US thermometry is not yet available in clinical systems, but efforts have been made to develop thermal strain imaging which is a technique that correlates changes in the speed of sound and tissue thermal expansion with temperature [186], [187]. Currently monitoring of real time HIFU thermal ablation in clinical systems using ultrasound relies on observing hyper-echoes produced by boiling in the treated tissue which is subjective and can potentially lead to overtreating the area.

5.3 MR guidance for monitoring designed tissue mimicking phantoms HIFU thermal protocols

The acoustically tissue mimicking phantoms described in previous chapters were designed to serve as useful tools in testing thermal HIFU protocols. As mentioned in the previous section, MRI is currently the only modality used in clinical systems that provides quantitative methods for monitoring in near real time the raise of temperature during treatment. Therefore for the remainder of this project the evaluation of the phantoms during HIFU sonications was conducted using an MRI scanner. Description of MRI Scanner used for guiding focused ultrasound thermal protocols in phantoms

For the purposes of this project a 1.5 Tesla (T) actively shielded superconducting magnetic resonance imaging system (General Electric Signa Excite HD, Milwaukee, Wisconsin, USA) installed at a private hospital (Ygia Polyclinic, Limassol, Cyprus) was used. The superconducting coils of the magnet were cooled with liquid helium cryogen. The system was equipped with a 60 cm bore and with an Echo Speed Plus set of gradients. The maximum amplitude of the gradients was 33 $mT.m^{-1}$ with a slew rate of 120 $mT.m^{-1}.ms^{-1}$. The data pipeline of the system uses 8 independent channels with 16 quadrature inputs. The receiver of each channel samples the MR signal at a high bandwidth with maximum frequency of 1 MHz, enabling acquisition of images with high fidelity at high productivity. The MRI system is illustrated in Figure 5.1.

Parallel imaging was also available for some multi-element coils using the GE's encoding Technique named ASSET (Array Spatial Sensitivity Encoding Technique). This technique uses the sensitivity profile of each enabled element produced in a calibration scan to unwrap aliased images and restore missing k-space lines. ASSET technique accelerates the acquisition of compatible sequences with ASSET compatible coils, which

allows the user to balance appropriately between image quality and time management depending on the application.

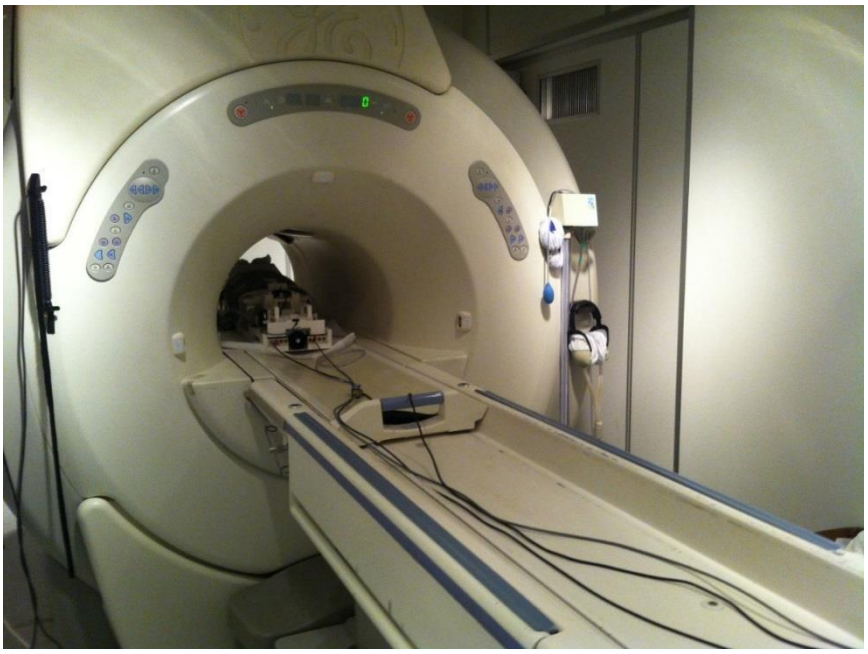

Figure 5.1: Photograph of the 1.5 T GE Signa Excite HD MRI system used for guiding HIFU thermal exposures of the designed tissue mimicking phantoms.

The General Purpose Flexible coil (GPFLEX), which is a single channel-single element receive only surface coil that wraps around the anatomy of interest, was mainly used for imaging and conducting MR thermometry of the phantoms. It is usually used in clinical applications for imaging irregular-shaped regions like the hip, shoulder, brachial plexus, large knees that cannot fit inside the dedicated knee coil, ankle, thigh, elbow, etc.

HIFU transducers used for sonicating the developed phantoms were moved inside the bore of the magnet using an MR compatible robot, which occupied most of the available free space. The GPFLEX coil seemed ideal for imaging in confined space and without orientation limitations. Additionally being a single element coil made it easier to reconstruct phase sensitive images used for MR thermometry compared to multi-elements coils that require tedious reconstruction of the raw data.

5.3.1 Soft Tissue Phantoms relaxometry

MRI offers excellent soft tissue contrast which is ideal for monitoring accurately lesion formation and tissue morphological changes under HIFU hyperthermia. Tissue contrasts in MRI depend simultaneously on intrinsic properties of tissue like T_1 and T_2 relaxation times and proton density (PD). By varying specific acquisition parameters the

contrast weighting of *PD*, T_1, and T_2 can be exaggerated or suppressed to enhance tissue differentiation and pathological changes in the image.

It is common practice in MR guided HIFU procedures to acquire T_2-weighted images prior to therapy and use them for treatment planning. T_1-weighted gadolinium enhanced images are also acquired at the end of the treatment to assess tissue necrosis and check the coincidence of the non-perfused volume (*NPV*) with the thermal map. Despite the fact that the designed soft tissue phantoms were homogeneous and were not expected to present any MR signal heterogeneity, their T_1 and T_2 relaxation times were characterized and compared with the replicated tissues for reference purposes.

5.3.1.1 T_1 relaxometry

Materials and Methods

For measuring the T_1 spin-lattice relaxation time, a conventional spin echo Inversion Recovery (*IR*) sequences was used [188]. An *IR* sequence starts at a time t=0 with the application of a 180° radiofrequency (*RF*) slice selective pulse. This excitation forces the fully relaxed longitudinal magnetization vector M_z (t), where M_z (0) equals the net magnetization M_o, to invert towards the opposite direction. Immediately after the application of the inverting pulse, the longitudinal magnetization vector points in the opposite direction (M_z $(0^+) = -M_o$). Once the *RF* pulse is switched off the longitudinal magnetization relaxes back to establish thermal equilibrium at a rate $R_1 = 1/T_1$. At a time $t = TI$, where *TI* represents the inversion time, a second 90° excitation *RF* pulse is applied and flips any net longitudinal magnetization that managed to relax in the meantime to the transverse plane. The signal is rephased by a second 180° pulse and sampled after some time *TE* in order to form the MRI images. The sequence is repeated at time *TR* after the initial 180° until all phase encoding steps are completed. For a conventional *IR* sequence the longitudinal magnetization M_z can be expressed as a function of inversion time *TI* with the following equation:

$$\boldsymbol{M_z(TI) = M_o(1 - 2e^{-\frac{TI}{T_1}})} \tag{5.1}$$

In order to detect a signal in MRI, the longitudinal magnetization must be flipped in the transverse *xy*-plane. Therefore the magnitude of the longitudinal magnetization controls the magnitude of the detected signal. By solving the equation above we can see that M_z (*TI*) becomes zero when $TI = T_1/ln2$ and therefore no magnetization is flipped with the 90° pulse to the transverse plane. This prediction was used to estimate the T_1 time of the soft tissue phantoms developed in previous chapters.

In order to quantify the associated T_1 relaxation time of the brain mimicking phantom, the gel was first immersed in a water tank to increase the coil's loading and acquire images with acceptable signal to noise ratio. For measuring the spin–lattice relaxation time (T_1) the phantom was imaged using the (cervical-thoracic-lumbar) CTL spine coil using an Inversion Recovery Spin Echo (*IR-SE*) pulse sequence [188] with the following acquisition parameters: *TR* = 5000 ms, *TE* = 20 ms, slice thickness = 5 mm, *NEX* = 4, matrix = 320 × 160 and a variable *TI* = 66, 316, 616, 750 ms. The mean pixel value of an image slice passing through the mid-section of the brain phantom for each of the different inversion times was calculated. The calculation was done by using a region of interest statistics tool which was available on the scanner. The mean pixel value is directly proportional to the magnetization signal in the transverse plane. When the inversion time reached the limiting value of T_1/ln2 as explained before, this signal consequently became zero. The spin lattice relaxation time was estimated by applying a 3rd order polynomial fit to the data and were interpolated to find the nulling inversion time. The same methodology was used to estimate T_1 for the muscle tissue mimicking phantom recipe.

5.3.1.2 T_2 relaxometry

Materials and Methods

The T_2 or spin-spin relaxation time was estimated by taking a series of Fast Spin Echo (*FSE) T2* weighted sequences for different effective *TE*: 18, 36, 63, 81 and 99 ms [188]. In a *FSE* T_2 weighted sequence a 90º *RF* excitation pulse flips the fully relaxed longitudinal magnetization M_z to the transverse plane. The loss of phase coherence of the spins results in a gradual decay of the signal in *xy* plane. By acquiring the decaying signal at different echo times *TE* per *TR* the rate of spin-spin relaxation can be estimated. In order to estimate the brain recipe's T_2, the phantom was scanned using the same setup and equipment as in the T_1 relaxometry session. The scanning parameters used were: *TR* = 2500 ms, slice thickness = 3 mm, matrix = 256×256, FOV = 16 cm, Number of *NEX* = 1 and Echo Train Length (*ETL*) = 8. For a sufficiently long *TR* that allowed a full longitudinal magnetization relaxation between successive 90º excitations, the signal of a T_2 weighted image can be approximated by equation 5.2, where M_{xy} stands for the transverse magnetization signal at a time *TE* following the excitation.

$$\boldsymbol{M_{xy}\,(TE) = M_o e^{-\frac{TE}{T2}}} \qquad (5.2)$$

Mean pixel values from the T_2 weighted images of the phantom at the different echo times were plotted. T_2 relaxation time was deduced by applying an exponential fit to the data. The same methodology was used for estimating T_2 characteristic time for the muscle and breast mimicking phantom recipe.

5.3.2 Phantom relaxometry results

The data acquired for the estimation of T_1 relaxation time of the brain, muscle and breast recipe are shown in Figure 5.2 and Figure 5.3 respectively. The *TI* for which the mean pixel value became zero was interpolated. This value was substituted in the limiting condition where *TI* is equal to $T_1/ln2$ in equation 5.1 and the associated T_1 times for each of the two phantom recipes were estimated. The results of the estimated spin lattice relaxation times T_1 are shown in Table 5-1.

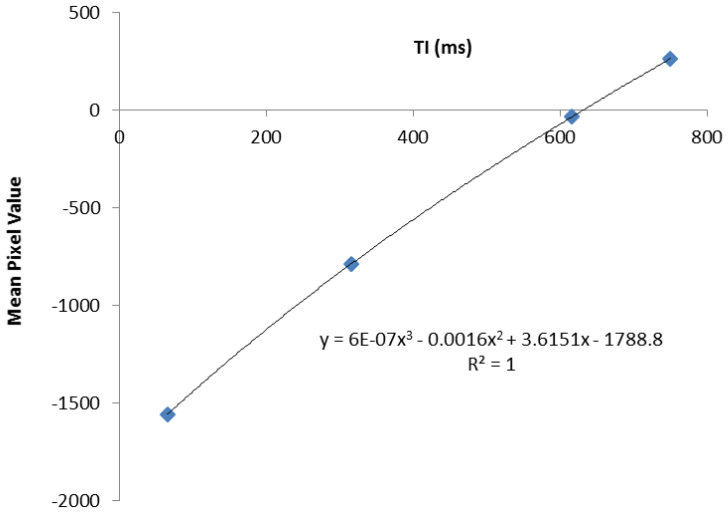

Figure 5.2: Inversion Recovery fitted data for estimating the spin-lattice (T_1) relaxation time of the brain gel phantom.

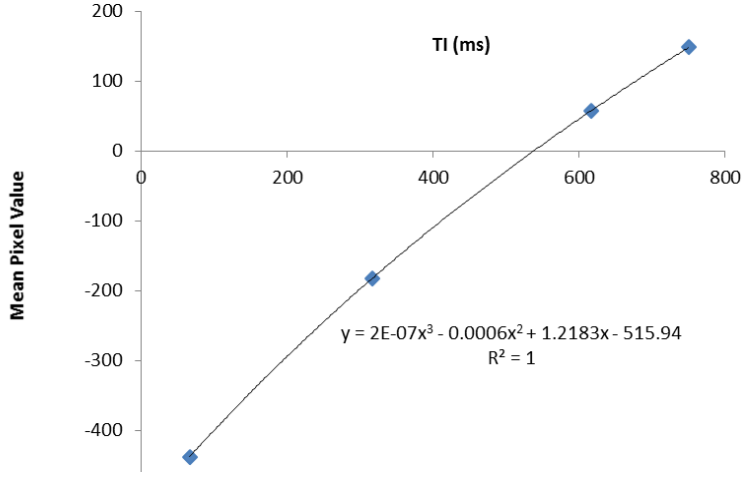

Figure 5.3: Inversion Recovery fitted data for estimating the spin-lattice (T_1) relaxation time of the muscle gel phantom.

The data for estimating the spin-spin (T_2) relaxation time of the two phantom recipes were plotted in Figure 5.4 and Figure 5.5 respectively. An exponential trend line was used to fit the data acquired. An exponential trend line was used to fit the data acquired. The measured mean pixel value in a region of interest covering at least 50 % of the phantom was recorded for each *TE*. Since the *MR* signal was directly proportional to the transverse magnetization Mxy, the same can be assumed for the MPV. According to equation 5.2 and T_2 was calculated by finding the reciprocal of the fit's exponent. All relaxometry results are summarized in Table 5-1.

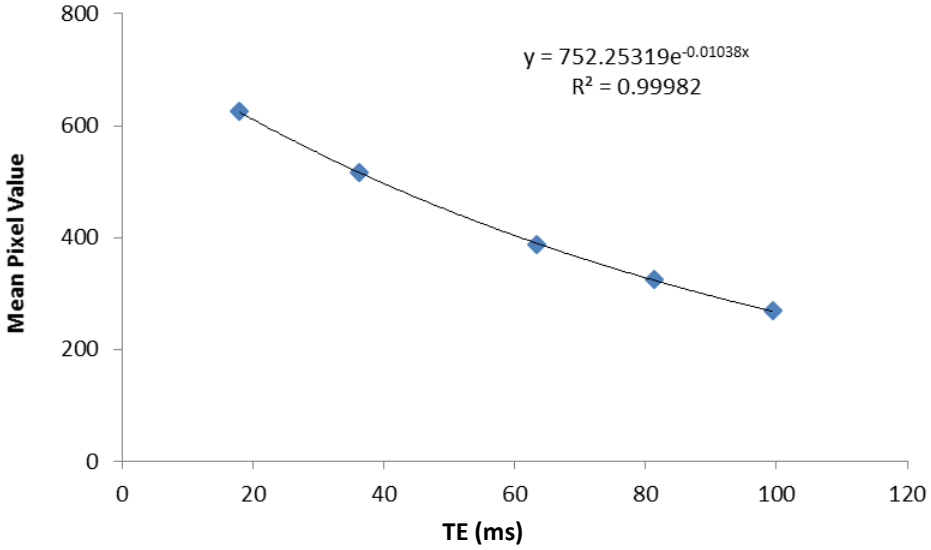

Figure 5.4: Fast Spin Echo sequence data fitted for estimating the spin-spin (T_2) relaxation time of the brain phantom.

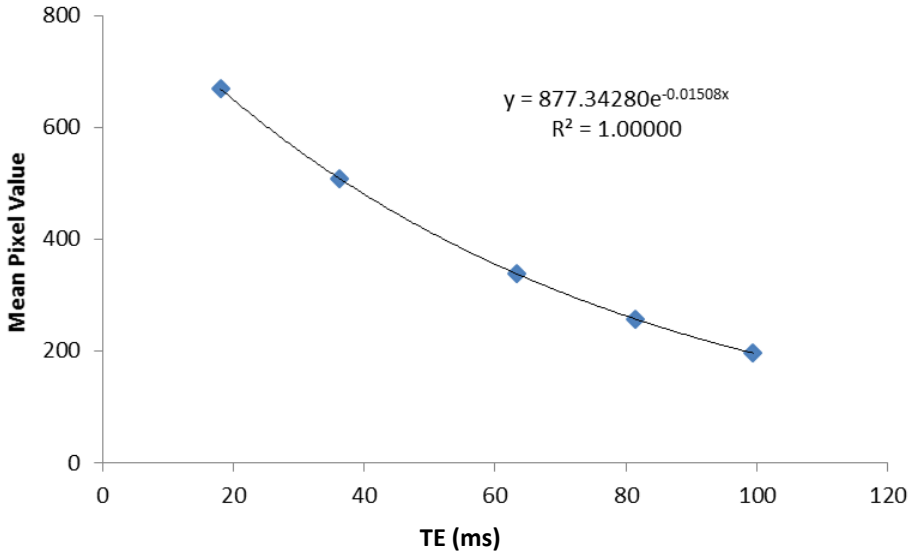

Figure 5.5: Fast Spin Echo sequence data fitted for estimating the spin-spin (T_2) relaxation time of the muscle phantom.

Table 5-1: Summary of T_1 and T_2 estimations for the proposed soft tissue phantom recipes

Phantom recipe	T_1 (ms)	T_2 (ms)
Brain phantom	910	97
Muscle phantom	785	66

Conclusions

The results agreed with the range of relaxation times found in white (T_1:560-756 ms, T_2:67-87 ms) and gray (T_1:1105-1200 ms, T_2:77-92ms) matter at 1.5 Tesla relaxometry studies [189]–[193]. The estimated T_1 was in the mid-range of bibliographic data whereas T_2 was on the higher end. *In vivo* relaxometry studies [194], [195] of skeletal muscle demonstrated a significantly higher range of T_1 times (1008 -1180 ms) and slightly lower T_2 times ranging between 35 and 44 ms. Breast tissue relaxometry results are usually reported separately for adipose and glandular tissue due to the large difference in their relaxation times. Relevant studies [196], [197] reported a T_1 range of 367-423 ms for adipose tissue and 1445-1680 ms for glandular tissue. Similarly T_2 in breast adipose tissue ranged between 53-154 ms and 54-71 ms for glandular tissue. The breast phantom developed was homogeneous and both of its characteristic times were found in range of the reported values for the main types of tissue present in a breast. The relaxation times of the two recipes seemed to be affected by the introduction of different milk concentrations that controlled water, fat and protein content per unit volume. The differences in T_1 and T_2 times can be attributed to their dependence in the molecular tumbling rate. Fat and protein molecules are larger in size compared to water molecules and tumble in a slow rate therefore exhibiting shorter relaxation times. Nevertheless the priority of this project was not to match the MR properties of the tissue mimicking phantoms and therefore deviations from tissue characteristic relaxation times was not a matter of great concern. As part of future work these recipes can be doped with agents that control T_1 and T_2 independently.

5.4 MR Imaging of Skull-Brain Composite Phantom.

The skull-brain composite phantom was chosen to check the appearance of the developed phantoms in conventional MRI T_1 and T_2 weighted images. The phantom was immersed inside a water tank and was scanned using the 1.5T GE Signa Excite MRI scanner (GE, Milwaukee, USA) with conventional FSE T_1 and T_2 sequences. The acquisition parameters for the FSE T_1 sequence were TR: 600 ms, TE: 20 ms, flip angle:90º, matrix:256×256, bandwidth:15 kHz, Echo Train Length:4 and for the FSE T_2

were TR:2400 ms, TE:80 ms, flip angle:90^0, matrix:256×256, bandwidth:15 kHz, Echo Train Length:12. The CTL spine coil (GE, Milwaukee, USA) was used since it produced the maximum signal to noise ratio from the rest of the coils. The T_1 and T_2 weighted of the composite skull-brain phantom images are shown in Figure 5.6.

These images provided sufficient proof that the phantom contained only MR compatible materials. As expected no severe artifacts were induced in the vicinity of the phantom. Some susceptibility artefacts were observed on the T_1w image near the plastic skull/water interface. The plastic skull part appeared dark in both sequences due to the absence of water content. In the T_1w image there was little contrast between the phantom and the surrounding water probably due the selection of a rather short *TR* compared to the phantom's T_1, whereas in the T_2w image the contrast increased. Water appeared brighter from the brain phantom because of its long T_2 relaxation time compared to the short T_2 of the phantom that resulted in a fast MR signal decay. The contrast of the brain phantom with water in the T_1w image looked quite similar compared to the contrast of the real brain with the cerebrospinal fluid (CSF) gathered in the ventricles. Similarly in the T_2w image the CSF appeared much brighter compared to the darker brain tissue, as it was the case in the phantom image. Of course the composite skull-brain phantom lacked morphological structures visible in a real brain image resulting from the range of relaxation times apparent due to the coexistence of gray and white matter and other structures. Unlike the phantom's case skull bone produces MR signal with the frontal sinuses being void. These cavities were flooded with surrounding water in the case of the phantom and followed water's signal intensity behavior. Last the phantom did not replicate skin and muscle tissue surrounding the skull.

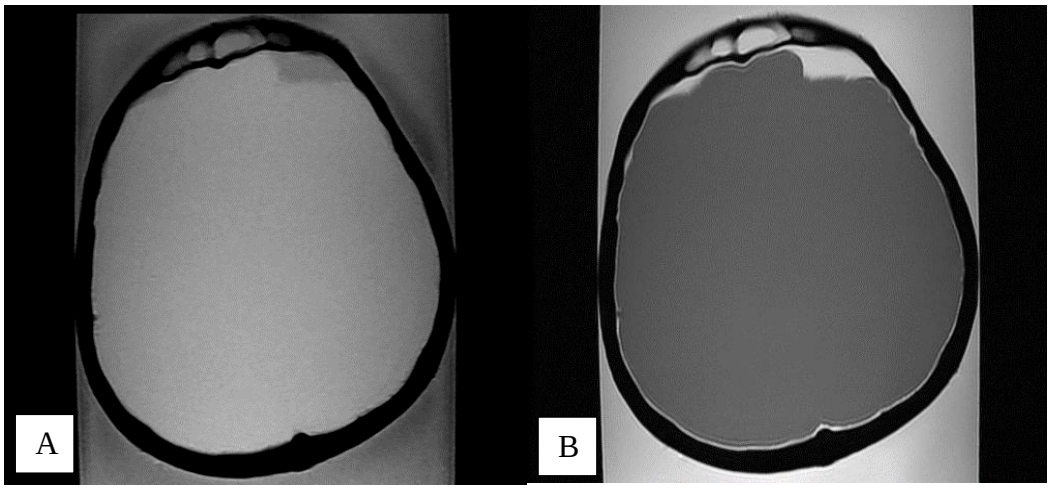

Figure 5.6: A) T1 weighted image and B) T2 weighted images of the head phantom immersed in a water tank.

For comparison purposes, typical T_1 and T_2 weighted images of an adult human head are shown in Figure 5.7.

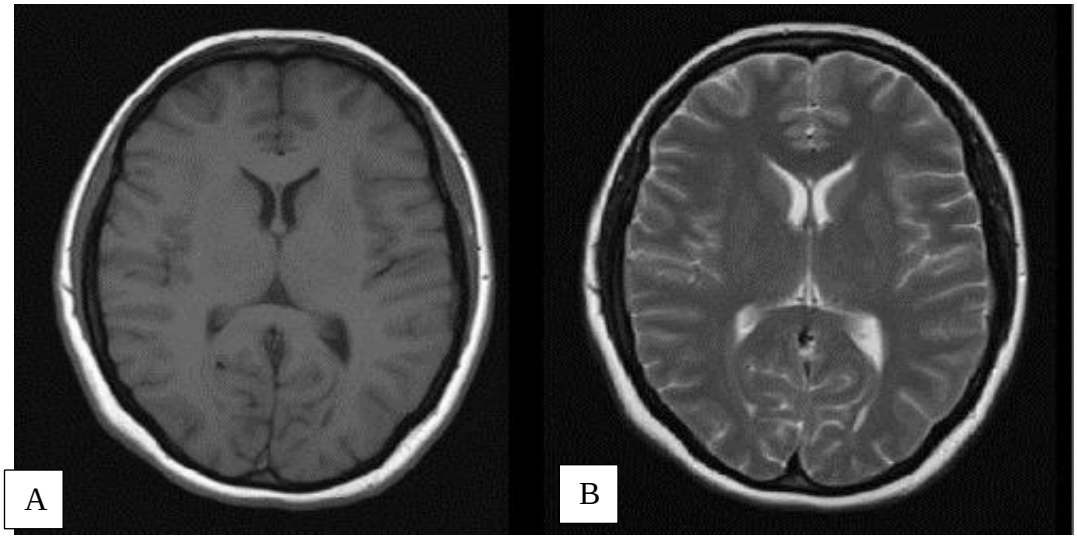

Figure 5.7: Typical A) FSE T_1 weighted image and B) FSE T_2 weighted images of an adult's head in a 1.5 T MRI scanner [198].

5.5 Proton Resonance Frequency shift (PRFS) MR Thermometry.

This technique is characterized by an excellent linearity for a wide range of temperatures (-15 ^{0}C to 100 ^{0}C) [199] and a near independence with tissue type and its thermal history [200]. *PRFS* has the best sensitivity response to temperature changes of less than 1 ^{0}C and using accelerated MRI acquisition techniques it is feasible to achieve a temporal resolution below 1 second combined with a spatial resolution of about 2 mm [201].

PRFS thermometry can be applied through spectroscopic or phase imaging. The first involves the acquisition of a considerably large voxel and calculating the water resonance peak shift with a change in temperature from an internal reference. The internal reference of the acquired frequency spectrum is provided by the lipids resonance peak (fat) which is known of being insensitive to temperature [202]. Unfortunately spectroscopy sequences are slow and lack spatial resolution making them unsuitable for a real time accurate thermometry tool in MRI [185].

On the other hand phase imaging calculates the phase change of the MR signal which is related to the temperature dependent *PRFS*. The phase imaging method can produce superior temporal and spatial thermal maps that satisfy the prerequisite of accurate real time temperature monitoring [200]. The biggest disadvantage of this method is its vulnerability in motion that can cause pixel misregistration and produce erroneous

temperature results [203]. Like in almost all other MR thermometry methods, implementation of fat suppression techniques is required to suppress the temperature insensitive MR signal from fat-rich organs.

For the purposes of this project *PRFS* thermometry was chosen to assess the application of HIFU thermal protocols in the developed phantoms due to the aforementioned advantages over the other techniques. The sensitivity of PRFS to motion artifacts was not an issue since the phantoms were immobile and the use of low fat content materials minimized the possibility of false thermometry results.

5.5.1 Theory behind PRFS MR Thermometry.

The signal in clinical MRI is originates from resonating hydrogen protons of water molecules that constitute over 70 % of a human's body weight. The hydrogen nucleus of a water molecule in free-state is shielded by the molecule's mobile electrons. The degree of electronic screening around the hydrogen nucleus (proton), depends on its configuration and temperature. In biological tissue, water molecules are hydrogen bonded and form a liquid. Hydrogen bonds reduce electronic screening due to electrostatic attraction of the electropositive proton to its neighboring water molecule's electronegative oxygen. In the vicinity of an externally applied magnetic field B_o, the apparent field experienced by the molecule's hydrogen nucleus B_o' is smaller than B_o. When temperature increases, water molecules spend less time in a hydrogen bonded state since this type of bonds are weak and require small amounts of energy to deflect or even break. The induced electronic screening increase and the apparent field's decrease are observed as a temperature dependent decrease of the Larmor precession frequency.

The apparent magnetic field (B_o') felt by these protons is related to the externally applied field (B_o) with following expression, where $\sigma(T)$ refers to the temperature dependent electronic screening constant which is measure in *ppm* (parts per million).

$$\boldsymbol{B_o' = [1 - \sigma(T)] \times B_o} \tag{5.3}$$

As a result the shifted proton resonance frequency ($f_{p,T}$) is a function of temperature (T) and it can be calculated by the following Larmor Equation, where γ stands for the shielded proton gyromagnetic ratio (42.58 MHz /T or 267.513×10^6 rad/s-T).

$$\boldsymbol{f_{p,T} = \gamma \times B_o' = \gamma \times [1 - \sigma(T)] \times B_o} \tag{5.4}$$

From equation 5.4 it can be concluded that an increase of temperature tends to decrease the Larmour precession frequency.Temperature change from an initial reference temperature level (T_o) to a new level (T_1) can be deduced by calculating the accumulated phase difference that results from the change in the precession frequency [204]. The change in temperature from baseline ($\Delta T_{To,\,T1}$) is given in equation 5.5, where $\Delta f_{To,T1}$ is the shift in frequency in Hz and α is the proportionality constant. This constant is tissue independent and has been estimated to be -0.0098±0.0005 ppm/ºC [205].

$$\Delta \boldsymbol{T}_{\boldsymbol{T_o,T_1}} = \frac{\Delta \boldsymbol{f}_{\boldsymbol{T_o,T_1}}}{\boldsymbol{\gamma \times \alpha \times B_o}} \tag{5.5}$$

Using a gradient echo MR sequence, the equivalent phase shift in radians ($\Delta \Phi_{T_o,T_1}$) accumulated for a time equal to *TE* can be calculated by modifying equation 5.5 to the following expression.

$$\Delta \boldsymbol{T}_{\boldsymbol{T_o,T_1}} = \frac{\Delta \boldsymbol{\Phi}_{\boldsymbol{T_o,T_1}}}{\boldsymbol{2\pi \times \gamma \times \alpha \times B_o \times TE}} \tag{5.6}$$

Spin echo MR sequences are not used in phase imaging since the 180º pulse refocuses the temperature induced phase.

5.6 Development of an MR Thermometry analysis software based on PRFS method.

5.6.1 Overview of the Temperature Mapping Software.

A graphic user interface (GUI) was developed in Matlab R*2014A* (Mathworks, Natick , Massachusetts, USA) for calculating 2-dimensional temperature elevation maps direclty from MRI phase images using the *PRFS* method. Matlab is a popular programming language optimized for solving engineering and scientific problems with libraries and functions dedicated for image processing and analysis. The TempMap1 GUI was designed to subtract a phase image acquired at baseline temperature (Mask Image) from a phase image at the same location immediately thoughout the HIFU thermal treatment (Ablation Image).

5.6.2 Data collection using a phase sensitive imaging coil.

Images for thermometry analysis were acquired using the GPFLEX coil, which is a phase sensitive coil that supports quadrature detection. In quadrature detection the received circularly polarised MR signal is collected by the receivng coil in two orthogonal directions. In routine imaging this is done to increase the signal to noise ratio by a factor of $\sqrt{2}$ since the same signal for each point in k-space is sampled twice. The two 90° phase shifted signals can be convieniently assigned to the real and imaginary part of each complex data point in k-space which can be manipulated appropriately to recover the magnitude and relative phase of the detected MR signal. Signals from real and imaginary channels shown in Figure 5.8 are projections of the bulk magnetization's vector in two arbitrary orthogonal axes.

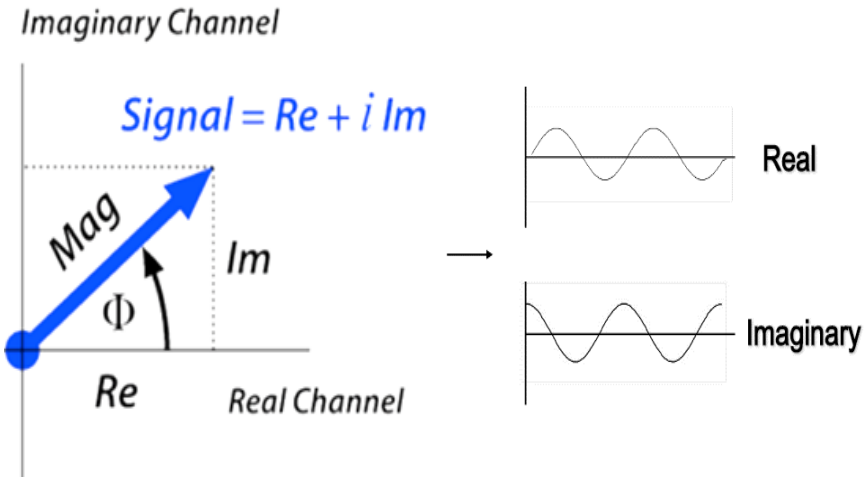

Figure 5.8: Representation of the 90° phase shifted complex data.

The signals from the Real (*Re*) and Imaginary (*Im*) channels are mathematically correlated with the magnitude (*Mag*) of the detected signal and its phase angle (Φ) as described in the following expressions.

$$\boldsymbol{Mag} = \sqrt{\boldsymbol{Re^2 + Im^2}} \tag{5.7}$$

$$\Phi = tan^{-1}\left(\frac{Im}{Re}\right) \tag{5.8}$$

The expressions above were used to construct complex data for the required reference and ablation images in order to implement *PRFS* Thermometry.

5.6.3 Complex data reconstruction for PRFS Thermometry.

Reconstruction of image type other than magnitude was not available in normal operating mode of the GE Signa Excite 1.5 Tesla MRI system. Therefore, before acquiring any images the scan was initiated in research mode and reconstruction of magnitude, real and imaginary images was enabled by setting appropriately the 'rhrcctrl' variable. The 'rhrcctrl' belongs to a huge list of system specific variables which control scanner behaviour and are usually not accessible under normal operating conditions. This variable reflects a 4-bit word where the ordering of bits moving from high to low correspond to enabling or disabling reconstruction of imaginary, real, phase and magnitude images. Depending on which types of reconstructed images the user wishes to produce, the 'rhrcctrl' variable can take values between 0 and 15. The 'rhrcctrl' variable was set to 13 which corresponded to reconstructing all types of images except phase. Although the system was capable of reconstructing phase images that are necessary for *PRFS* thermometry, individual phase images were calculated from the corresponding real and imaginary images using equation 5.8. This was done since the MRI scanner applies a correction for gradient non-linearity at the end of every acquisition ('Gradwarp' by GE Healthcare) that involves multiple interpolations which can set the phase data to deviate from their real values. The three data files produced for each instance are exported in a unique series folder and are sorted as Magnitude, Real and Imaginary.

5.6.4 Description of the TempMap1 GUI.

The interface of the GUI consisted of a set of pushbuttons, each executing some sort of function and an images panel for displaying the resulting images. The software takes DICOM (Digital Imaging and Communications in Medicine) files as inputs. DICOM is a protocol for handling data produced by imaging modalities. A DICOM file consists of a header that contains attributes related to patient and the scan including a dedicated attribute to pixel data. Unfortunatelly although MATLAB reads the image data of DICOM files (*dicomread* function) and the header's tags (*dicominfo* function), it does not support a DICOM server functionality. This means that the user cannot import images directly from the MRI scanner and an external application is needed to query, retrieve and store the DICOM files used by the GUI. The TempMap1 GUI user interface is shown in Figure 5.9.

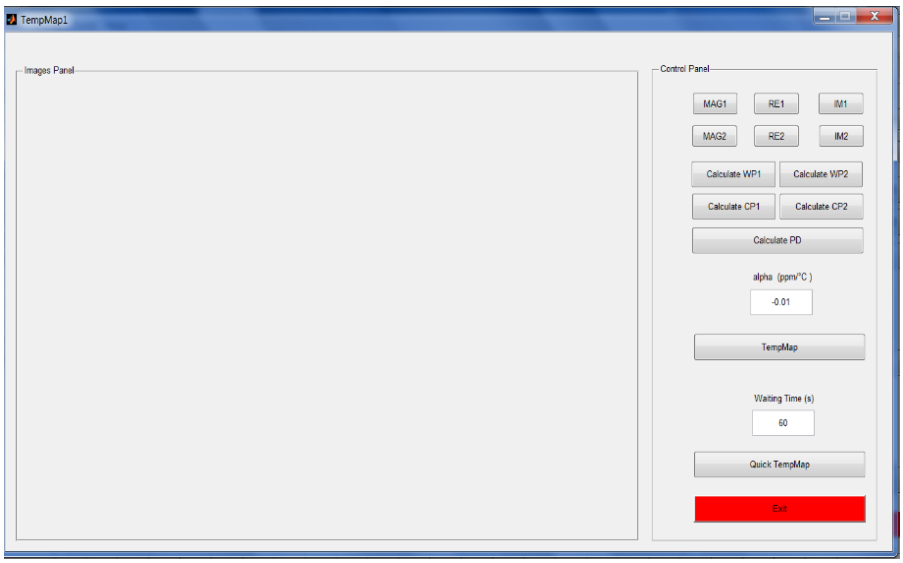

Figure 5.9: TempMap1 GUI user interface

5.6.4.1 Single pair analysis

In single pair analysis mode the user creates the complex data for one pair of reference and ablation images. At the end of the sequence a single temperature evolution map is produced. Each of pushbuttons *MAG1*, *RE1* and *IM1* opens a dialog box where the user is asked to browse and import the reconstructed magnitude, real and imaginary images produced by the MRI which are necessary for calculating the reference complex image. Similarly pushbuttons *MAG2*, *RE2* and *IM2* are used to calculate the ablation complex image. Importing of the aforementioned data must be done in the order described above (left to right in the control panel) otherwise the GUI produces a warning message. *WP1* and *WP2* buttons are used to create a matrix of equal size to the preloaded data, where each voxel value is equal to $tan^{-1}(IM1/RE1)$ and $tan^{-1}(IM2/RE2)$.Each voxel value represents the phase angle (Φ) of the MR signal and MATLAB calculates it using the *atan2* function. This function returns phase angles defined in $[-\pi, \pi]$ interval and therefore any calculated phase angle outside this range is wrapped around. Pushbuttons *IC1* and *IC2* reconstruct the final images of the pair using the complex number polar form for each voxel (Z) with coordinates (i, j) as shown in equation 5.9, since it was easier to manipulate calculations in the code.

$$\boldsymbol{Z(i,j)} = \boldsymbol{Mag(i,j)} \times \boldsymbol{e^{i\Phi(i,j)}} \tag{5.9}$$

The next step of the single pair analysis is the calculation of the complex difference phase angle matrix $\Delta\Phi$ (i, j) which is done by pushbutton *CD*. First the complex difference matrix Z_{CD} (i, j) is reconstructed by calculating for every element (i, j) of the matrix the product of the complex reference image Z_{ref} (i, j) with the complex conjugate of the ablation image Z_{abl} (i, j) as shown in the following expressions.

$$\boldsymbol{Z_{CD}}\,\boldsymbol{(i,j)} = \boldsymbol{Z_{ref}(i,j)} \times \boldsymbol{conj}[\boldsymbol{Z_{abl}(i,j)}] \tag{5.10}$$

$$\boldsymbol{Z_{CD}}\,\boldsymbol{(i,j)} = \boldsymbol{Mag_{ref}(i,j)} \times \boldsymbol{Mag_{abl}(i,j)} \times \boldsymbol{e^{i(\Phi_{ref}(i,j)-\Phi_{abl}(i,j))}} \tag{5.11}$$

The complex difference phase angle $\Delta\Phi$ (i, j) is calculated using MATLAB's *angle* function which returns the angle in radians of the complex difference matrix Z_{CD} (i, j). This angle represents the phase angle difference of the bulk magnetisation vectors between the reference and ablation images out of which the Temperature Evolution map ΔT (i, j) is calculated using the *PRFS* equation 5.5 . The complex difference phase $\Delta\Phi$ (i, j) matrix is then processed by an unwrapping algorithm before pressing the *TempMap* pushbutton which is the last of the sequence. Details for the unwrapping algorithm are given in the following sections.

TempMap1 produces the final colour coded temperature evolution map using the *PRFS* equation. Calculation requires an input in the editable field where the user defines the tissue temperature sensitivity coefficient α in ppm/ºC. The rest of the parameters required for *PRFS* thermometry are automatically extracted from the DICOM header using the *dicominfo* function at the beginning of the sequence. Single pair analysis is designed for offline analysis where the input data are exported to the localhost at the end of the MRI acquisition.

5.6.4.2 Multiple pair Thermometry analysis

The Multiple pair analysis mode processes a series of ablation images and can serve as a quasi-real time temperature monitoring tool. The first step is exactly the same as in the single pair mode where the user must select the three DICOM files (*MAG1, RE1 and IM1*), calculate the wrapped phase matrix (*WP1*) and complex image (*IC1*) reference image. The series of ablation data are streamed to the GUI by a third party application developed in C# by other members of our group because Matlab lacks DICOM server functionality. In fact the application saves in a text file defined inside the GUI's code, the localhost or remote host address of the ablation images folder (*MAG2, RE2 and IM2*).

The GUI automatically browses to the declared address and runs the sequence. The user defines prior to initiation of the analysis (*Quick TempMap* pushbutton) a configurable waiting time period in seconds. This is the time that the GUI runs over a loop and checks for changes in the ablation images folder address. Every triplet of new images produced are saved in a new folder and the GUI detects this by comparing the previous and current folder address string. Once a new triplet of images is detected the sequence runs again until the waiting time period expires. The output of this mode is a multi-frame colour coded figure that contains all the temperature maps produced.

5.6.4.3 Phase Unwrapping algorithm

Phase unwrapping is one of the most common and difficult problems to tackle in medical and optical imaging. Without correction wrapped phase images appear as alternating bright and dark bands. Matlab offers an *unwrap* function which corrects the radian phase angles of a wrapped phase image using a modified two-dimensional version of Itoh's method [206], [207]. It does that by adding multiples of $\pm 2\pi$ up until phase differences between consecutive voxels of the matrix are greater than or equal to π radians. The sequence is applied for every row of the voxel matrix and then the same process is repeated for every column. Unfortunately this method is very sensitive to noise present in the image which can be misconceived by the algorithm as wrapped phase outside the permissible phase range. Therefore elevated noise levels lead to error propagation across rows and columns which are catastrophic for making quantitative phase measurements.

The TempMap1 GUI uses a robust and computationally efficient unwrapping algorithm proposed by Herraez et al [208]. Instead of using a continuous unwrapping path like in Itoh's method, this algorithm uses a quality guided non-continuous unwrapping path which is based on the voxels edges reliability. Each pixel is assigned to a reliability index (R) which is the reciprocal of the resultant second difference (*RSD*). The *RSD* of each pixel is a function of the individual second differences across the 4 available directions (horizontal, vertical, 1^{st} diagonal, 2^{nd} diagonal). An example of a pixel reliability index calculation is demonstrated in Appendix B. The algorithm then calculates the edge reliability index all over the pixel matrix. The edge reliability index is equal to the sum of the two pixels reliability adjoined at the edge. The algorithm unwraps each couple of pixel in a preferential order, starting with maximum edge reliability to minimum. Pixel clusters with minimum phase discontinuities (high signal-to-noise ratio (*SNR*)) are unwrapped first and error propagations from random noise are limited.

5.6.4.4 Compensation of phase offset artifacts in MR Thermometry.

Intermittent artifacts were observed while monitoring with MR Thermometry the application of HIFU sonications in the developed composite and soft tissue phantoms. More specifically a background phase offset compared to the reference image was apparent in some of the ablation images and as a result the quantitative ability of *PRFS* thermometry was obstructed.The phase offset was apparent on some images even in the absence of HIFU sonication or the transducer. Therefore it was soon concluded that the source of the problem was related to the imaging system and/or timing of the sequence. Although it was not investigated thoroughly, there was speculation that the source of the aforementioned artifacts emerged from the induction of Eddy currents. Eddy currents develop in MRI systems during the application of the pulsed magnetic field gradients used from excitation and MR signal spatial encoding. These currents are known of resulting in undesired secondary field gradients and magnetic field shifts that distort the MR signal [209]. Time dependent homogeneous field shift arising from a spatial offset between the gradient isocentre and the centre point of the eddy-current-carrying structures and the magnet's bore tube have been reported [210].

In order to overcome this transient problem, a correction was applied for every couple of reference and ablation images. Precession frequency shift of hydrogen in lipids is not temperature sensitive due to the absence of hydrogen bonds. External references in the form of small plastic tubes filled with sunflower oil were wrapped around the phantoms and were used to compensate for the spatial and temporal phase shifts. An illustration of the oil references used to correct PRFS Thermometry in an agar-based gel is shown in Figure 5.10.

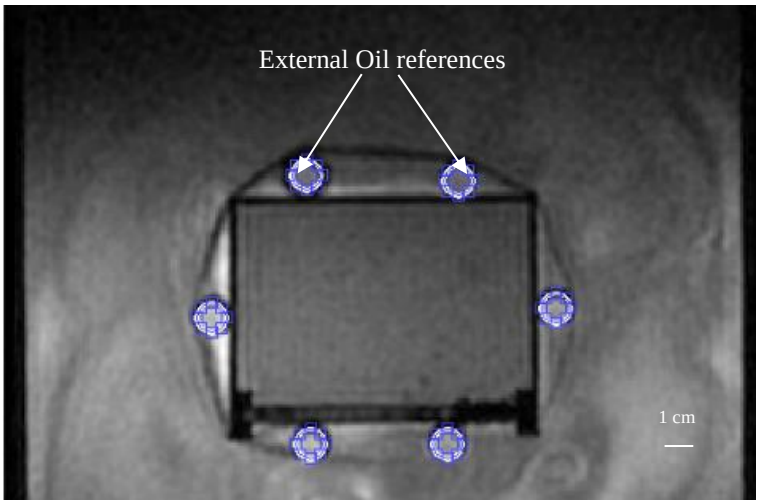

Figure 5.10: Magnitude image of a tissue mimicking agar based gel wrapped around with six sunflower oil external references for compensating system induced phase shifts during PRFS thermometry.

The phase shift compensation workflow is embedded inside the TempMap1 GUI code. Immediately after the user selects the magnitude reference image (*MAG1*), the code successively creates six (6) Regions of Interest (ROIs). The user drags and drops each of the circular ROIs to be contained within each of the available oil references. The GUI code records the mean pixel values of each of the user defined ROIs in the final unwrapped complex difference phase image. Ideally the complex difference phase should be zero everywhere expect the area which has been heated by HIFU. Phase difference measured inside the oil references is immune to temperature fluctuations and is only affected by systemic spatial-temporal perturbations of phase. The external oil references phase difference values were used to fit with Matlab a linear polynomial surface through least squares regression in order to extrapolate the phase shifts developed inside the phantom. A linear polynomial fitting was chosen since there were no higher orders of phase difference fluctuations observed but rather a phase offset of constant magnitude that covered the whole 2D matrix of pixels. The fitted compensation matrix is described by the following expression were α_0, α_1, α_2 are the polynomial coefficients and *i*, *j* correspond to the Cartesian coordinates of the extrapolated pixels.

$$\boldsymbol{M(i,j)} = \boldsymbol{a_0} + \boldsymbol{a_1} \times \boldsymbol{i} + \boldsymbol{a_2} \times \boldsymbol{j} \tag{5.12}$$

An example of a typical 2D compensation matrix applied is shown in Figure 5.11.

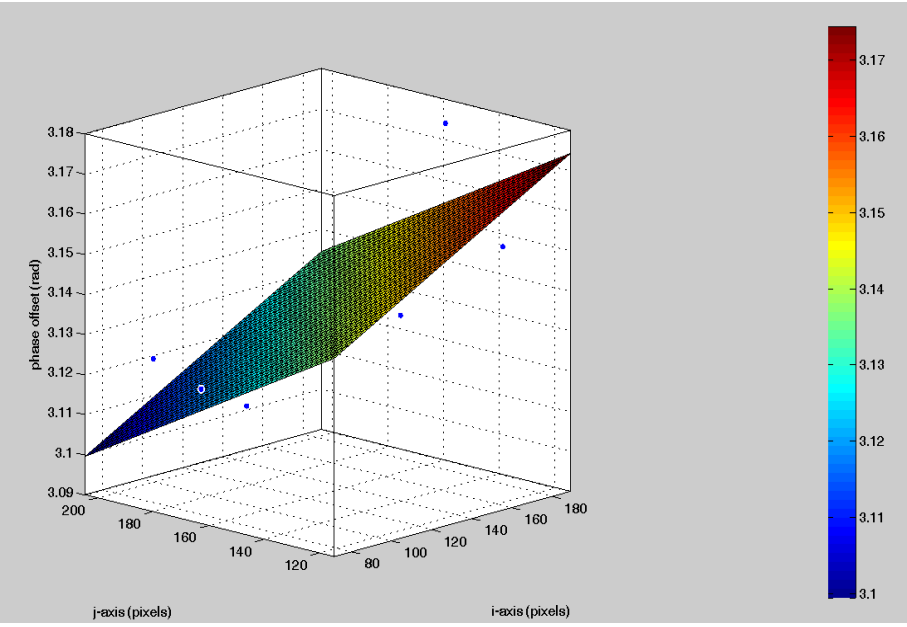

Figure 5.11: Example of a 2D compensation matrix calculated by fitting external oil references phase data to a linear polynomial surface using a least absolute residuals (LAR) fitting method.

The blue dots in Figure 5.11 represent the mean phase difference measured in each of the oil references ROIs. The 2D surface is fitted using equation 5.12 using the least absolutes residual criterion (LAR). Once the compensation matrix is calculated, it is then used to deduct pixel by pixel the pseudophase offset that potentially masks temperature induced phase shifts. When the placement of oil references was not possible a 2D correction matrix was created by positioning the ROIs in phantom areas that were as far as possible from the heated region and free of any image artefacts.

5.6.5 SPGR Pulse Sequence for MR Thermometry.

Temporal resolution of the order of a few seconds is required when monitoring HIFU thermal protocols with MR Thermometry. HIFU hyperthermia applications are delivered within minutes while ablative HIFU applications involve steep temperature gradients delivered within 30-60 seconds sonications with the temperature profile constantly changing rapidly across the volume of tissue surrounding the acoustic focus. The temporal resolution of any conventional pulse sequence depends on *TR*, the number of encoding steps in phase direction (N_p) and *NEX*. The minimum *TR* is limited by the duration of the *RF* pulses, the gradient system limitations and *TE*.

An SPGR pulse sequence readily available from the MRI scanner was selected for conducting MR Thermometry. It belongs to the GRE family of sequences which are more appropriate compared to spin echo when fast imaging is required. SPGR differs from conventional gradient echo pulse sequences in the sense that any residual transverse magnetization is "spoiled" at the end of every cycle and before the next excitation *RF* pulse. Spoiling is necessary when $TR<T_2$ to disrupt transverse coherences that can affect the phase of the transverse magnetization in successive cycles.

The selection of the acquisition parameters and the reasoning behind it are described below:

1) *TR*: 38.5 ms

This was the minimum repetition time allowed by the system for the minimum allowable matrix size of 128 × 128. In order to fill the whole of k-space for a single image the scanner requires 4928 ms (128 × 38.5 ms). A temporal resolution of approximately 5s was considered acceptable for monitoring the application of HIFU thermal protocols of 30-60 seconds duration.

2) *TE*: 20 ms

This selection was based on a compromise between high signal-to-noise ratio (short transverse magnetization decay for phantoms with T_2 ~ 66ms) and temperature-to-noise ratio in temperature maps (larger accumulation of phase for longer *TE*).

3) Flip angle (α): 30º

A low flip angle was used in order to allow a significant amount of longitudinal magnetization to recover for this short *TR*. Although the Ernst angle which is the angle for maximum longitudinal magnetization for every *TR* and T_1 combination is lower than 30º, a wider flip angle was used in order to increase the T_1 contrast on the magnitude images between the hot lesion and the background of the phantom.

4) Matrix Size: 128 × 128

The smallest possible pixel matrix allowed by the scanner was used to minimize the number of phase encoding steps and the overall scan time. On top of the requirement for an acceptable temporal resolution, this matrix size corresponded to an in-plane spatial resolution that varied between 1.5 – 2.3 mm per pixel for the sizes of FOV used. Such spatial resolution was considered adequate for monitoring the acoustic focus produced by the HIFU transducer (Sonic Concepts, Inc., Bothell, WA, USA) inside the phantoms which according to the manufacturer the -6 dB ellipsoidal iso-pressure contour spans over a width of 3.48 mm and 58.25 mm length [211].

5) Slice Thickness: 5 mm

A 5 mm slice thickness was large enough to contain the short axis of the focus (3.48 mm). A thicker slice would increase the signal-to-noise ratio but in expense of partial volume effects that would lead to underestimation of temperature shift. A thinner slice would decrease the signal-to-noise ratio and require steeper gradient fields. As mentioned previously the application of fast switching gradient fields is a potential source of Eddy currents.

6) FOV: 20-30 cm

Depending on the dimension of the phantom imaged and the direction of the acquired imaging slice, the FOV varied within the range of 20-30 cm. In some cases the FOV was adjusted appropriate to eliminate wrap-around artifacts. Although this phenomenon may occur in the frequency-encode direction, it is generally more severe along the phase-

encode axis. The easiest remedy to overcome this signal misregistration problem is to increase the FOV in the appropriate direction to include all the region that produces MR signal detectable by the *RF* imaging coil.

7) NEX: 1

The minimum number of excitations was used to keep the total scan time to minimum.

8) rBW: 15 kHz

An intermediated rBW was chosen to balance between signal-to-noise ratio which is proportional to reciprocal of the rBW square root and with minimum allowable *TE* that affects the total scan time.

5.6.6 Temperature error estimation in MR thermometry.

The temperature error (*ΔT)* in each voxel of the thermometry maps is associated with the signal-to-noise ratio (*SNR)* of the magnitude image and can be estimated using the following equation [212], [213]. All other variables included in the expression have the usual meaning.

$$\boldsymbol{\Delta T}[℃] = \frac{\mathbf{400}}{\boldsymbol{SNR}.\boldsymbol{B_o}[\boldsymbol{T}].\boldsymbol{TE}[\boldsymbol{ms}]} \tag{5.13}$$

SNR was calculated using the National Electrical Manufacturers Association (NEMA) standard [214]. Signal was set to be equal to the mean pixel intensity of the phantom's magnitude image prior to sonication, for a square region of interest containing 100 pixels. The standard deviation (σ) of pixel intensities was calculated by taking the mean of zero NMR signal region pixel intensities (in air) surrounding the phantom. Noise in MRI magnitude images follows a Rician distribution since pixel intensities are assigned to only positive values therefore underestimating true noise levels. The NEMA standard recommends using the following equation for determining true noise (*N*).

$$\boldsymbol{N} = \frac{\boldsymbol{\sigma}}{\mathbf{0.66}} \tag{5.14}$$

The Matlab code for TempMap1 GUI is illustrated in Appendix C.

5.7 Summary

The spin-lattice (T_1) and spin-spin (T_2) relaxation times of the developed agar-based gel recipes were characterizing using relaxometry techniques. The estimated relaxation times were close to the replicated tissues times and therefore they are expected to induce similar temperature induced contrasts in conventional T_1 and T_2 weighted images. The chapter also described the development of a stand-alone *TempMap1* GUI that calculated thermal maps using the PRFS technique. The *TempMap1* GUI was created to assess the functionality of the developed composite phantoms using focused ultrasound thermal protocols in configurations that simulate clinical applications.

6 Functionality tests of the developed composite tissue mimicking phantoms using MR guided focused ultrasound.

This chapter describes a set of functionality tests ran to test the performance of the developed phantoms. These tests involve important quality control metrics of the soft tissue mimicking phantoms and assessment of the composite phantoms with setups that emulate clinical HIFU applications guided by MRI.

6.1 MR compatible transducer for HIFU sonications.

A single element piezoelectric MR compatible spherically focused ultrasound transducer by Sonic Concepts (H-196, Sonic Concepts, Bothell, Washington, USA) shown in Figure 6.1, was used to apply high intensity sonications in continuous mode. According to the manufacturer's datasheet [211], the transducer operates at the fundamental frequency f_o (1.1 MHz) or its 3rd harmonic $3f_o$ (3.41 MHz). The radius of curvature (*ROC*) of the spherically focused transducer was 100 mm with an active element transducer diameter (*D*) equal to 40 mm. At 1.1 MHz and maximum electric power (400 W) the peak pressure at focus in water reaches 8.34 MPa corresponding to a spatial peak intensity at focus I_{sp} equal to 2321 W/cm^2. The dimensions of the cigar shaped focus defined by the -6dB beam contour (L×W) are 58.25 mm and 3.48 mm respectively.

Figure 6.1: Spherically focused MR compatible HIFU transducer

6.2 Thermal repeatability test.

Materials and Methods

The thermal repeatability of the two tissue mimicking phantom recipes (brain and muscle) was assessed using *PRFS* thermometry. The agar based phantoms were molded inside a rectangular plastic box. Each phantom was positioned for a top to bottom sonication inside a water tank filled with degassed water. The phantoms were sonicated using the

single element MR compatible HIFU transducer operating at 1.1 MHz. The HIFU transducer was driven by the RFG-750 amplifier (JJ&A Instruments). The amplifier and transducer were connected via a matching network to minimize the reflected power.

This test used five sonications (acoustic power of 25W and duration of 60 s) targeting the four corners and the center of the rectangular phantom in order to avoid residual heating from neighboring sonications. The transducer was attached on plastic rails that allowed manual adjustment of its position in the horizontal plane and its distance from the phantom's top surface. Targeting of focus was approximately 3.8 cm deep for the brain phantom and 1.9 cm for the muscle phantom. Temperature assessment was conducted using a 2D SPGR pulse sequence (*TR*: 38.5 ms, *TE*: 20 ms, *rBW*: 15 kHz, matrix size: 128 × 128, slice thickness: 5 mm, *NEX*: 1, *DFOV*: 25 x 25 cm^2). MR Thermometry was used to record temperature evolution over time in 12 s intervals. Although the temporal resolution of the sequence was 5 s, the scanner increased that to 12 s by introducing a delay between series to adjust transmitter–receiver gain and the center frequency of the *RF* pulse. The average coefficient of variation (CV_{avg}) was calculated by averaging the individual coefficients of variation for each point in time for all five locations. Figure 6.2 demonstrates the experimental setup for the brain mimicking phantom recipe.

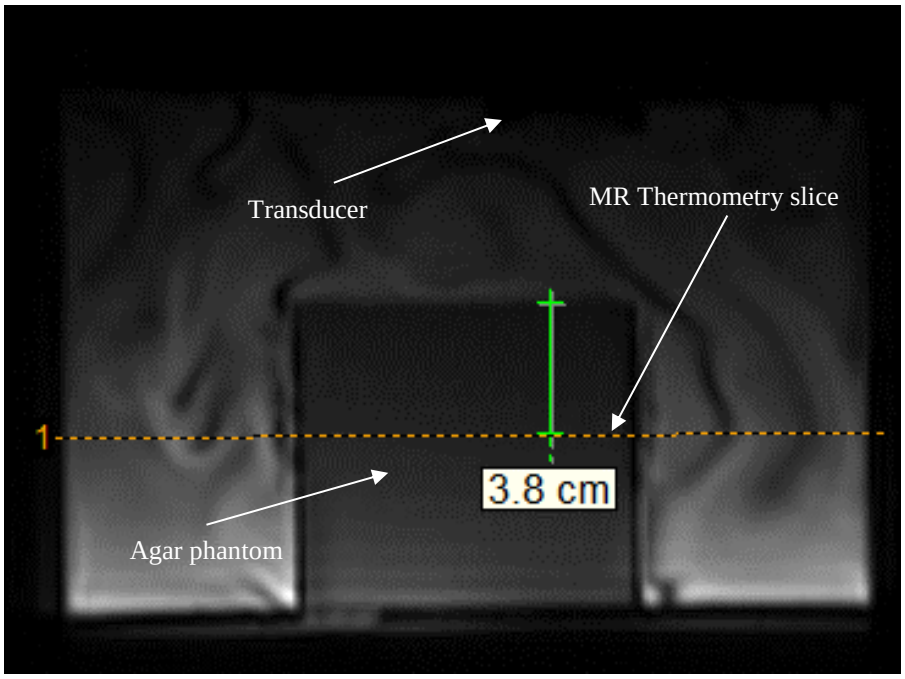

Figure 6.2: Axial magnitude image demonstrating the experimental setup for measuring the thermal repeatability of the brain tissue mimicking phantom.

Results

Plots of the temperature evolution with time in the brain and muscle phantoms are shown in Figure 6.3 and Figure 6.4. The average peak temperature rise developed in the muscle phantom (67.0 ºC) was significantly higher from the brain phantom since it was positioned shallower compared to the brain phantom (32.8 ºC), which introduced lower attenuation. Both waveforms demonstrated a rapid drop of temperature after 60 seconds when the HIFU beam was disabled. The rate by which temperature initially dropped was higher for the muscle phantom since heat transfer to the colder surrounding is faster at steeper temperature gradients.

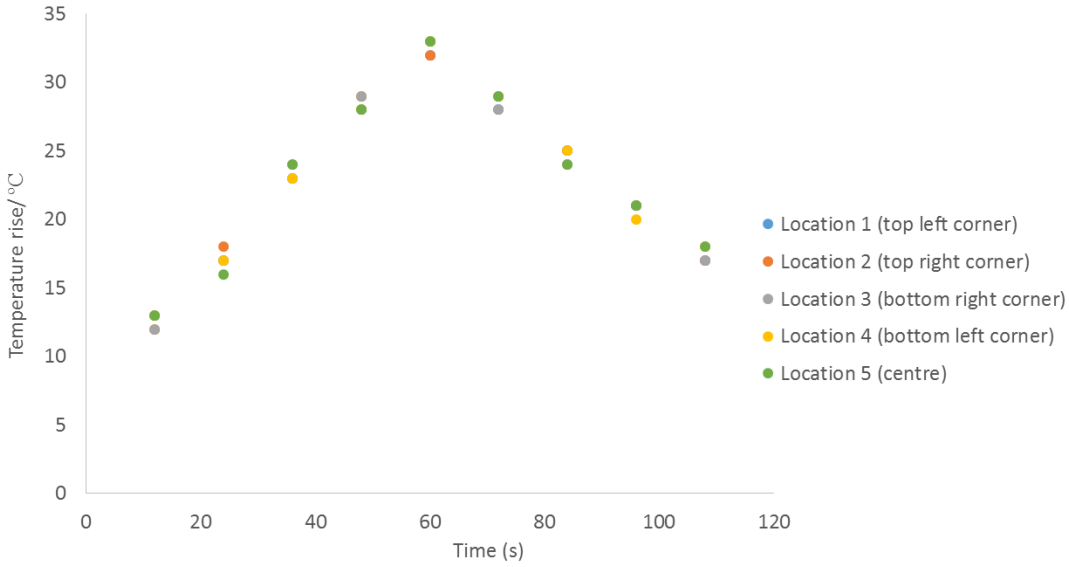

Figure 6.3: Temperature rise over time in brain phantom (3.8 cm deep) for an acoustical power of 25 W and 60 s sonication in 5 different locations.

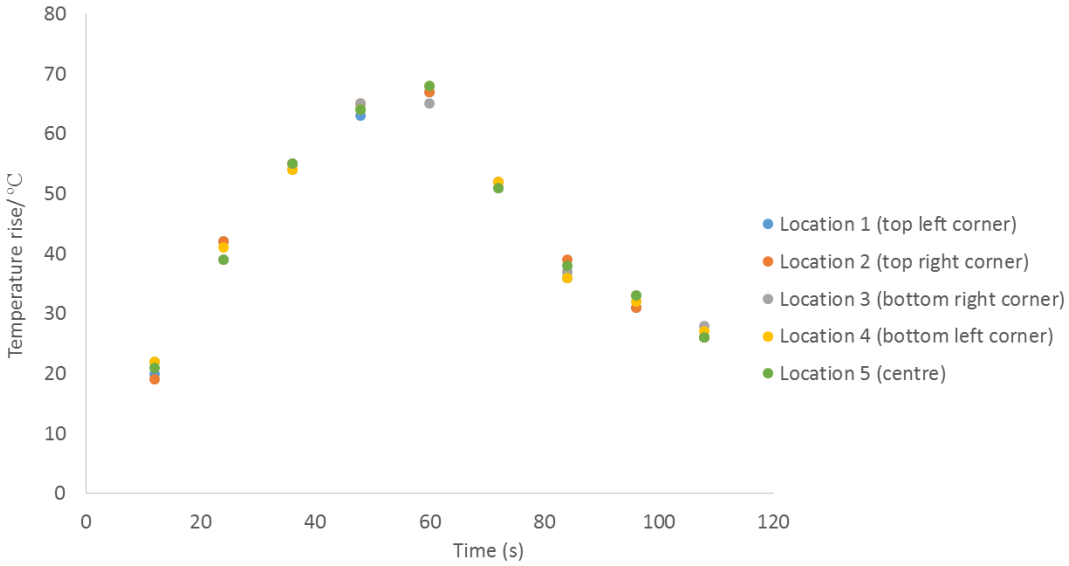

Figure 6.4: Temperature rise over time in muscle phantom (1.9 cm deep) for an acoustical power of 25 W and 60 s sonication in 5 different locations.

Conclusions

The thermal repeatability test showed that both phantom recipes performed with similar response. The CV_{avg} of temperature measurements in the brain phantom was 2.6 % and for 2.7 % for the muscle phantom. This result can be interpreted as a low spatial variability of the phantoms acoustic properties, which is an important prerequisite since the assessment of FUS thermal protocols depends on observing the distribution of temperature across the imaging plane. The CV_{avg} accumulates the error in temperature measurements, which is a function of the image's *SNR* and the inherent spatial inhomogeneity of the acoustic properties which can be attributed to the nature of the fabrication method (inadequate mixing of ingredients, presence of air bubbles, etc).

6.3 Qualitative evaluation of focused ultrasound induced heating dependence using a phantom of variable depth

Materials and Methods

A brain mimicking phantom was molded in a step like shape to create three different propagation depths (Figure 6.5A and Figure 6.5B).

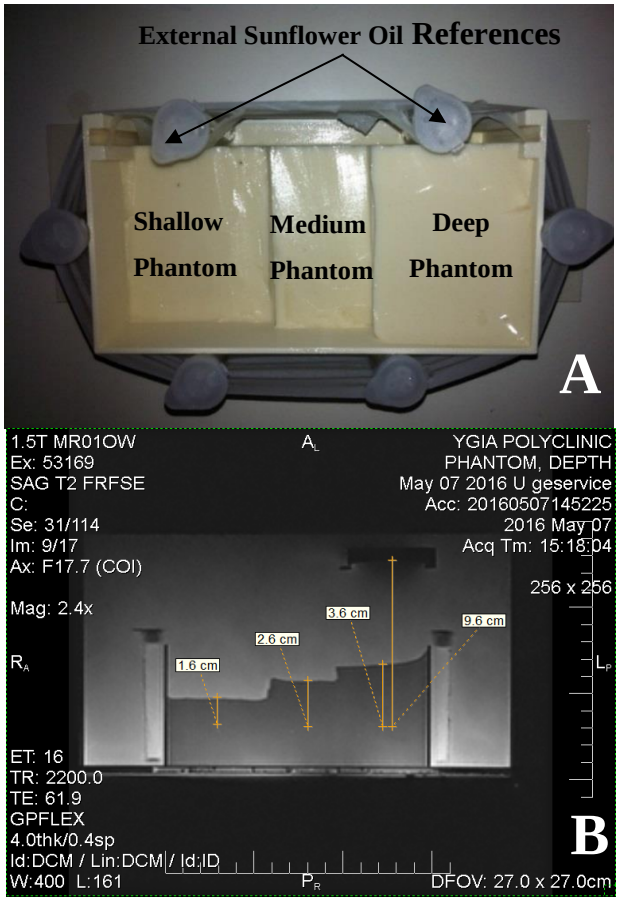

Figure 6.5: A) Top view of the depth agar phantom demonstrating the three regions and external oil references surrounding the phantom, B) Sagittal T_2w FRFSE image (TR: 2000 ms, TE :61.9 ms, ETL: 16) illustrating a lateral view of the phantom.

The purpose of this study was to demonstrate qualitatively the correlation of target depth inside the phantom (shallow, medium and deep). Small tubes filled with sunflower oil were strapped around the phantom as external references to provide phase offset correction to the produced temperature maps. The phantom was immersed inside a tank filled with degassed water in a top to bottom sonication configuration. The sonication protocols used are summarized in Table 6-1.

Table 6-1: Sonication protocols used for evaluating depth phantom

Phantom depth (cm)	Acoustic Power (W)	Duration (s)	Orientation
3.6	25	60	Coronal
3.6	25	60	Axial
2.6	25	60	Coronal
2.6	25	60	Axial
1.6	25	60	Coronal
1.6	25	60	Axial

Thermometry was conducted using the following 2D SPGR pulse sequence (TR: 38.5 ms, TE: 20 ms, rBW: 15 kHz, Matrix: 128 × 128, slice thickness: 10 mm, NEX: 1, DFOV: 25 × 25 cm^2), with the slices prescribed in the coronal and axial plane. The coronal slices were designed to coincide with the expected acoustic focus (96 mm from the transducer's front face) in a plane perpendicular to the propagation direction of the acoustic beam. The axial thermometry slices were designed in a parallel plane using the same pulse sequence but with a 5 mm slice thickness. This was done to minimize partial volume effects that would mask the small dimensions of the focus in that plane. Thermometry images were analyzed using the TempMap1 GUI.

Results

Temperature at focus increased with decreasing phantom depth. Deeper phantoms introduced more material along the beam's pathway and consequently higher degrees of attenuation (See Figure 6.6a-e). The maximum temperature rise reached in the deep phantom was 11.9 ºC in the coronal plane and 9.1 ºC in the axial plane for the same sonication settings (25 W acoustical power-60 s). Temperature rise in the coronal plane (20.1 ºC) of the medium phantom was approximately equal to the one measured in the axial plane (20.8 ºC) whereas temperatures in the shallow phantom were significantly different between the two orientations (37.2 ºC in coronal and 21.9 ºC in axial orientations). Coronal thermometry slices (perpendicular to acoustic field) produced more

reliable temperature measurements from axial slices. Axial slices must be aligned perfectly with the central long axis of the beam in order to contain only voxels with protons that lie inside the focal region. Considering that the 5 mm slice thickness was larger than the -6 dB focal width (3.48 mm), any misalignment underestimates temperature measurements as a result of partial volume averaging. Far field heating was evident in axial images due to absorption at the bottom of the plastic container that conducted heat to adjacent phantom.

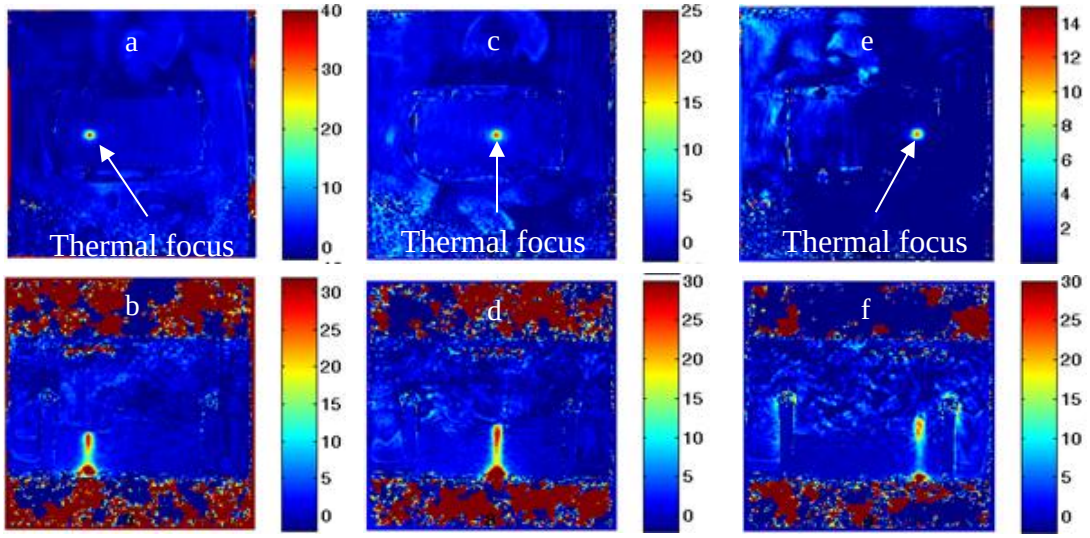

Figure 6.6: Coronal and axial thermometry maps at maximum temperature for the (a, b) shallow phantom, (c, d) medium phantom and (e, f) deep phantom.

The full time series of thermometry maps for both coronal and axial plane for the three different phantom depths is shown in Figures 1-6 in Appendix C.

Conclusions

The agar phantom attenuated the acoustic beam effectively. The degree of attenuation was depth dependent, which is consistent with the exponential decay of acoustic wave intensity along the direction of propagation. Far field heating was observed for all depths and it was indicative of reflection at the interface. Maximum temperature readings in the coronal and axial plane were different due to partial volume averaging. Additionally by visually inspecting the thermometry maps, the location of maximum temperature in the axial plane was systematically observed at a distance shorter than the focal length. This was attributed to nonlinear propagation that induced a shift to the thermal focus.

6.4 Composite head phantom monitoring during HIFU thermal sonications using invasive temperature measurements.

Materials and Methods

This experiment was the first conducted amongst others to demonstrate the functionality of the developed composite phantoms by exposing them to continuous wave HIFU sonications. At the time when the phantom head phantom was developed MR Thermometry was not available and therefore temperature measurements were taken invasively by embedding a thermocouple wire (Omega Engineering, Inc., Norwalk Connecticut, USA) inside the gel phantom. The 3D printed ABS skull was firmly fixed on a plastic base. The size of the base was designed to fit firmly inside the water tank. The tip of the thermocouple was set in an anterior-posterior axis and perpendicular to the acoustic beam's pathway. The position of the thermocouple wire inside the skull before molding the brain mimicking gel is shown in Figure 6.7.

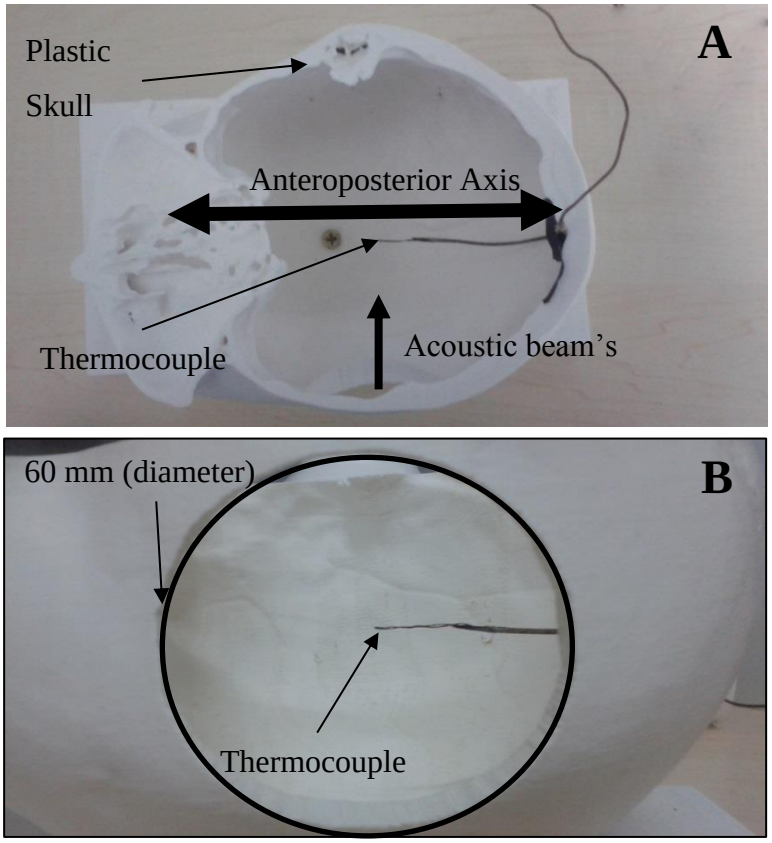

Figure 6.7: (A) Top view of the 3D-printed skull cavity, (B) Beam's eye view through the 60 mm circular craniotomy section showing the tip of the thermocouple wire.

This orientation was such to allow an easier beam targeting of the thermocouple's tip. The height of the thermocouple's position was also adjusted to place its tip in the center of the craniotomy. The distance of the thermocouple tip from the plastic skull's craniotomy section was approximately 3.5 cm. The craniotomy section was retrofitted with bronze pins to be easily detachable in order to perform sonications with and without intervening plastic skull. The skull was filled with brain mimicking gel according to the

brain mimicking phantom recipe presented previously (agar 2 % w/v, silica dioxide 1.2 % w/v, evaporated milk 25 % v/v). The total volume of the gel (800 ml) was poured inside the skull. Care was taken to avoid pouring the gel directly on the thermocouple and displacing it. The gel was moulded inside the skull and was left to reach room temperature and solidify. The composite head phantom with its base were immersed in a tank filled with degassed water. The temperature of the phantom was left to equalize with the temperature of the surrounding water (16 ºC). Temperature was monitored for a low sonication frequency that is typically used in transcranial HIFU deep brain treatment ablations [215]–[217]. A single element spherical transducer of 0.6 MHz central frequency (Piezotechnologies, S/N: 602015, diameter (D): 50 mm and focal length (R): 100 mm) was used. The transducer was attached on a custom made plastic holder that allowed manual adjustment of its position in all three orthogonal axes. The transducer front face was placed to point towards the craniotomy's opening center. The transducer was driven by an Agilent 33220A (Keysight Technologies, California, USA) waveform generator and the signal was amplified with a Kalmus LA100H 100 W Broadband RF power amplifier (Advanced Test Equipment Corp., San Diego, California, USA). The transducer was connected to the amplifier via an impedance matching circuit. The matching circuit minimized the reflected power. The setup configuration is shown in Figure 6.8.

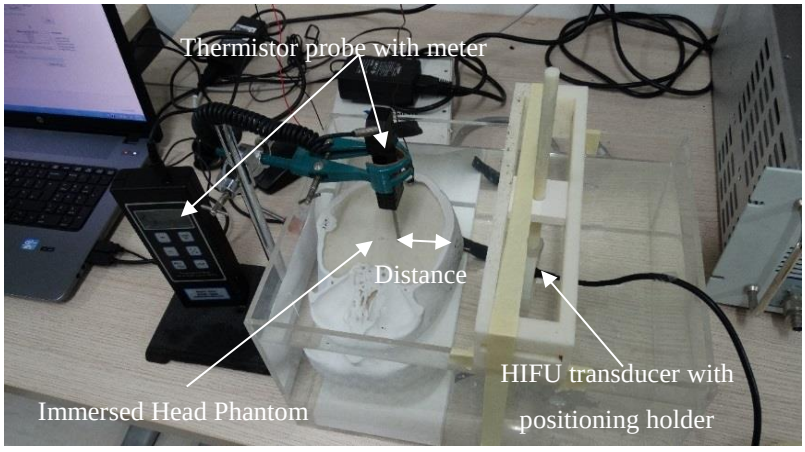

Figure 6.8: Setup of composite head phantom invasive temperature measurements using thermocouple and thermistor thermometers.

Prior to the measurement, the transducer's position was fine adjusted relative to the thermocouple by identifying the position of maximum temperature elevated with a fast cooling rate, which indicated focal localization. Beam alignment was performed at low power to avoid excessive agar heating. Maximum temperature elevation

measurements in three characteristic regions of the acoustic field (near field, focus, far field) and on brain surface were recorded for an acoustic power of 30 W. Sonications lasted up until temperature readings reached a maximum. Measurements at the focus (3.5 cm) were repeated for intact skull and in the absence of the craniotomy section.

Results

Temperature elevations at different locations across the beam's propagation axis are shown in Table 6-2.

Table 6-2: Maximum Temperature elevations reached at different locations and skull state for acoustical power of 30 W sonications at 0.6 MHz.

Plastic skull state	Thermometer Type	Position	Distance(cm)	Temperature Elevation (^{0}C)
Intact	Thermistor probe	Brain phantom surface	0	38
Intact	Thermistor probe	Near field	2	9
Intact	Thermocouple	Focus	3.5	2
Intact	Thermistor probe	Far field	6	1
Skull removed	Thermocouple	Focus	3.5	31

Conclusions

Exposing the intact skull with moderate acoustic power (30 W) sonications at 0.6 MHz (high penetration) resulted in focal temperature increments that did not exceed ambient by more than 2 ºC, whereas temperature at brain phantom surface was indicative of excessive skull heating (38 ºC). This experiment demonstrated a common problem of transcranial HIFU where acoustic energy is not transferred efficiently at focus while skull bone is heated. The small active area of the single element HIFU transducer (~20 cm^2) focused the beam over an even smaller area on the plastic skull surface transferring considerably large amounts of power per unit area. The high intensity pressure wave propagating though the skull was converted to heat by plastic skull which possessed an attenuation coefficient in the range of skull bone tissue (16 dB/cm-MHz). MRgFUS vendors use semispherical helmet-like phased arrays to manage skull excessive heating by distributing acoustic energy over a larger surface area [218], [219] .

Acoustic wavefront dephasing occurred during propagation through the skull of high variability in thickness. The dephasing effect was intensified further by the high

propagation speed of ultrasound in ABS. The acoustic field's dephasing limited the focusing gain which was observed in small focal temperature elevations. These phase aberrations are compensated in clinical systems by applying appropriate phase shift corrections calculated by computed tomography data. In the absence of skull phantom, temperature was elevated significantly as a result of adequate acoustic energy delivery and lack of significant phase aberrations. Increased temperature levels in the near field were possibly a result of heat conduction by the plastic skull rather than of absorption by the brain mimicking agar based gel phantom.

As expected it was not possible to transcranially focus the beam using a single element transducer. Excessive skull heating can be reduced by increasing the single element's aperture area but compensation of skull induced phase aberrations requires an adaptive focusing approach that is only achievable by phased array of transducers [15], [220]. This functionality test demonstrated that the composite skull phantom can be a very useful tool for assessing the performance of transcranial HIFU instrumentation and the efficiency of adaptive focusing algorithm by looking in to temperature elevations and its profile across the treatment volume.

6.4.1 MRI for testing composite head phantom functionality during HIFU thermal sonications.

Materials and Methods

The composite head phantom was simultaneously imaged under MRI while exposing it to a sonication using the 1.1 MHz (Sonic Concepts) transducer. MR thermometry was not available since the signal recorded in the complex data (real and imaginary) was erroneous. A possible cause was the large FOV (30 cm) used to cover the whole head phantom exceeded the sensitive range of the GPFLEX imaging coil. Instead temperature elevations were observed qualitatively using a SPGR pulse sequence. Since SPGR was a T_1-weighted pulse sequence, it was expected to detect regions with increased temperature regions as hypointense since heat induced T_1 increments progressively relax smaller amounts of longitudinal magnetization.

The composite head phantom was positioned on the treatment platform of an MR compatible positioning device for treating brain diseases with HIFU [221] as shown in Figure 6.9. The phantom was placed laterally on to the platform with the craniotomy section facing down. The platform was immersed a few millimeters deep in a tank filled with degassed water. This configuration ensured a coupling between the phantom and the

transducer also immersed in the water tank and underneath the treatment platform. The front face of the transducer was positioned for a bottom to top sonication. The positioning device was capable of moving the transducer in all three orthogonal directions (*xyz*) for precise beam targeting.

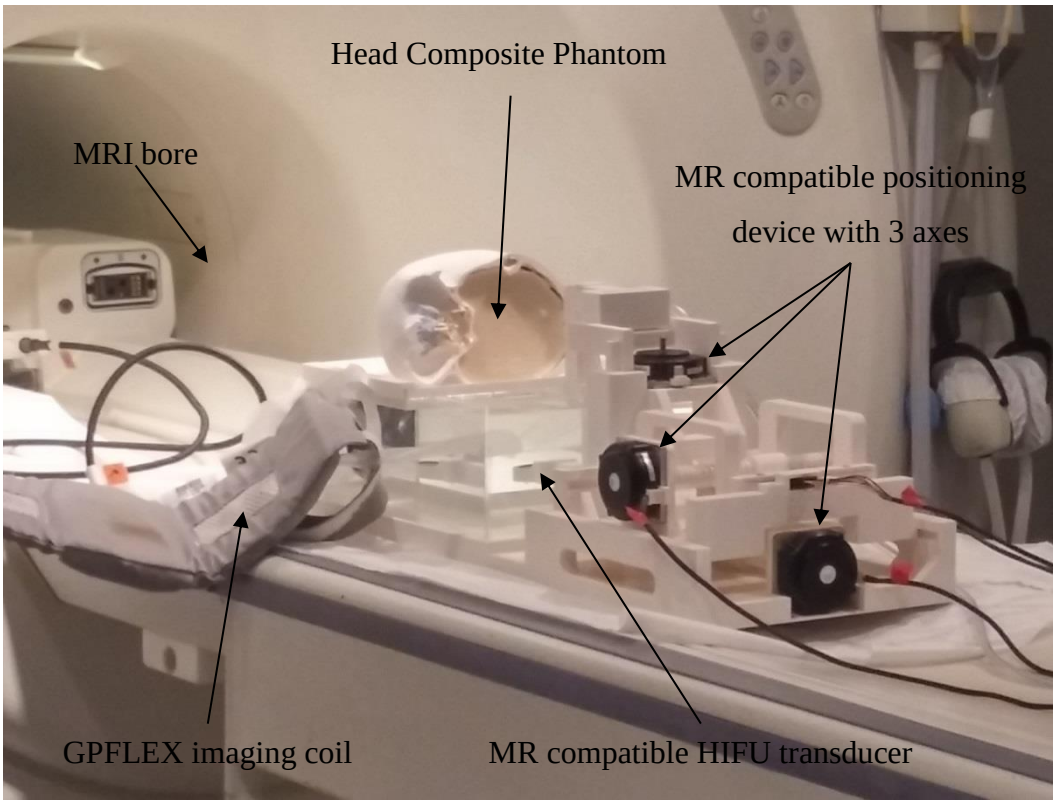

Figure 6.9 - Experimental configuration used during sonications of the composite head phantom under MR imaging.

The positioning device consisted only by MR compatible materials such as ABS plastic for the main body, brass screws, racks and pinions. Brass is a non-ferromagnetic material and does not induce serious safety or image artifacts in the vicinity of the MRI. The device employed three MR compatible piezoelectric ultrasonic motors (PUM) (Shinsei USR60E3N, Shinsei Corp., Kasuya-Setagaya-ku Tokyo, Japan) for moving the transducer independently in the three linear orthogonal directions. The positioning device and sonication parameters were controlled via a custom made interface. The latest version of the control software was developed in C# and was capable of moving the transducer in all 3 directions by controlling the PUM drivers (Shinsei USR60 Series). A computer communicated via an interface with a Digital Acquisition (DAQ) devices (National Instruments Corp.). The DAQ was responsible for translating digital inputs from the interface to the motor drivers which executed the displacement of the robot in the three

axes. Additionally the DAQ was returning feedback from linear encoders from each axes for its current position. The robot's motor drivers and encoder wires were passed in the MRI room through a waveguide of the Faraday's cage. The transducer was driven by the power generator (JJ&A Instruments), which was equipped with a built-in-frequency generator operating in the range of 700 kHz to 5 MHz, an adjustable power level between 1 and 750 W output and was capable of working both in continuous and pulse mode. The generator was controlled by a series of string commands sent via a standard USB interface. The power line of the transducer was filtered by a low pass filter and was fed via an impedance matching circuit. The complete control station of the MR compatible positioning device, RF power generator and HIFU transducer is illustrated in Figure 6.10.

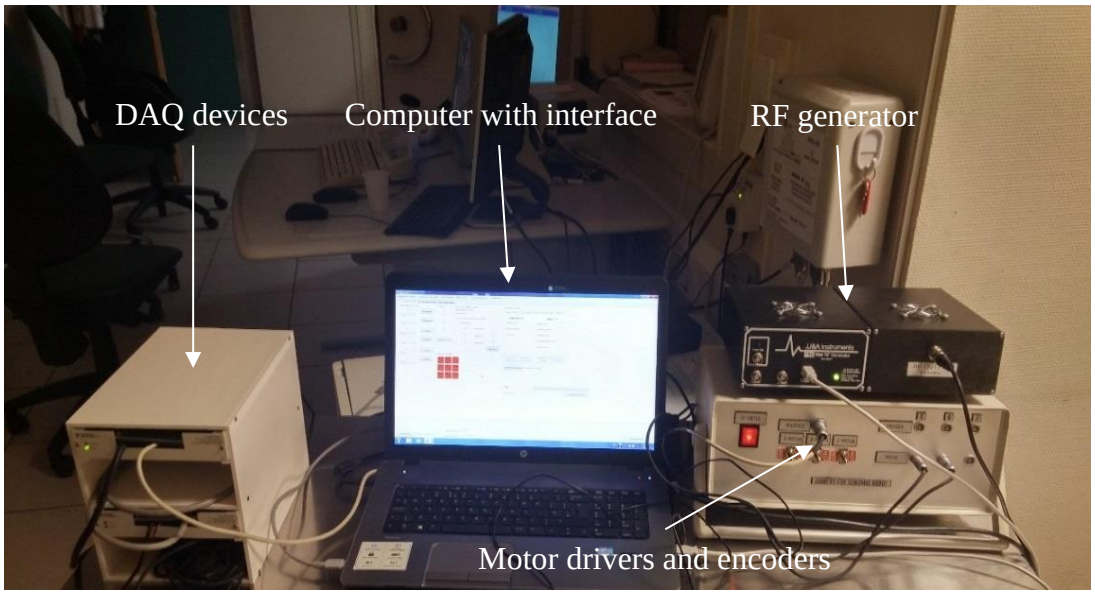

Figure 6.10: Control station of positioning device and RF power for driving the HIFU transducer under MRI guidance.

The transducer's power line was passed inside the MRI room via a BNC connector on both sides of the Faraday's cage penetration panel. Any cables going in and out of the MRI room were passed through the penetration panel to prevent interference from external RF signals. The transducer's power line through the panel's BNC connection is shown in Figure 6.11. The head phantom was sonicated with the craniotomy section detached with two different protocols (50 W-60 s and 90 W-90 s) at 1.1 MHz in order to observe changes over the T_1 weighted image. Using the same configuration, but this time with the craniotomy section attached to simulate a non-invasive transcranial approach, the phantom was exposed to similar acoustic energy levels (50 W-60 s). Temperature increment induced changes were monitored with a T_1 weighted SPGR sequence (TR: 38.5

ms, TE: 2.7 ms, slice thickness: 10 mm, ETL: 1, NEX: 1, matrix size: 128 × 128, DFOV: 30 × 30 cm). TE was set to minimum in order to minimize T_2 contrast. Imaging slices were prescribed along the central beam axis of the axial and sagittal plane. Images in time series for each sonication protocol were acquired every 12 s and covered both heating and cooling phase.

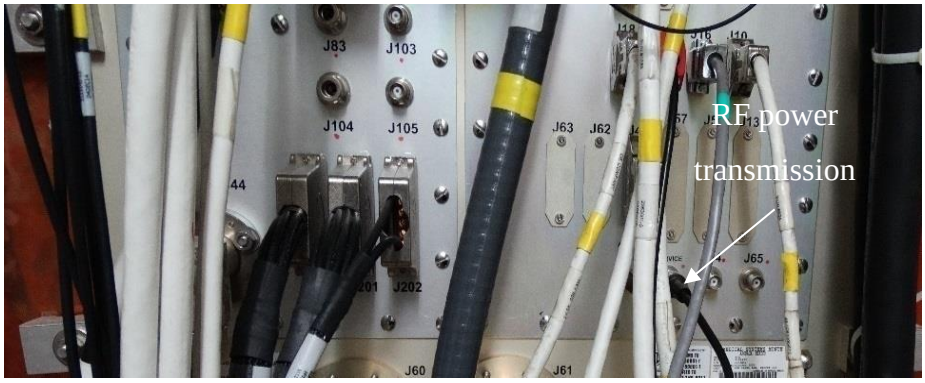

Figure 6.11: RF transmission connection through the MRI's Faraday cage penetration panel.

Results

In the absence of skull, sonications induced a local increase of the temperature dependent T_1 relaxation time. For the 50 W acoustical power and 60 s sonication, regions of increased temperature appeared with hypointense signal in the T_1 weighted images (Figure 6.12A and Figure 6.12B).

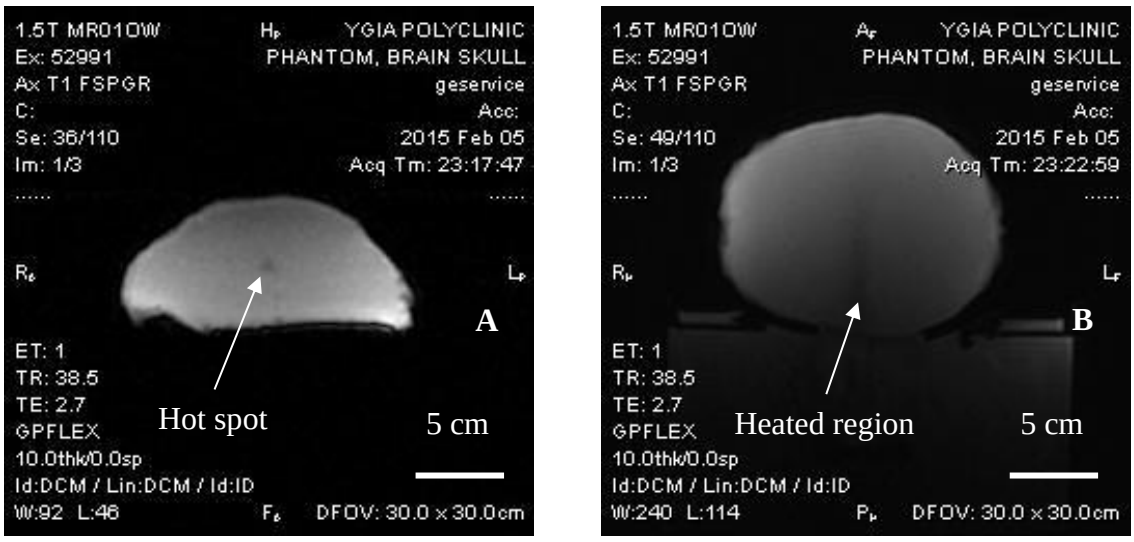

Figure 6.12: T_1 weighted image at maximum heat deposition (60 s) in the absence of craniotomy section for a 50 W-60 s sonication in the A) sagittal and B) axial plane.

The slice in the sagittal plane was perpendicular to the beam axis and the heated region appeared as a circular-like hot spot (Figure 6.12A). Figure 6.12B illustrates the axial slice set parallel to the beam's long axis where a cigar-shaped region of hypointense signal was observed. Observations in both planes were indicative of the temperature gradients developed across the focused field. The temperature increment for the 50 W-60 s and the 90 W-90 s sonications were compared qualitatively by observing the contrast of the formed hot spot to its background in the T_1 weighted images (Figure 6.13A and Figure 6.13B). The window level and width were kept the same for both images to avoid contrast saturation. The hot spot in the 90 W-90 s was significantly darker as a result of the higher HIFU induced temperature.

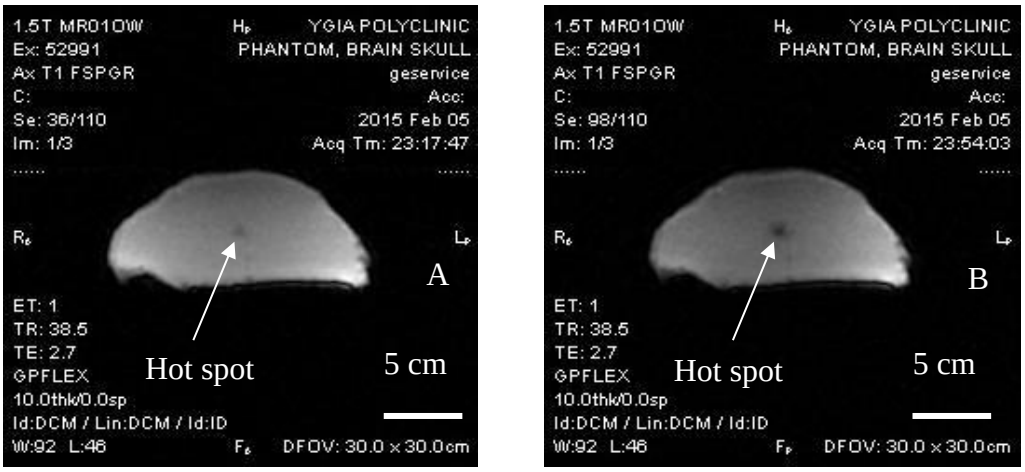

Figure 6.13: Sagittal T_1 weighted images at peak temperature in the absence of craniotomy section for A) 50 W-60 s and B) 90 W-90 s sonication.

The equivalent images of 50 W-60 s sonications with intact skull in the axial and sagittal plane showed no observable formation of hot regions (Figure 6.14A and Figure 6.14B).

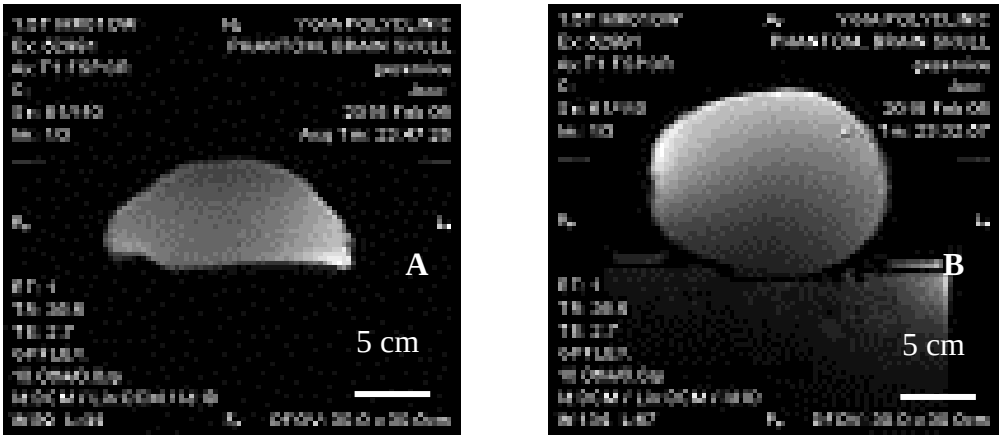

Figure 6.14: T_1 weighted image at maximum heat deposition (60 s) in the presence of skull phantom for a 50 W-60 s sonication in the A) sagittal and B) axial plane.

A careful observation of the images revealed a diffuse grey band of hypointense signal on brain phantom adjacent to the skull (Figure 6.14B). Temperature increase in that area was a result of conduction from the hot skull phantom. These results were in agreement with thermocouple measurements (30 W-60 s) where temperature rise at focus did not exceed 2 ºC whilst adjacent to the skull phantom a temperature rise of 38 ºC was reached. Skull thickness in the craniotomy section ranged from 3 to 12 mm which resulted in deleterious phase aberrations and uneven attenuation across the acoustic wavefront that could not be corrected using a single element transducer. Hot spots hypointense signal diffused during the cooling phase since heat conducted in the colder background. The full time series for each sonication protocol tested using the composite head phantom are illustrated in Appendix C.

Conclusions

Although temperature measurements via MR Thermometry were not available during HIFU sonications, results were presented through invasive thermocouple measurements and observations in T_1 changes. In the absence of the craniotomy section, the brain phantom absorbed acoustic energy adequately. According to thermocouple readings the focal temperature reached ablative levels within seconds (54 ºC in 60 s). Observations in T_1 weighted images in a plane perpendicular to the direction of acoustic propagation illustrated the formation of a fine circularly shaped region of hypointense signal. The contrast of the hypointense spot with its background increased for higher acoustic power sonications. In the transcranial configuration, the single element transducer did not focus the beam through the skull. The hot skull craniotomy section conducted heat to adjacent brain phantom whereas inadequate amounts of heat were delivered at the focus. Temperature increment at focus measured with the thermocouple (2 ºC after 60 s of sonication) was considered inadequate for ablating brain tissue in a clinical setting.

6.5 HIFU thermal sonications of composite femur bone-muscle phantom under MR Thermometry monitoring.

***Materials* and Methods**

This particular functionality test was designed to simulate the existing approach used in bone palliative treatments and assess the performance of the developed phantom under MR thermometry. The phantom was placed on top of the MR compatible positing device's platform central square opening and immersed by a few millimeters inside a tank

filled with degassed water. The device was the same used for the head phantom functionality test. The MR compatible spherically HIFU transducer (Sonic Concepts) with a 40 mm diameter and 100 mm radius of curvature was also immersed underneath the phantom. This configuration was set for a bottom to top sonication (Figure 6.15).

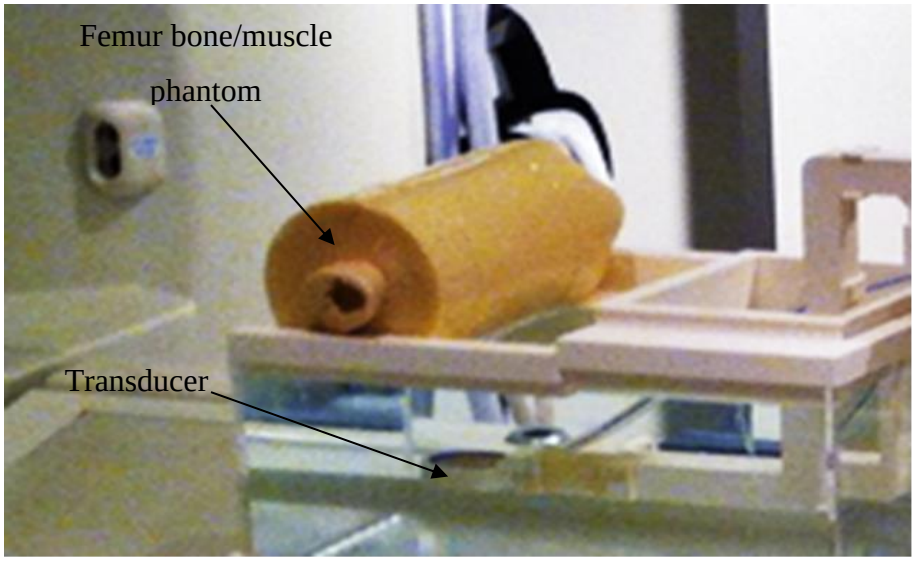

Figure 6.15: Experimental configuration used during sonication sonications of the composite femur bone-muscle phantom monitored by MR Thermometry.

A fast gradient echo pulse sequence (FGRE) localizer was used to fine adjust the transducer's position relative to the phantom (TR: 4.9 ms, TE: 1.4 ms, flip angle: 30º, rBW: 62 kHz, Matrix size: 256×128 and DFOV: 44 cm). Using a sagittal localizer the transducer was positioned 100 mm below the bone/tissue interface. This was identical to the clinical setup for bone metastases palliation treatments where the transducer focuses the acoustic beam at the bone/tissue interface. The phantom was treated with several sonication protocols shown in Table 6-3.

Table 6-3: Maximum temperature (T_{max}) for all the tested sonication protocols monitored by MR Thermometry in the axial plane

Sonication protocol	**Monitoring Period (s)**	**No. of thermal maps**
30 W-30 s (axial)	144	12
60 W-30 s (axial)	144	12
90 W-30 s (axial)	144	12
30 W-60 s (axial)	216	18
60 W-60 s (axial)	216	18
60 W-60 (sagittal)	216	18

Temperature elevation was monitored using PRFS thermometry. A SPGR pulse sequence (TR: 32ms, TE: 20 ms, Flip angle: 30º, rBW=15 kHz, slice thickness: 10 mm, matrix size: 128×128 and DFOV: 19 cm) was used to acquire complex data needed to construct the thermal maps in the axial plane as described in previous chapters. The actual temporal resolution of the MR thermometry sequence was 12 s per map. The phantom was monitored with a single MR thermometry slice orientated in a plane parallel to the beam's propagation central axis (axial) for sonications of 30 W - 30 s, 30 W - 60 s, 60 W - 30 s, 60 W - 60 s and 90 W - 30 s (Figure 6.16). Thermometry was also conducted for a 60 W - 60 s sonication in a plane perpendicular (sagittal) to the beam's axis and 5mm away from the interface.

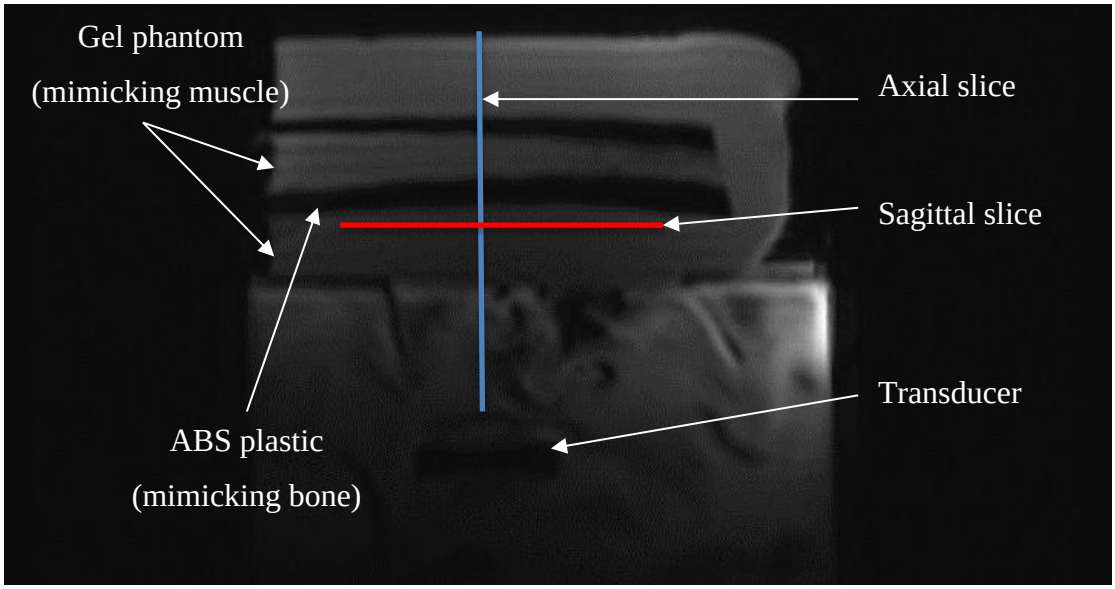

Figure 6.16: FGRE image of the phantom transducer setup cross section demonstrating the prescribed sagittal and axial thermometry slices.

All sonications lasting 30 s were monitored with MR Thermometry for 144 s (12 thermal maps) and 60 s sonications for 216 s (18 thermal maps). This was done to record phantom thermal performance in the cooling stage. The distance of the transducer to the muscle/bone interface was set to 10 cm which was approximately equal to the focal length. This way the thermal focus was expected to form on the interface. Since no MR signal was expected to be produced by the plastic bone model, temperature increment was assessed in regions adjacent to the sonicated bone model layer. This is exactly what is done in all *in vivo* experiments where the MR signal of bones is short lived because of their extremely short T_2 relaxation time. Thus, the efficacy of treatment was assessed on

the basis of an apparent temperature of the muscle phantom adjacent to the treated bone phantom. Thermometry data were analyzed using the TempMap1 GUI.

Results

A magnitude image of the exact prescribed axial thermometry slice is displayed in Figure 6.17 for reference purposes.

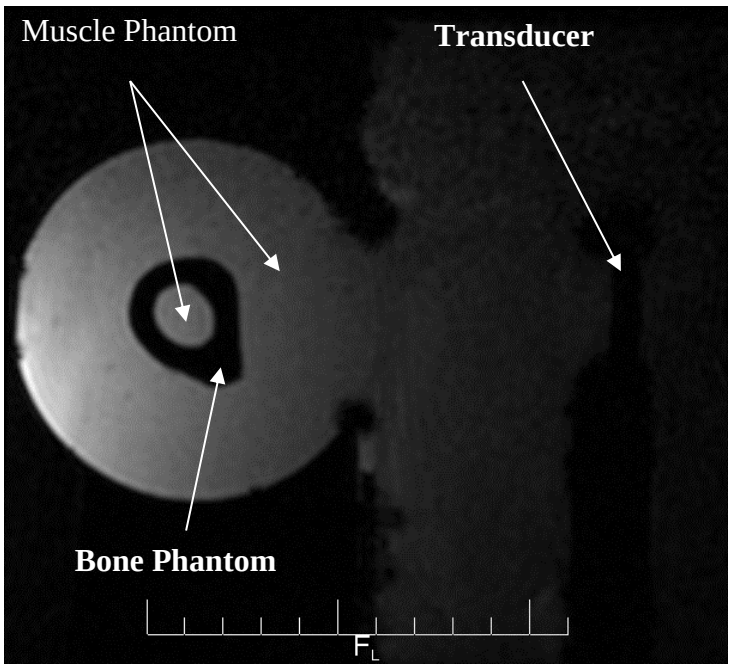

Figure 6.17: Magnitude image of the axial slice used in PRFS thermometry.

The maximum temperature rise from background developed in the phantom during sonication 30W - 30s was approximately 18.6 ºC (thermal map 3). The maximum temperature rise was determined by identifying the pixel with highest reading within 5 pixels from the interface corresponding to a distance of 7.5 mm. Temperature kept increasing even after the ultrasound was switched off since bone phantom absorbed acoustic energy efficiently and transferred heat via thermal conduction to the surrounding muscle phantom. The maximum temperature rise was 22.9 ºC in thermal map 8. Thermal map 8 was recorded approximately 66 s after sonication was switched off and temperature increment was attributed to heat conducting from adjacent bone phantom. This rather delayed heating effect was attributed to the low thermal diffusivity of the ABS bone phantom. The maximum temperature in the last map during the cooling phase (108 s post sonication) was 18.4 ºC. The same analysis was followed for all sonication protocols and the max temperature rise (T_{max}) at the end of each sonication protocol is shown in Table 6-4.

Table 6-4: Max temperature rise (T_{max}) at the end of each sonication protocol

Sonication protocol	T_{max} at the end of sonication (ºC)
30 W - 30 s (axial)	18.6
60 W - 30 s (axial)	27.3
90 W - 30 s (axial)	49.7
30 W - 60 s (axial)	30.8
60 W - 60 s (axial)	85.6
60 W - 60 (sagittal)	35.7

Typical thermal maps (T_{max}) for axial sonications at 30W - 30s, 60W - 30s and 90W - 30s are shown in Figure 6.18 A-C respectively.

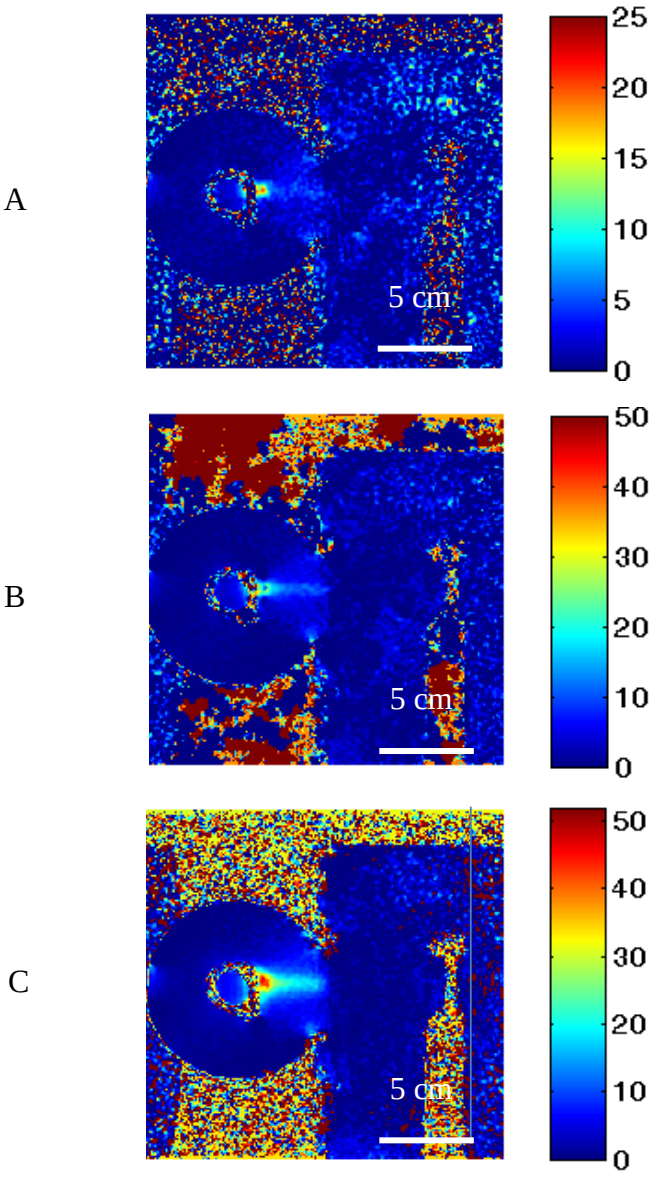

Figure 6.18: Typical thermal maps at (T_{max}) for A) 30W - 30s, B) 60W - 30s and C) 90W - 30s.

Cooling rate was faster for sonications where higher maximum temperature were reached due to higher temperature gradients. The calculated *SNR* for the bone/muscle phantom was 18.5 which corresponded according to equation 5.13 to a pixel temperature error equal to 0.7 ºC. Pixel statistics were calculated using *ImageJ* (National Institutes of Health, USA), which is a Java open source image analysis software. The heating profile of the hot region formed adjacent to the bone phantom during the sonication period was similar to what was seen in patients [91]. Some temperature increment was also observed in the agar-based phantom residing in the middle of the bone. This was indicative of heat transferring to the gel via conduction from the hot bone phantom. For some of the tested sonication protocols ablative temperatures were reached. HIFU induced measured temperatures were consistent with HIFU dosage which was directly proportional to the product of acoustic power with sonication time. The 60 W- 60 s induced the maximum temperature and the 30 W-30 s the minimum. With 30 s sonication, the 90 W was the only exposure reaching ablative temperature levels (>60 ºC). The full time series for each axial sonication protocol are illustrated in Appendix C.

The sagittal thermometry slice was set approximately 5 mm in front of the bone/tissue interface (Figure 6.26), to monitor a 60 W- 60 s sonication in a plane perpendicular to the direction of propagation. The acquisition parameters of the SPGR pulse sequence used for calculating the sagittal thermal maps were the same with the ones used in the axial plane, except slice thickness and DFOV which were 5 mm and 18 cm respectively. The maximum temperature elevation was 35.7 ºC with an error equal to 1.2 ºC. Increased temperature error was a result of signal reduction since voxel volume in the sagittal slice was approximately 47 % of voxel volume used in the axial slice. Thermometry demonstrated a Gaussian temperature distribution which is typical when monitoring the formed focus in a plane perpendicular to the propagation direction (sagittal). During cooling period the Gaussian profile spread as heat diffused in the surrounding agar phantom. The SNR in the region of the muscle phantom adjacent to the treated bone is governing up to date apparent temperature in surrounding muscle is the index used for controlling ablation of bone lesions. The estimated SNR levels (18.5 for axial slice and 10.9 for sagittal slice) were found to be in the range of clinical studies conducted to assess the quality of MR thermometry during palliative HIFU treatment of bone metastases [222]. In this study the average SNR of surrounding muscle retrieved from 13 treatments ranged from 8.7 to 39. The good quality of temperature monitoring using this phantom was reflected by the estimated temperature errors (0.7 ºC-1.2 ºC), which were close to accuracy required (1 ºC) for closed-loop control of energy deposition

in commercial MRgFUS systems. Typical thermal maps demonstrating the thermal lesion formed at peak temperature and at maximum cooling are demonstrated in Figure 6.19 A and Figure 6.19B respectively.

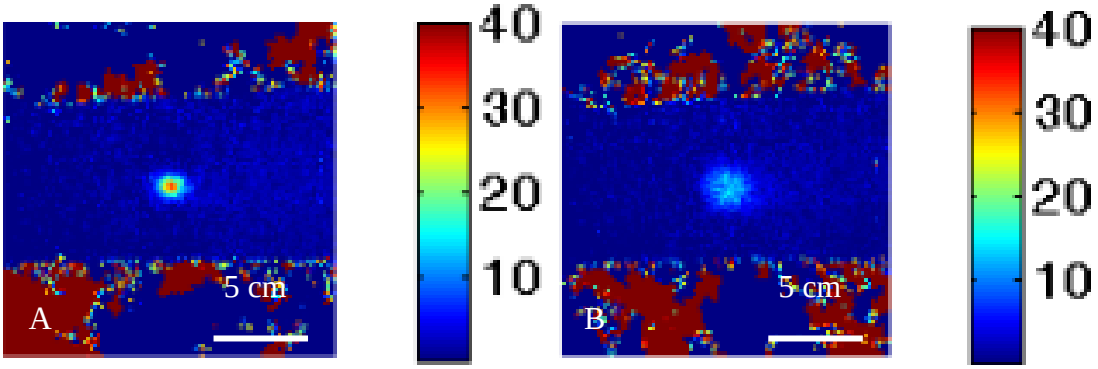

Figure 6.19: Thermal maps at (A) T_{max}, (B) at maximum cooling in the sagittal plane for a 60 W-60 s sonication using a SPGR pulse sequence.

The full time series for the sagittal sonication protocol is illustrated in Appendix C.

Conclusions

This work demonstrated the functionality of the developed bone/muscle phantom for assessing MRgFUS protocols. The phantom was made out of MRI compatible materials and introduced no image artifacts, whist image quality in MR thermometry produced readings with similar accuracy obtained in clinical systems. The phantom's materials possessed acoustic properties close to the replicated biological tissues, therefore the developed temperature levels were similar to HIFU clinical treatments. Phantom heating profiles corresponded as expected to HIFU dosage and ablative temperatures were reached for some of the protocols.

The proposed design avoided the use of biological tissue in the form of cadavers which unless used fresh they require formalin fixation for preservation. *In vivo* studies that use small animal models differ significantly in geometry and size and their results cannot be translated reliably to the clinical setting with humans. Therefore this phantom is not only a step forward in replacing animal models but can also improve the transferability of research findings in human applications. This phantom can be developed further in the future and serve as reference phantom of thermal dosimetry in MRgFUS exposures and can be used to calibrate such systems or to provide intercomparison between similar systems of different vendors. It is literally customizable to individual patient's bone geometry and has the potential of becoming a valuable treatment planning or educational tool. The muscle mimicking agar-based phantom was doped with

appropriate concentrations of silica dioxide and evaporated milk for controlling acoustic scatter and absorption independently. The cumulative effect of these additives was to approximate the attenuation coefficient of muscle tissue while simultaneously retaining the relative contributions of scatter and absorption.

6.6 HIFU thermal sonications of Composite breast-rib phantom under MR Thermometry monitoring.

Materials and Methods

The phantom was placed with the breast phantom pointing downwards for a bottom to top HIFU sonication. The phantom was resting on top of the tissue holder of the MR robotic positioning device used to drive the HIFU transducer. The phantom weight was supported with a thin Mylar film. The breast phantom was partially sunk in the water tank which was later filled with degassed water to provide the necessary coupling. Lateral and top views of the phantom's setup are illustrated in Figure 6.20.

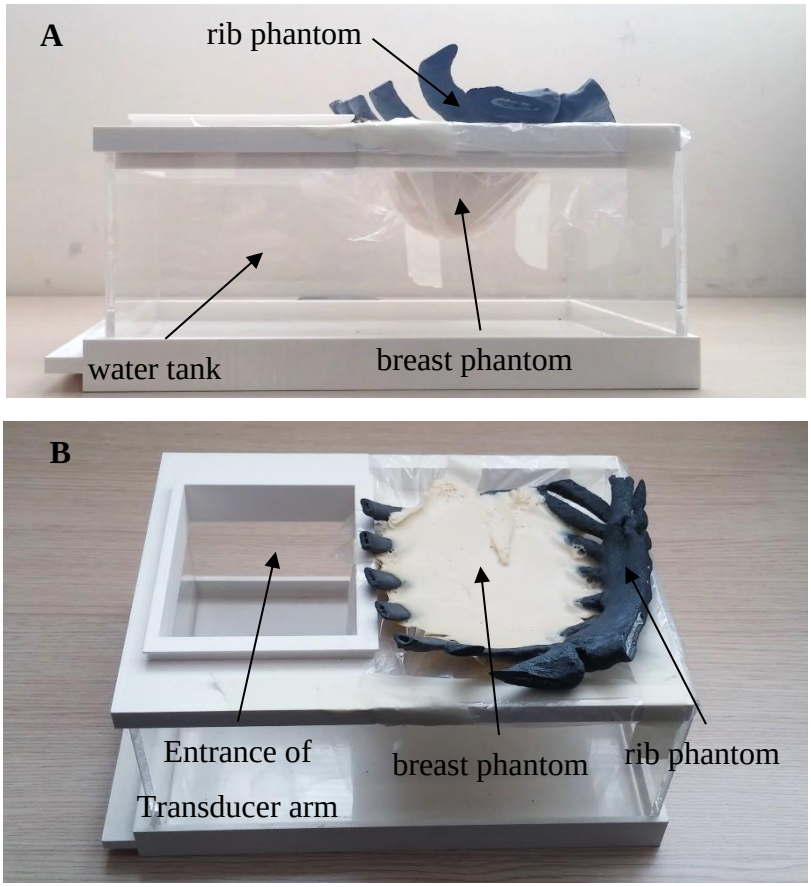

Figure 6.20: (A) Lateral and (B) top view of the composite breast-rib phantom resting on the treatment platform, with breast phantom partially sunk inside the water tank.

The robotic positioning device used for this set of experiments was different from the one used for the bone/muscle phantom. A motorized angular axis was added that allowed the

transducer to rotate around the subject. The purpose of this modification was to demonstrate the effect of avoiding structures like bone by changing the acoustic beam's angle of incidence. The upgraded positioning device was originally developed for isocentric bone HIFU applications [223]. Details of the upgraded design are given in the following chapter.

The plastic arm with the attached MR compatible 1.1 MHz transducer (Sonic Concepts) were immersed inside the water tank. Care was taken to remove any air bubbles from the transducer's and the breast's surface that could attenuate the beam. The position of the transducer relative to the phantom was set centrally underneath the breast phantom via the robotic system. The robotic system along with the phantom were positioned and centered on the MRI table. The phantom was wrapped around by the GPFLEX imaging coil. A SPGR pulse sequence was used for PRFS thermometry with the following acquisition parameters: *TR*: 38.5 ms, *TE*: 20 ms, *rBW*: 15 kHz, matrix size: 128 × 128, slice thickness: 10 mm, *NEX*: 1, *DFOV*: 25 x 25 cm. Figure 6.21 shows an axial SPGR magnitude image with the transducer positioned in the central axis of propagation.

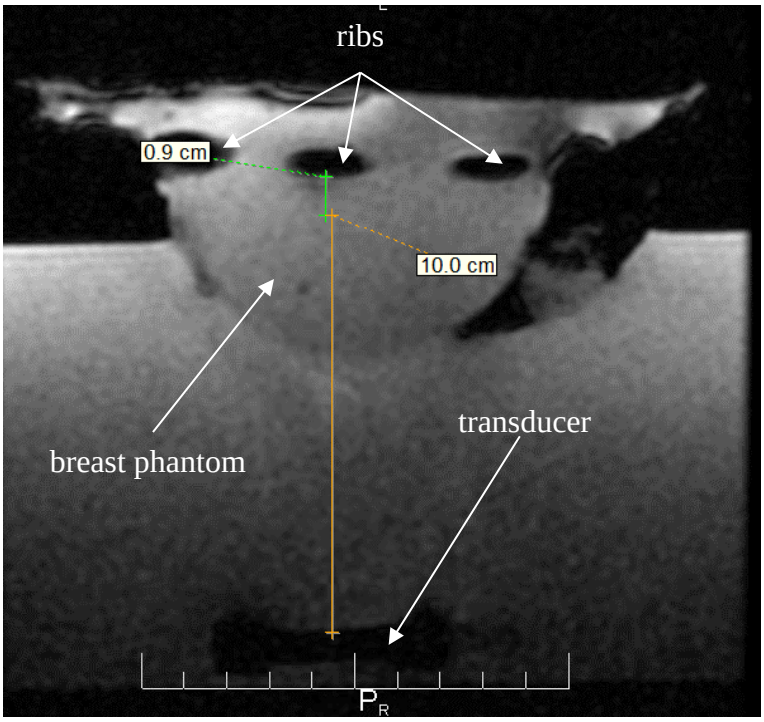

Figure 6.21: Axial magnitude image of the transducer's position relative to the breast-rib phantom.

The focus of the acoustic field was expected to form approximately 9 mm in front of the breast/rib interface at a distance equal to the focal length of the transducer (10 cm). Coronal thermometry slices were positioned at a distance equal to the transducer's focal length (10 cm). A second coronal thermometry slice was also prescribed 5 mm from the

rib/breast phantom interface in order to assess the adverse heating from rib phantom residing in the far field. Thermometry maps were also calculated in the axial and sagittal plane. Figure 6.22 illustrates the various thermometry slice planes used while monitoring various sonication protocols. The sonication protocols used are shown in Table 6-5.

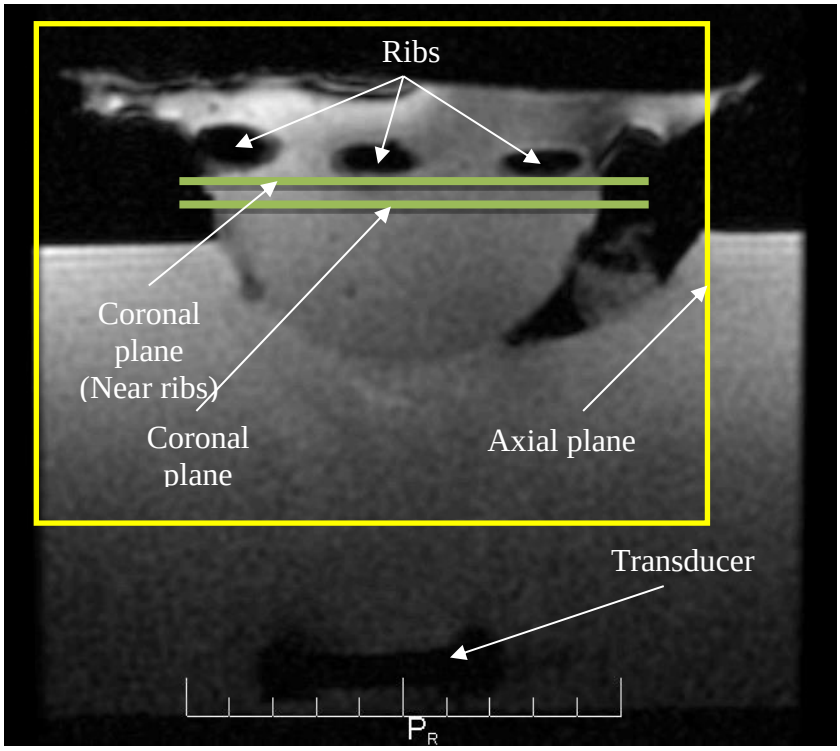

Figure 6.22: Illustration of thermometry slices prescribed in different planes for assessing sonication protocols in composite rib cage/breast phantom.

Table 6-5: Sonication protocols used during functionality tests of the composite breast-rib phantom

No.	Acoustic Power (W)	Sonication Duration (s)	Propagation Direction	Thermometry plane
1	45	60	Bottom to top	Axial
2	45	60	Bottom to top	Coronal (near ribs)
3	45	60	Bottom to top	Coronal (on focus)
4	45	60	Lateral	Axial

The transducer was activated for the first 5 maps (60 s for 12 s/map temporal resolution). All protocols were monitored using PRFS technique and temperature elevations were calculated using the TempMap1 GUI. Total temperature monitoring period lasted for 108 s (9 thermometry maps).

Results

Thermometry maps in the axial plane for a bottom to top sonication and with the rib bone positioned in the far field simulated a very common problem that clinicians face when applying HIFU (Figure 6.23A). Excessive heating well above 100 ºC was observed in some pixels adjacent to rib/breast interface whereas temperature raised in the focal area exceeding 90 ºC. These temperature levels were beyond agar's melting point and possibly the artifacts observed (distribution of signal discontinuities in front of the interface) can be attributed to this effect. Once the transducer was rotated in the theta axis, a lateral sonication using the same power and duration (45 W - 60 s) the maximum temperature elevation decreased dramatically down to 32.5 ºC (Figure 6.23B). The presence of an acoustically reflective and absorptive material like the bone phantom in the line of propagation perturbed the distribution and magnitude of temperatures in the thermometry plane. It was speculated that thermometry in the beam's long axis was not precise since slice thickness (10 mm) was large compared to focal width (3.48 mm) and temperature measurements suffered from partial volume averaging.

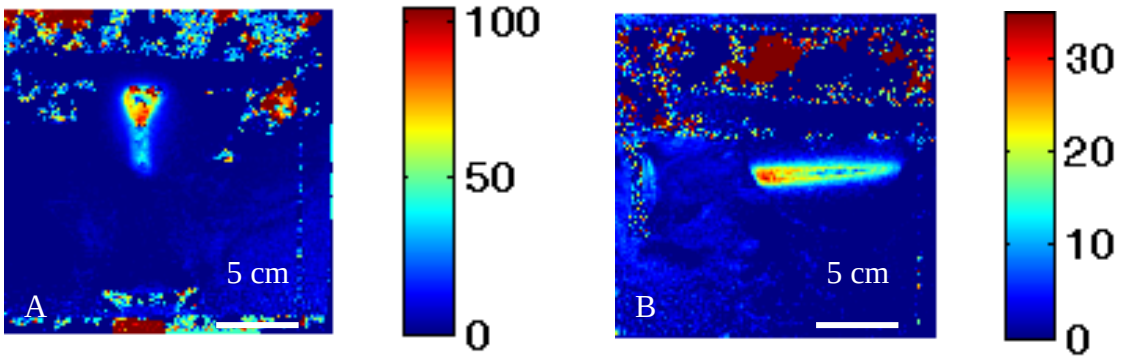

Figure 6.23: Typical axial thermal maps at T_{max} for (A) 45 W-60 s sonication for a bottom to top approach and with the rib bone phantom residing in the far field and (B) 45W-60s sonication for a lateral approach while avoiding the rib bone in the far field.

Coronal thermal maps were prescribed in a plane perpendicular to the beam's propagating direction were expected to produce more realistic temperatures. Voxels of the slice were filled with spins that their *PRF* has shifted by approximately the same degree as a result of temperature increment. Thermal maps acquired 5 mm in front of the rib phantom demonstrated a maximum temperature elevation equal to 60.3 ºC (Figure 6.24A). The estimated error in temperature measurements based on *SNR* measurements was calculated to be 0.7 ºC. The equivalent measurement for the thermal at a distance from the transducer equal to its focal length was 63.4 ºC with an estimated temperature

error equal to 0.8 ºC (Figure 6.24B). The high temperature developed distally to the focus and near the ribs was attributed to the combined effect of the acoustic focus length dimension, which according to manufacturer datasheet the focus -6 dB contour was 58.25 mm and strong reflections at the rib/breast interface. This effect was demonstrated by Nell *et al* [224], where their experiments using bone phantoms showed that at sufficiently high acoustic power, reflection of the HIFU beam from bone introduced temperature fluctuations as much as +/-15 %.

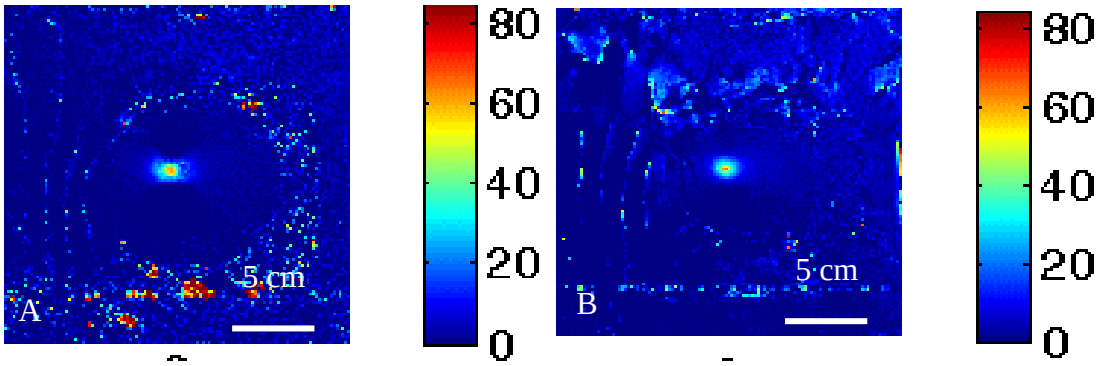

Figure 6.24: Typical coronal thermal maps at T_{max} for A) 45 W-60 s sonication for a bottom to top approach and the thermometry slice prescribed 5 mm in front of the rib phantom and (B) 45 W-60 s sonication for a bottom to top approach and the thermometry slice prescribed at the focus.

Cooling in the focal plane took place in a faster rate due to the steep temperature gradient with the surroundings reaching 24.4 ºC at 48 s after the transducer was deactivated. The decay of maximum temperature during the cooling phase near ribs for the same time post sonication was 33.2 ºC indicating a slower cooling rate. A possible explanation for the slower heat dissipation rate was that this plane was at the proximity of the heat conducting bone phantom.

Conclusions

The functionality of this phantom was evaluated initially with a protocol applied using a bottom to top penetration and later using a lateral approach that avoided rib heating. The proposed phantom involved a model with the target (tissue mimicking breast phantom) intervening between the transducer and the ribs. It was shown using MRI thermometry, that when the ribs were exposed to the focused ultrasound beam (far-field), excessive heating was created. When the ribs were avoided, the estimated temperature using the same exposure was much lower, indicating that lateral ablation has clear benefits in breast ablation.

Planning of thermometry slices played an important role in the accuracy of thermometry results. Although one would expect the same maximum temperature shifts for the same power and different slice orientations, it was concluded observed that this was not strictly true. Slices along the long axis of the beam are prone to positioning and partial volume errors. The presence of other materials near the isocentre (positioning device motors, transducer) can give rise to a field inhomogeneity associated with phase errors. These errors present a directional predominance depending on the spatial distribution of such materials in the vicinity of the static magnetic field. Another speculation was that in areas of high magnetic susceptibility difference like the rib/breast phantom interface, the field was distorted resulting in local phase errors when using sequences of the GRE family.

The proposed phantom combined into a single phantom both breast tissue equivalent (agar/silica/evaporated milk) and bone equivalent (ABS plastic). The main acoustic parameter contributing to energy loss during FUS exposure (attenuation) was carefully adjusted in the replicated soft tissue phantom to match the values found in humans. The cost of manufacturing the proposed phantom was low and therefore it can be easily offered to users in order to evaluate the performance of FUS protocols, new hardware, new adaptive focusing and beam steering algorithms. Since the proposed phantom was designed based on information extracted from human CT images, the dimensions involved in the phantom were considered realistic.

6.7 Summary

The agar-based soft tissue mimicking phantoms were assessed for their thermal repeatability and attenuation capability at different depths. Functionality tests of the developed tissue mimicking composite phantoms were performed using MR thermometry. This involved observing the spatial distribution of temperature elevations induced by a single element focused ultrasound transducer operating at 1 MHz across the thermometry slice. The destructive interaction of the skull phantom with ultrasound resulting in the absence of a thermal focus, the high efficiency of the femur bone phantom in absorbing acoustic energy and the strong reflections from ribcage residing in the far field during breast tissue ablative sonications were demonstrated. These results were similar to treatment safety and efficiency related observations made in relevant preclinical studies and prove the usefulness of these phantoms in replacing animal models for testing focused ultrasound thermal applications.

7 Functionality and MR compatibility assessment of a robotic device designed for HIFU thermal bone treatments.

7.1 Introduction

The purpose of this study was to test the functionality of a new robotic device developed and assess its MR compatibility. Using three linear and one angular stage, the positioning device navigates the transducer to easily access any target. The advantage of using the proposed system over conformal bone systems is that the focus is steered mechanically instead of electronically making it less complex, affordable and compact.

Transcranial HIFU applications make the use of a phased array mandatory to overcome skull induced aberrations. In applications where only transmission through soft tissue is involved, treatment using a single element transducer is feasible. The possibility of using single-element transducer HIFU systems was supported by results of the bone/muscle and rib/breast phantoms. Functionality tests showed sufficient heat at the targeted site. The developed device was used in synergy with the rib-breast phantom to demonstrate the effect of avoiding the ribs in the far field through lateral sonications.

7.2 Short description of the system

The aforementioned device was a continuation of several other technologies designed for various applications by our group. Knowledge and experience was gained during the development and design of its predecessors like the brain ablation prototype by Mylonas *et al* [221], the first [225] and upgraded [226] version of the endorectal MRgFUS prostate ablation system by Yiallouras *et al* and the recent endovaginal treatment system by Epaminonda *et al* [227]. The proposed system was produced with four directional degrees of freedom. These included linear motion in three orthogonal axes (*xyz*) and a rotation around the *z*-axis for acoustic propagations in the *xy* plane.

7.2.1 Mechanical parts

The main body of the robotic system made out of ABS was prototyped using the FDM 400 3D printer (FDM400, Stratasys). The system was equipped with four piezoelectric ultrasonic motors (USR60-S3N, Shinsei Kogyo Corp.) for driving the HIFU transducer linearly in one of the three orthogonal axes and for angular rotation. The device has maximum dimensions (height: 25 cm, length: 38 cm and width: 22.5 cm) and can easily be used without space restrictions inside the cylindrical bore of any conventional

high-field MRI system. The range of motion of the robotic system was set to *x*: 8 cm, *y*: 8 cm, *z*: 8 cm and to an azimuthal angle (θ) in *xy* plane spanning between 0 and 180 degrees in a clockwise rotation. The total weight of the device was approximately 2 kg. Figure 7.1 illustrates the setup of the positioning device for a top to bottom bone treatment.

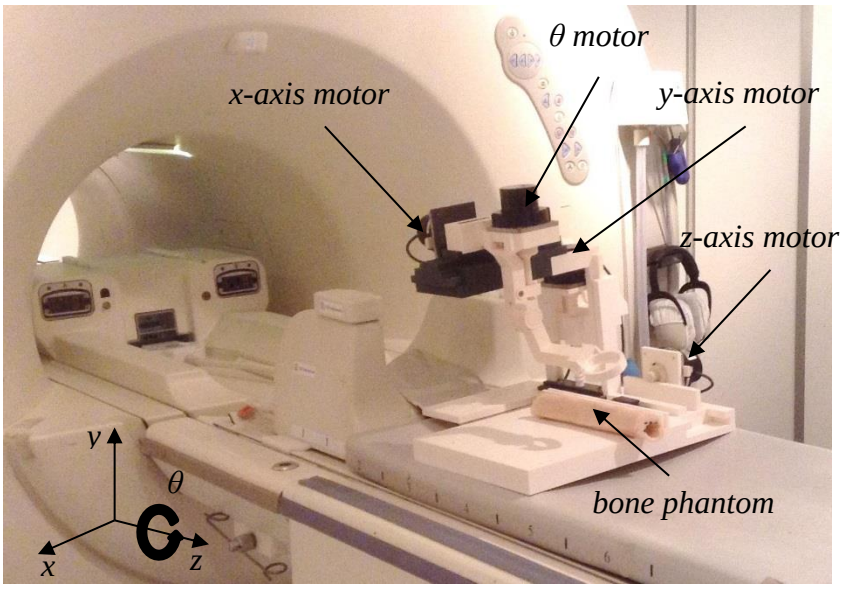

Figure 7.1: Setup of HIFU bone treatment positioning device on the MRI table with notations pointing the PUM motors that control motion in the xyz axes and theta (θ) rotation..

7.2.2 Device control interface.

The device was controlled via a custom made user-friendly interface developed in C#. Motion in the four directions was controlled by the software in user-defined steps or in grid sequence patterns. Drivers for controlling the PUM motors and powered by a 24 V- 2 A DC supply, were controlled via a USB 6251 data acquisition (DAQ) interface card (National instruments) that included timing and digital output modules. Control and monitoring of secondary functions was also available via the interface.

7.2.3 Motion encoding and angular axis.

Optical encoders (EM1, US Digital Corporation, Vancouver, WA, USA) installed on the stationary parts of the device's body returned back to the interface a digital feedback of the device's displacement. The displacement was encoded by installing reflective linear strips on sliding racks which were displaced by each of the *xyz* PUM motors. Rotation of the angular axis was controlled by an optical encoder monitoring a

linear strip wrapped around a coupling frame between the PUM motor and the upper section of an axle. The lower end of the axle was equipped with threads which were coupled with a gear responsible for rotating the transducer's arm. A CAD of the angular axis is shown in Figure 7.2.

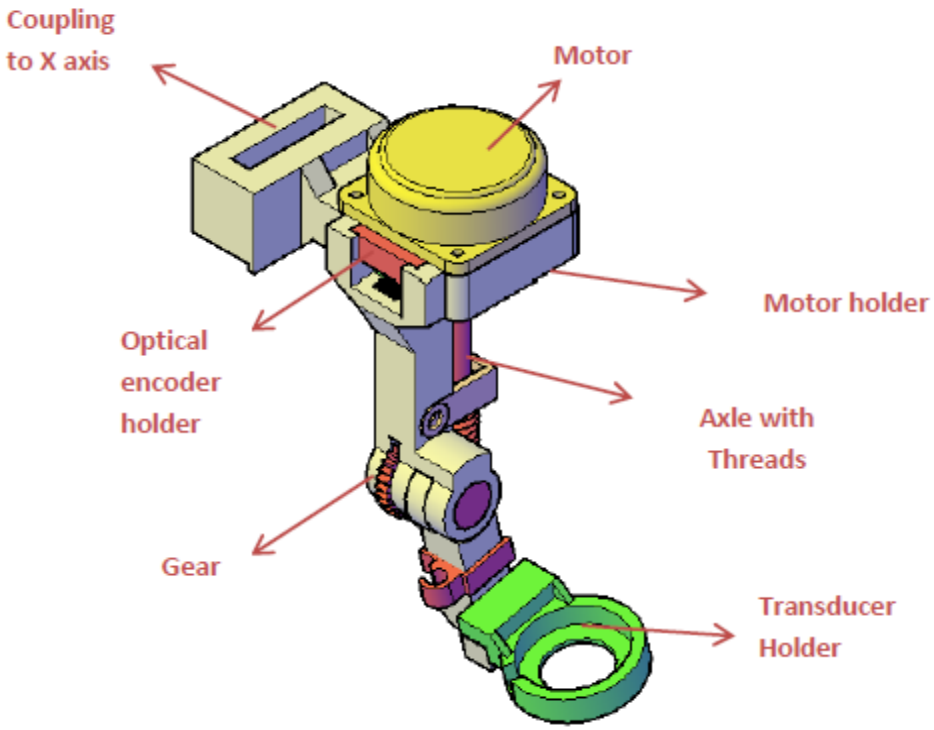

Figure 7.2: CAD drawing of the angular axis complete assembly.

7.2.4 HIFU system used for conducting the functionality tests.

The HIFU system consists of a signal generator (Agilent technologies), an RF amplifier (AR), and a spherical transducer made from piezoelectric ceramic (Etalon, Lebanon, IN, USA). The spherically focused transducer operates at 1 MHz, with a focal length of 10 cm and a diameter of 3 cm.

7.2.5 Functionality test of the newly developed angular axis.

The functionality of the robotic device was evaluated by creating discrete and overlapping thermal lesions using HIFU in gel phantoms (ONDA Corporation) using the newly developed angular axis, that did not exist in any of the previous robotic systems developed by our group. The gel by ONDA Corporation under evaluation was placed in a degassed water tank. The transducer was attached to the arm of the positioning device and was immersed in the water tank to establish adequate acoustic coupling between the gel and transducer. During the first set of sonications two thermal lesions were created 2

cm deep inside the gel phantom by rotating 20 º the arm holding the transducer. The ultrasound intensity used was 1500 W/cm^2 (spatial average *in situ*) for 60 s. The second set of sonications produced overlapping thermal lesions using 9 steps of 5 º. The intensity used was 1500 W/cm2 (spatial average in situ) for 60 s. Figure 7.3 demonstrates the formed thermal lesions for the 20 º and 5 º angular steps.

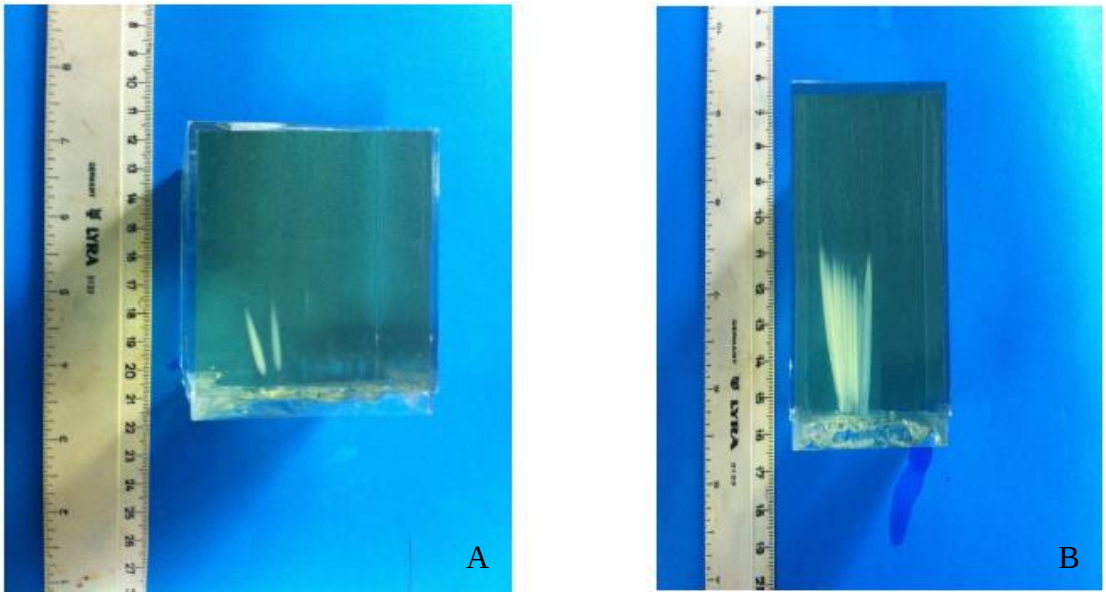

Figure 7.3: A)Two thermal lesions in the gel phantom created by moving the angular axis of the robotic system using a discrete step of 20º and B) Overlapping thermal lesions created in the gel phantom by moving the angular axis of the robotic system using 9 steps of 5 º.

7.3 MR compatibility assessment of the robotic device.

The American Society of Testing and Materials (ASTM) standard F2503-05 [228], indicates the conditions for which it has been determined that a medical device or other item may be safely placed and used in the MR environment. HIFU positioning devices are no exemption and they must be tested prior to using them with humans. The standard makes the distinction between “MR safe” and “MR conditional” devices. “MR safe” corresponds to a device which poses no hazard to the patient when used in the MR environment but without guaranteeing of image quality degradation and loss of diagnostic information. The “MR conditional” classification is usually assigned to a device that poses no known hazards in the MR environment but with specified conditions of use.

The MR compatibility of the positioning device in terms of induced image artefacts and signal degradation in the vicinity of the piezoelectric motors, transducers and encoders was assessed. The robotic HIFU system was tested in a 1.5 T MR system

(General Electric) using the abdominal imaging coil (USA instruments, Cleveland, OH, USA). The DQA phantom ($NiCl_2$-H_2O, GE-Dielectric Corporation, Menomonee Falls, WI, USA) was used to measure the *SNR* was under various conditions (Motor/encoder activation, and transducer activation). A *FSPGR* pulse sequence was used to assess the *SNR* (TR: 32 ms, TE: 4.4 ms, FOV: 30 cm, matrix size: 128×128, flip angle: 30 º, rBW: 15 kHz and NEX: 1). Being a fast gradient echo sequence *FSPGR* was considered particularly sensitive in any external interferences that could perturb the homogeneity of the static field and the linearity of the encoding gradients.

The *SNR* of the DQA liquid phantom was calculated for different states (ON, OFF) for each of the robotic system's component that required electricity for activation (piezoelectric motor, optical encoder and transducer). The results are presented as a percentage of the maximum SNR in
Figure *7.4*.

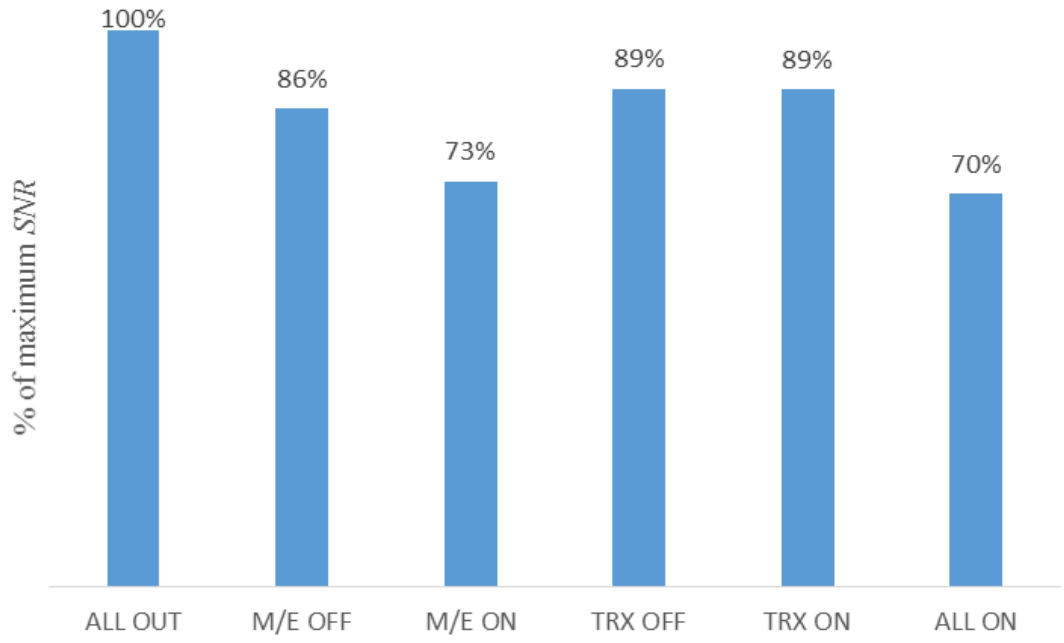

Figure 7.4: SNR calculations of the DQA phantom magnitude image for different scenarios: (ALL OUT) all the components removed from the bore, motor/ encoder (M/E OFF) added to the system and deactivated, motor/ encoder (M/E ON) added to the system and activated, transducer (TRX OFF) added to the system and deactivated, transducer (TRX ON) added to the system and activated, (ALL ON) all components added and activated.

The piezoelectric motor and optical encoder of the angular axis were the two most proximal components to the imaging plane. The motor/encoder pair was activated and

deactivated simultaneously. As expected the maximum *SNR* was measured when all the components were removed from the bore of the magnet. There was some decrease in the *SNR* in the presence of the motor/encoder pair. Although these components did not contain metallic materials possibly the presence of solder contributed in to signal degradation by distorting the homogeneity of the static magnetic field. A further decrease in *SNR* was observed when the motor/encoder were activated. The motor was powered by a DC current which itself induced a secondary magnetic field around the power carrying wire that interacted with the MRI static field. The presence of the transducer also caused an *SNR* drop but smaller compared to the motor/encoder pair. No measureable change in the *SNR* was observed after the transducer was activated. The transducer was powered by an AC current which induced an alternating magnetic field. Possibly the nature and magnitude of the alternating magnetic field was inadequate to produce any measurable *SNR* drop. When all the component were activated the cumulative effect was to decrease the *SNR* to its minimum. The *SNR* drop in the worst case scenario was approximately 30%. No severe image geometric distortion or signal inhomogeneity was observed when all components were present and activated.

By comparing the phantom's magnitude images for the best and worst case scenario it was easy to visually observe the drop in the SNR in the vicinity of all activated components inside the bore of the magnet (Figure 7.5).

Figure 7.5: Magnitude image of the DQA phantom using the MRI sequence FSPGR when the motor/encoder and transducer were deactivated, and B) Corresponding image when the motor/encoder and transducer were all activated.

A "zipper" artifact appearing as a dashed line extending perpendicular to the frequency's encoding direction was observed. The artifact was attributed to RF interference signal produced by the motors, encoders and transducer. Additionally unshielded transmitting wires were possible carriers of the interfering signal, which was picked by the receiver chain of the imaging sub-systems.

7.4 Summary

The work described in this chapter demonstrated the functionality test for the updated version of a HIFU positioning device that is capable of performing sonications at different angles of incidence in the subject. The formation of the thermal lesions inside the ONDA gel indicating the line of propagation of the focused field was an index for the beam's angle of incidence. Angular steps of the device for wide and narrow angle were completed successfully. This was a confirmation that this device can avoid obstructing structures like bone and air. The mechanically steered system offers a cheaper and less complex solution compared to other system that employ a phased array. A mechanically steered device that employs a single element transducer can be used for any soft tissue applications that do not require adaptive focusing.

The conditional testing was completed in a 1.5 T MRI system operating at standard operating conditions and the *SNR* measurements indicated a 30% loss when all current carrying components were activated with no severe image quality degradation. RF interference can be isolated in the future by shielding and low pass filtering all components.

8 Discussion and Future Work

8.1 Discussion

The aim of the thesis was to design and develop MR compatible phantoms for research in the area of focused ultrasound. The basic prerequisites set at the beginning of the project was to use materials that mimic at least the attenuation coefficient and the geometry of the replicated tissue and to be MR compatible. The approach was to create a set of composite phantoms representing human anatomies that combined soft and bone tissue mimicking parts. Upon following relevant literature, it was evident that safety and efficacy studies of HIFU applications often report adverse effects when a bone tissue is within the acoustic field. Additionally the efficacy of HIFU applications targeting a soft tissue lesion are often limited when the acoustic beam transmits through a bone.

Bone tissue was mimicked using ABS. ABS seemed to be a possible bone mimicking candidate, since it is a popular thermoplastic polymer used in rapid prototyping machines for producing true size 3D models. Testing ABS as a bone replica was attractive since it combined strength and rigidity with good chemical resistance and dimensional stability which were essential for building a long lasting and inert phantom. Being a plastic it was expected to have a very low magnetic permeability, thus making it ideal for safe use inside the MRI environment while inducing minimum susceptibility image artefacts. Using a set of 3.5 MHz planar transducers and samples of ABS, the polymer's acoustic properties were characterized using pulse echo and transmission through techniques. The attenuation coefficient of ABS was extrapolated from 3.5 MHz at 1 MHz in dB/cm assuming a linear dependence with frequency. The derived coefficient of 16.01 ± 6.18 dB/cm at 1 MHz was within the broad range of the reported values found in literature for multi-layered bones (diploe) [173], [229], [230]. The result was in agreement even for studies that reported BUA of cortical bone[231], [232] separately from trabecular bone layers[231], [233], [234], spanned over orders of magnitude due to great biological variability. Trabecular bone has a higher BUA due to increasing contribution of scatter from trabeculae especially in high frequencies. Attenuation in cortical bone is primarily a result of acoustic absorption with values in the lower end of the range. The large error in ABS attenuation measurement was due to significant signal drop. The small transmitting signal's amplitude approached the minimum Volts per division setting on the oscilloscope which induced high uncertainty on the reading. The speed of sound in the ABS specimen was estimated at 2048 ± 79 m/s which was in the

low end of the range of values found in literature [16], [17]. The combination of the measured speed of sound in ABS with its low mass density (1.04 g/cm^3) given by the manufacturer (Stratasys) produced an acoustic impedance equal to 2.14 MRayls. Comparing with values reported for the acoustic impedance of human bones (3.75-7.38 MRayls) by Goss et al [16], it was deduced that the ABS phantom would reflect ultrasound less than most human bones. Using a dedicated software bone models were created by segmenting bony tissue from medical CT images. The dimensional accuracy of the segmented 3D model was dependent on the user defined mask. The bone mask was relatively easy to define manually by observing CT images with appropriate windowing. Bone is a dense tissue which appears as hyper intense signal in grayscale images with high contrast relative to background tissue.

The suitability of agar based gel phantoms was investigated for creating the soft tissue phantom parts. The novel approach for building these agar based phantoms was the introduction of both absorption and scatter agents. Phantoms presented in literature have used different concentrations of either scattering agents or absorption agents to control and match the attenuation coefficient of the replicated tissue. This was considered an important difference compared with our approach since the main purpose of an acoustically tissue mimicking phantom is to reproduce the whole spectrum of acoustic interactions as realistically as possible. A phantom doped only with a scattering agent will result in significant loss of acoustic energy along the beam's path between the transducer and the focus. Scattering events that redistribute acoustic energy out of the plane of propagation will result in a lower heating rate and lower apparent absorption in the focal plane compared to real tissue. Similarly a phantom doped only with an absorbing agent will convert acoustic energy more efficiently to heat and therefore exaggerate the heating rate at focal plane compared to a real tissue with the same total attenuation coefficient.

Silica dioxide in powdered form with particle size ranging between 0.5 -10 μm was used as a scattering agent whereas absorption was controlled with the addition of evaporated milk. The attenuation coefficient of agar based gels (2 % w/v) was assessed for different concentrations of either silica or evaporated milk once again using the pulse echo immersion technique. Although data in literature reporting the relative contributions of scatter and absorption to attenuation for different tissue types are rare, it was made possible to extract typical values for brain and muscle tissue. These data were used to linearly combine the required agents' concentrations to achieve the desired relative contributions of scatter and absorption to total attenuation coefficient for mimicking the brain and muscle tissue. The finalised gel samples for brain (2 % w/v agar, 1.2 % w/v

silica dioxide, 25 % evaporated milk) and muscle (2 % w/v agar, 2 % w/v silica dioxide, 40 % evaporated milk) were characterized for speed of sound, mass density , acoustic impedance, thermal conductivity and diffusivity.

The choice of the agar as a gelling agent was due to its preservation of structural integrity up to 85 ºC, which covers HIFU applications requiring ablative temperature levels. Additionally agar is not toxic unlike similar studies that used polyacrylamide which is a known neurotoxin that can be passed to human by either oral or even inhalation exposure. Preparation of agar gels does not require specialised equipment and duration of the whole process does not last more than 2 hours. The low cost of preparation that did not exceed €1 per 100 ml was the main reason for not adding preservatives to the gels. Fresh gels were made for every experiment and were refrigerated for up to one week after which they were disposed. The most important disadvantages of agar gels were the opaque texture and brittleness upon exertion of strain or stress. The opaqueness of the gels was not a real problem since the phantoms were designed for monitoring HIFU thermal exposures with MRI.

Three composite phantoms were fabricated following the selection of the candidate mimicking materials for bone and soft tissue. First a head phantom which was composed from an ABS skull part with an agar based brain mimicking gel moulded inside it. The second phantom was a partial ABS model of a femur bone embedded in a cylindrically shaped agar based muscle mimicking gel and the third one was a unilateral composite ABS ribs-breast phantom. A simplified approach was used for building the breast phantom which was mimicked using the muscle recipe. In reality the average breast of an adult female consists mainly from layers of adipose tissue (fat), dense fibro-glandular tissue and pectoral muscle which variability in their acoustic properties. On the other hand the acoustic properties of brain and muscle tissue are usually reported in literature as a homogeneous media.

All phantoms were tested for their functionality under MRI monitoring. Conventional MRI monitoring in HIFU thermal treatments involves the implementation of MR thermometry techniques in order to non-invasively assess in quasi real time the evolution of the temperature distribution across the treatment envelope. The functionality of the composite head phantom was assessed in a transcranial treatment configuration where an extracorporeal 1.1 MHz single element HIFU transducer targeting a region inside the brain phantom. Sonications were conducted with and without intact skull while temperature was monitored using an implanted thermistor probe in different positions of the focal plane. The results of this study demonstrated inadequate focal heating due to

complete defocussing of the beam when the skull phantom intervened with excessive temperature increment near brain surface. Similar qualitative results were drawn when the head phantom was monitored with a SPGR T_{1w} weighted pulse sequence.

A custom made GUI designed in Matlab for employing *PRFS* thermometry was developed, since the MRI system used was not equipped with integrated thermometry capabilities. *PRFS* Thermometry is up to date the only temperature monitoring technique employed in commercial systems since the precession frequency shifts linearly for a range of temperatures that covers HIFU hyperthermia and ablation applications. Another advantage is that the *PRFS* sensitivity coefficient measured in ppm/ºC is independent of tissue type. The GUI retrieved complex image data from the MRI, calculated the phase wrapped images and applied on the fly a non-continuous pathway unwrapping algorithm based on pixel reliability. The advantage of using this algorithm was that noise in the image was unwrapped last and therefore phase unwrapping errors did not propagate across the final image. Internal and external references in the form of tubes filled with oil and surrounding the phantoms were used to correct for an intermittent phase background offset. The unwrapped reference and post treatment images were combined to calculate their complex difference image. The final temperature elevation map was calculated by applying the *PRFS* equation pixel by pixel on the complex difference image. The thermal repeatability of the soft tissue phantoms was assessed with the TempMap1 GUI by calculating the coefficient of variation in temperature readings recorder at different locations of the phantom. Temperature readings for the same sonication protocol and setup were independent of phantom location.

The femur bone/muscle phantom functionality was demonstrated by targeting the focus on the bone/muscle interface. This configuration replicated palliative sonications conducted to ablate the periosteum in patients suffering from bone metastases. The apparent temperatures measured by the TempMap1 GUI in the muscle tissue adjacent to the bone phantom reached ablative temperature even at moderate acoustic power settings. A frequent adverse effect that occurs when a bone resides in the far field was demonstrated during the ribs/breast phantom functionality test. The MR compatible transducer was set for a bottom to top sonication of patient laying in prone position. The rib cage was positioned distally to the focus and high temperatures were developed at the interface. Adverse bone heating was avoided using an MR compatible positioning device that mechanically steered the transducer for lateral sonication. The temperature level developed inside the breast phantom was significantly lower for the same power setting. Maximum temperature elevation was confined within the focal region. The positioning

device was assessed for its functionality and MR compatibility and showed that it could be a possible replacement at a lower cost and complexity compared to the phased array transducer systems for applications that no adaptive focusing is required.

8.2 Future work

This following section describes a series of improvements or additions to the existing work that upon completion are expected to improve the performance of the designed phantoms.

An important limitation of this study was the complete absence of perfusion in the designed tissue mimicking phantoms. Highly perfused tissues might be more resistant to thermal ablation than poorly perfused areas owing to the heat-sink effect of their blood supply [235]. Early studies indicated that for short pulse lengths (less than or equal to 2 s) and small focal diameters (approximately 3 mm) produced temperature elevation and thermal dose which was nearly perfusion independent [236]. Nevertheless the majority of clinical applications would exceed this time threshold and therefore perfusion needs to be simulated in a tissue mimicking phantom designed for assessing reliably HIFU thermal applications. A possible improvement would be to introduce vessels in the agar-based phantoms. Water sustained at body temperature (36 ºC) pumped by a peristaltic pump to simulate blood flow in a wall-less vessel around the targeted lesion to approximate isotropic perfusion. This would be particularly useful for the brain phantom which represents one of the most highly perfused human organs.

Breasts consist of adipose, glandular and muscle tissue that all possess slightly different acoustic properties. Fabricating a breast tissue phantom in a multilayer format with agar-based gels of different attenuation coefficient according to the replicated tissue layer would be more realistic than the homogeneous phantom built during this project.

Regions of enhanced contrast can be added to the phantom in order to test the spatial accuracy of the HIFU treatment. Gadolinium and agar are T_1 and T_2 relaxation time modifiers and can be used to create targets that differentiate from the background in T_1 and T_2 weighted images respectively. These images can be fused with the thermometry maps to quantify the displacement of the thermal focus relative to the target.

Many studies in literature use physical phantoms to compare with numerical models. The nonlinear parabolic Khokhlov-Zabolotskaya-Kuznetsov equation which accounts for nonlinearity, diffraction, and absorption has been applied to calculate the pressure field produced by HIFU source in a medium [237]. The Pennes Bioheat Equation has also been used in numerical models to predict the temperature distribution across a

perfused medium sonicated by a HIFU source [238]. The implementation of these models requires declaration of certain boundary conditions and characterization of medium specific parameters. The majority of the soft tissue mimicking gels parameters has been characterized (absorption coefficient, speed of sound, mass density, thermal conductivity and diffusivity and specific heat) in this study except the nonlinearity coefficient (*B/A*). This coefficient determines the rate of acoustic energy loss from the fundamental frequency to higher harmonics as a result of nonlinear propagation in high pressure fields. The *B/A* coefficient for both recipes should be measured in order to compensate the accumulation of nonlinear effects along the propagation direction.

A coating of high acoustic impedance like acrylic resin can applied to the surface of ABS bone phantoms to introduce reflections closer to the ones produced in human bone interfaces. A coating of submillimetre thickness is not expected to alter significantly the attenuation characteristic of the bone phantoms.

Appendices

Appendix A

List of Publications.

[1] G. Menikou, T. Dadakova, M. Pavlina, M. Bock, and C. Damianou, "MRI compatible head phantom for ultrasound surgery." Ultrasonics, vol. 57, pp. 144–52, Mar. 2015.

[2] G. Menikou, M. Yiannakou, C. Yiallouras, C. Ioannides, and C. Damianou, "MRI-compatible bone phantom for evaluating ultrasonic thermal exposures." Ultrasonics, vol. 71, pp. 12–9, Sep. 2016.

[3] G. Menikou, C. Yiallouras, M. Yiannakou, and C. Damianou, "MRI-guided focused ultrasound robotic system for the treatment of bone cancer," The International Journal of Medical Robotics and Computer Assisted Surgery., vol.13, no.1, e1753, Mar.2017.

[4] N. Papadopoulos, G. Menikou, M. Yiannakou, C. Yiallouras, K. Ioannides, and C. Damianou, "Evaluation of a small flat rectangular therapeutic ultrasonic transducer intended for intravascular use.," Ultrasonics, vol. 74, pp. 196–203, Oct. 2016.

[5] M. Yiannakou, G. Menikou, C. Yiallouras, and C. Damianou, "MRI-guided coupling for a focused ultrasound system using a top-to-bottom propagation," Journal of Therapeutic Ultrasound., vol. 5, no. 1, p. 6, Dec. 2017.

[6] M. Yiannakou, G. Menikou, C. Yiallouras, C. Ioannides, and C. Damianou, "MRI guided focused ultrasound robotic system for animal experiments," The International Journal of Medical Robotics and Computer Assisted Surgery., e1804, Feb. 2017.

[7] G. Menikou and C. Damianou, "Acoustic and thermal characterization of agar based phantoms used for evaluating focused ultrasound exposures", " Journal of Therapeutic Ultrasound ,.5:14 ,Jun. 2017.

[8] G.Menikou, M.Yiannakou, C. Yiallouras, C. Ioannides and C.Damianou, "MRI-compatible breast/rib phantom for evaluating ultrasonic thermal exposures.,",The International Journal of Medical Robotics and Computer Assisted Surgery., DOI: 10.1002/rcs.1849, published online Jul.2017.

Abstracts in Conferences

[1] Georgios Menikou and Christakis Damianou, "MRI guided Focused Ultrasound Surgery (MRgFUS) skull phantom", *International Society for Therapeutic Ultrasound Conference 2014*.

[2] George Menikou and Christakis Damianou, “Bone phantom for evaluating mri-guided focused ultrasound thermal protocols”, *International Society for Therapeutic Ultrasound Conference 2016*.

Appendix B

Example of pixel reliability index calculation

This example demonstrates the calculation of the reliability index for a central pixel in a 3 x 3 pixel matrix. Second difference is defined as the difference of the first differences*.

3	2	-1
2	3	0
-4	2	1

Horizontal original sequence	2		3		0
1st Difference		-1		3	
2nd Difference (H)			-4		

3	2	-1
2	3	0
-4	2	1

Vertical original sequence	2		3		2
1st Difference		-1		1	
2nd Difference (V)			-2		

3	2	-1
2	3	0
-4	2	1

1st Diagonal original sequence	3		3		1
1st Difference		0		2	
2nd Difference (D_1)			-2		

3	2	-1
2	3	0
-4	2	1

2nd Diagonal original sequence	-1		3		-4
1st Difference		-4		7	
2nd Difference (D_2)			-11		

Resultant Second Difference of central pixel (RSD) = $\sqrt{H^2 + V^2 + {D_1}^2 + {D_2}^2}$ = 12.04

Reliability Index (R) = $\frac{1}{RSD}$ = 0.083

*Note: During first differences calculation a simple unwrapping operation is applied were ±2π jumps are removed.

Appendix C

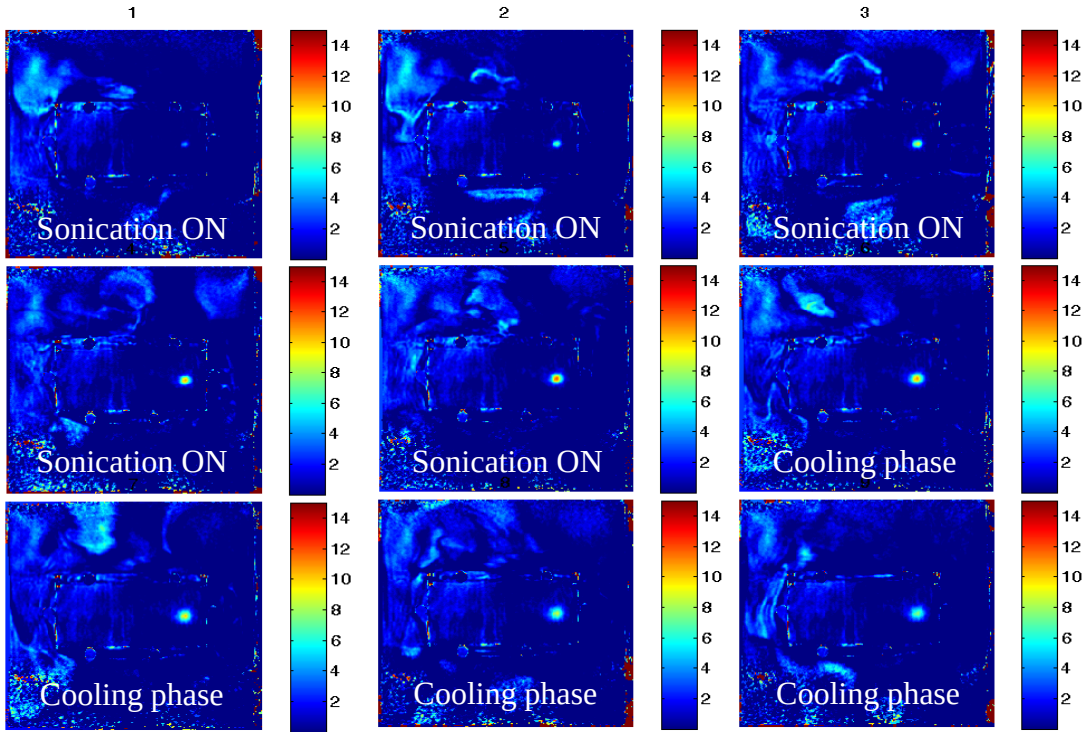

Figure 1: Time series of coronal thermometry maps (1-9) in deep phantom during 25W - 60 s sonication.

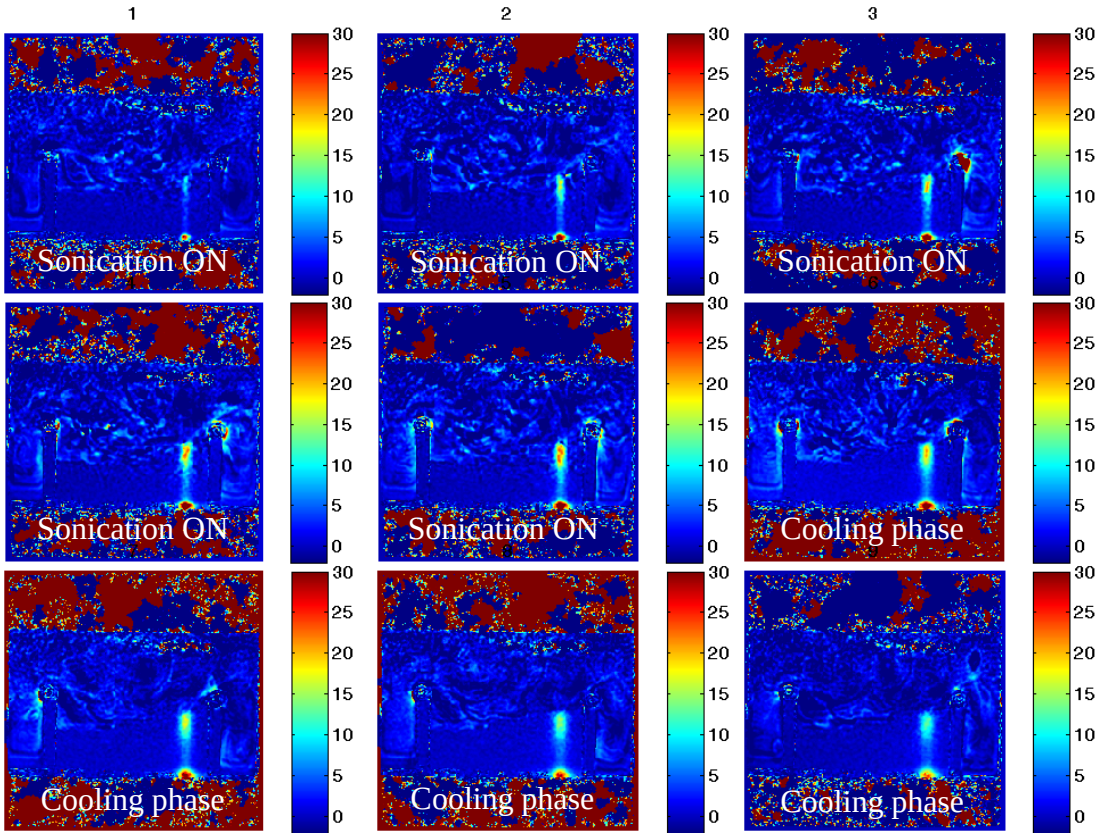

Figure 2: Time series of axial thermometry maps (1-9) in deep phantom during 25W - 60 s sonication.

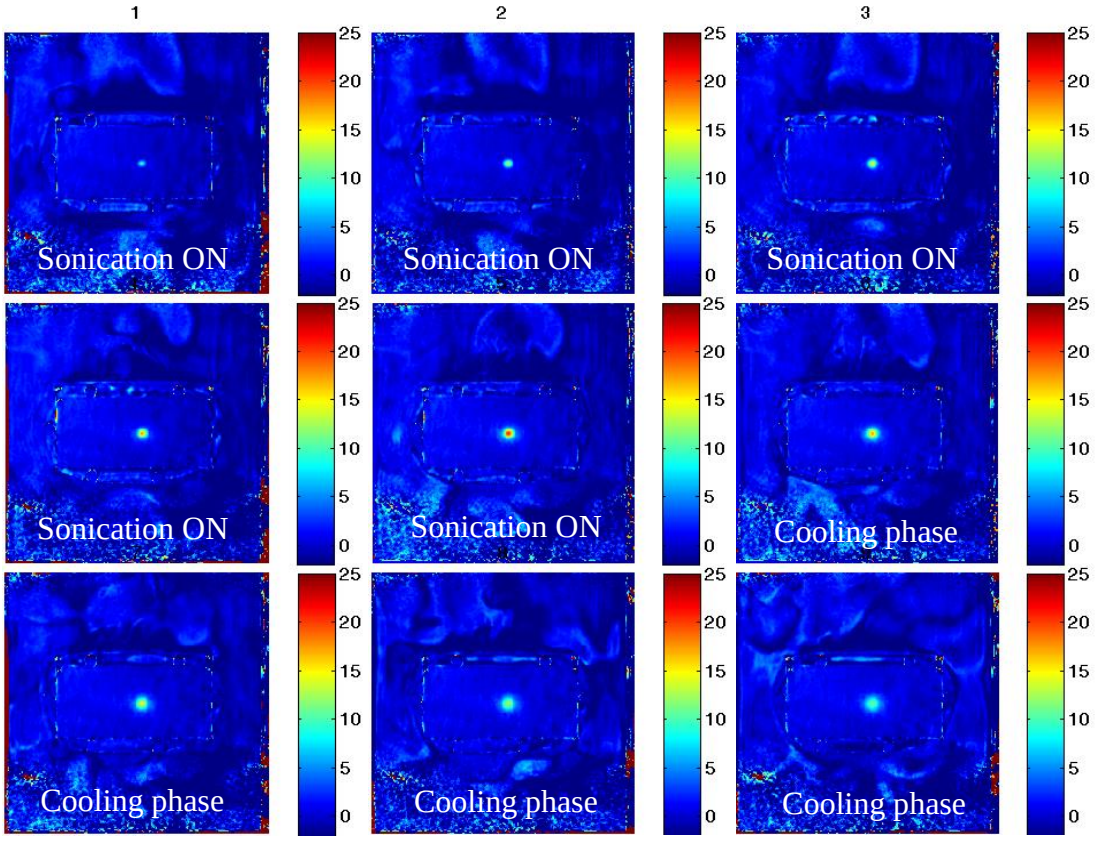

Figure 3: Time series of coronal thermometry maps (1-9) in medium phantom during 25W - 60 s sonication.

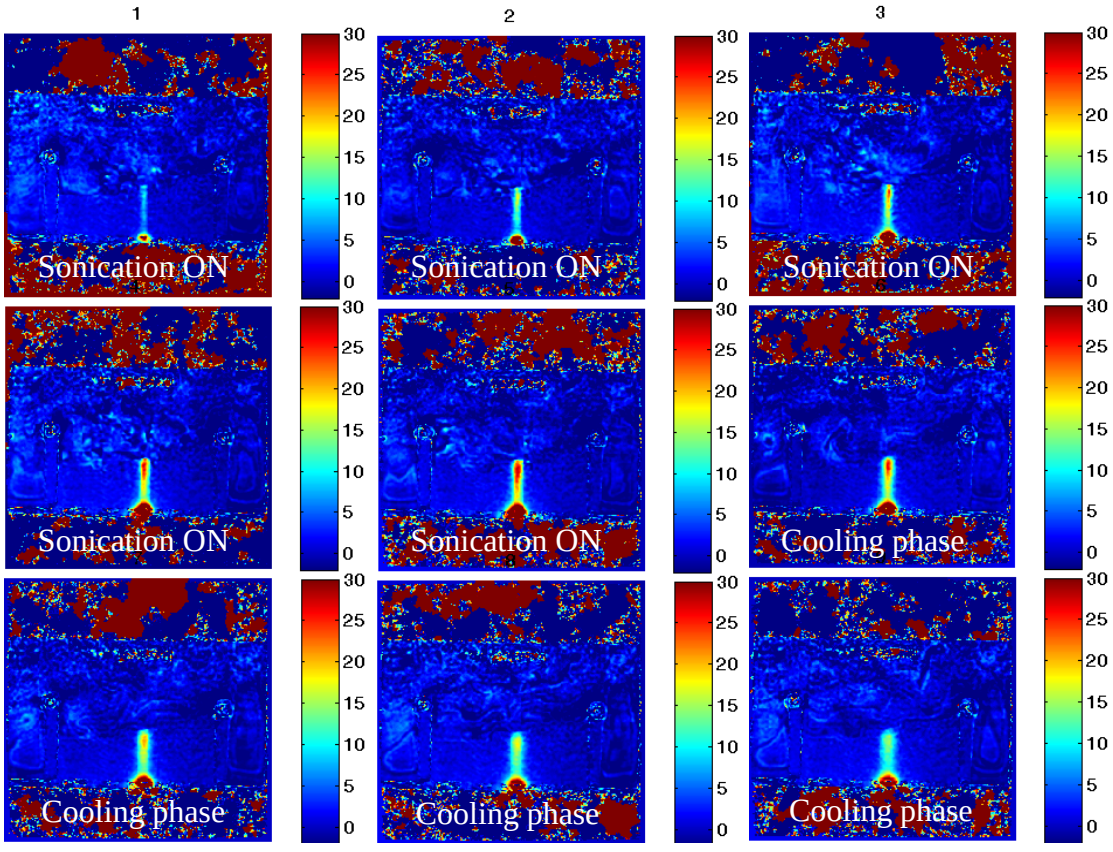

Figure 4: Time series of axial thermometry maps (1-9) in medium phantom during 25W - 60 s sonication.

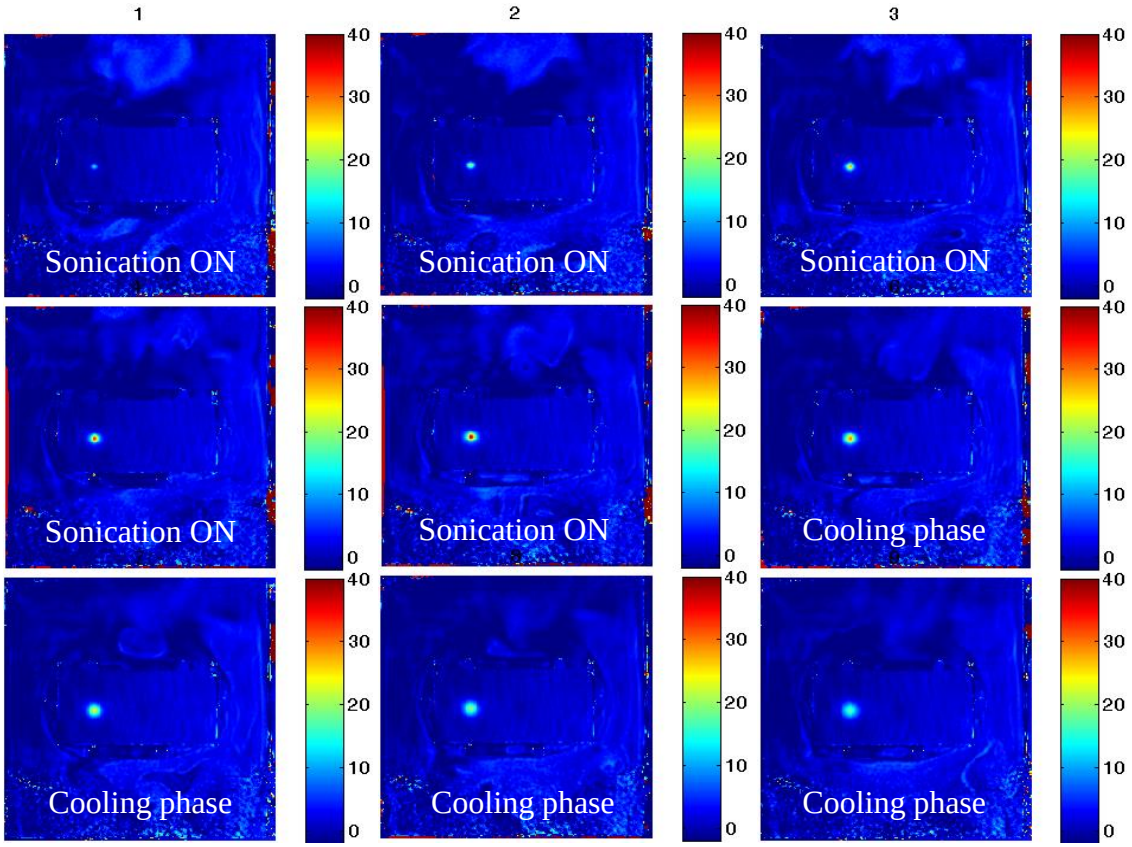

Figure 5: Time series of coronal thermometry maps (1-9) in shallow phantom during 25W - 60 s sonication.

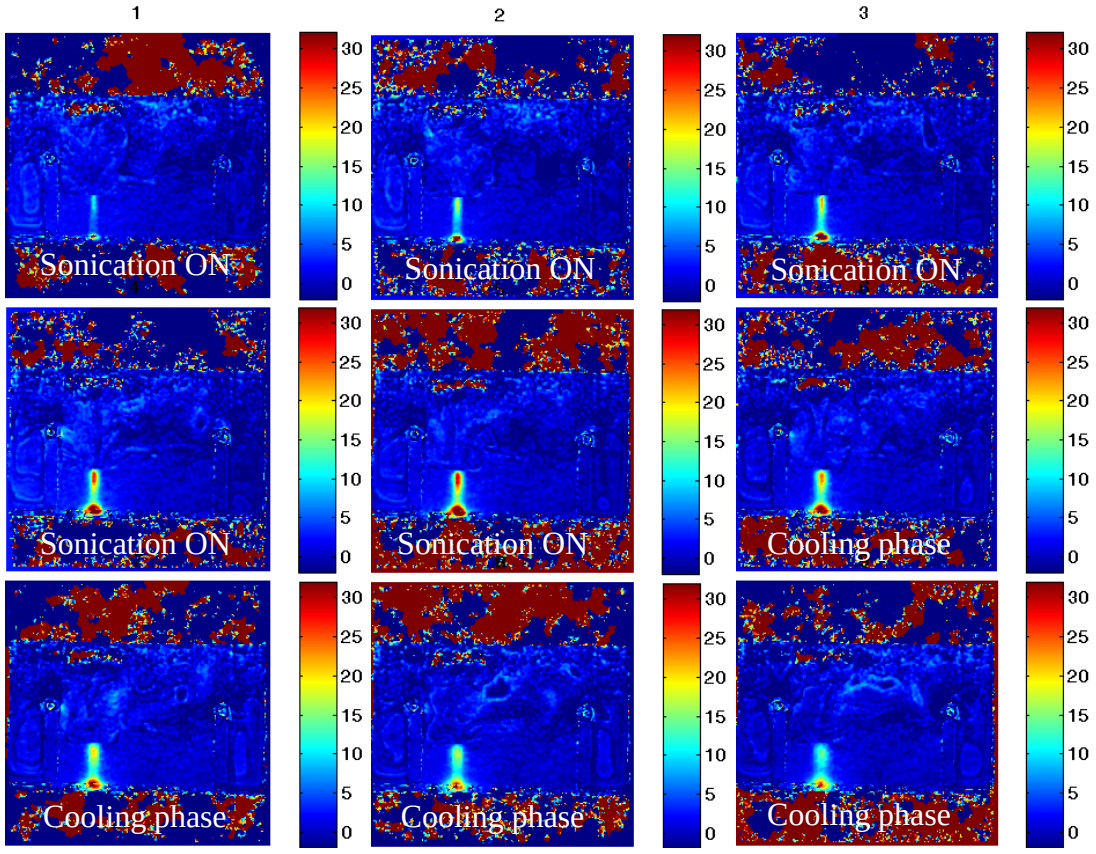

Figure 6: Time series of axial thermometry maps (1-9) in shallow phantom during 25W - 60 s sonication.

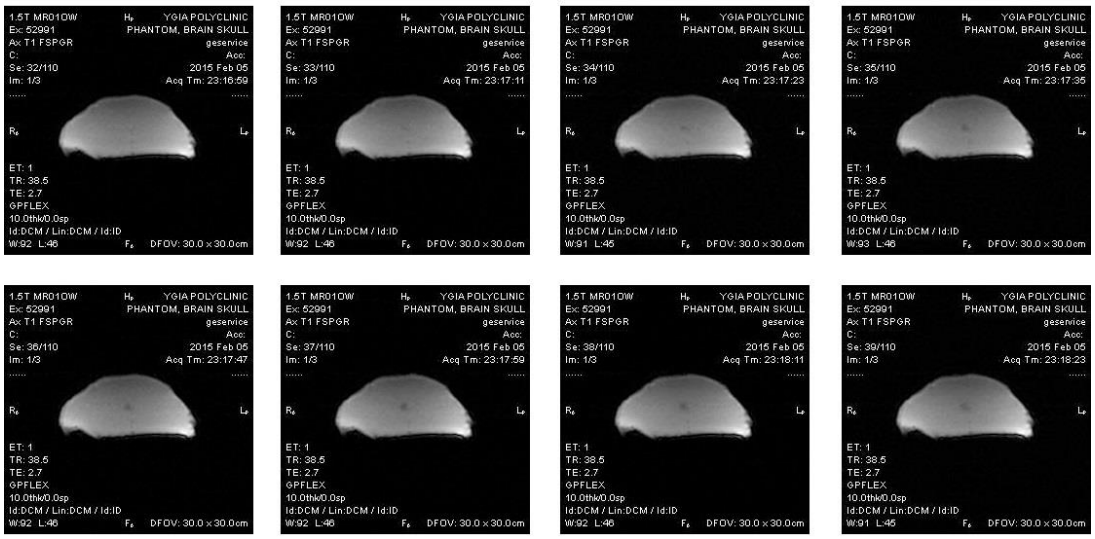

Figure 7: Sagittal T_1w images for 50W-60 s sonication in the absence of plastic skull.

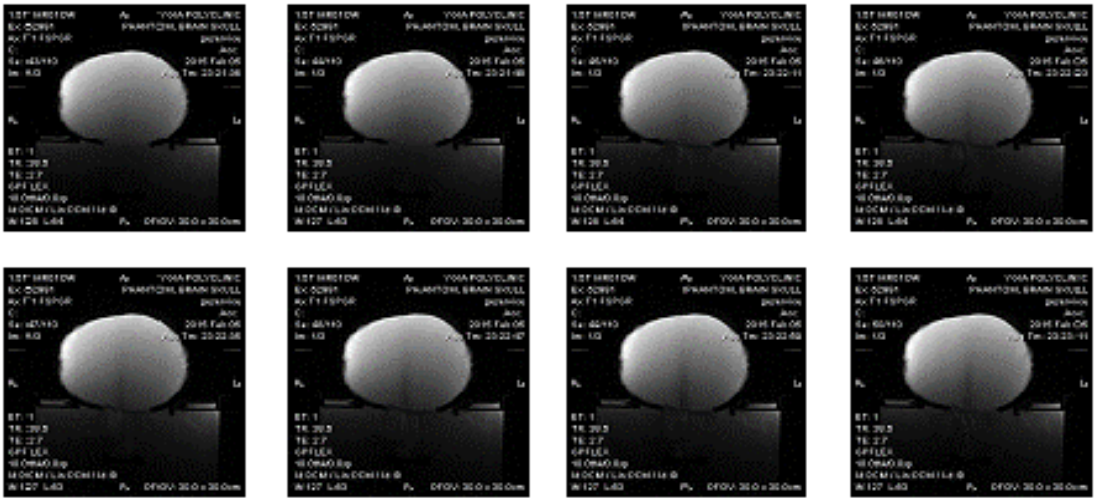

Figure 8: Axial T_1w images for 50 W-60 s sonication in the absence of plastic skull.

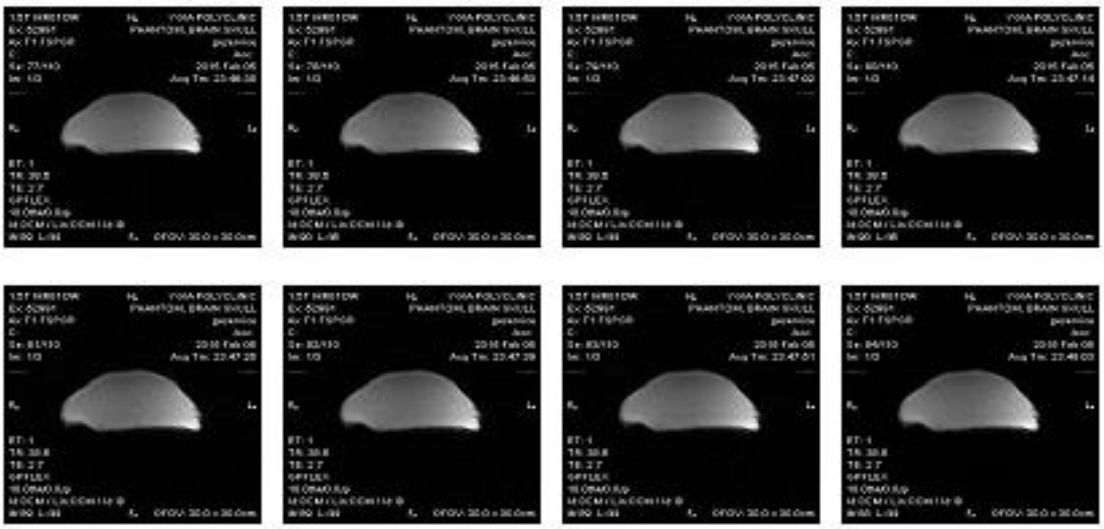

Figure 9: Sagittal T_1w images for 50 W-60 s sonication with intact plastic skull.

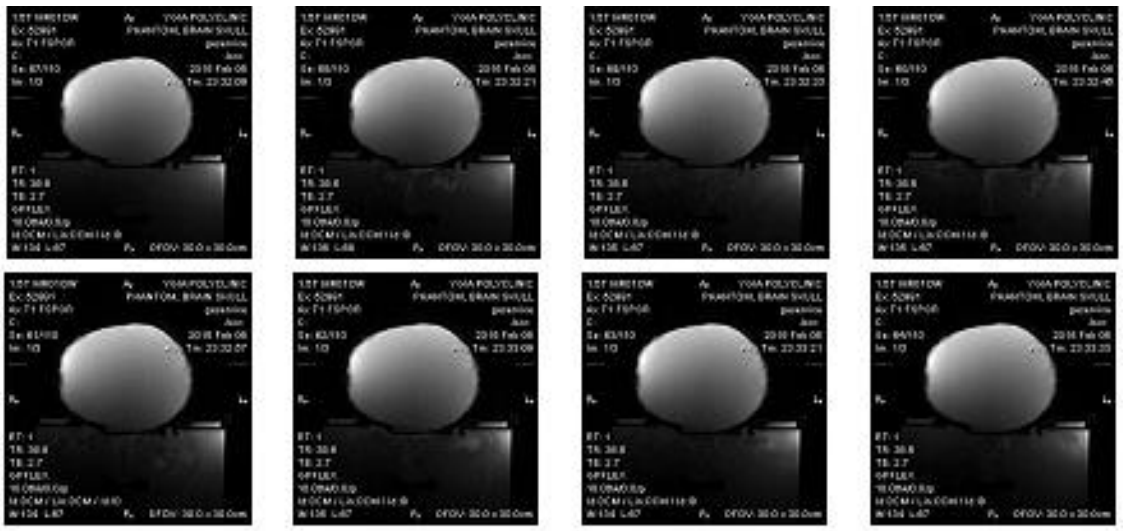

Figure 10: Axial T_1w images for 50 W-60 s sonication with intact plastic skull.

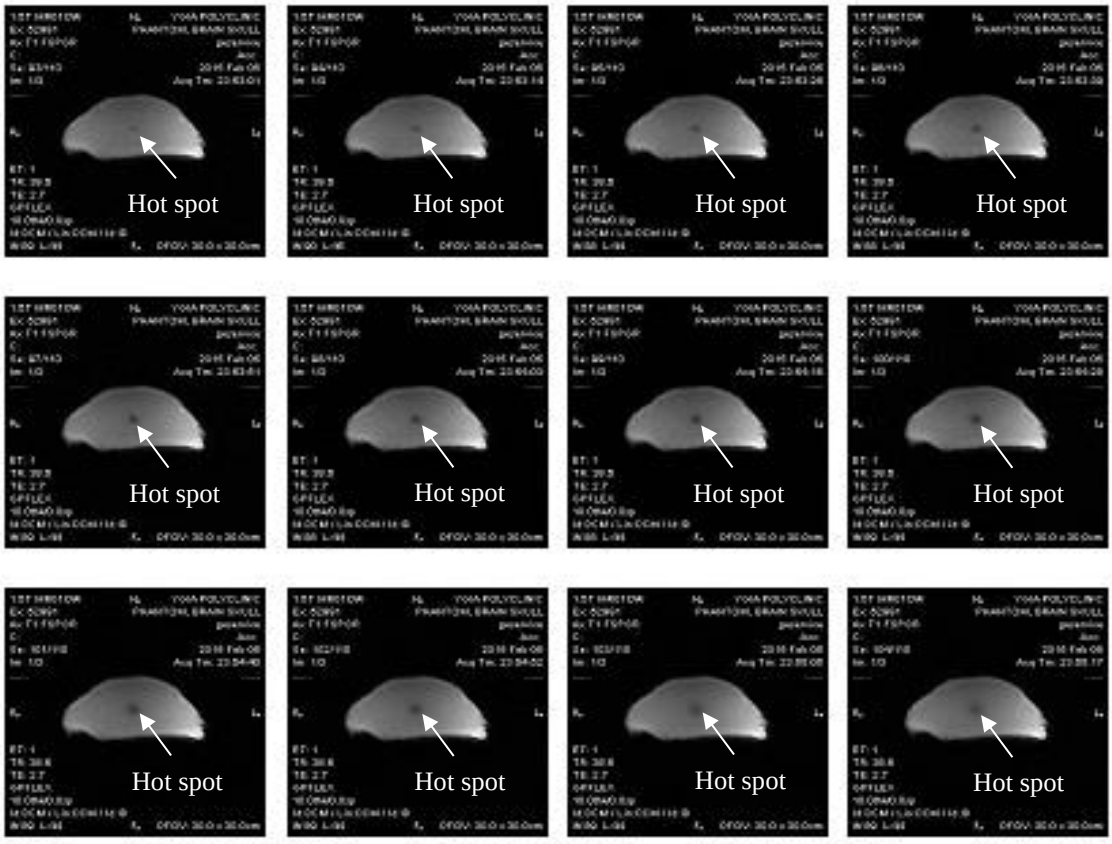

Figure 11: Sagittal T_1w images for 90 W-60 s sonication in the absence of plastic skull.

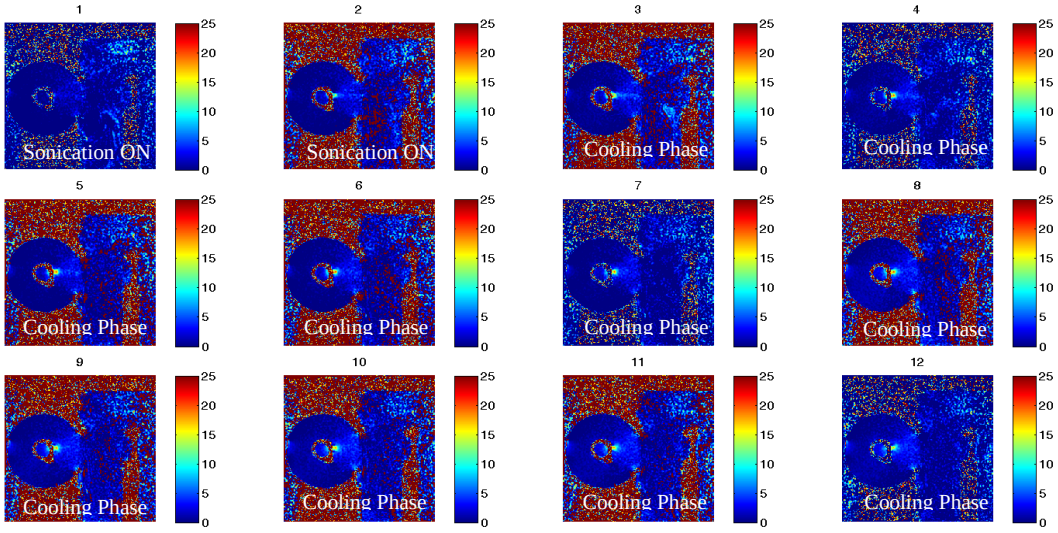

Figure 12: Thermal maps (1-12) of the bone/muscle phantom in the axial plane for 30 W-30 s sonication using a SPGR pulse sequence.

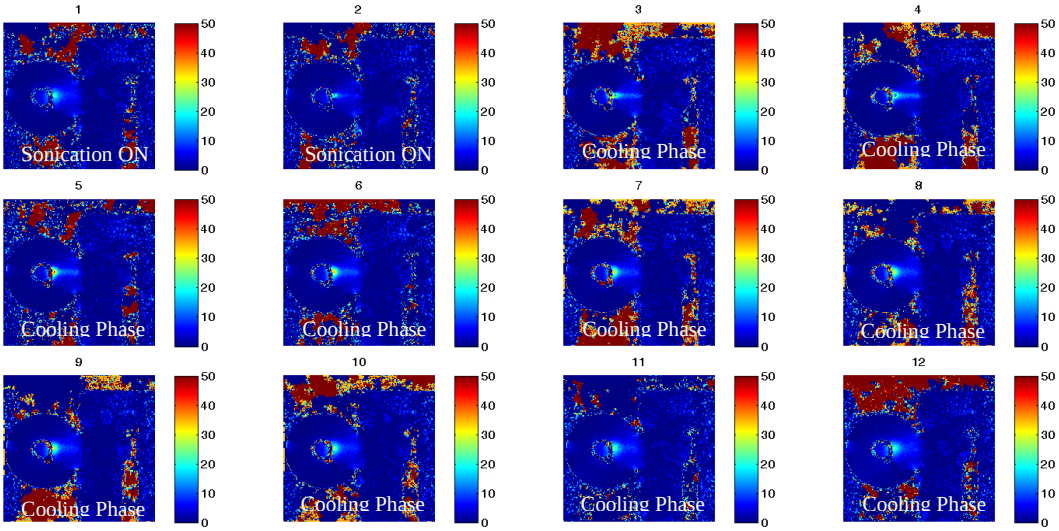

Figure 13: Thermal maps (1-12) of the bone/muscle phantom in the axial plane for 60 W-30 s sonication using a SPGR pulse sequence.

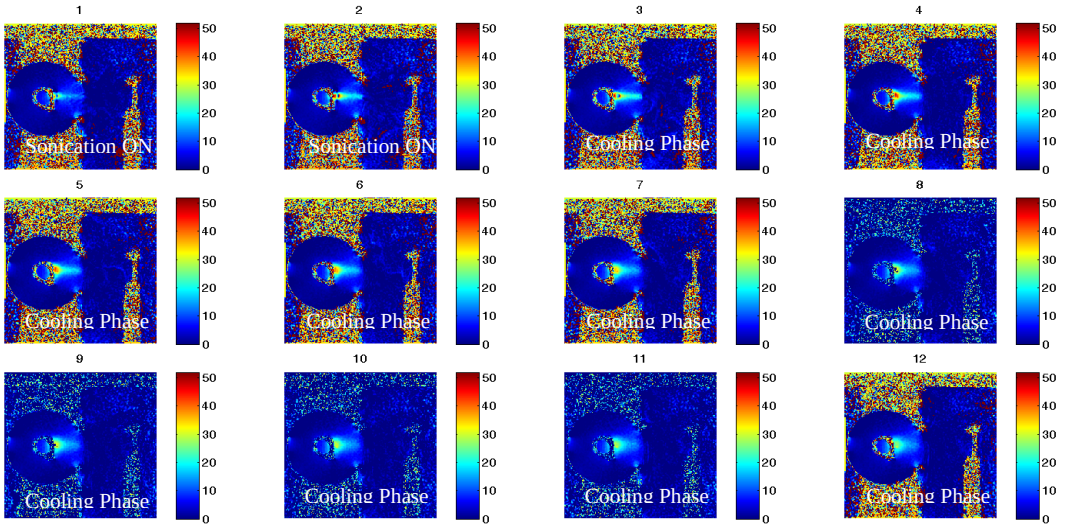

Figure 14: Thermal maps (1-12) of the bone/muscle phantom in the axial plane for 90 W-30 s sonication using a SPGR pulse sequence.

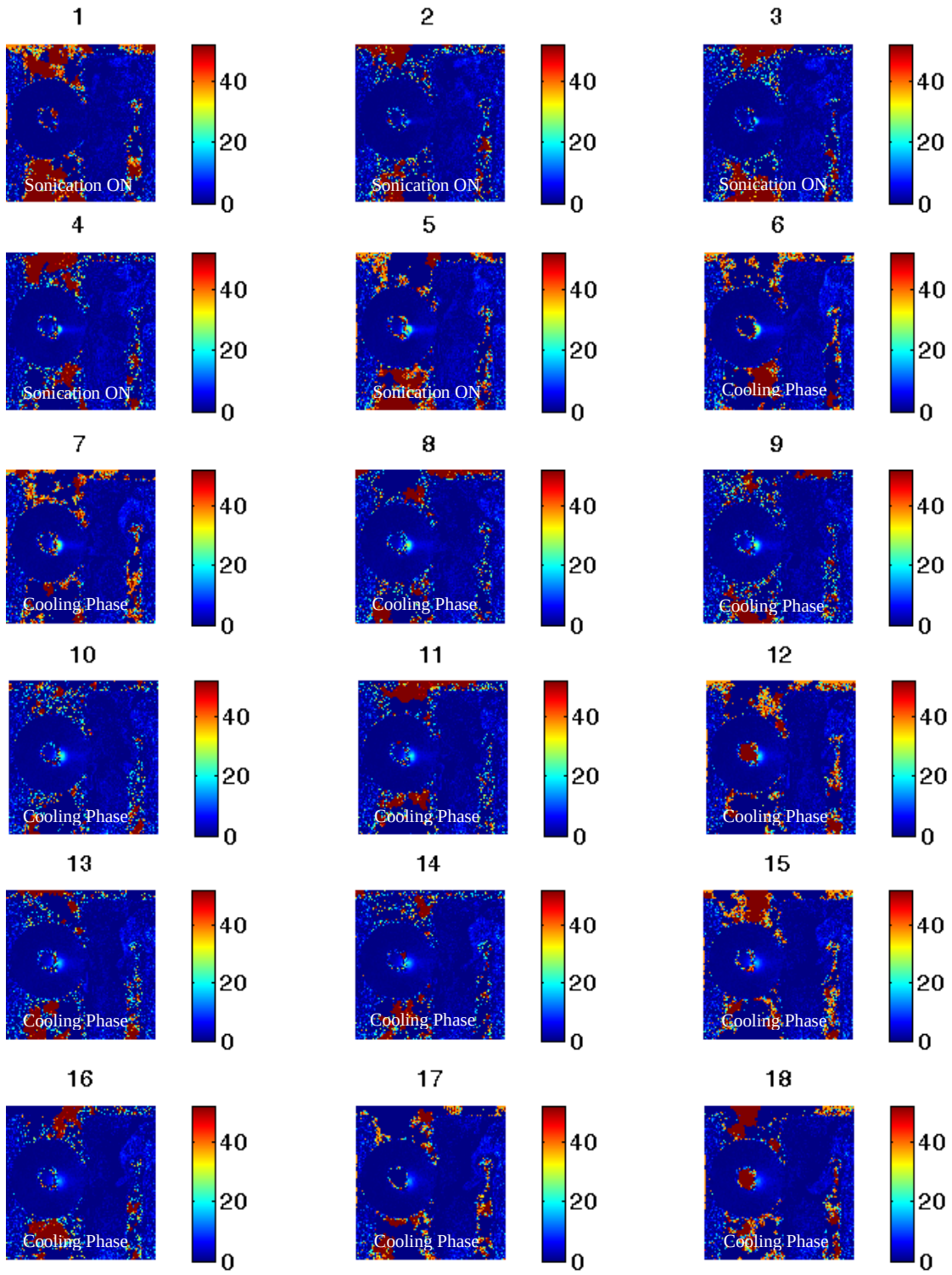

Figure 15: Thermal maps (1-18) of the bone/muscle phantom in the axial plane for 30 W-60 s sonication using a SPGR pulse sequence.

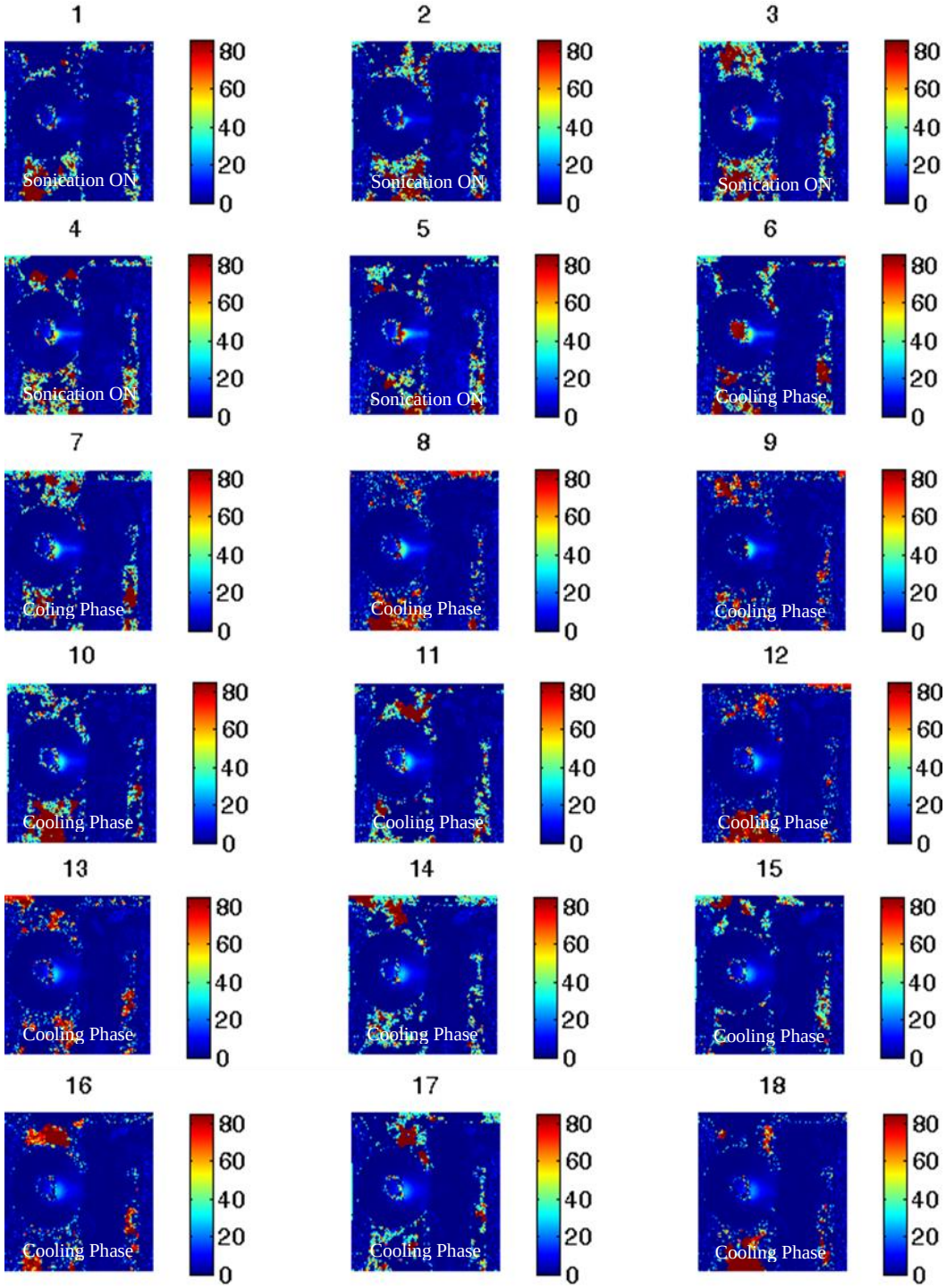

Figure 16: Thermal maps (1-18) of the bone/muscle phantom in the axial plane for 60 W-60 s sonication using a SPGR pulse sequence.

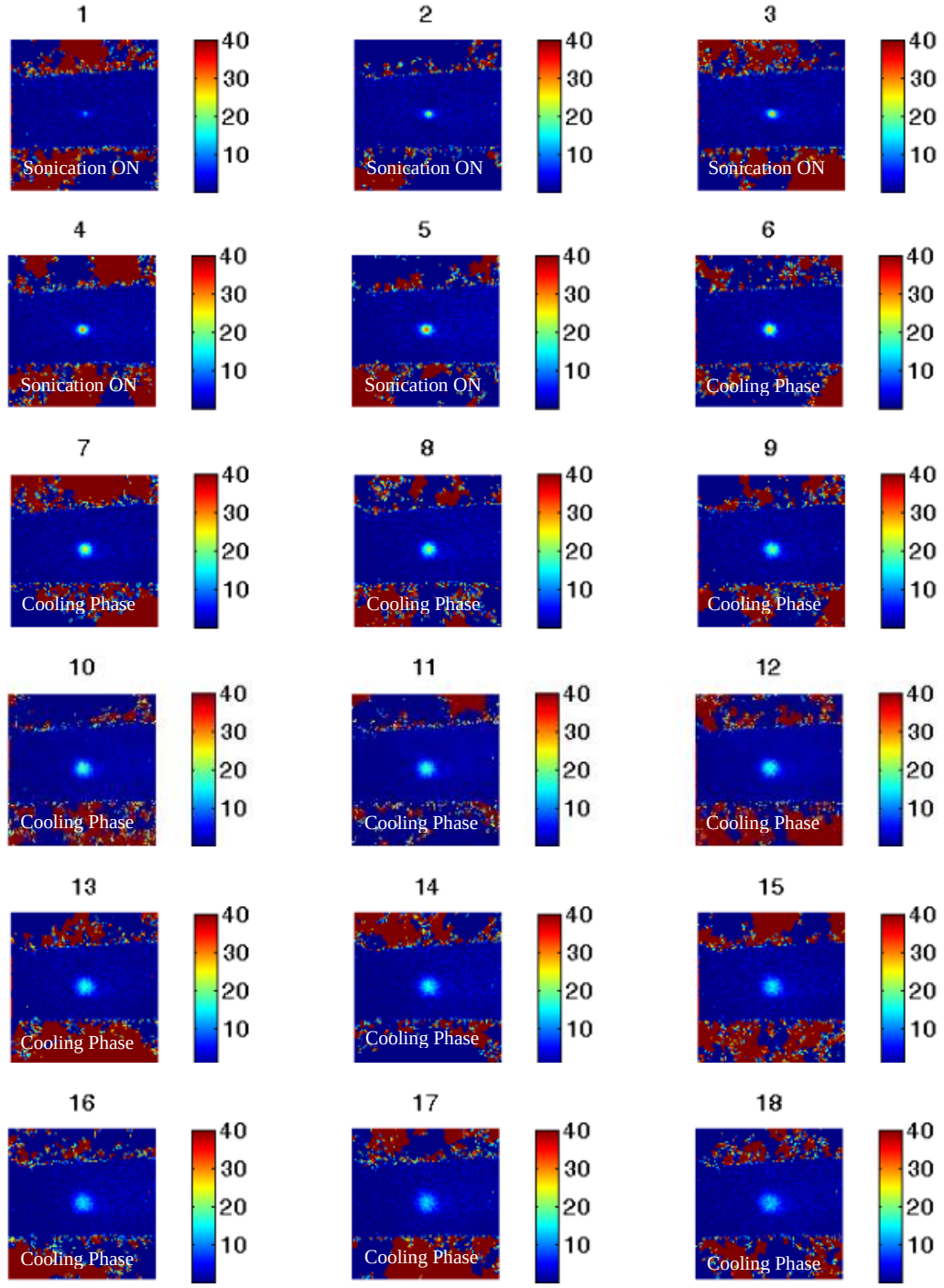

Figure 17: Thermal maps (1-18) of the bone/muscle phantom in the sagittal plane for 30 W-60 s sonication using a SPGR pulse sequence.

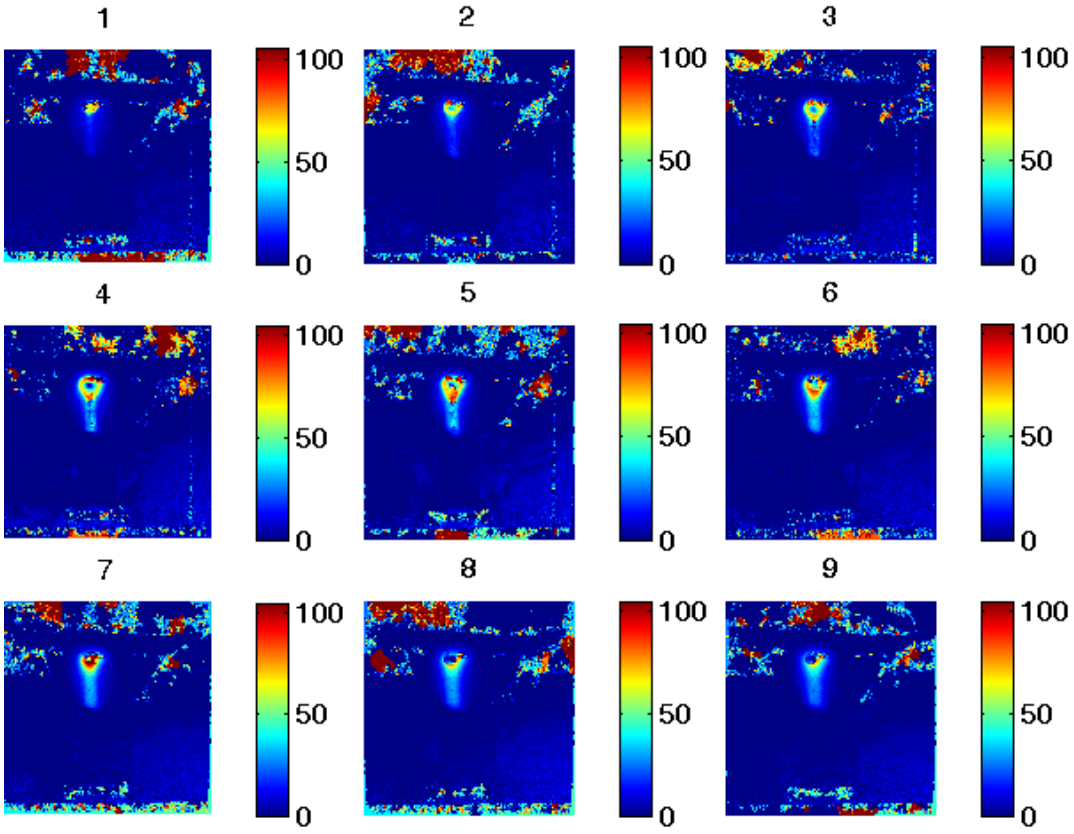

Figure 18: Axial thermal maps for a 45 W-60 s of the breast/rib phantom sonication for a bottom to top approach and with the rib bone residing in the far acoustic field.

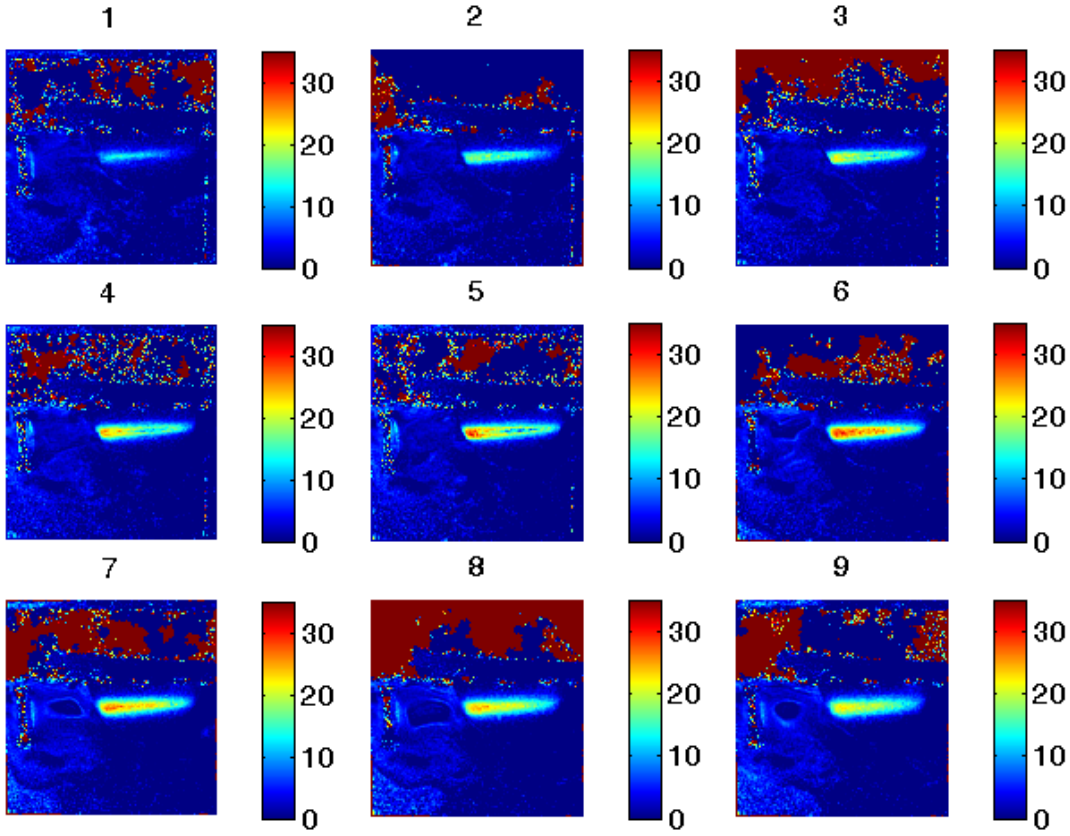

Figure 19: Axial thermal maps for a 90W-60s sonication of the breast/rib phantom for a lateral approach while avoiding the rib bone in the far field

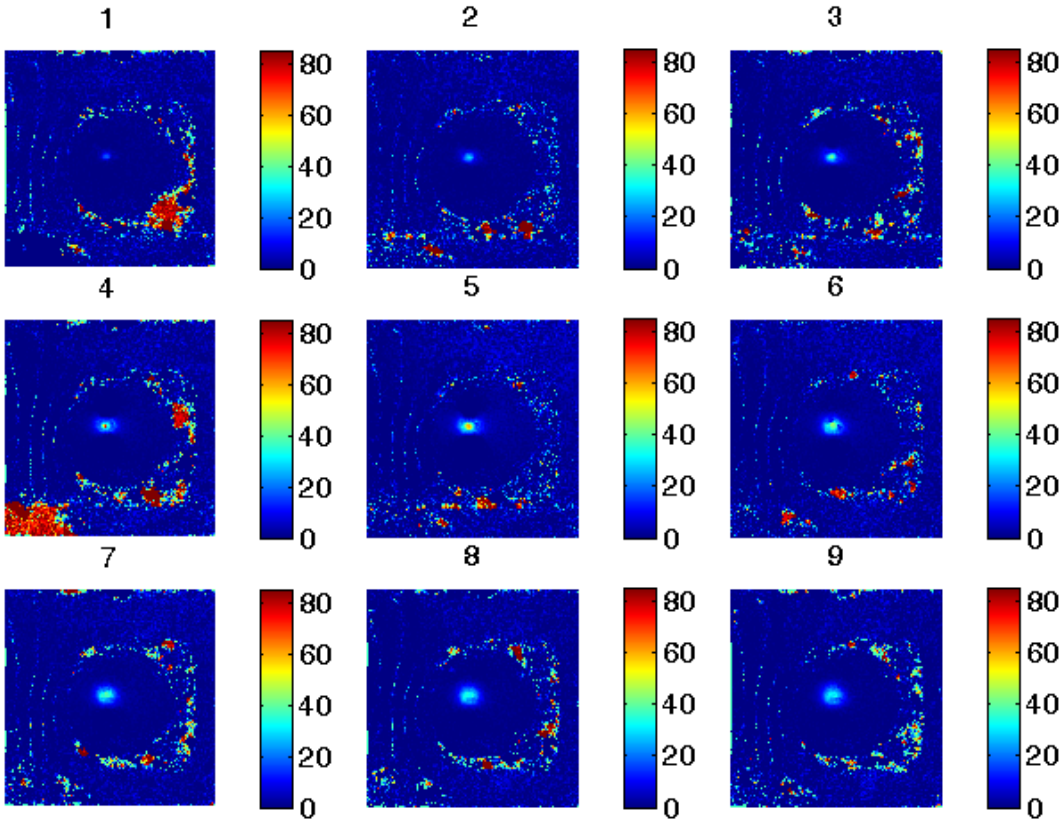

Figure 20: Coronal thermal maps for a 45 W-60 s sonication of the breast/rib phantom for a bottom to top approach and the thermometry slice prescribed 5 mm in front of the rib phantom.

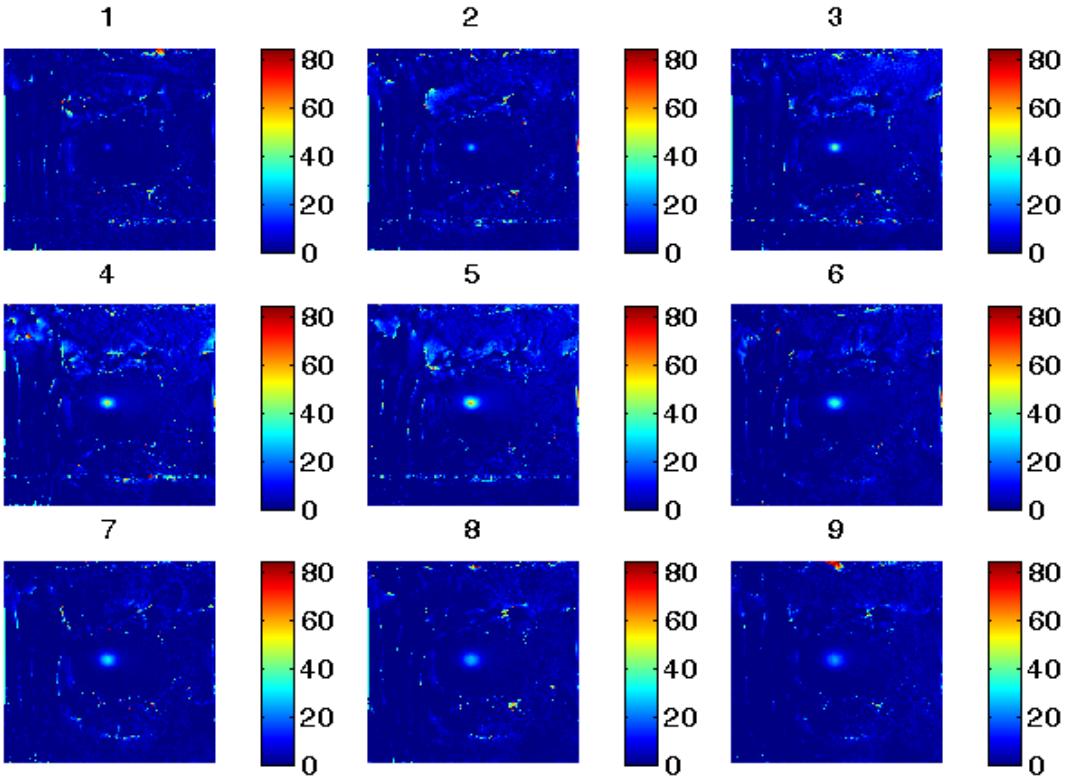

Figure 21: Coronal thermal map for a 45 W-60 s sonication of the breast/rib phantom for a bottom to top approach and the thermometry slice prescribed at the focus.

Appendix D

TempMap1 GUI Matlab code

```
% TEMPMAP1 MATLAB code for TempMap1.fig

function varargout = TempMap1(varargin)

% Initialization of GUI

gui_Singleton = 1;

gui_State = struct('gui_Name',       mfilename, ...

                   'gui_Singleton',  gui_Singleton, ...

                   'gui_OpeningFcn', @TempMap1_OpeningFcn, ...

                   'gui_OutputFcn',  @TempMap1_OutputFcn, ...

                   'gui_LayoutFcn',  [] , ...

                   'gui_Callback',   []);

if nargin && ischar(varargin{1})

   gui_State.gui_Callback = str2func(varargin{1});

end

if nargout

   [varargout{1:nargout}] = gui_mainfcn(gui_State, varargin{:});

else

   gui_mainfcn(gui_State, varargin{:});

end

% End initialization code

% Executes just before TempMap1 is made visible.

function TempMap1_OpeningFcn(hObject, eventdata, handles, varargin)

% Choose default command line output for TempMap1 and set default user defined values for
alpha and waiting time.

set(handles.alpha, 'String', -0.01);

set (handles.WaitingTime, 'String', 60);

handles.output = hObject;

% Update handles structure

guidata(hObject, handles);

% TempMap1 waits for user response

% uiwait(handles.figure1);

% Outputs from this function are returned to the command line.

function varargout = TempMap1_OutputFcn(hObject, eventdata, handles)
```

```
% varargout  cell array for returning output args (see VARARGOUT);
% hObject    handle to figure
% eventdata  reserved - to be defined in a future version of MATLAB
% handles    structure with handles and user data (see GUIDATA)
% Get default command line output from handles structure
varargout{1} = handles.output;


% Executes on button press in pushbutton1.
function pushbutton1_Callback(hObject, eventdata, handles)
% Browse and load magnitude (reference) image DICOM file.
[filename, pathname] = uigetfile('*.*', 'Select a Magnitude Image');
% Check if file is empty and give warning for cancellation.
if ~isequal(filename,0)
% Create array MG1 and set equal to matrix of read pixel data.
   MG1= dicomread (fullfile(pathname,filename))
% Create struct with fields MG1info and set equal to DICOM file metadata.
   MG1info= dicominfo (fullfile(pathname,filename))
 % Show magnitude image MG1 in figure (1) with in grayscale in full dynamic range
   figure(1);
   imshow (MG1, []);
% Create handles of 6 elliptical ROI with radii of (10 x 10 pixels) and center at (0, 0).  The use drags and drops by double clicking the ROI at each external oil reference. Position and size of ROI can be adjusted.
   h1 = imellipse(gca, [0 0 10 10]);
   wait(h1);
   h2 = imellipse(gca, [0 0 10 10]);
   wait(h2);
   h3 = imellipse(gca, [0 0 10 10]);
   wait (h3);
   h4 = imellipse(gca, [0 0 10 10]);
   wait (h4);
   h5 = imellipse(gca, [0 0 10 10]);
   wait (h5);
   h6 = imellipse(gca, [0 0 10 10]);
```

```
    wait (h6);
    fig=gcf;
else
% Error message if user cancels reference magnitude image selection.
    msgbox ('User cancelled image selection', 'Error','Error');
end
%Carry useful handles to other pushbutton within GUI
handles.MG1 = MG1;
handles.h1=h1;
handles.h2=h2;
handles.h3=h3;
handles.h4=h4;
handles.h5=h5;
handles.h6=h6;
handles.fig=fig;
handles.MG1info = MG1info;
guidata(hObject, handles);

% --- Executes on button press in pushbutton2.
function pushbutton2_Callback(hObject, eventdata, handles)
% Browse and load Real (reference) image from DICOM file.
 [filename, pathname] = uigetfile('*.*', 'Select a Real Image');
% Check if file is empty and give warning for cancellation
if ~isequal(filename,0)
% Create array RE1 and set equal to matrix of Real image read pixel data.
    RE1= dicomread (fullfile(pathname,filename));
else
    msgbox ('User cancelled image selection', 'Error','Error');
end
%Carry useful handles to other pushbutton within GUI
handles.RE1 = RE1;
guidata(hObject, handles);
% Executes on button press in pushbutton3.
function pushbutton3_Callback(hObject, eventdata, handles)
```

```
% Browse and load Imaginary (reference) image from DICOM file.
 [filename, pathname] = uigetfile('*.*', 'Select an Imaginary Image');
% Check if file is empty and give warning for cancellation
if ~isequal(filename,0)
   IM1= dicomread (fullfile(pathname,filename));
else
   msgbox ('User cancelled image selection', 'Error','Error');
end
%Carry useful handles to other pushbutton within GUI
handles.IM1 = IM1;
guidata(hObject, handles);
```

% If the user selects to follow the Single Pair Analysis then he must run all three pushbuttons 4, 5 and 6. These pushbuttons are used to browse and load pixel data of the Ablation Image to matrix arrays in the code (MG2, RE2, and IM2). Comments for this part of the code are omitted.

```
% Executes on button press in pushbutton4
 [filename, pathname] = uigetfile('*.*', 'Select a Magnitude Image');
if ~isequal(filename,0)
   MG2= dicomread (fullfile(pathname,filename));
   MG2info = dicominfo (fullfile(pathname,filename))
else
   msgbox ('User cancelled image selection', 'Error','Error');
end
handles.MG2 = MG2;
handles.MG2info = MG2info;
guidata(hObject, handles);

% --- Executes on button press in pushbutton5.
function pushbutton5_Callback(hObject, eventdata, handles)
 [filename, pathname] = uigetfile('*.*', 'Select a Real Image');
if ~isequal(filename,0)
   RE2= dicomread (fullfile(pathname,filename));
else
```

```
    msgbox ('User cancelled image selection', 'Error','Error');
end
handles.RE2 = RE2;
guidata(hObject, handles);

% --- Executes on button press in pushbutton6.
function pushbutton6_Callback(hObject, eventdata, handles)
 [filename, pathname] = uigetfile('*.*', 'Select an Imaginary Image');
if ~isequal(filename,0)
    IM2= dicomread (fullfile(pathname,filename));
else
    msgbox ('User cancelled image selection', 'Error','Error');
end
handles.IM2 = IM2;
guidata(hObject, handles);



% --- Executes on button press in pushbutton7.
function pushbutton7_Callback(hObject, eventdata, handles)
% Retrieves from GUI handles the RE1 and IM1 to calculate reference wrapped phase image
WP1
RE1 = double (handles.RE1)
IM1 = double (handles.IM1)
%Check if variables are empty
if isempty(RE1)
        msgbox ('Select a Real Mask Image!', 'Error','Error');
elseif isempty(IM1)
        msgbox ('Select an Imaginary Mask Image!', 'Error','Error');
else

%Calculate reference wrapped phase image WP1 using the atan2 function from Matlab Library
WP1=atan2(IM1,RE1);
end
%Carry useful handles to other pushbutton within GUI
```

```
handles.WP1 = WP1;
guidata(hObject, handles);

% --- Executes on button press in pushbutton8.
function pushbutton8_Callback(hObject, eventdata, handles)
% Retrieves from GUI handles the RE2 and IM2 to calculate ablation wrapped phase image WP2
RE2 = double (handles.RE2);
IM2 = double (handles.IM2);
% Check if variables are empty
if isempty(RE2)
    msgbox ('Select a Real Mask Image!', 'Error','Error');
elseif isempty(IM2)
    msgbox ('Select an Imaginary Mask Image!', 'Error','Error');
else
%Calculate ablation wrapped phase image WP2 using the atan2 function from Matlab Library
    WP2=atan2(IM2,RE2);
end
%Carry useful handles to other pushbutton within GUI
handles.WP2 = WP2;
guidata(hObject, handles);

% --- Executes on button press in pushbutton9.
function pushbutton9_Callback(hObject, eventdata, handles)
%Retrieve handles of external variables
RE1=handles.RE1;
IM1=handles.IM1;
MG1 = double (handles.MG1);
WP1 = double (handles.WP1);

% Calculate complex reference image IC1
IC1=MG1.* exp(1i *(WP1));
%Carry useful handles to other pushbutton within GUI
handles.IC1 = IC1;
guidata(hObject, handles);
```

```
% --- Executes on button press in pushbutton10.
function pushbutton10_Callback(hObject, eventdata, handles)
%Retrieve handles of external variables
RE2=handles.RE2;
IM2=handles.IM2;
MG2 = double (handles.MG2);
WP2 = double (handles.WP2);
%Calculate complex ablation image IC2
IC2=MG2.* exp(1i *(WP2));
%Carry useful handles to other pushbutton within GUI
handles.IC2 = IC2;
guidata(hObject, handles);

% --- Executes on button press in pushbutton11.
function pushbutton11_Callback(hObject, eventdata, handles)
%Retrieve handles of external variables
RE1=double(handles.RE1);
IM1=double(handles.IM1);
MG1=handles.MG1;
WP1=handles.WP1;
IC1=handles.IC1;
RE2=double(handles.RE2);
IM2=double(handles.IM2);
MG2=handles.MG2;
WP2=handles.WP2;
IC2=handles.IC2;
fig=handles.fig;
h1=handles.h1;
h2=handles.h2;
h3=handles.h3;
h4=handles.h4;
h5=handles.h5;
h6=handles.h6;
```

```
%Calculate complex difference CD by multiplying IC1 with complex conjugate of IC2.
CD = double(IC1) .* conj(double(IC2)); % complex
%Calculate phase difference angle PDa matrix array from complex difference data CD.
PDa = angle(CD);
%Unwrap PDa using Miguel Herrraez unwrapping algorithm
PDb=Miguel_2D_unwrapper(single(PDa));
%Show PDb in axes1 on grayscale with min and max equal to –pi to +pi
axes(handles.axes1);
imshow(PDb,[-3.14 3.14]);colormap(jet(264)); colorbar;
title ('Mask phase(rad)')
%Create array with mean pixel values of predefined ROI handles for each external oil reference
roi=[mean(PDb(createMask(h1)));mean(PDb(createMask(h2)));mean(PDb(createMask(h3)));mean(PDb(createMask(h4)));mean(PDb(createMask(h5)));mean(PDb(createMask(h6)));];
%Get position of each ROI
a1=getPosition(h1);
a2=getPosition(h2);
a3=getPosition(h3);
a4=getPosition(h4);
a5=getPosition(h5);
a6=getPosition(h6);
%Contsruct X and Y vectors where the xy coordinates of ROI are saved.
X=[a1(1)+a1(3)/2;a2(1)+a2(3)/2;a3(1)+a3(3)/2;a4(1)+a4(3)/2;a5(1)+a5(3)/2;a6(1)+a6(3)/2];
Y=[a1(2)+a1(4)/2;a2(2)+a2(4)/2;a3(2)+a3(4)/2;a4(2)+a4(4)/2;a5(2)+a5(4)/2;a6(2)+a6(4)/2];


% Mean pixel values are used to fit a 1st degree polynomial using least absolute residuals criterion
f1=fit([X Y],roi,'poly11','Robust','LAR');
figure(3);
plot(f1, [X Y], roi);
coef=coeffvalues(f1);
M=zeros(256);
for i=1:256;
  for  j=1:256;
%A 256 by 256 correction matrix with fitted data is created to correct for pseudophase offset
```

```
M(i,j)=coef(1)+coef(2)*i+coef(3)*j;
  end
end
% Final phase difference matrix array is created by subtracting the phase correction matrix M
PD=PDb-M;
% Show WP2
axes(handles.axes3);
imshow(WP2,[-3.14 3.14]);colormap(jet(264)); colorbar;
title ('Ablation phase(rad)')
%Carry useful handles to other pushbutton within GUI
handles.CD=CD;
handles.PD = PD;
handles.PDb=PDb;
handles.roi=roi;
handles.M=M;
guidata(hObject, handles);

% --- Executes on button press in pushbutton13.
function pushbutton13_Callback(hObject, eventdata, handles)
%Retrieve handles of external variables
alpha = str2num(get(handles.alpha, 'String'));
CD=handles.CD;
PD=handles.PD;
PDb=handles.PDb;
MG2info=handles.MG2info;
%PRFS equation for calculating temperature shift
dT = PD./(gamma*alpha*TE*B0);
axes(handles.axes4);
% Show Temperature map
imagesc(dT,[-3 25]); axis off; colormap(jet(264)); colorbar;
title('Temperature Change(^{o}C)');
datacursormode on;

% --- Executes on button press in pushbutton14.
```

The user selects to follow the Multiple Pair Analysis. The preloaded data of the reference image are used. The GUI waits for incoming new files to automatically analyze for a period equal to Waiting Time.

```
function pushbutton14_Callback(hObject, eventdata, handles)

%Import alpha and waiting time (time for checking new images during Quick TempMap)

%settings from GUI

alpha = str2num(get(handles.alpha, 'String'));

WaitingTime= str2num(get(handles.WaitingTime, 'String'));

% Set counting

counting=1;

fig=handles.fig;

h1=handles.h1;

h2=handles.h2;

h3=handles.h3;

h4=handles.h4;

h5=handles.h5;

h6=handles.h6;

%Retrieve handle of reference complex image

IC1 = handles.IC1;

WP1 = handles.WP1;

% Initialize image folders

previousfolder = '';

%Start Timer

tic;

% While loop checking parsed time less than set WaitingTime

while (toc<=WaitingTime)

 % Set image current folder. The string of current folder is updated by 3rd party application which sends the new address of the an incoming folder of DICOM files.

 currentfolder=fileread('C:\Users\xbmc\Desktop\currentfolder.txt');

 %Check if current folder is same with previous folder (new incoming images)

 test=strcmp(currentfolder,previousfolder);

 %Dir current folder for later use (image counting)

DirChecker= dir ([currentfolder, '\*.*']);

%If new images arrived ,currentfolder not empty and with at least 3 images
```

```
if (test==0 && isempty(currentfolder)~=1 && length(DirChecker(not([DirChecker.isdir])))>=3)

pathway =  strcat(currentfolder,'\**\*');

% DIR to current folder

 d=rdir(pathway);

% Sort images chronologically (last modified) and pick last three which correspond to last magnitude, real and imaginary.

dates = [d.datenum];

[~, Index] = sort (dates);

first = d(Index(end-2));

MG2=double(dicomread(first.name));

MG2info=dicominfo(first.name);

second = d(Index(end-1));

RE2 = double(dicomread(second.name));

third = d(Index(end));

IM2 = double(dicomread(third.name));

WP2=atan2(IM2,RE2);

% Create ablation complex data image IC2

IC2=MG2.* exp(1i *(WP2));

% Calculate complex difference by multiplying with conjugate

CD = double(IC1) .* conj(double(IC2));

% Calculate phase angle difference matrix

PDa = angle(CD);

%Unwrap phase angle difference matrix using Miguel Herraez unwrapping algorithm.

PDb= Miguel_2D_unwrapper(single(PDa));

% Display PDb

figure(2);

imshow(PDb,[]);

% Calculate mean pixel values at each predefined ROI for pseudophase offset correction.

roi=[mean(PDb(createMask(h1)));mean(PDb(createMask(h2)));mean(PDb(createMask(h3)));mean(PDb(createMask(h4)));mean(PDb(createMask(h5)));mean(PDb(createMask(h6)));];

 a1=getPosition(h1);

 a2=getPosition(h2);

 a3=getPosition(h3);

 a4=getPosition(h4);
```

```
 a5=getPosition(h5);
 a6=getPosition(h6);
% Create X Y vectors based on ROI x,y coordinates.
X=[a1(1)+a1(3)/2;a2(1)+a2(3)/2;a3(1)+a3(3)/2;a4(1)+a4(3)/2;a5(1)+a5(3)/2;a6(1)+a6(3)/2];
Y=[a1(2)+a1(4)/2;a2(2)+a2(4)/2;a3(2)+a3(4)/2;a4(2)+a4(4)/2;a5(2)+a5(4)/2;a6(2)+a6(4)/2];
% 1st degree polynomial fit of ROI mean pixel values with and X, Y vectors to a 2D surface.
f1=fit([X Y],roi,'poly11');
coef=coeffvalues(f1);
% Create correction matrix using the coefficients of the fit
M=zeros(256);
for i=1:256;
  for  j=1:256;
   M(i,j)=coef(1)+coef(2)*i+coef(3)*j;
  end
end
% Apply correction to current unwrapped phase image.
PD=PDb-M;
% Get alpha value set by user in GUI
alpha = str2num(get(handles.alpha, 'String'));
 %Declare parameters for PRFS equation
 gamma=2.675*10^8; % in rad/s*T
 alpha= alpha*10^(-6); % in 1/degree_celcius
B0=1.5; % in T
TE = MG2info.EchoTime * 10^(-3); % in s
%Declare PRFS equation
dT = PD./(gamma*alpha*TE*B0);
% Use of subtightplot function to display maps in a predefined 3 x 3 multi-frame format.
figure (3);
subtightplot(3,3,counting);
imshow (dT,[0 105]); axis off; colormap(jet(264));colorbar
title(counting);
% Changes previousfolder value and  counter value;
previousfolder=currentfolder;
counting=counting+1;
```

```
    else
    end
% End of loop of the Multiple pair analysis. The loop returns at the beginning for as long as the Waiting Time is not expired.
end


% --- Executes on button press in pushbutton15.
function pushbutton15_Callback(hObject, eventdata, handles)
% Delete all handles and close GUI.
close all;
```

References

[1] Focused Ultrasound Foundation, “http://www.fusfoundation.org/diseases-and-conditions/overview,” *Overview*, 2015. .

[2] Y.-F. Zhou, “High intensity focused ultrasound in clinical tumor ablation.,” *World J. Clin. Oncol.*, vol. 2, pp. 8–27, 2011.

[3] T. J. Dubinsky, C. Cuevas, M. K. Dighe, O. Kolokythas, and J. H. Hwang, “High-intensity focused ultrasound: current potential and oncologic applications.,” *AJR. Am. J. Roentgenol.*, vol. 190, no. 1, pp. 191–9, Jan. 2008.

[4] F. Y. Yap, J. T. Bui, M. G. Knuttinen, D. Ph, C. A. Owens, and R. C. Gaba, “Current Tumor Ablation Technologies : Basic Science and Device Review,” vol. 1, no. 212, pp. 247–254, 2010.

[5] D. Haemmerich and B. J. Wood, “Hepatic radiofrequency ablation at low frequencies preferentially heats tumour tissue.,” *Int. J. Hyperthermia*, vol. 22, no. 7, pp. 563–74, Nov. 2006.

[6] Z. Liu, M. Ahmed, Y. Weinstein, M. Yi, R. L. Mahajan, and S. N. Goldberg, “Characterization of the RF ablation-induced ‘oven effect’: the importance of background tissue thermal conductivity on tissue heating.,” *Int. J. Hyperthermia*, vol. 22, no. 4, pp. 327–42, Jun. 2006.

[7] M. G. Lubner, C. L. Brace, J. L. Hinshaw, and F. T. Lee, “Microwave tumor ablation: mechanism of action, clinical results, and devices.,” *J. Vasc. Interv. Radiol.*, vol. 21, no. 8 Suppl, pp. S192-203, Aug. 2010.

[8] C. L. Brace, “Microwave tissue ablation: biophysics, technology, and applications.,” *Crit. Rev. Biomed. Eng.*, vol. 38, no. 1, pp. 65–78, Jan. 2010.

[9] T. Lee, N. Mendhiratta, D. Sperling, and H. Lepor, “Focal laser ablation for localized prostate cancer: principles, clinical trials, and our initial experience.,” *Rev. Urol.*, vol. 16, no. 2, pp. 55–66, Jan. 2014.

[10] K. Ahrar, A. Gowda, S. Javadi, A. Borne, M. Fox, R. McNichols, J. U. Ahrar, C. Stephens, and R. J. Stafford, “Preclinical assessment of a 980-nm diode laser ablation system in a large animal tumor model.,” *J. Vasc. Interv. Radiol.*, vol. 21, no. 4, pp. 555–61, Apr. 2010.

[11] J. G. Baust, A. A. Gage, T. E. Bjerklund Johansen, and J. M. Baust, “Mechanisms of cryoablation: clinical consequences on malignant tumors.,” *Cryobiology*, vol. 68, no. 1, pp. 1–11, Feb. 2014.

[12] M. Inoue, S. Nakatsuka, and M. Jinzaki, “Cryoablation of early-stage primary lung cancer.,” *Biomed Res. Int.*, vol. 2014, p. 521691, Jan. 2014.

[13] W. R. Hendee and E. R. Ritenour, *Medical Imaging Physics*. 2003.

[14] P. R. Hoskins, *Diagnostic Ultrasound: Physics and Equipment*, 2nd ed. Cambridge University Press, 2010.

[15] M. Pernot, J. F. Aubry, M. Tanter, J. L. Thomas, and M. Fink, “High power transcranial beam steering for ultrasonic brain therapy.,” *Phys. Med. Biol.*, vol. 48, pp. 2577–2589, 2003.

[16] S. A. Goss, “Comprehensive compilation of empirical ultrasonic properties of mammalian tissues,” *J. Acoust. Soc. Am.*, vol. 64, no. 2, p. 423, 1978.

[17] F. A. Duck, *Physical Properties of Tissues*. Elsevier, 1990.

[18] H. Azhari, “Appendix A: Typical Acoustic Properties of Tissues,” in *Basics of Biomedical Ultrasound for Engineers*, Hoboken, NJ, USA: John Wiley & Sons, Inc., 2010, pp. 313–314.

[19] M. N. Fadhel, E. S. L. Berndl, E. M. Strohm, and M. C. Kolios, “High-Frequency Acoustic Impedance Imaging of Cancer Cells,” *Ultrasound Med. Biol.*, vol. 41, no. 10, pp. 2700–2713, Oct. 2015.

[20] S. A. Goss, L. A. Frizzell, and F. Dunn, “Ultrasonic absorption and attenuation in mammalian tissues,” *Ultrasound Med. Biol.*, vol. 5, no. 2, pp. 181–186, Jan. 1979.

[21] C. Hill, *Physical principles of medical ultrasonics*. Chichester ;New York: E. Horwood ;;Halsted Press, 1986.

[22] J. C. Bamber, “Ultrasound in medicine,” Bristol, UK: Institute of Physics Publishing, 1998.

[23] K. A. Wear, “Frequency dependence of ultrasonic backscatter from human trabecular bone: theory and experiment.,” *J. Acoust. Soc. Am.*, vol. 106, no. 6, pp. 3659–64, Dec. 1999.

[24] S. A. Sapareto and W. C. Dewey, “Thermal dose determination in cancer therapy.,” *Int. J. Radiat. Oncol. Biol. Phys.*, vol. 10, no. 6, pp. 787–800, Jun. 1984.

[25] F. C. HENRIQUES, “Studies of thermal injury; the predictability and the significance of thermally induced rate processes leading to irreversible epidermal injury.,” *Arch. Pathol.*, vol. 43, no. 5, pp. 489–502, May 1947.

[26] W. C. Dewey, L. E. Hopwood, S. A. Sapareto, and L. E. Gerweck, “Cellular responses to combinations of hyperthermia and radiation.,” *Radiology*, vol. 123, no. 2, pp. 463–74, May 1977.

[27] S. B. Field and C. C. Morris, “The relationship between heating time and temperature: its relevance to clinical hyperthermia.,” *Radiother. Oncol.*, vol. 1, no. 2, pp. 179–86, Nov. 1983.

[28] M. W. Dewhirst, B. L. Viglianti, M. Lora-Michiels, P. J. Hoopes, and M. Hanson, “THERMAL DOSE REQUIREMENT FOR TISSUE EFFECT: EXPERIMENTAL AND CLINICAL FINDINGS.,” *Proc. Soc. Photo. Opt. Instrum. Eng.*, vol. 4954, p. 37, Jun. 2003.

[29] H. G. Flynn, “Generation of transient cavities in liquids by microsecond pulses of ultrasound,” *J. Acoust. Soc. Am.*, vol. 72, no. 6, p. 1926, Dec. 1982.

[30] W. G. Pitt, G. A. Husseini, and B. J. Staples, “Ultrasonic drug delivery--a general review.,” *Expert Opin. Drug Deliv.*, vol. 1, no. 1, pp. 37–56, Nov. 2004.

[31] V. Frenkel, “Ultrasound mediated delivery of drugs and genes to solid tumors.,” *Adv. Drug Deliv. Rev.*, vol. 60, no. 10, pp. 1193–208, Jun. 2008.

[32] N. I. Vykhodtseva, K. Hynynen, and C. Damianou, “Pulse duration and peak intensity during focused ultrasound surgery: theoretical and experimental effects in rabbit brain in vivo.,” *Ultrasound Med. Biol.*, vol. 20, no. 9, pp. 987–1000, Jan. 1994.

[33] N. B. Smith and K. Hynynen, “The feasibility of using focused ultrasound for transmyocardial revascularization.,” *Ultrasound Med. Biol.*, vol. 24, no. 7, pp. 1045–54, Sep. 1998.

[34] Focused Ultrasound Foundation, “State of the Field 2017,” Charlottesville, VA, USA, 2017.

[35] S. Monteith, J. Sheehan, and R. Medel, “Potential intracranial applications of magnetic resonance–guided focused ultrasound surgery: a review,” *J. ...*, vol. 118, no. 2, pp. 215–21, 2013.

[36] K. Hynynen, N. I. Vykhodtseva, A. H. Chung, V. Sorrentino, V. Colucci, and F. A. Jolesz, “Thermal effects of focused ultrasound on the brain: determination with MR imaging.,” *Radiology*, vol. 204, no. 1, pp. 247–53, Jul. 1997.

[37] K. Hynynen and G. Clement, “500-element ultrasound phased array system for noninvasive focal surgery of the brain: A preliminary rabbit study with ex vivo human skulls,” *Magn. Reson. ...*, vol. 52, no. 1, pp. 100–107, Jul. 2004.

[38] M. Pernot, J.-F. Aubry, M. Tanter, A.-L. Boch, F. Marquet, M. Kujas, D. Seilhean, and M. Fink, “In vivo transcranial brain surgery with an ultrasonic time reversal mirror.,” *J. Neurosurg.*, vol. 106, pp. 1061–1066, 2007.

[39] K. Hynynen, N. McDannold, G. Clement, F. A. Jolesz, E. Zadicario, R. Killiany, T. Moore, and D. Rosen, “Pre-clinical testing of a phased array ultrasound system for MRI-guided noninvasive surgery of the brain--a primate study.,” *Eur. J. Radiol.*, vol. 59, no. 2, pp. 149–56, Aug. 2006.

[40] M. Tanter, M. Pernot, J. F. Aubry, G. Montaldo, F. Marquet, and M. Fink, “Compensating for bone interfaces and respiratory motion in high-intensity focused ultrasound.,” *Int. J. Hyperthermia*, vol. 23, pp. 141–151, 2007.

[41] F. Marquet, Y.-S. Tung, T. Teichert, V. P. Ferrera, and E. E. Konofagou, “Noninvasive, transient and selective blood-brain barrier opening in non-human primates in vivo.,” *PLoS One*, vol. 6, no. 7, p. e22598, Jan. 2011.

[42] N. McDannold, G. T. Clement, P. Black, F. Jolesz, and K. Hynynen, “Transcranial magnetic resonance imaging- guided focused ultrasound surgery of brain tumors: initial findings in 3 patients.,” *Neurosurgery*, vol. 66, no. 2, p. 323–32; discussion 332, Feb. 2010.

[43] W. J. Elias, D. Huss, T. Voss, J. Loomba, M. Khaled, E. Zadicario, R. C. Frysinger, S. a Sperling, S. Wylie, S. J. Monteith, J. Druzgal, B. B. Shah, M.

Harrison, and M. Wintermark, “A pilot study of focused ultrasound thalamotomy for essential tremor.,” *N. Engl. J. Med.*, vol. 369, no. 7, pp. 640–8, Aug. 2013.

[44] N. Lipsman, M. Schwartz, Y. Huang, and L. Lee, “MR-guided focused ultrasound thalamotomy for essential tremor: a proof-of-concept study,” *Lancet …*, vol. 12, no. 5, pp. 462–468, May 2013.

[45] D. Jeanmonod, D. Moser, A. Magara, M. Kowalski, R. Bühler, P. Pourtehrani, T. Coray, and J. Vogel, “Current and Future Applications of Focused Ultrasound 2012, 3rd International Symposium,” in *Study on Incisionless Transcranial Magnetic Resonance-Guided Focused Ultrasound Treatment of Parkinson’s Disease: Safety, Accuracy and Clinical Outcomes*, p. 23.

[46] A. Magara, R. Bühler, D. Moser, M. Kowalski, P. Pourtehrani, and D. Jeanmonod, “First experience with MR-guided focused ultrasound in the treatment of Parkinson’s disease,” *J. Ther. Ultrasound*, vol. 2, no. 1, p. 11, 2014.

[47] W. J. Elias, N. Lipsman, W. G. Ondo, P. Ghanouni, Y. G. Kim, W. Lee, M. Schwartz, K. Hynynen, A. M. Lozano, B. B. Shah, D. Huss, R. F. Dallapiazza, R. Gwinn, J. Witt, S. Ro, H. M. Eisenberg, P. S. Fishman, D. Gandhi, C. H. Halpern, R. Chuang, K. Butts Pauly, T. S. Tierney, M. T. Hayes, G. R. Cosgrove, T. Yamaguchi, K. Abe, T. Taira, and J. W. Chang, “A Randomized Trial of Focused Ultrasound Thalamotomy for Essential Tremor.,” *N. Engl. J. Med.*, vol. 375, no. 8, pp. 730–739, Aug. 2016.

[48] D. Jeanmonod, B. Werner, and A. Morel, “Transcranial magnetic resonance imaging–guided focused ultrasound: noninvasive central lateral thalamotomy for chronic neuropathic pain,” *... Focus*, vol. 32, no. 1, p. E1, 2012.

[49] S. Monteith, R. Medel, and N. Kassell, “Transcranial magnetic resonance–guided focused ultrasound surgery for trigeminal neuralgia: a cadaveric and laboratory feasibility study: Laboratory investigation,” *J. …*, vol. 118, no. 2, pp. 319–28, 2013.

[50] E. Konofagou, “Ultrasound-Induced Blood-Brain Barrier Opening,” *Current Pharmaceutical Biotechnology*, vol. 13. 2012.

[51] G. Samiotaki and E. E. Konofagou, “Dependence of the reversibility of focused-ultrasound-induced blood-brain barrier opening on pressure and pulse length in vivo,” *IEEE Trans. Ultrason. Ferroelectr. Freq. Control*, vol. 60, pp. 2257–2265, 2013.

[52] K. Hynynen, N. McDannold, and N. Sheikov, “Local and reversible blood–brain barrier disruption by noninvasive focused ultrasound at frequencies suitable for trans-skull sonications,” *Neuroimage*, vol. 24, no. 1, pp. 12–20, Jan. 2005.

[53] N. McDannold and C. Arvanitis, “Temporary disruption of the blood–brain barrier by use of ultrasound and microbubbles: safety and efficacy evaluation in rhesus macaques,” *Cancer Res.*, vol. 72, no. 14, pp. 3652–3663, Jul. 2012.

[54] S. B. Raymond, L. H. Treat, J. D. Dewey, N. J. McDannold, K. Hynynen, and B. J. Bacskai, “Ultrasound enhanced delivery of molecular imaging and therapeutic agents in Alzheimer’s disease mouse models,” *PLoS One*, vol. 3, 2008.

[55] J. J. Choi, S. Wang, T. R. Brown, S. A. Small, K. E. K. Duff, and E. E. Konofagou, “Noninvasive and transient blood-brain barrier opening in the hippocampus of Alzheimer’s double transgenic mice using focused ultrasound.,” *Ultrason. Imaging*, vol. 30, no. 3, pp. 189–200, Jul. 2008.

[56] V. Frenkel, M. J. Stone, C. Deng, B. J. Wood, M. H. Iii, and K. C. P. Li, “Pulsed High-Intensity Focused Ultrasound Enhances Methods : Results : Conclusion :,” vol. 239, no. 1, 2006.

[57] G. J. Shaw, J. M. Meunier, S.-L. Huang, C. J. Lindsell, D. D. McPherson, and C. K. Holland, “Ultrasound-enhanced thrombolysis with tPA-loaded echogenic liposomes.,” *Thromb. Res.*, vol. 124, no. 3, pp. 306–10, Jul. 2009.

[58] T. Hölscher, D. J. Fisher, R. Raman, K. Ernstrom, E. Zadicario, W. G. Bradley, and A. Voie, “Neurology & Neurophysiology Noninvasive Transcranial Clot Lysis Using High Intensity Focused Ultrasound,” no. 1, pp. 1–6, 2011.

[59] S. T. Laing, M. Moody, B. Smulevitz, H. Kim, P. Kee, S. Huang, C. K. Holland, and D. D. McPherson, “Ultrasound-enhanced thrombolytic effect of tissue plasminogen activator-loaded echogenic liposomes in an in vivo rabbit aorta thrombus model-brief report,” *Arterioscler. Thromb. Vasc. Biol.*, vol. 31, pp. 1357–1359, 2011.

[60] M. J. Stone, V. Frenkel, S. Dromi, P. Thomas, R. P. Lewis, K. C. P. Li, M. Horne, and B. J. Wood, “Pulsed-high intensity focused ultrasound enhanced tPA mediated thrombolysis in a novel in vivo clot model, a pilot study,” *Thromb. Res.*, vol. 121, pp. 193–202, 2007.

[61] C. Damianou, V. Hadjisavvas, N. Mylonas, A. Couppis, and K. Ioannides, “MRI-guided sonothrombolysis of rabbit carotid artery,” *J. Stroke Cerebrovasc. Dis.*, vol. 23, 2014.

[62] C. Damianou, V. Hadjisavvas, and K. Ioannides, “In Vitro and In Vivo Evaluation of a Magnetic Resonance Imaging-guided Focused Ultrasound System for Dissolving Clots in Combination with Thrombolytic Drugs.,” *J Stroke Cerebrovasc Dis*, 2014.

[63] A. V Alexandrov, A. W. Wojner, and J. C. Grotta, “CLOTBUST: design of a randomized trial of ultrasound-enhanced thrombolysis for acute ischemic stroke,” *J Neuroimaging*, vol. 14, pp. 108–112, 2004.

[64] J. Broderick, “Combined Intravenous and Intra-Arterial Recanalization for Acute Ischemic Stroke: The Interventional Management of Stroke Study,” *Stroke*, vol. 35, pp. 904–911, 2004.

[65] M. Daffertshofer, A. Gass, P. Ringleb, M. Sitzer, U. Sliwka, T. Els, O. Sedlaczek, W. J. Koroshetz, and M. G. Hennerici, “Transcranial Low-Frequency Ultrasound-Mediated Thrombolysis in Brain Ischemia,” *Stroke*, vol. 36, pp. 1441–1446, 2005.

[66] C. Baron, J. F. Aubry, M. Tanter, S. Meairs, and M. Fink, “Simulation of Intracranial Acoustic Fields in Clinical Trials of Sonothrombolysis,” *Ultrasound Med. Biol.*, vol. 35, pp. 1148–1158, 2009.

[67] A. D. Barreto, V. K. Sharma, A. Y. Lao, P. D. Schellinger, P. Amarenco, P. Sierzenski, A. V. Alexandrov, and C. A. Molina, “Safety and dose-escalation study design of Transcranial Ultrasound in Clinical SONolysis for acute ischemic stroke: The TUCSON Trial,” *Int. J. Stroke*, vol. 4, pp. 42–48, 2009.

[68] K. Hynynen, N. McDannold, and G. Clement, “Pre-clinical testing of a phased array ultrasound system for MRI-guided noninvasive surgery of the brain—a primate study,” *Eur. J. …*, vol. 59, no. 2, pp. 149–156, Aug. 2006.

[69] N. McDannold, G. T. Clement, P. Black, F. Jolesz, and K. Hynynen, “Transcranial magnetic resonance imaging- guided focused ultrasound surgery of brain tumors: initial findings in 3 patients.,” *Neurosurgery*, vol. 66, no. 2, p. 323–32; discussion 332, Feb. 2010.

[70] G. R. Mundy, “Mechanisms of bone metastasis.,” *Cancer*, vol. 80, no. 8 Suppl, pp. 1546–1556, Apr. 1997.

[71] L. J. Suva, R. J. Griffin, and I. Makhoul, “Mechanisms of bone metastases of breast cancer,” *Endocr. Relat. Cancer*, vol. 16, no. 3, pp. 703–713, 2009.

[72] A. C. Society, “Cancer Facts and Figures,” *American Cancer Society;*, 2007. [Online]. Available: http://www.cancer.org/downloads/STT/CAFF2007PWSecured.pdf.

[73] R. E. Coleman, “Metastatic bone disease: clinical features, pathophysiology and treatment strategies.,” *Cancer Treat. Rev.*, vol. 27, no. 3, pp. 165–76, Jun. 2001.

[74] J. R. Berenson, L. Rajdev, and M. Broder, “Pathophysiology of bone metastases.,” *Cancer Biol. Ther.*, vol. 5, no. 9, pp. 1078–81, Sep. 2006.

[75] A. Delaney, S. M. Fleetwood-Walker, L. A. Colvin, and M. Fallon, “Translational medicine: cancer pain mechanisms and management.,” *Br. J. Anaesth.*, vol. 101, no. 1, pp. 87–94, Jul. 2008.

[76] O. M. Salazar, N. W. DaMotta, S. M. Bridgman, N. M. Cardiges, and R. G. Slawson, “Fractionated half-body irradiation for pain palliation in widely metastatic cancers: comparison with single dose,” *Int J Radiat Oncol Biol Phys*, vol. 36, no. 1, pp. 49–60, 1996.

[77] S. Pal, S. Dutta, S. S. Adhikary, B. Bhattacharya, B. Ghosh, and N. B. Patra, “Hemi body irradiation: An economical way of palliation of pain in bone metastasis in advanced cancer.,” *South Asian J. cancer*, vol. 3, no. 1, pp. 28–32, 2014.

[78] M. G. E. H. Lam, J. M. H. de Klerk, P. P. van Rijk, and B. A. Zonnenberg, “Bone seeking radiopharmaceuticals for palliation of pain in cancer patients with osseous metastases.,” *Anticancer. Agents Med. Chem.*, vol. 7, no. 4, pp. 381–97, Jul. 2007.

[79] D. Brady, C. C. Parker, and J. M. O’Sullivan, “Bone-targeting radiopharmaceuticals including radium-223.,” *Cancer J.*, vol. 19, no. 1, pp. 71–8, 2013.

[80] G. Rubini, A. Nicoletti, D. Rubini, and A. N. Asabella, “Radiometabolic

treatment of bone-metastasizing cancer: from 186rhenium to 223radium.," *Cancer Biother. Radiopharm.*, vol. 29, no. 1, pp. 1–11, 2014.

[81] W. Leppert, "The role of biphosphonates in the treatment of pain in patients with the dissemination to skeletal system," *Onkol. Pol.*, vol. 10, no. 4, pp. 164–168, 2007.

[82] U. Niang, S. Kamer, Z. Ozsaran, A. Haydaroglu, and S. Kilciksiz, "The management of painful bone metastases with biphosphonates and palliative radiotherapy: a retrospective evaluation of 372 cases.," *J. BUON.*, vol. 14, no. 2, pp. 245–9, 2009.

[83] M. Goblirsch, W. Mathews, C. Lynch, P. Alaei, B. J. Gerbi, P. W. Mantyh, and D. R. Clohisy, "Radiation Treatment Decreases Bone Cancer Pain, Osteolysis and Tumor Size," *Radiat. Res.*, vol. 161, no. 2, pp. 228–234, Feb. 2004.

[84] M. Huisman, M. A. A. J. van den Bosch, J. W. Wijlemans, M. van Vulpen, Y. M. van der Linden, and H. M. Verkooijen, "Effectiveness of reirradiation for painful bone metastases: a systematic review and meta-analysis.," *Int. J. Radiat. Oncol. Biol. Phys.*, vol. 84, no. 1, pp. 8–14, Sep. 2012.

[85] E. Wong, P. Hoskin, G. Bedard, M. Poon, L. Zeng, H. Lam, H. Vulpe, M. Tsao, N. Pulenzas, and E. Chow, "Re-irradiation for painful bone metastases - a systematic review.," *Radiother. Oncol.*, vol. 110, no. 1, pp. 61–70, Jan. 2014.

[86] L. Thanos, S. Mylona, P. Galani, D. Tzavoulis, V. Kalioras, S. Tanteles, and M. Pomoni, "Radiofrequency ablation of osseous metastases for the palliation of pain.," *Skeletal Radiol.*, vol. 37, no. 3, pp. 189–94, Mar. 2008.

[87] A. Kastler, H. Alnassan, S. Aubry, and B. Kastler, "Microwave thermal ablation of spinal metastatic bone tumors.," *J. Vasc. Interv. Radiol.*, vol. 25, no. 9, pp. 1470–5, Sep. 2014.

[88] K. Ahrar and R. J. Stafford, "Magnetic resonance imaging-guided laser ablation of bone tumors.," *Tech. Vasc. Interv. Radiol.*, vol. 14, no. 3, pp. 177–82, Sep. 2011.

[89] J. Bickels, Y. Kollender, O. Merimsky, J. Isaakov, R. Petyan-Brand, and I. Meller, "Closed argon-based cryoablation of bone tumours.," *J. Bone Joint Surg. Br.*, vol. 86, no. 5, pp. 714–8, Jul. 2004.

[90] D. B. Rodrigues, P. R. Stauffer, D. Vrba, and M. D. Hurwitz, "Focused ultrasound for treatment of bone tumours.," *Int. J. Hyperthermia*, vol. 31, no. 3, pp. 260–71, May 2015.

[91] R. Catane, a Beck, Y. Inbar, T. Rabin, N. Shabshin, S. Hengst, R. M. Pfeffer, a Hanannel, O. Dogadkin, B. Liberman, and D. Kopelman, "MR-guided focused ultrasound surgery (MRgFUS) for the palliation of pain in patients with bone metastases--preliminary clinical experience.," *Ann. Oncol.*, vol. 18, no. 1, pp. 163–7, Jan. 2007.

[92] D. Gianfelice, C. Gupta, W. Kucharczyk, P. Bret, D. Havill, and M. Clemons, "Palliative treatment of painful bone metastases with MR imaging--guided focused ultrasound.," *Radiology*, vol. 249, no. 1, pp. 355–63, Oct. 2008.

[93] A. Napoli, M. Anzidei, B. C. Marincola, G. Brachetti, F. Ciolina, G. Cartocci, C. Marsecano, F. Zaccagna, L. Marchetti, E. Cortesi, and C. Catalano, "Primary pain palliation and local tumor control in bone metastases treated with magnetic resonance-guided focused ultrasound.," *Invest. Radiol.*, vol. 48, no. 6, pp. 351–8, Jun. 2013.

[94] B. Liberman, D. Gianfelice, Y. Inbar, A. Beck, T. Rabin, N. Shabshin, G. Chander, S. Hengst, R. Pfeffer, A. Chechick, A. Hanannel, O. Dogadkin, and R. Catane, "Pain palliation in patients with bone metastases using MR-guided focused ultrasound surgery: a multicenter study.," *Ann. Surg. Oncol.*, vol. 16, no. 1, pp. 140–6, Jan. 2009.

[95] M. Hurwitz and P. Ghanouni, "Magnetic Resonance–Guided Focused Ultrasound for Patients With Painful Bone Metastases: Phase III Trial Results," *J. ...*, vol. 106, no. 5, pp. 1–9, May 2014.

[96] M. Huisman, M. K. Lam, L. W. Bartels, R. J. Nijenhuis, C. T. Moonen, F. M. Knuttel, H. M. Verkooijen, M. van Vulpen, and M. A. van den Bosch, "Feasibility of volumetric MRI-guided high intensity focused ultrasound (MR-HIFU) for painful bone metastases.," *J. Ther. ultrasound*, vol. 2, p. 16, Jan. 2014.

[97] B. Joo, M.-S. Park, S. H. Lee, H. J. Choi, S. T. Lim, S. Y. Rha, I. Rachmilevitch, Y. H. Lee, and J.-S. Suh, "Pain palliation in patients with bone metastases using magnetic resonance-guided focused ultrasound with conformal bone system: a preliminary report.," *Yonsei Med. J.*, vol. 56, no. 2, pp. 503–9, Mar. 2015.

[98] M. D. Hurwitz, P. Ghanouni, S. V Kanaev, D. Iozeffi, D. Gianfelice, F. M. Fennessy, A. Kuten, J. E. Meyer, S. D. LeBlang, A. Roberts, J. Choi, J. M. Larner, A. Napoli, V. G. Turkevich, Y. Inbar, C. M. C. Tempany, and R. M. Pfeffer, "Magnetic resonance-guided focused ultrasound for patients with painful bone metastases: phase III trial results.," *J. Natl. Cancer Inst.*, vol. 106, no. 5, May 2014.

[99] "World Cancer Research Fund international-Breast cancer statistics." [Online]. Available: http://www.wcrf.org/int/cancer-facts-figures/data-specific-cancers/breast-cancer-statistics.

[100] S. H. Landis, T. Murray, S. Bolden, and P. A. Wingo, "Cancer statistics, 1999.," *CA. Cancer J. Clin.*, vol. 49, no. 1, pp. 8–31, 1, Jan. .

[101] W. S. Halsted, "I. The Results of Radical Operations for the Cure of Carcinoma of the Breast.," *Ann. Surg.*, vol. 46, no. 1, pp. 1–19, Jul. 1907.

[102] J. R. C. Sainsbury, "Diseases of the breast. J. R. Harris, M. E. Lippman, M. Morrow and S. Hellman (eds). 285 × 225 mm. Pp. 1047. Illustrated. 1996. Philadelphia, Pennsylvania: Lippincott-Raven," *Br. J. Surg.*, vol. 83, no. 11, pp. 1660–1660, Nov. 1996.

[103] B. Fisher, C. Redmond, R. Poisson, R. Margolese, N. Wolmark, L. Wickerham, E. Fisher, M. Deutsch, R. Caplan, and Y. Pilch, "Eight-year results of a randomized clinical trial comparing total mastectomy and lumpectomy with or without irradiation in the treatment of breast cancer.," *N. Engl. J. Med.*, vol. 320, no. 13, pp. 822–8, Mar. 1989.

[104] G. ter Haar, “Ultrasound focal beam surgery.,” *Ultrasound Med. Biol.*, vol. 21, no. 9, pp. 1089–100, Jan. 1995.

[105] C. R. Hill and G. R. ter Haar, “Review article: high intensity focused ultrasound--potential for cancer treatment.,” *Br. J. Radiol.*, vol. 68, no. 816, pp. 1296–1303, Dec. 1995.

[106] C. Boetes, R. D. Mus, R. Holland, J. O. Barentsz, S. P. Strijk, T. Wobbes, J. H. Hendriks, and S. H. Ruys, “Breast tumors: comparative accuracy of MR imaging relative to mammography and US for demonstrating extent.,” *Radiology*, vol. 197, no. 3, pp. 743–7, Dec. 1995.

[107] H. Mumtaz, M. A. Hall-Craggs, T. Davidson, K. Walmsley, W. Thurell, M. W. Kissin, and I. Taylor, “Staging of symptomatic primary breast cancer with MR imaging.,” *AJR. Am. J. Roentgenol.*, vol. 169, no. 2, pp. 417–24, Aug. 1997.

[108] a H. Chung, F. a Jolesz, and K. Hynynen, “Thermal dosimetry of a focused ultrasound beam in vivo by magnetic resonance imaging.,” *Med. Phys.*, vol. 26, no. 9, pp. 2017–26, Sep. 1999.

[109] P. Huber, B. Stepanow, J. Debus, K. Jochle, M. Mory, J. Jenne, A. Werner, G. van Kaick, and W. J. Lorenz, “Temperature monitoring of focused ultrasound therapy by MRI,” in *Proceedings of IEEE Ultrasonics Symposium ULTSYM-94*, 1994, vol. 3, pp. 1825–1828 vol.3.

[110] K. Hynynen, O. Pomeroy, D. N. Smith, P. E. Huber, N. J. McDannold, J. Kettenbach, J. Baum, S. Singer, and F. a Jolesz, “MR imaging-guided focused ultrasound surgery of fibroadenomas in the breast: a feasibility study.,” *Radiology*, vol. 219, no. 1, pp. 176–85, Apr. 2001.

[111] P. E. Huber, J. W. Jenne, R. Rastert, I. Simiantonakis, H. P. Sinn, H. J. Strittmatter, D. von Fournier, M. F. Wannenmacher, and J. Debus, “A new noninvasive approach in breast cancer therapy using magnetic resonance imaging-guided focused ultrasound surgery.,” *Cancer Res.*, vol. 61, pp. 8441–8447, 2001.

[112] F. Wu, Z.-B. Wang, Y.-D. Cao, W.-Z. Chen, J. Bai, J.-Z. Zou, and H. Zhu, “A randomised clinical trial of high-intensity focused ultrasound ablation for the treatment of patients with localised breast cancer.,” *Br. J. Cancer*, vol. 89, no. 12, pp. 2227–33, Dec. 2003.

[113] D. Gianfelice, A. Khiat, M. Amara, A. Belblidia, and Y. Boulanger, “MR imaging-guided focused US ablation of breast cancer: histopathologic assessment of effectiveness-- initial experience.,” *Radiology*, vol. 227, no. 3, pp. 849–55, Jun. 2003.

[114] D. B. Zippel and M. Z. Papa, “The use of MR imaging guided focused ultrasound in breast cancer patients; a preliminary phase one study and review.,” *Breast Cancer*, vol. 12, no. 1, pp. 32–8, 2005.

[115] H. Furusawa, K. Namba, and S. Thomsen, “Magnetic resonance–guided focused ultrasound surgery of breast cancer: reliability and effectiveness,” *... Coll. Surg.*, vol. 203, no. 1, pp. 54–63, Jul. 2006.

[116] R. Kovatcheva, J.-N. Guglielmina, M. Abehsera, L. Boulanger, N. Laurent, and E. Poncelet, “Ultrasound-guided high-intensity focused ultrasound treatment of breast fibroadenoma-a multicenter experience.,” *J. Ther. ultrasound*, vol. 3, no. 1, p. 1, Jan. 2015.

[117] W. M. S. Russell and R. L. Burch, *The principles of humane experimental technique*. Methuen, 1959.

[118] R. and R. of A. in R. U. National Centre for the Replacement, “https://www.nc3rs.org.uk/the-3rs.” .

[119] L. Marsac, D. Chauvet, B. Larrat, and M. Pernot, “MR-guided adaptive focusing of therapeutic ultrasound beams in the human head,” *Med. …*, vol. 39, no. 2, p. 1141, 2012.

[120] D. Chauvet, L. Marsac, M. Pernot, A.-L. Boch, R. Guillevin, N. Salameh, L. Souris, L. Darrasse, M. Fink, M. Tanter, and J.-F. Aubry, “Targeting accuracy of transcranial magnetic resonance-guided high-intensity focused ultrasound brain therapy: a fresh cadaver model.,” *J. Neurosurg.*, vol. 118, no. 5, pp. 1046–52, May 2013.

[121] M. D. Eames, A. Hananel, J. W. Snell, N. F. Kassell, and J.-F. Aubry, “Trans-cranial focused ultrasound without hair shaving: feasibility study in an ex vivo cadaver model.,” *J. Ther. ultrasound*, vol. 1, p. 24, Jan. 2013.

[122] M. D. C. Eames, M. Farnum, M. Khaled, W. Jeff Elias, A. Hananel, J. W. Snell, N. F. Kassell, and J.-F. Aubry, “Head phantoms for transcranial focused ultrasound.,” *Med. Phys.*, vol. 42, no. 4, p. 1518, Apr. 2015.

[123] C. Damianou, V. Hadjisavvas, and K. Ioannides, “An MR-Compatible Plastic Phantom for Evaluating the Propagation of High Intensity Focused Ultrasound Through the Skull,” *Ultrasound Med. Biol.*, vol. 37, no. 8, pp. S73–S74, Aug. 2011.

[124] A. J. Clarke, J. A. Evans, J. G. Truscott, R. Milner, and M. A. Smith, “A phantom for quantitative ultrasound of trabecular bone.,” *Phys. Med. Biol.*, vol. 39, no. 10, pp. 1677–87, Oct. 1994.

[125] M. B. Tavakoli and J. A. Evans, “Dependence of the velocity and attenuation of ultrasound in bone on the mineral content.,” *Phys. Med. Biol.*, vol. 36, no. 11, pp. 1529–37, Nov. 1991.

[126] A. Tatarinov, I. Pontaga, and U. Vilks, “Modeling the influence of mineral content and porosity on ultrasound parameters in bone by using synthetic phantoms,” *Mech. Compos. Mater.*, vol. 35, no. 2, pp. 147–154, Mar. 1999.

[127] A. Tatarinov, N. Sarvazyan, and A. Sarvazyan, “Use of multiple acoustic wave modes for assessment of long bones: model study.,” *Ultrasonics*, vol. 43, no. 8, pp. 672–80, Aug. 2005.

[128] R. Hodgskinson, C. F. Njeh, M. A. Whitehead, and C. M. Langton, “The non-linear relationship between BUA and porosity in cancellous bone.,” *Phys. Med. Biol.*, vol. 41, no. 11, pp. 2411–20, Nov. 1996.

[129] E. L. Madsen, J. A. Zagzebski, R. A. Banjavie, and R. E. Jutila, “Tissue mimicking materials for ultrasound phantoms.,” *Med. Phys.*, vol. 5, no. 5, pp. 391–4, Jan. .

[130] J. R. Cook, R. R. Bouchard, and S. Y. Emelianov, “Tissue-mimicking phantoms for photoacoustic and ultrasonic imaging.,” *Biomed. Opt. Express*, vol. 2, no. 11, pp. 3193–206, Nov. 2011.

[131] R. Bude and R. Adler, “An easily made, low-cost, tissue-like ultrasound phantom material,” *J. Clin. ultrasound*, no. May, pp. 271–273, May 1995.

[132] E. L. Madsen, G. R. Frank, and F. Dong, “Liquid or solid ultrasonically tissue-mimicking materials with very low scatter.,” *Ultrasound Med. Biol.*, vol. 24, no. 4, pp. 535–42, May 1998.

[133] M. M. Burlew, E. L. Madsen, J. A. Zagzebski, R. A. Banjavic, and S. W. Sum, “A new ultrasound tissue-equivalent material.,” *Radiology*, vol. 134, no. 2, pp. 517–20, Feb. 1980.

[134] K. Zell, J. Sperl, and M. Vogel, “Acoustical properties of selected tissue phantom materials for ultrasound imaging,” *Phys. Med. …*, vol. 52, no. 20, pp. N475–N484, Oct. 2007.

[135] M. Gyöngy and C.-C. Coussios, “Passive spatial mapping of inertial cavitation during HIFU exposure.,” *IEEE Trans. Biomed. Eng.*, vol. 57, no. 1, pp. 48–56, Jan. 2010.

[136] A. Partanen, C. Mougenot, and T. Vaara, “Feasibility of Agar-Silica Phantoms in Quality Assurance of MRgHIFU,” *8TH Int. …*, vol. 1113, no. 1, pp. 296–300, 2009.

[137] T. Kondo, M. Kitatuji, and H. Kanda, “New tissue mimicking materials for ultrasound phantoms,” in *IEEE Ultrasonics Symposium, 2005.*, vol. 3, pp. 1664–1667.

[138] C. Lafon, V. Zderic, M. L. Noble, J. C. Yuen, P. J. Kaczkowski, O. a. Sapozhnikov, F. Chavrier, L. a. Crum, and S. Vaezy, “Gel phantom for use in high-intensity focused ultrasound dosimetry,” *Ultrasound Med. Biol.*, vol. 31, no. 10, pp. 1383–1389, Oct. 2005.

[139] M. R. Bailey, L. N. Couret, O. A. Sapozhnikov, V. A. Khokhlova, G. ter Haar, S. Vaezy, X. Shi, R. Martin, and L. A. Crum, “Use of overpressure to assess the role of bubbles in focused ultrasound lesion shape in vitro.,” *Ultrasound Med. Biol.*, vol. 27, no. 5, pp. 695–708, May 2001.

[140] K. Takegami, Y. Kaneko, T. Watanabe, T. Maruyama, Y. Matsumoto, and H. Nagawa, “Polyacrylamide gel containing egg white as new model for irradiation experiments using focused ultrasound,” *Ultrasound Med. Biol.*, vol. 30, no. 10, pp. 1419–1422, Oct. 2004.

[141] C. P. Labuda and C. C. Church, “Augmentation of HIFU-induced heating with fibers embedded in a phantom,” *Ultrasound Med. Biol.*, vol. 37, no. 3, pp. 442–449, Mar. 2011.

[142] M. J. Choi, S. R. Guntur, K. Il Lee, D. G. Paeng, and A. Coleman, "A tissue mimicking polyacrylamide hydrogel phantom for visualizing thermal lesions generated by high intensity focused ultrasound.," *Ultrasound Med. Biol.*, vol. 39, no. 3, pp. 439–48, Mar. 2013.

[143] Onda Corp, "http://www.ondacorp.com/products_hifusol_phantoms.shtml." .

[144] M.-K. Sun, J. Shieh, C.-W. Lo, C.-S. Chen, B.-T. Chen, C.-W. Huang, and W.-S. Chen, "Reusable tissue-mimicking hydrogel phantoms for focused ultrasound ablation," *Ultrason. Sonochem.*, vol. 23, pp. 399–405, Mar. 2015.

[145] K. Surry and H. Austin, "Poly (vinyl alcohol) cryogel phantoms for use in ultrasound and MR imaging," *Phys. Med. ...*, vol. 49, no. 24, pp. 5529–5546, Dec. 2004.

[146] I. Reinertsen and D. Collins, "A realistic phantom for brain-shift simulations," *Med. Phys.*, vol. 33, no. 9, pp. 3234–3240, 2006.

[147] M. Earle, G. De Portu, E. DeVos, M. Shorter, D. J. Macias, H. H. Kimberly, A. Murray, M. Mennicke, et al., P. Brass, M. Hellmich, L. Kolodziej, et al., S. Shah, B. A. Bellows, A. A. Adedipe, et al., M. Y. Woo, J. Frank, A. C. Lee, et al., V. Cheruparambath, S. Sampath, L. N. Deshikar, et al., S. Di Domenico, M. Licausi, E. Porcile, M. Wells, L. Goldstein, B. A. VanderWielen, R. Harris, R. E. Galgon, et al., S. Sparks, D. Evans, D. Byars, M. K. Sun, J. Shieh, C. W. Lo, and et al., "Agar ultrasound phantoms for low-cost training without refrigeration," *African J. Emerg. Med.*, vol. 6, no. 1, pp. 18–23, Mar. 2016.

[148] A. Dabbagh, B. J. J. Abdullah, C. Ramasindarum, and N. H. Abu Kasim, "Tissue-mimicking gel phantoms for thermal therapy studies.," *Ultrason. Imaging*, vol. 36, no. 4, pp. 291–316, Oct. 2014.

[149] A. I. Farrer, H. Odéen, J. de Bever, B. Coats, D. L. Parker, A. Payne, and D. A. Christensen, "Characterization and evaluation of tissue-mimicking gelatin phantoms for use with MRgFUS.," *J. Ther. ultrasound*, vol. 3, p. 9, Jan. 2015.

[150] C.-Y. Lai, D. Kruse, J. W. Seo, A. Kheirolomoom, and K. W. Ferrara, "A phantom for visualization of three-dimensional drug release by ultrasound-induced mild hyperthermia.," *Med. Phys.*, vol. 40, no. 8, p. 83301, Aug. 2013.

[151] S. Umchid, "Frequency dependent ultrasonic attenuation coefficient measurement," pp. 234–238, 2008.

[152] M. H. Youssef and N. K. Gobran, "Modified treatment of ultrasonic pulse-echo immersion technique," *Ultrasonics*, vol. 39, no. 7, pp. 473–477, Apr. 2002.

[153] R. G. Holt and R. A. Roy, "Measurements of bubble-enhanced heating from focused, MHz-frequency ultrasound in a tissue-mimicking material.," *Ultrasound Med. Biol.*, vol. 27, no. 10, pp. 1399–412, Oct. 2001.

[154] J. Huang, R. G. Holt, R. O. Cleveland, and R. A. Roy, "Experimental validation of a tractable numerical model for focused ultrasound heating in flow-through tissue phantoms.," *J. Acoust. Soc. Am.*, vol. 116, no. 4 Pt 1, pp. 2451–8, Oct. 2004.

[155] A. B. Nover, G. Y. Hou, Y. Han, S. Wang, G. D. O'Connell, G. A. Ateshian, E. E. Konofagou, and C. T. Hung, "High intensity focused ultrasound as a tool for tissue engineering: Application to cartilage.," *Med. Eng. Phys.*, vol. 38, no. 2, pp. 192–8, Feb. 2016.

[156] K. Nam, I. M. Rosado-Mendez, L. A. Wirtzfeld, A. D. Pawlicki, V. Kumar, E. L. Madsen, G. Ghoshal, R. J. Lavarello, M. L. Oelze, T. A. Bigelow, J. A. Zagzebski, W. D. O'Brien, and T. J. Hall, "Ultrasonic attenuation and backscatter coefficient estimates of rodent-tumor-mimicking structures: comparison of results among clinical scanners.," *Ultrason. Imaging*, vol. 33, no. 4, pp. 233–50, Oct. 2011.

[157] Stratasys, "ABS-M30 Spec Sheet." [Online]. Available: http://www.stratasys.com/materials/fdm/abs-m30.

[158] H. L. M. Cheng and D. B. Plewes, "Tissue thermal conductivity by magnetic resonance thermometry and focused ultrasound heating," *J. Magn. Reson. Imaging*, vol. 16, no. 5, pp. 598–609, 2002.

[159] H. Pennes, "Analysis of tissue and arterial blood temperatures in the resting human forearm," *J. Appl. Physiol.*, vol. 1, no. 2, pp. 93–122, 1948.

[160] H. E. Cline, K. Hynynen, C. J. Hardy, R. D. Watkins, J. F. Schenck, and F. A. Jolesz, "MR Temperature Mapping of Focused Ultrasound Surgery," *Magn. Reson. Med.*, vol. 31, no. 6, pp. 628–636, 1994.

[161] J. Hu, O. Sari, S. Eicher, and A. Rija Rakotozanakajy, "Determination of specific heat of milk at different fat content between 1 °C and 59 °C using micro DSC," *J. Food Eng.*, vol. 90, no. 3, pp. 395–399, 2009.

[162] M. O. Culjat, D. Goldenberg, P. Tewari, and R. S. Singh, "A review of tissue substitutes for ultrasound imaging," *Ultrasound Med. Biol.*, vol. 36, no. 6, pp. 861–873, Jun. 2010.

[163] C. Sehgal, "Scattering of ultrasound by tissues," *Ultrason. Imaging*, vol. 6, no. 1, pp. 60–80, Jan. 1984.

[164] D. K. Nassiri, D. Nicholas, and C. R. Hill, "Attenuation of ultrasound in skeletal muscle.," *Ultrasonics*, vol. 17, no. 5, pp. 230–2, Sep. 1979.

[165] P. Laugier and G. Haïat, "Introduction to the Physics of Ultrasound," in *Bone Quantitative Ultrasound*, Dordrecht: Springer Netherlands, 2011, pp. 29–45.

[166] K. A. Topp and W. D. O'Brien, "Anisotropy of ultrasonic propagation and scattering properties in fresh rat skeletal muscle in vitro.," *J. Acoust. Soc. Am.*, vol. 107, no. 2, pp. 1027–33, Feb. 2000.

[167] Y. Xia, W. Lin, and Y.-X. Qin, "The influence of cortical end-plate on broadband ultrasound attenuation measurements at the human calcaneus using scanning confocal ultrasound.," *J. Acoust. Soc. Am.*, vol. 118, no. 3 Pt 1, pp. 1801–7, Sep. 2005.

[168] J. Saulgozis, I. Pontaga, G. Lowet, and G. Van der Perre, "The effect of fracture and fracture fixation on ultrasonic velocity and attenuation.," *Physiol. Meas.*, vol.

17, no. 3, pp. 201–11, Aug. 1996.

[169] R. Lakes, H. S. Yoon, and J. L. Katz, “Ultrasonic wave propagation and attenuation in wet bone.,” *J. Biomed. Eng.*, vol. 8, no. 2, pp. 143–8, Apr. 1986.

[170] C. M. Langton, A. V Ali, C. M. Riggs, G. P. Evans, and W. Bonfield, “A contact method for the assessment of ultrasonic velocity and broadband attenuation in cortical and cancellous bone.,” *Clin. Phys. Physiol. Meas. an Off. J. Hosp. Phys. Assoc. Dtsch. Gesellschaft für Medizinische Phys. Eur. Fed. Organ. Med. Phys.*, vol. 11, no. 3, pp. 243–9, Aug. 1990.

[171] J. Wu and F. Cubberley, “Measurement of velocity and attenuation of shear waves in bovine compact bone using ultrasonic spectroscopy.,” *Ultrasound Med. Biol.*, vol. 23, no. 1, pp. 129–34, 1997.

[172] R. Zheng, L. H. Le, M. D. Sacchi, D. Ta, and E. Lou, “Spectral ratio method to estimate broadband ultrasound attenuation of cortical bones in vitro using multiple reflections.,” *Phys. Med. Biol.*, vol. 52, no. 19, pp. 5855–69, Oct. 2007.

[173] J. F. Aubry, M. Tanter, M. Pernot, J. L. Thomas, and M. Fink, “Experimental demonstration of noninvasive transskull adaptive focusing based on prior computed tomography scans.,” *J. Acoust. Soc. Am.*, vol. 113, no. 1, pp. 84–93, Jan. 2003.

[174] J. Crezee and J. J. Lagendijk, “Temperature uniformity during hyperthermia: the impact of large vessels.,” *Phys. Med. Biol.*, vol. 37, no. 6, pp. 1321–1337, 1992.

[175] C. J. Diederich, S. Clegg, and R. B. Roemer, “A spherical source model for the thermal pulse decay method of measuring blood perfusion: a sensitivity analysis.,” *Journal of biomechanical engineering*, vol. 111, no. 1. pp. 55–61, 1989.

[176] D. Siwek and R. Hoyt, “Anatomy of the Human Skull,” 2008. [Online]. Available: http://www.skullanatomy.info/basic_organization.htm.

[177] N. R. Pal and S. K. Pal, “A review on image segmentation techniques,” *Pattern Recognit.*, vol. 26, no. 9, pp. 1277–1294, Sep. 1993.

[178] M. R. Norton and C. Gamble, “Bone classification: an objective scale of bone density using the computerized tomography scan.,” *Clin. Oral Implants Res.*, vol. 12, no. 1, pp. 79–84, Mar. 2001.

[179] “Femur bone anatomy - Bone Disease.” [Online]. Available: http://www.bonedisease.info/human-body/femur-bone-anatomy/. [Accessed: 10-Mar-2017].

[180] I. Katz-Hanani, T. Rothstein, D. Gaitini, Z. Gallimidi, and H. Azhari, “Age-related ultrasonic properties of breast tissue in vivo.,” *Ultrasound Med. Biol.*, vol. 40, no. 9, pp. 2265–71, Sep. 2014.

[181] L. Zhang and Z.-B. Wang, “High-intensity focused ultrasound tumor ablation: review of ten years of clinical experience.,” *Front. Med. China*, vol. 4, no. 3, pp. 294–302, Sep. 2010.

[182] R. J. Stafford, R. E. Price, C. J. Diederich, M. Kangasniemi, L. E. Olsson, and J. D. Hazle, “Interleaved echo-planar imaging for fast multiplanar magnetic resonance temperature imaging of ultrasound thermal ablation therapy.,” *J. Magn. Reson. Imaging*, vol. 20, no. 4, pp. 706–14, Oct. 2004.

[183] C. Weidensteiner, B. Quesson, B. Caire-Gana, N. Kerioui, A. Rullier, H. Trillaud, and C. T. W. Moonen, “Real-time MR temperature mapping of rabbit liver in vivo during thermal ablation.,” *Magn. Reson. Med.*, vol. 50, no. 2, pp. 322–30, Aug. 2003.

[184] J. A. Bankson, R. J. Stafford, and J. D. Hazle, “Partially parallel imaging with phase-sensitive data: Increased temporal resolution for magnetic resonance temperature imaging.,” *Magn. Reson. Med.*, vol. 53, no. 3, pp. 658–65, Mar. 2005.

[185] V. Rieke and K. Butts Pauly, “MR thermometry.,” *J. Magn. Reson. Imaging*, vol. 27, no. 2, pp. 376–90, Feb. 2008.

[186] C. H. Seo, Y. Shi, S. Huang, K. Kim, and M. O’Donnell, “Thermal strain imaging: a review.,” *Interface Focus*, vol. 1, no. 4, pp. 649–64, 2011.

[187] R. Souchon, G. Bouchoux, E. Maciejko, C. Lafon, D. Cathignol, M. Bertrand, and J. Y. Chapelon, “Monitoring the formation of thermal lesions with heat-induced echo-strain imaging: A feasibility study,” *Ultrasound Med. Biol.*, vol. 31, no. 2, pp. 251–259, 2005.

[188] P. Tofts, *Quantitative MRI of the Brain: Measuring Changes Caused by Disease*. 2003.

[189] K. P. Whittall, A. L. MacKay, D. A. Graeb, R. A. Nugent, D. K. Li, and D. W. Paty, “In vivo measurement of T2 distributions and water contents in normal human brain.,” *Magn. Reson. Med.*, vol. 37, no. 1, pp. 34–43, Jan. 1997.

[190] J. Zhou, X. Golay, P. C. van Zijl, M. J. Silvennoinen, R. Kauppinen, J. Pekar, and M. Kraut, “Inverse T(2) contrast at 1.5 Tesla between gray matter and white matter in the occipital lobe of normal adult human brain.,” *Magn. Reson. Med.*, vol. 46, no. 2, pp. 401–6, Aug. 2001.

[191] P. Schmitt, M. A. Griswold, P. M. Jakob, M. Kotas, V. Gulani, M. Flentje, and A. Haase, “Inversion recovery TrueFISP: quantification of T(1), T(2), and spin density.,” *Magn. Reson. Med.*, vol. 51, no. 4, pp. 661–7, Apr. 2004.

[192] S. Steinhoff and M. Zaitsev, “Fast T1 mapping with volume coverage,” *Magn. Reson. …*, vol. C, pp. 131–140, 2001.

[193] A. Pfefferbaum, E. V Sullivan, M. Hedehus, M. Moseley, and K. O. Lim, “Brain gray and white matter transverse relaxation time in schizophrenia,” *Psychiatry Res. Neuroimaging*, vol. 91, no. 2, pp. 93–100, Aug. 1999.

[194] G. J. Stanisz, E. E. Odrobina, J. Pun, M. Escaravage, S. J. Graham, M. J. Bronskill, and R. M. Henkelman, “T1, T2 relaxation and magnetization transfer in tissue at 3T,” *Magn. Reson. Med.*, vol. 54, no. 3, pp. 507–512, Sep. 2005.

[195] G. E. Gold, E. Han, J. Stainsby, G. Wright, J. Brittain, and C. Beaulieu,

"Musculoskeletal MRI at 3.0 T: Relaxation Times and Image Contrast," *Am. J. Roentgenol.*, vol. 183, no. 2, pp. 343–351, Aug. 2004.

[196] R. Rakow-Penner, B. Daniel, H. Yu, A. Sawyer-Glover, and G. H. Glover, "Relaxation times of breast tissue at 1.5T and 3T measured using IDEAL.," *J. Magn. Reson. Imaging*, vol. 23, no. 1, pp. 87–91, Jan. 2006.

[197] R. A. E. Edden, S. A. Smith, and P. B. Barker, "Longitudinal and multi-echo transverse relaxation times of normal breast tissue at 3 Tesla.," *J. Magn. Reson. Imaging*, vol. 32, no. 4, pp. 982–7, Oct. 2010.

[198] "MRI - Radiology at St. Vincent's University Hospital." [Online]. Available: http://www.svuhradiology.ie/diagnostic-imaging/mri/. [Accessed: 11-Mar-2017].

[199] J. C. Hindman, "Proton Resonance Shift of Water in the Gas and Liquid States," *J. Chem. Phys.*, vol. 44, no. 12, p. 4582, May 1966.

[200] J. Yuan, C.-S. Mei, L. P. Panych, N. J. McDannold, and B. Madore, "Towards fast and accurate temperature mapping with proton resonance frequency-based MR thermometry.," *Quant. Imaging Med. Surg.*, vol. 2, no. 1, pp. 21–32, Jan. 2012.

[201] B. Quesson, "Magnetic resonance temperature imaging for guidance of thermotherapy," *... Magn. Reson. ...*, vol. 12, no. 4, pp. 525–533, 2000.

[202] K. Kuroda, K. Oshio, A. H. Chung, K. Hynynen, and F. A. Jolesz, "Temperature mapping using the water proton chemical shift: a chemical shift selective phase mapping method.," *Magn. Reson. Med.*, vol. 38, no. 5, pp. 845–51, Nov. 1997.

[203] A. Cernicanu and M. Lepetit-Coiffe, "Validation of fast MR thermometry at 1.5 T with gradient-echo echo planar imaging sequences: phantom and clinical feasibility studies," *NMR ...*, vol. 21, no. 8, pp. 849–858, 2008.

[204] Y. Ishihara, A. Calderon, H. Watanabe, K. Okamoto, Y. Suzuki, and K. Kuroda, "A precise and fast temperature mapping using water proton chemical shift.," *Magn. Reson. Med.*, vol. 34, no. 6, pp. 814–23, Dec. 1995.

[205] L. Chen, J. P. Wansapura, G. Heit, and K. Butts, "Study of laser ablation in the in vivo rabbit brain with MR thermometry.," *J. Magn. Reson. Imaging*, vol. 16, no. 2, pp. 147–52, Aug. 2002.

[206] K. Itoh, "Analysis of the phase unwrapping algorithm.," *Appl. Opt.*, vol. 21, no. 14, p. 2470, Jul. 1982.

[207] G. Domínguez-Guzmán, J. Castillo-Mixcóatl, G. Beltrán-Pérez, and S. Muñoz-Aguirre, "Itoh algorithm to unwrap 2D phase," in *Seventh Symposium on Optics in Industry*, 2009, p. 74990H–74990H–4.

[208] M. A. Herráez, D. R. Burton, M. J. Lalor, and M. A. Gdeisat, "Fast two-dimensional phase-unwrapping algorithm based on sorting by reliability following a noncontinuous path.," *Appl. Opt.*, vol. 41, no. 35, pp. 7437–44, Dec. 2002.

[209] W. M. Spees, N. Buhl, P. Sun, J. J. H. Ackerman, J. J. Neil, and J. R. Garbow,

"Quantification and compensation of eddy-current-induced magnetic-field gradients.," *J. Magn. Reson.*, vol. 212, no. 1, pp. 116–23, Sep. 2011.

[210] D. G. Hughes, S. Robertson, and P. S. Allen, "Intensity artifacts in MRI caused by gradient switching in an animal-size NMR magnet," *Magn. Reson. Med.*, vol. 25, no. 1, pp. 167–179, May 1992.

[211] "Therapy Transducers – Sonic Concepts, Inc.," *H-Transducers Series Datasheet*. [Online]. Available: http://sonicconcepts.com/therapy-transducers/. [Accessed: 30-Dec-2016].

[212] R. Salomir, J. Palussière, F. C. Vimeux, J. a de Zwart, B. Quesson, M. Gauchet, P. Lelong, J. Pergrale, N. Grenier, and C. T. Moonen, "Local hyperthermia with MR-guided focused ultrasound: spiral trajectory of the focal point optimized for temperature uniformity in the target region.," *J. Magn. Reson. Imaging*, vol. 12, no. 4, pp. 571–83, Oct. 2000.

[213] K. D. Price, V. W. Sin, C. Mougenot, S. Pichardo, T. Looi, A. C. Waspe, and J. M. Drake, "Design and validation of an MR-conditional robot for transcranial focused ultrasound surgery in infants," *Med. Phys.*, vol. 43, no. 9, pp. 4983–4995, Aug. 2016.

[214] *Determination of Signal-to-Noise Ratio (SNR) in Diagnostic Magnetic Resonance Imaging*, no. NEMA MS 1-2008 (R2014). 2015.

[215] J. W. Jenne, "Non-invasive transcranial brain ablation with high-intensity focused ultrasound.," *Front. Neurol. Neurosci.*, vol. 36, pp. 94–105, 2015.

[216] Y.-F. Zhou, "High intensity focused ultrasound in clinical tumor ablation.," *World J. Clin. Oncol.*, vol. 2, no. 1, pp. 8–27, Jan. 2011.

[217] D. L. Miller, N. B. Smith, M. R. Bailey, G. J. Czarnota, K. Hynynen, I. R. S. Makin, and A. I. of U. in M. B. Bioeffects Committee of the American Institute of Ultrasound in Medicine, "Overview of therapeutic ultrasound applications and safety considerations.," *J. Ultrasound Med.*, vol. 31, no. 4, pp. 623–34, Apr. 2012.

[218] P. Ghanouni, K. B. Pauly, W. J. Elias, J. Henderson, J. Sheehan, S. Monteith, and M. Wintermark, "Transcranial MRI-Guided Focused Ultrasound: A Review of the Technologic and Neurologic Applications.," *AJR. Am. J. Roentgenol.*, vol. 205, no. 1, pp. 150–9, Jul. 2015.

[219] V. Rieke, R. Instrella, J. Rosenberg, W. Grissom, B. Werner, E. Martin, and K. B. Pauly, "Comparison of temperature processing methods for monitoring focused ultrasound ablation in the brain.," *J. Magn. Reson. Imaging*, vol. 38, no. 6, pp. 1462–71, Dec. 2013.

[220] J.-F. Aubry, M. Tanter, M. Pernot, J.-L. Thomas, and M. Fink, "Experimental demonstration of noninvasive transskull adaptive focusing based on prior computed tomography scans," *J. Acoust. Soc. Am.*, vol. 113, no. 1, p. 84, Jan. 2003.

[221] N. Mylonas and C. Damianou, "MR compatible positioning device for guiding a focused ultrasound system for the treatment of brain deseases.," *Int. J. Med.*

Robot., vol. 10, no. 1, pp. 1–10, Mar. 2014.

[222] M. E. Ikink, M. J. Voogt, H. M. Verkooijen, P. N. M. Lohle, K. J. Schweitzer, A. Franx, W. P. T. M. Mali, L. W. Bartels, and M. A. A. J. van den Bosch, "Mid-term clinical efficacy of a volumetric magnetic resonance-guided high-intensity focused ultrasound technique for treatment of symptomatic uterine fibroids.," *Eur. Radiol.*, vol. 23, no. 11, pp. 3054–61, Nov. 2013.

[223] G. Menikou, C. Yiallouras, M. Yiannakou, and C. Damianou, "MRI-guided focused ultrasound robotic system for the treatment of bone cancer," *International Journal of Medical Robotics and Computer Assisted Surgery*, 2016.

[224] D. M. Nell and M. R. Myers, "Thermal effects generated by high-intensity focused ultrasound beams at normal incidence to a bone surface," *J. Acoust. Soc. Am.*, vol. 127, no. 1, pp. 549–559, Jan. 2010.

[225] C. Yiallouras, N. Mylonas, and C. Damianou, "MRI-compatible positioning device for guiding a focused ultrasound system for transrectal treatment of prostate cancer.," *Int. J. Comput. Assist. Radiol. Surg.*, vol. 9, no. 4, pp. 745–53, Jul. 2014.

[226] C. Yiallouras, K. Ioannides, T. Dadakova, M. Pavlina, M. Bock, and C. Damianou, "Three-axis MR-conditional robot for high-intensity focused ultrasound for treating prostate diseases transrectally.," *J. Ther. ultrasound*, vol. 3, p. 2, Jan. 2015.

[227] E. Epaminonda, T. Drakos, C. Kalogirou, M. Theodoulou, C. Yiallouras, and C. Damianou, "MRI guided focused ultrasound robotic system for the treatment of gynaecological tumors.," *Int. J. Med. Robot.*, vol. 12, no. 1, pp. 46–52, Mar. 2016.

[228] *ASTM F2503 - 13 Standard Practice for Marking Medical Devices and Other Items for Safety in the Magnetic Resonance Environment*. .

[229] F. Fry and J. Barger, "Acoustical properties of the human skull," *... J. Acoust. Soc. Am.*, vol. 63, no. May, pp. 1576–1590, 1978.

[230] G. Pinton, J. Aubry, E. Bossy, M. Muller, and M. Pernot, "Attenuation , scattering , and absorption of ultrasound in the skull bone Attenuation , scattering , and absorption of ultrasound in the skull bone," vol. 299, 2012.

[231] S. Han, J. Rho, J. Medige, and I. Ziv, "Ultrasound velocity and broadband attenuation over a wide range of bone mineral density.," *Osteoporos. Int.*, vol. 6, no. 4, pp. 291–6, 1996.

[232] M. Sasso, G. Haïat, Y. Yamato, S. Naili, and M. Matsukawa, "Frequency Dependence of Ultrasonic Attenuation in Bovine Cortical Bone: An In Vitro Study," *Ultrasound Med. Biol.*, vol. 33, no. 12, pp. 1933–1942, 2007.

[233] J. M. Alves, W. Xu, D. Lin, R. S. Siffert, J. T. Ryaby, and J. J. Kaufman, "Ultrasonic assessment of human and bovine trabecular bone: a comparison study," *IEEE Trans. Biomed. Eng.*, vol. 43, no. 3, pp. 249–58, 1996.

[234] K. Il Lee, H.-S. Roh, and S. W. Yoon, "Acoustic wave propagation in bovine

cancellous bone: application of the Modified Biot-Attenborough model.," *J. Acoust. Soc. Am.*, vol. 114, no. 4 Pt 1, pp. 2284–2293, 2003.

[235] J. E. Kennedy, "High-intensity focused ultrasound in the treatment of solid tumours.," *Nat. Rev. Cancer*, vol. 5, no. 4, pp. 321–7, Apr. 2005.

[236] B. E. Billard, K. Hynynen, and R. B. Roemer, "Effects of physical parameters on high temperature ultrasound hyperthermia.," *Ultrasound Med. Biol.*, vol. 16, no. 4, pp. 409–20, 1990.

[237] Zabolotskaya and E. A., "Quasiplane waves in the nonlinear acoustics of confined beams," *Sov. Phys. Acoust.*, vol. 15, pp. 35–40, 1969.

[238] H. H. Pennes, "Analysis of tissue and arterial blood temperatures in the resting human forearm.," *J. Appl. Physiol.*, vol. 1, no. 2, pp. 93–122, Aug. 1948.